UNIVERSITY
OF TRENTO - Italy
Department of Materials Engineering
and Industrial Technologies

Doctorate School in Materials Engineering – XX cycle

Preparation and properties of micro- and nanocomposites based on high density polyethylene

Matteo Traina

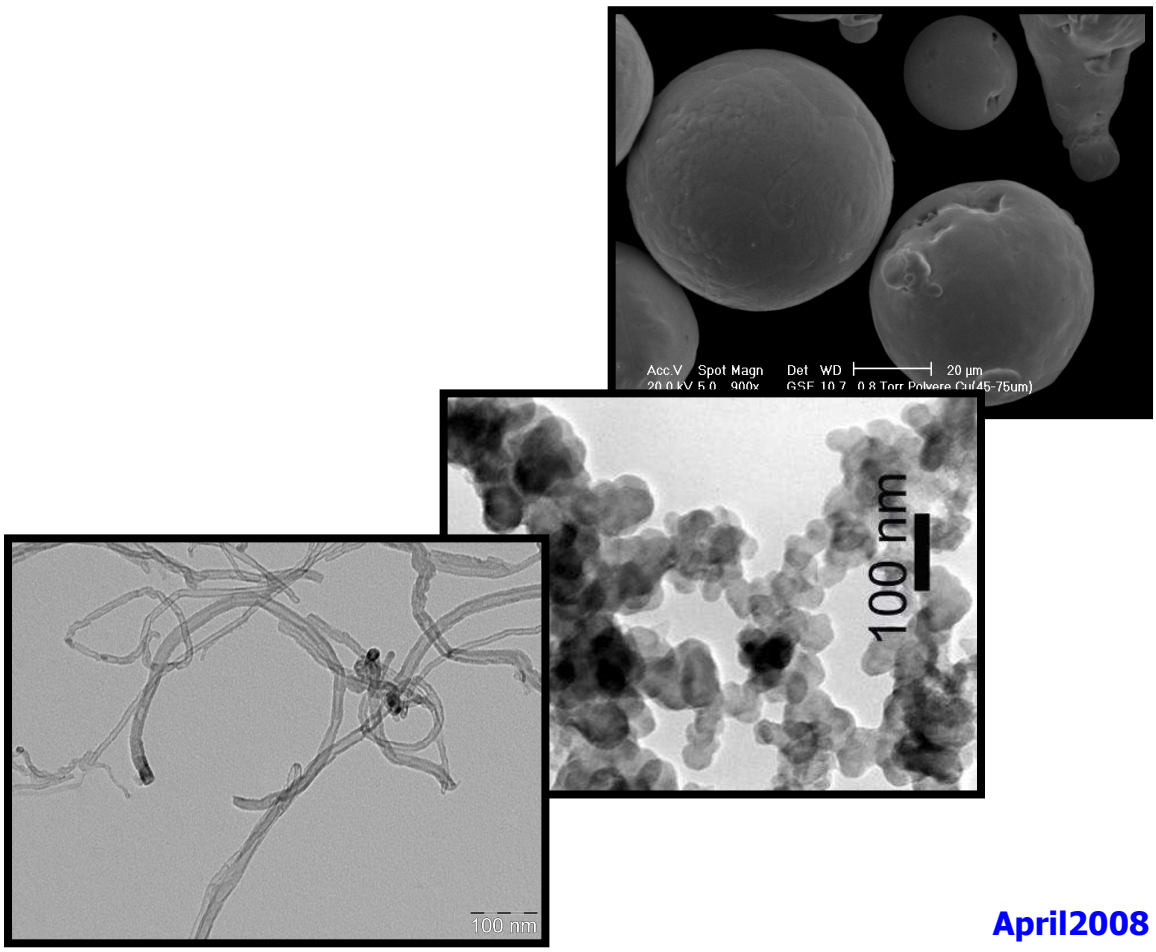

April2008

UNIVERSITY
OF TRENTO - Italy
Department of Materials Engineering
and Industrial Technologies

Doctorate School in Materials Engineering – XX cycle

Preparation and properties of micro- and nanocomposites based on high density polyethylene

Matteo Traina

Tutors:

prof. Amabile Penati

prof. Alessandro Pegoretti

April2008

Table of Contents

List of figures

List of tables

Acronyms

BET	Brunauer-Emmet-Teller (procedure)
CB	carbon black
CNT	carbon nanotube
DBP	dibutyl phthalate
DENT	double edge notched tension
DMTA	dynamic mechanical thermal analysis
DSC	differential scanning calorimetry
EDAX	energy dispersive X-ray (spectroscopy) analysis
EWF	essential work of fracture
FTIR	Fourier transform infrared spectroscopy
GPC	gel permeation chromatography
HDPE	high density polyethylene
LDPE	low density polyethylene
MA-g-PE	maleated polyethylene
MFI	melt flow index
MWCNT	multiwalled carbon nanotube
OAN	oil adsorption number
OM	optical microscope
PC	polycarbonate
PET	polyethylene terephthalate
PP	polypropylene
PS	polystyrene
PVOH	polyvinyl alcohol
SEM	scanning electron microscopy
SWCNT	single-walled nanotube
TEM	transmission electron microscope
TGA	thermogravimetric analysis
WLF	Williams, Landel and Ferry (equation)

Abstract

The primary objectives of this thesis were to investigate and compare the fracture and creep behaviour of micro- and nanocomposites based on polyethylene (PE) produced by melt mixing. To achieve these objectives, different fillers were considered: micrometric copper particles, nanometric carbon blacks (CBs) and multiwalled carbon nanotubes (MWCNTs).

In the first part of this dissertation, the fracture behaviour of PE-CB composites was investigated via the *Essential Work of Fracture* (EWF) approach by producing composites with different CBs in order to investigate the effect of the filler particle size. Moreover, several processing (i.e., extrusion) parameters were varied to obtain different degrees of filler dispersion. Experimental results reveal that fracture toughness increases significantly when CB particle size is smaller and as the *extent of dispersion* of the filler in the polymer matrix is better. Fracture toughness depends on the thermo-mechanical degradation of the polymer matrix that occurs during extrusion.

In the second part of this project, creep behaviour of PE-based composites was investigated at several temperatures with assistance from the *principle of time-temperature superposition*. In particular, the effect of filler dimensions was analyzed by comparing viscoelastic results for composites that contain micrometric copper particles (with an average diameter of 15 and 45 μm) and nanometric carbon blacks (with an average diameter of 15 and 30 nm). In general, these fillers substantially increase the creep resistance of PE, and this phenomenon was more prominent at smaller particle size. This effect was detectable in the linear viscoelastic region (i.e. at low stresses or temperatures), and it became more evident in the non-linear viscoelastic region (i.e. at high stresses or temperatures). In particular, creep compliance and creep rate decrease at smaller particle size. It is postulated that filler particles function as physical crosslink junctions which hinder polymer chain motion and reduce creep deformation. When particle size is reduced at constant filler volume fraction, the physical crosslink density increases such that chain mobility decreases significantly under stress.

Finally, the creep behaviour of PE-MWCNT composites were investigated via direct dispersion of MWCNT in the polymer matrix and by using a commercial masterbatch of MWCNT. In all cases, the increase in creep resistance is statistically significant in the linear viscoelastic region (i.e. at low

stresses or temperatures) when sufficient dispersion of the nanotubes is achieved. Interestingly enough, creep resistance increases in the non-linear viscoelastic region (i.e. at high stresses or temperatures) regardless of the *degree of nanotube dispersion* in the matrix. This phenomenon is attributed to nanotube orientation induced by high levels of stress.

1 Introduction

Polymer composite materials hold a very important position in the world of plastic materials: the addition of an inorganic fillers allows to adjust the physical, mechanical, thermal and electrical properties of polymeric matrices in relation to the application. From a general point of view they are employed in several fields such as automotive, medical, aerospace, sports and recreation, renewable energies, and so on. In recent years the filler particle dimensions progressively decreased from micrometric to nanometric range and for this reasons the term *nanocomposites* has been introduced [1-5]. The main thrust of this route is related to the possibility to improve the properties of the materials with lower filler content (in the order of 0.5 to 5 wt%) and to the possibility have materials with new properties not reachable with traditional micrometric fillers (as for example transparency and smoothness). Both industrial and academic world look with great interest to the development of new nanocomposite materials: in fact, according to the ISI Web of Science database [6], about 10000 papers published in scientific journal in the period 1990-2008 contain the keywords “nanocomposite*” and “polymer*”, where the asterisk is a wild character. A considerable amount of work in order to improve products and manufacturing processes for a wide range of applications.

The aim of this work was mainly to investigate and compare the properties of micro- and nanocomposites based on polyethylene matrix that still represents one of the most used and versatile polymers [7]. In particular, to achieve these purposes, different kinds of composites were considered:

- ***microcomposites with micrometric inorganic fillers with a low aspect ratio***.
  In this case the composites were based on high density polyethylene (HDPE) and low density polyethylene (LDPE) matrices filled with micrometric copper (Cu) and iron (Fe) particles. In both cases two different dimensions of Cu and Fe powders were considered: a powder with a nominal characteristic dimension of 10 μm or less (but always in micrometer range) and a powder with a nominal characteristic dimension of 50 μm or more. These

composites were produced by melt mixing in a twin screw extruder and then injection or compression moulding (see chapter 4);

- ***nanocomposites with nanometric inorganic fillers with a low aspect ratio.***
  In this case the composites were based on HDPE matrix filled with several carbon blacks (CBs) having different specific surface areas, i.e. primary particle dimensions. These composites were produced by melt mixing in a twin screw extruder: the produced materials were grounded and extruded several times in order to achieve different degrees of dispersion of the filler in the matrix (see chapter 5);
- ***nanocomposites with nanometric inorganic fillers with an high aspect ratio.***
  In this case the composites were filled with multiwalled carbon nanotubes (MWCNTs). In a first part of the work, MWCNTs were dispersed in the HDPE matrix through a commercial masterbatch and the effect of the addition of a maleated polyethylene (MA-g-PE) was evaluated. These composites were produced by melt mixing in an internal mixer (see chapter 6). In a second part of the work, the MWCNTs were directly dispersed in the polymeric matrix. In this case HDPE and polyvinyl alcohol (PVOH) were used as polymeric matrices by using melt mixing (i.e. a twin screw extruder and an internal mixer) and solution mixing with the help of sonication (see chapter 7).

These materials were mainly characterized in terms of creep behaviour and fracture behaviour. In particular the creep behaviour was analyzed because the literature offers limited data on the comparison between micro- and nanocomposites (see paragraph 2.3.2). In more detail:

- HDPE-CB composites were used to analyze *the effect of filler **dispersion** and **dimension** (in the nanometric range) on the **fracture** behaviour*. In particular the Essential Work of Fracture (EWF) approach was considered because this method is particularly indicated for a fracture mechanics approach on materials with high ductility as HDPE (see paragraph 2.2);
- HDPE-Cu and HDPE-CB composites were used to analyze *the effect of the filler **dimension** (from micrometric to nanometric range) on the **creep** behaviour*. In particular the creep behaviour was investigated with short term tests (i.e. one hour for each test) by varying temperatures and applied stresses in order to evaluate the creep behaviour in the linear and in the non-linear viscoelastic region. Moreover, creep compliance master curves (i.e. the extrapolation of the creep behaviour on very long times) was elaborated (see paragraph 2.1). Even if marginally, HDPE-CB composites were also used to evaluate the effect of filler dispersion on the creep behaviour;
- HDPE-CB and HDPE-MWCNT composites were used to analyze *the effect of the filler **aspect ratio** on the **creep** behaviour* as in previous case. In particular HDPE-MWCNT

composites based on a commercial masterbatch of MWCNT were considered, and limited data were collected for HDPE-MWCNT composites base on MWCNTs directly dispersed in the polymeric matrix. It is worthwhile to observe as this part could be very interesting because the rather limited literature available for MWCNT filled composites (see paragraph 2.3.2).

In addition, several tools were used in order to correlate the fracture and creep behaviour to the microstructure of the produced. Most of all optical and electron microscopy to evaluate the filler dispersion; thermogravimetric and calorimetric analyses to evaluate the thermal behaviour; rotational rheometry to evaluate the rheological behaviour; and chromatography to evaluate the molecular weight distribution.

Even if the main part of this work is focused on a comparison of fracture and creep behaviour of micro- and nanocomposites, a certain amount of work regarded the production of *MWCNT filled composites* characterized by a good dispersion of the filler (see chapter 7). In particular:

- untreated MWCNTs (as purchased by the supplier) were directly dispersed in HDPE by using a twin screw extruder and an internal mixer with different setups in order to evaluate the effect of different processing conditions on the filler dispersion;
- the untreated MWCNTs (as purchased by the supplier) were directly dispersed in PVOH aqueous solution with the help of sonication in order to evaluate the advantages of solution mixing techniques in comparison to melt mixing techniques.

In this case the tools used to characterize the produced materials were concentrated to the evaluation of the filler dispersion and only few experiments were performed to evaluate the creep behaviour of these materials.

In addition modification treatments were attempted on the untreated MWCNTs (as purchased by the supplier) in order to improve the quality of the MWCNTs and the interaction with the polymeric matrix. In particular, MWCNTs were boiled in nitric acid to remove the impurities (as nanofiber, amorphous carbon and residual catalysts) and to introduce new chemical groups on the MWCNT surface. Moreover, a modification treatment with silane coupling agents was conducted in order to introduce short polymeric chains compatible with polyethylene on the MWCNT surface.

2 Background

2.1 Viscoelastic behaviour

The distinction between solid (or elastic) and liquid (or viscous) is not an absolute distinction between different classes of materials: the ability to detect elastic or viscous responses depends in many cases on the time scale of the experiment. In this way, from a strict point of view, all the materials have a viscoelastic behaviour, i.e. the strain do not depends only on the applied stress, but on the previous history of the material. Polymers are the most important viscoelastic systems [8-12]. The viscoelastic behaviour is investigated with several method: in this work creep experiments and dynamical experiments were adopted.

2.1.1 Creep loading condition

In a creep experiment a constant stress σ_0 is applied to a sample and the strain ε is monitored as a function of time t. Normally the strain increases with time and creep curves (i.e. strain as function of time) may exhibit three regions (Figure 2.1): *primary* creep in which the curve in concave down, *secondary* creep in which deformation is proportional to time, and *tertiary* creep in which deformation accelerates until creep rupture occurs. Similarly the strain rate $\dot{\varepsilon}$, i.e. the derivative of the strain, may exhibit three regions.

The material has a *linearly* viscoelastic behaviour if the stress is proportional to the strain at a given time: in this case it is also possible to apply the linear superposition principle. However, linearity does not hold at high strains: creep isochrones diagrams, i.e. curves of stress as a function of strain at a given time, may evidence the transition from linear to nonlinear behaviour in creep experiments (Figure 2.2).

The creep *compliance* function is the ratio of the strain to the stress and is generally a function of time. In linearly viscoelastic materials, the creep compliance is independent of the stress level.

Equation 2.1

$$D(t) = \frac{\varepsilon(t)}{\sigma_0}$$

Moreover, a compliance rate $\dot{D}$ can be defined as the derivative of the compliance over the time. Total strain at any instant of time $\varepsilon(t)$ in a creep test of a linear materials may be represented as the sum of the instantaneous elastic strain ε_E (i.e. the initial strain when the constant stress is applied) and the viscoelastic strain ε_V. Similarly the compliance can be divided into elastic and viscous components.

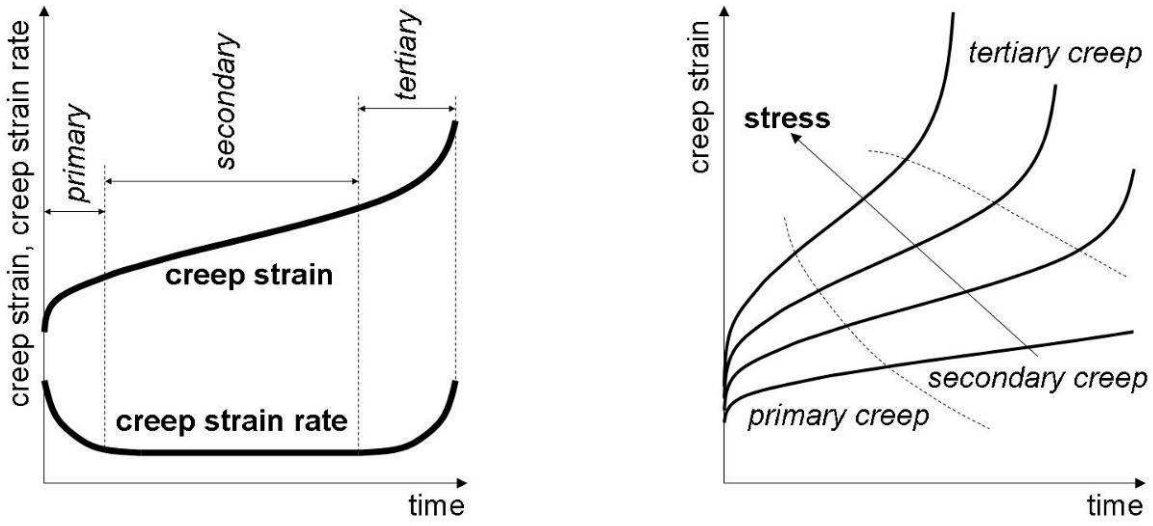

Figure 2.1. Creep strain and strain rate as a function of time at different applied stresses.

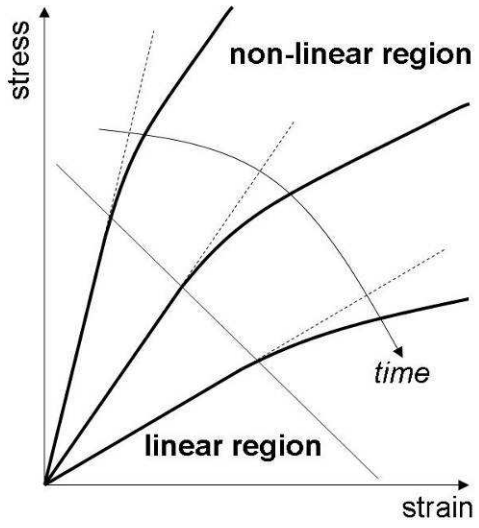

Figure 2.2. Isochronous stress-strain curves in creep experiments.

2.1.1.1 Linear superposition principle

As seen in the previous paragraph, linear viscoelasticity implies a *linear superposition principle.* These systems may be modelled as arrangements of springs (i.e. an elastic solid) and dashpots (i.e. a viscous liquid). The spring represents Hookean deformation (i.e. an element in which the force is proportional to the extension) and the dashpot Newtonian flow (i.e. an element in which the force is proportional to the strain rate). The behaviour of more complicated materials is described by connecting the basic elements in series or in parallel. In other words, stress, strain and time can be related with the characteristic constant of the mechanical elements. The overall system (*mechanical model*) behaves analogously to a real material, although the elements themselves may have no direct analogues in the actual material.

The basic configurations are the Kelvin (or Voigt) model and the Maxwell model (Figure 2.3). The first one results from a parallel combination of a spring and a dashpot, while the second one is represented by a spring connected in series with a dashpot. In both system a characteristic time τ, that is the ratio of the viscosity η (dashpot) to the elastic modulus E (spring), describes the viscoelastic behaviour of the material. This parameter is called *retardation time* for the Kelvin model, while *relaxation time* for the Maxwell model.

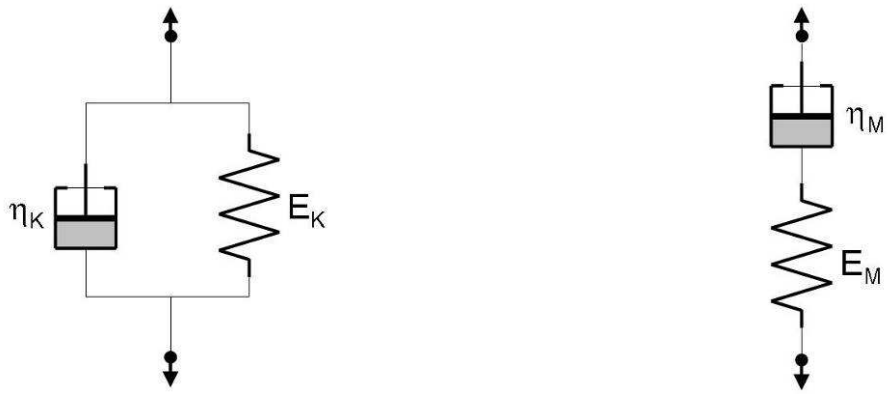

Figure 2.3. The simplest linear viscoelastic models: (a) the Kelvin model and (b) the Maxwell model.

More complicated and complex models could be introduced, but all the models can be reduced to two canonical forms. These are usually taken to be the generalized Voigt-Kelvin model and the generalized Maxwell-Wiechert model (Figure 2.4). The generalized Maxwell-Wiechert model may have a finite number or an enumerable infinity of Maxwell elements, each with a different relaxation time, and similarly the generalized Voigt-Kelvin model may have a finite number or an enumerable infinity of Kelvin elements. Thus, by a suitable choice of the model parameters, the

canonical forms themselves can be shown to be mechanically equivalent and it is also possible to compute the parameters of one canonical form from those of the other.

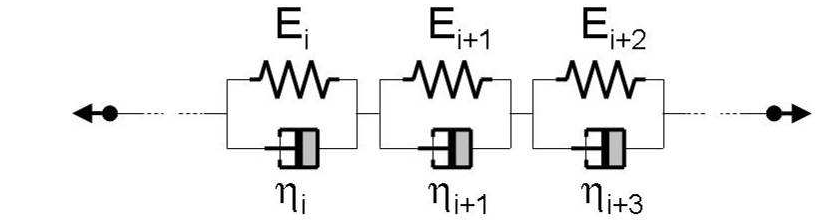

(a)

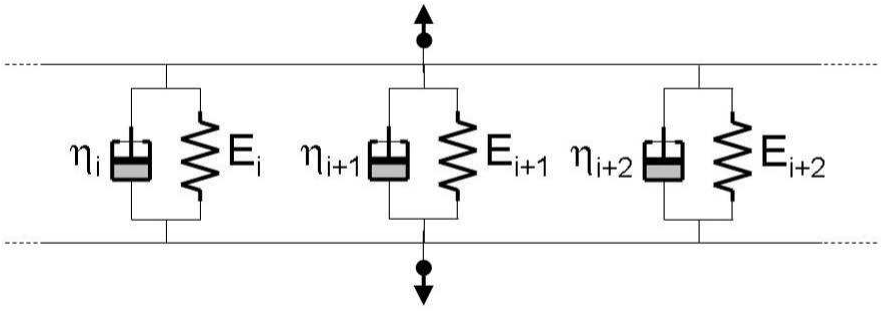

(b)

Figure 2.4. The generalized Maxwell-Wiechert model (a) and the generalized Kelvin model (b).

In this way, by taking into account the generalized models, an enumerable infinity or a continuous distribution of retardation or relaxation times is obtained. In particular the strain as a function of time with the generalized Kelvin model for a system with n pairs of elements has the following expression:

Equation 2.2

$$\varepsilon(t) = \sum_{i=1}^{n} \frac{1}{E_i \tau_i} \int_{-\infty}^{t} \{1 - \exp[-(t-t')/\tau_i]\} \sigma(t') dt'$$

where η_i and τ_i are the viscosity and the retardation times of the i.th Kelvin element. The extension to a continuous distribution of relaxation times is employed by introducing the *distribution function of retardation times* (or *retardation spectrum*) $N'(1/\tau)$: in detail $N'(1/\tau)d\tau$ represents the contributions to the total modulus of all the Kelvin elements with relaxation times lying between τ and $\tau + d\tau$. The strain equation becomes:

Equation 2.3

$$\varepsilon(t) = \int_{-\infty}^{t} \left\{ \int_{0}^{+\infty} \frac{N'(1/\tau)}{\tau} \{1 - \exp[-(t-t')/\tau]\} d\tau \right\} \sigma(t') dt'$$

Alternatively the retardation spectrum function $L(\tau) = N'(1/\tau)/\tau$ can be used.

The approximate value of $L(\tau)$ can be derived from the creep compliance function $D(t)$ by means of the relationship:

Equation 2.4

$$L(\tau) \cong D(t) \frac{d \log D(t)}{d \log t}\bigg|_{t=\tau}$$

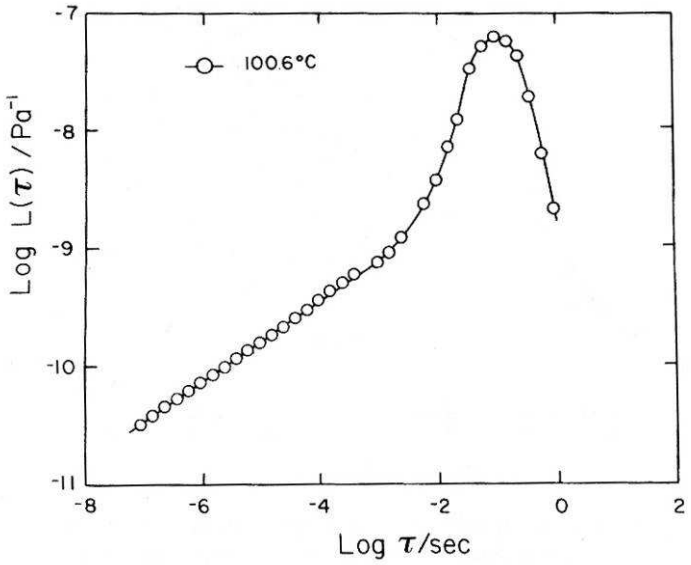

Figure 2.5. Example of retardation spectrum for polystyrene with a narrow molecular weight distribution [13]. The weight average molecular weight is 3.4 kDa.

2.1.1.2 Time-temperature superposition principle

The viscoelastic functions, i.e. the creep compliance as a function of the time, depend on the temperature too. Theoretical and experimental results indicate that for many materials the effect due to time and temperature in the linearly viscoelastic region can be combined into a single parameter trough the concept of the *time-temperature superposition principle* which implies that the following relations exist:

Equation 2.5

$$D(T,t) = D(T_0, t^*)$$

$$t^* = t / a_{T_0}(T)$$

where T is the temperature and t^* the *reduced time*. The reduced time is related to the real time t by the temperature *shift factor* $a_{T_0}(T)$ and T_0 is the reference temperature. In this way the effect of temperature on time-dependent mechanical behaviour is equivalent to a stretching (or shrinking) of real time for temperatures above (or below) the reference temperature; or alternatively, since viscoelastic properties are usually plotted as a function of the logarithm of time or frequency, a temperature change corresponds to a rigid horizontal shift of the material property curves on the abscissa. In other words, high-temperature response is analogous to low-strain-rate behaviour, and low-temperature response corresponds to high-strain-rate behaviour. Thus, the determination of the temperature shift factor $a_{T_0}(T)$ as a function of temperature will provide the necessary information for determination of the reduced time.

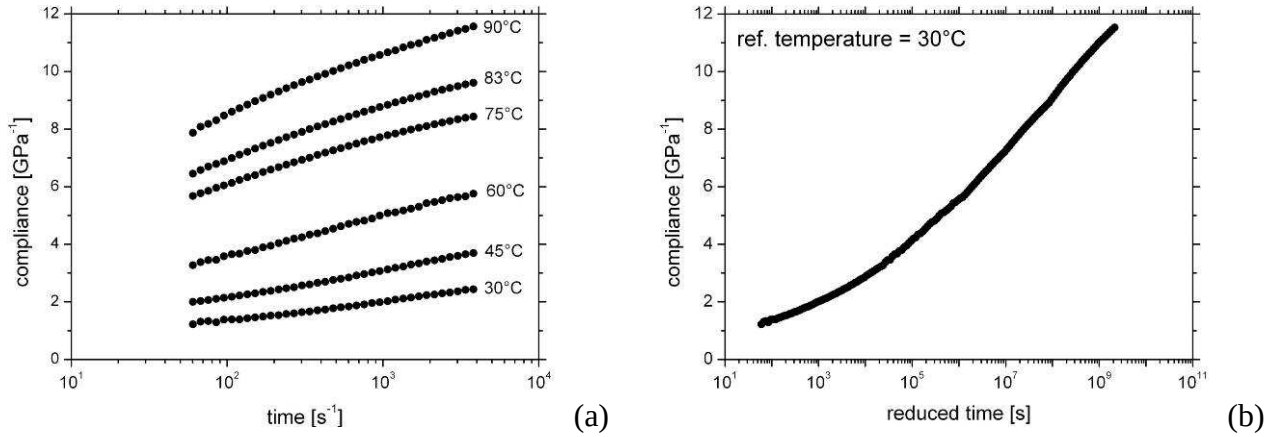

Figure 2.6. Example of master curve (b) from short term creep tests at different temperature (a). The data refers to an HDPE09 extruded 1x (see chapter 5).

Many materials exhibit temperature-creep behaviour that follows the Arrhenius relation for temperature lower than the glass temperature and the relation proposed by Williams, Landel and Ferry (WLF equation) for higher temperatures.

Equation 2.6

$$\ln a_{T_0}(T) = \frac{\Delta H}{R}\left(\frac{1}{T} - \frac{1}{T_0}\right) \qquad \text{(Arrhenius equation)}$$

Equation 2.7

$$\log a_{T_0}(T) = -\frac{C_1(T - T_0)}{C_2 + (T - T_0)} \quad \text{(WLF equation)}$$

In these expressions ΔH is an activation energy, R the ideal gas constant, and C_1 and C_2 are empirical constants that depend on the material. Experimentally, for many linear amorphous polymers, if the reference temperature is the glass transition temperature, the values of the constants in the WLF equation are independent of chemical structure ($C_1 = 17.44$ and $C_2 = 51.6$). Moreover the product of C_1 and C_2 (for any reference temperature) is almost always 900K.

The curves constructed on the basis of a time-temperature superposition principle are generally denoted as *master curves*.

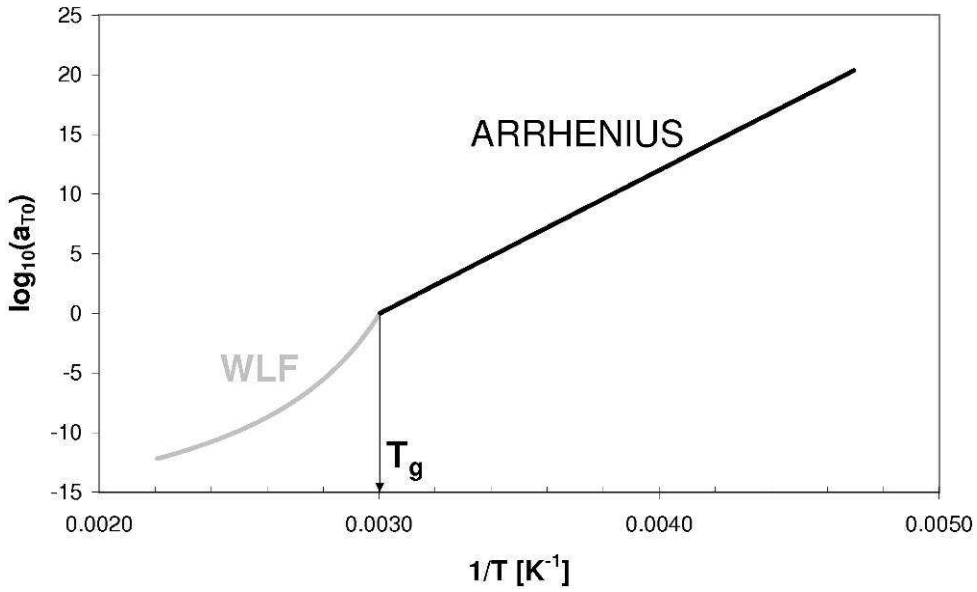

Figure 2.7. Example of shift factor as a function o temperature.

2.1.2 Dynamic loading condition

In dynamical experiment a sinusoidal strain $\varepsilon(t)$, with an amplitude ε_0 and a frequency ω, is imposed on a sample: the output stress $\sigma(t)$, that follows a sinusoidal function with an amplitude σ_0 and a phase shift δ, is monitored. These data can be analyzed in following terms:

- the *storage modulus* $E'(\omega) = (\sigma_0/\varepsilon_0)\cos(\delta)$, that is related to output stress components in phase with the applied strain;

- the loss modulus $E''(\omega)=(\sigma_0/\varepsilon_0)\sin(\delta)$, that is related to output stress components out of phase with the applied strain;
- the loss factor $\tan(\delta)=E''(\omega)/E'(\omega)$.

In a dynamical experiments, E', E'' and $\tan(\delta)$ are measured as a function of the frequency and follow typically the behaviour depicted in Figure 2.8.

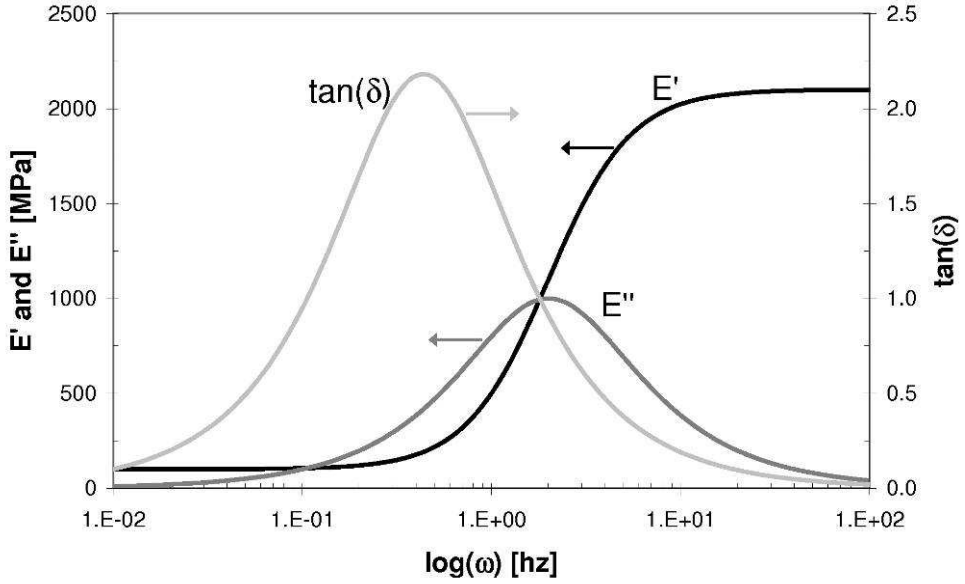

Figure 2.8. Examples of E', E'' and $\tan(\delta)$ as a function of frequency. E', E'' and $\tan(\delta)$ was calculated by using the one-time-constant Maxwell model with K_1 = 0.2 GPa, K_2 = 0.1 GPa and η = 1 GPa·s.

2.1.2.1 Linear superposition principle

If the linear viscoelasticity holds, it is possible to apply the linear superposition principle as for the creep behaviour. Similarly a *distribution function of relaxation times* (or *relaxation spectrum*) $H(\tau)$ is defined in relation to viscoelastic function:

Equation 2.8

$$E'(\omega)=\int_0^{+\infty} H(\tau)\frac{\omega^2\tau}{1+\omega^2\tau^2}\,d\tau$$

Equation 2.9

$$E''(\omega)=\int_{-\infty}^{+\infty} H(\tau)\frac{\omega}{1+\omega^2\tau^2}\,d\tau$$

The approximate value of $H(\tau)$ can be derived from the storage modulus function $E'(\omega)$ by means of the following relationship:

Equation 2.10

$$H(\tau) \cong E'(\omega) \left. \frac{d \log E'(\omega)}{d \log \omega} \right|_{\tau=1/\omega}$$

2.1.2.2 Time-temperature superposition principle

As for the creep experiments, it is also possible to apply the time-temperature superposition principle for the dynamical experiments. In this case the frequency is used instead of the time and the master curve is a function of the *reduced frequency* ω^*.

In practice the experiments are carried out at a limited number of frequencies (4 to 6) by scanning temperature. These data are used to build up a spectrum, i.e. the modulus as a function of the frequency at different temperatures, and then the time-temperature superposition principle is applied to obtain the master curve and the shift factor as a function of the temperature.

2.2 Essential Work of Fracture (EWF)

The essential work of fracture (EWF) method [4, 14-23] is an appropriate approach to experimentally characterize the ductile fracture of polymers and composites. According to Broberg [17] and Cotterel [18], the total work of fracture W_f can be divided into two parts: the *essential work of fracture* W_e, that is the work dissipated in the process zone close to the crack tip, and the *non-essential work of fracture* W_p, that is the work responsible for the plastic deformation outside the fracture-process zone (Figure 2.10). The total work of fracture may therefore be written as:

Equation 2.11

$$W_f = W_e + W_p$$

The principle of the technique is to measure the load-displacement trace and hence the energy to fracture for a series of notched specimens, ensuring that plasticity in the ligament (fracture region) is fully developed. Under plane stress conditions, it is possible to partition the work of fracture into an element taking place along the fracture line and another element taking place in a volume of material surrounding the crack. The former element is proportional to the fracture area and hence

the ligament length L, while the latter element is proportional to the volume of the outer region. For both metals and plastics, it has been observed that the volume of the outer region is proportional to the square of the ligament length. Thus the specific total work of fracture w_f may be written as:

Equation 2.12

$$w_f = \frac{W_f}{LB} = w_e + \beta \cdot w_p \cdot L$$

where B is the specimen thickness, β is a shape factor for the outer plastic zone, which depends upon the geometry of the specimen and the crack, and w_e and w_p are the specific essential and non-essential work of fracture, respectively. The parameter w_e is regarded as a material property quantifying the fracture toughness.

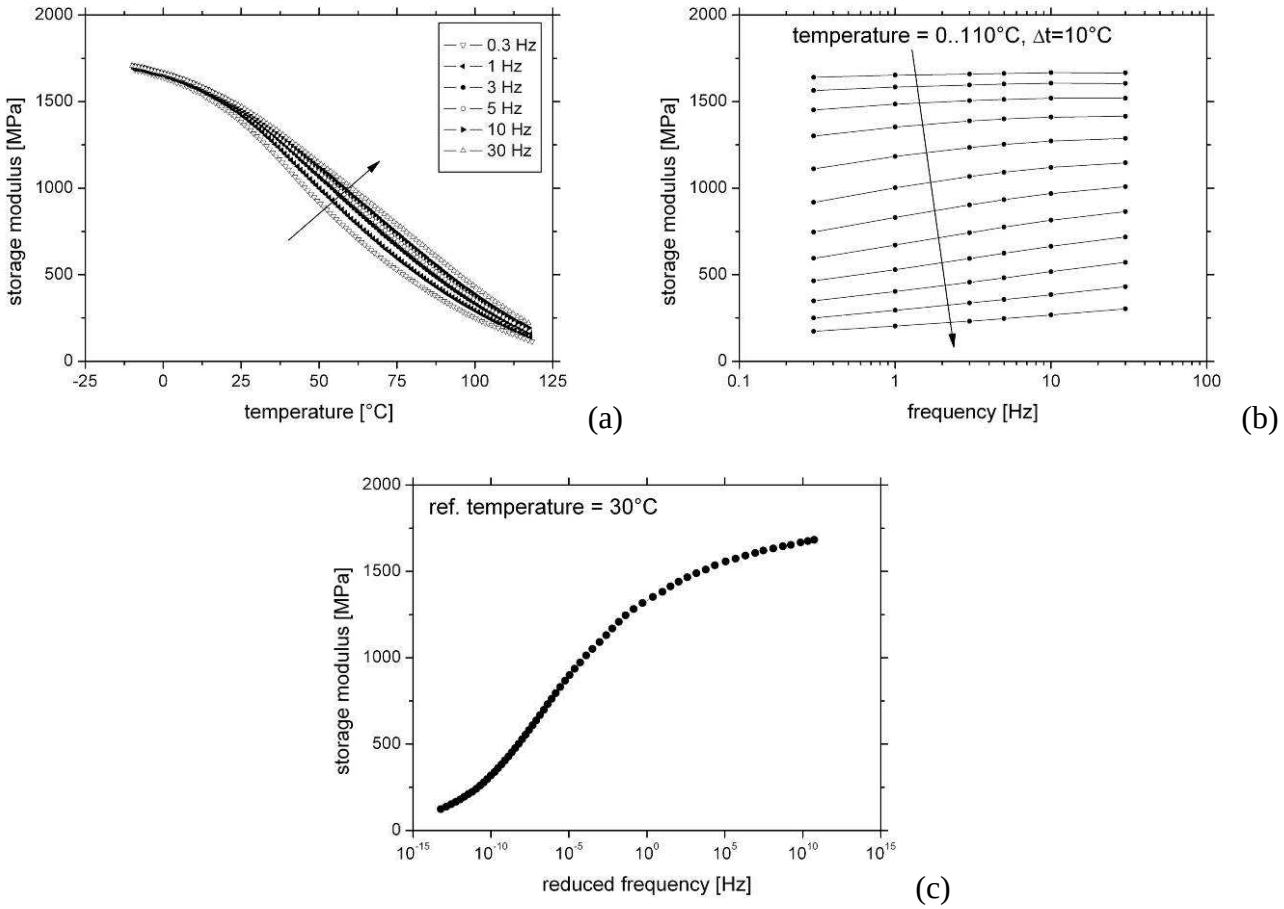

Figure 2.9. Example of the construction of the master curve of E': E' as a function of temperature at different frequency (a), the spectrum of E' (b) and finally the master curve (c). The data refers to an HDPE09 extruded 1x (see chapter 5).

2.2.1 Procedure for the EWF assessment

The parameters w_e and w_p can be evaluated by testing a series of specimens differing in ligament length, and by linearly interpolating a number of experimental data of w_f plotted against the ligament length L (Figure 2.12).

Specimen geometry such as the double edge notched tension (DENT) is commonly used for this purpose (Figure 2.10). A rectangular specimen of width W and length H is cut from the test material. In order to prevent the plastic zone being disturbed by edge effects and to ensure complete yielding of the ligament region before the crack starts to propagate, the maximum ligament length L used should be less than one third of the specimen width W or less than the plastic zone size, whichever is the lower [23]. On the other hand, the length H includes the gauge length h and the amount of material used in gripping the specimen. However, the choice of h is normally not critical. Moreover the ligament length L must be greater than three to five times the specimen thickness B to generate a state of pure plane-stress [21, 22]. Furthermore, for each specimen, two sharp edge notches, directly opposite one another, should be made. Several commonly techniques used are razor pushing, razor sliding and razor tapping.

The fracture tests are conducted in tensile mode on DENT specimens that have the ligament lengths spanning the range of all allowable ligament lengths (as explained above). In particular a minimum of 25 specimens is typically suggested [14].

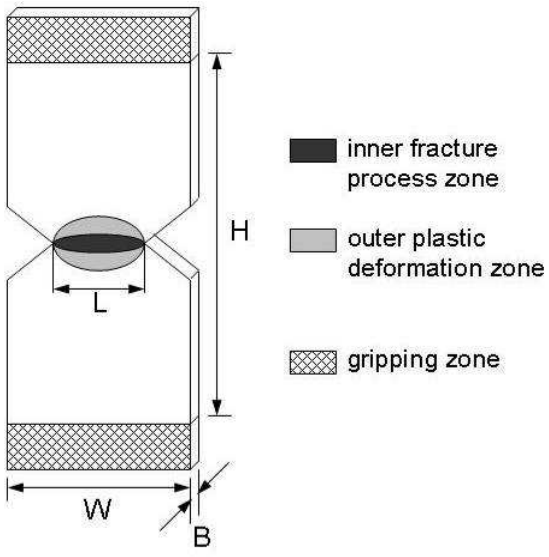

Figure 2.10. DENT specimen geometry: in evidence the crack tip deformation zones.

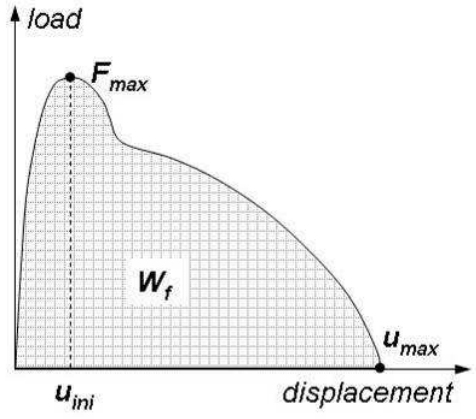

Figure 2.11. A typical load-displacement curve for DENT specimens.

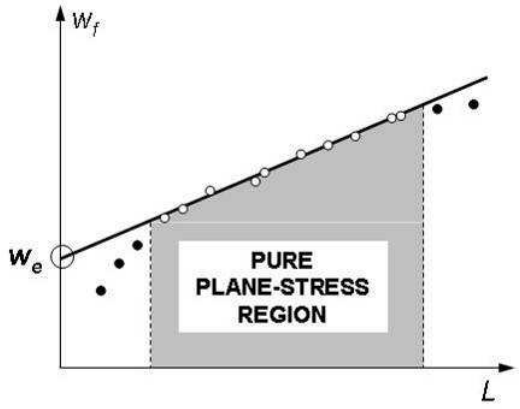

Figure 2.12. Schematic diagram of specific total work of fracture against ligament length.

In addition, by plotting the maximal net-section stress $\sigma_{\max}$, defined as the ratio between the maximum load and the net-section LB, versus the ligament length for each group of specimens, the data obtained can be checked with Hill's criterion [19] to verify that the tests were performed under plane-stress conditions. If the stress criterion is satisfied, the net-section stress is about $1.15\sigma_y$.

2.2.2 Partitioning of the work of fracture

In order to investigate the energy contribution to different fracture stages, a partition between the specific work of fracture for yielding and for necking and subsequent fracture [4, 15, 16, 20] can be introduced by considering the peak of the load–displacement curves as the cut-off point (Figure 2.12).

As the composed terms are under plane stress, Equation 2.11 and Equation 2.12 can be rewritten as:

Equation 2.13

$$w_f = w_y + w_n$$

Equation 2.14

$$w_y = w_{y,e} + \beta' \cdot w_{y,p} \cdot L$$

Equation 2.15

$$w_n = w_{n,e} + \beta'' \cdot w_{n,p} \cdot L$$

where $w_{y,e}$ and $w_{y,n}$ are the yielding and the necking and subsequent fracture related components of the specific essential work of fracture, respectively; $\beta' \cdot w_{y,p}$ and $\beta'' \cdot w_{n,p}$ are the yielding and the necking and subsequent fracture components of the specific non-essential work of fracture, respectively.

2.3 Micro- and nanocomposites

In the recent years, scientific and technological developments brought about two different types of polymer composites, distinguished by the characteristic size of the inorganic filler particles:

- traditional composites or micro-composites that contain micrometer-scale fillers [24, 25];
- *nanocomposites* that contain nanometer-scale fillers, i.e. fillers that have at least a characteristic size under 100 nm [1-3, 5, 26-29].

The nanofillers are divided in three categories according to the shape (Figure 2.13):

- one dimensional fillers (1-D), i.e. plate-like materials such as all the types of layered silicates and graphite nanoplates;
- two dimensional fillers (2-D), i.e. nanotubes or nanofibers such as carbon nanotubes, carbon nanofibers, boron/nitrogen nanotubes, nanotubes made of dichalcogenides (MoS_2, WS_2, etc.), nanotubes of several oxides (V_2O_5, MoO_3, etc.) and organic nanotubes.
- three dimensional fillers (3-D), i.e. particulate like-spherical materials such as metal oxides (ZnO, Al_2O_3, $CaCO_3$, TiO_2, etc.), fumed silica (SiO_2), silicon carbide (SiC), polyhedral oligomeric silsesquioxanes (POSS) and carbon black (CB)

(a) (b) (c)

Figure 2.13. Examples of nanofillers: plate-like materials (a), nanotubes (b) and equi-axed nanofillers (c).

Research and development of nanocomposites greatly increased in recent years for several reasons. Most of all, unprecedented combinations of properties have been observed in some polymer nanocomposites. For example mechanical properties exhibited improvement at filler volume fractions lower than those of the corresponding micro-composites and without loss of ductility. This is because small particles do not create large stress concentrations an they introduce new mechanisms for deformation energy adsorption [30, 31]. Nanocomposites are also capable of achieving optical clarity of the materials because very small nanoparticles do not scatter light significantly.

The unique properties of the nanocomposites are mainly related to the small size of the filler particles and to the particular properties of the particles themselves. Moreover controlling the degree of interaction between the filler and the polymer, i.e. the interphase and her properties, could permit the control of the composite properties because the polymer chains have a different behaviour than the bulk matrix (e.g. degrees of mobility, cross-linking or crystallinity). In the case of the nanocomposites the extent of the interphase (which typically has a thickness between 2 and 50 nm) is more crucial than in traditional micrometric composites because the small size of the particles themselves results in exceptionally large filler-polymer interfacial area. Thus this fact implies that the polymer matrix behaviour can be altered at much smaller loadings.

One key factor to obtain all these advantages is a proper dispersion, i.e. the level of the agglomeration of the filler particles, and a homogenous distribution of the filler nanoparticles throughout all the sample. Figure 2.14 shows examples of the different dispersion and distribution conditions that could be produced. Therefore the processing becomes very important and several techniques were employed such as traditional melt mixing with twin screw extruder and injection moulding, solution mixing assisted with the aids of sonication and surfactants, in-situ polymerization. In addition, the dispersion can be improved with modification treatment of the filler surface in order to hinder agglomeration phenomena: moreover these treatment can be employed to improve the filler-polymer interaction.

2.3.1 Nanoscale fillers

2.3.1.1 Carbon black

The carbon black (CB) [32, 33] is a particular form of carbon produced by incomplete combustion or thermal decomposition of gaseous or liquid hydrocarbons under controlled conditions. The carbon atoms are arranged in blocks of graphene layers with reduced dimensions and then these basic units are organized with a turbostratic structure to form spherical particles with diameter from

10 to 100 nm (Figure 2.15). The graphene layers are very similar to the graphitic structure: most of the carbon atoms in carbon black are sp^2-hybridized to form benzene rings as for graphite, but the ordered structure is maintained only over short lengths (3-4 layers).

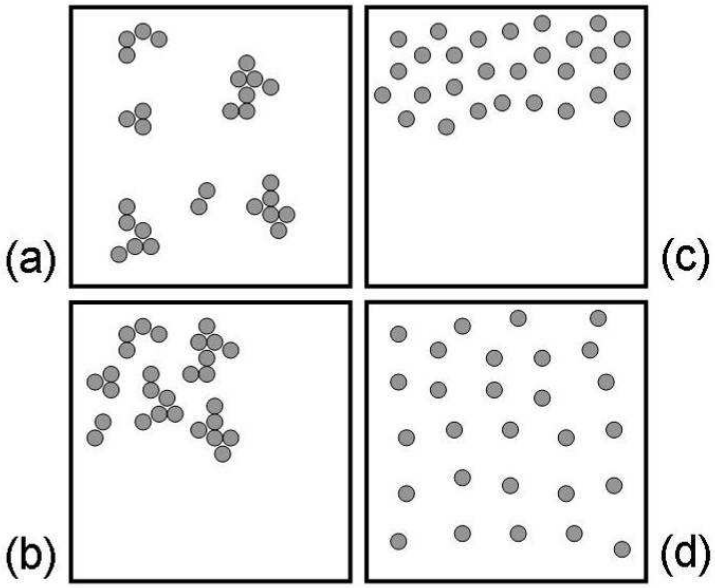

Figure 2.14. A schematic illustration of (a) good distribution but poor dispersion, (b) poor distribution and poor dispersion, (c) poor distribution but good dispersion and (d) good distribution and good dispersion.

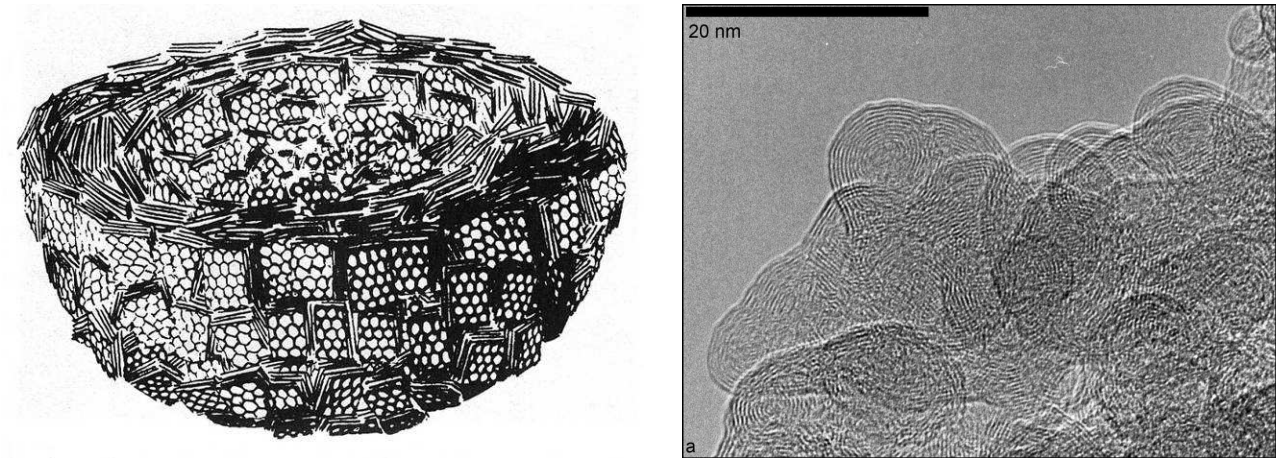

(a) (b)

Figure 2.15. (a) Model showing cutaway view of single carbon black particle [34] and (b) high resolution TEM micrograph of the structure of CB primary particles [35].

During the production process the *primary particles* fuses into *aggregates*. Moreover *agglomerates* can grow because the small distances between the aggregates and the strong van der Waals forces present. While an aggregate is indivisible, the agglomerate could be destroyed during the typical processing of the polymer (Figure 2.16). A CB characterized by primary aggregates composed of

many prime particles, with considerable branching and chaining, is referred to as a high-structure black. If the primary aggregates consist of relatively few prime particles, the CB is referred to as a low-structure black. Moreover from a general point of view the primary particle diameter and the structure complexity are not directly related (Figure 2.17).

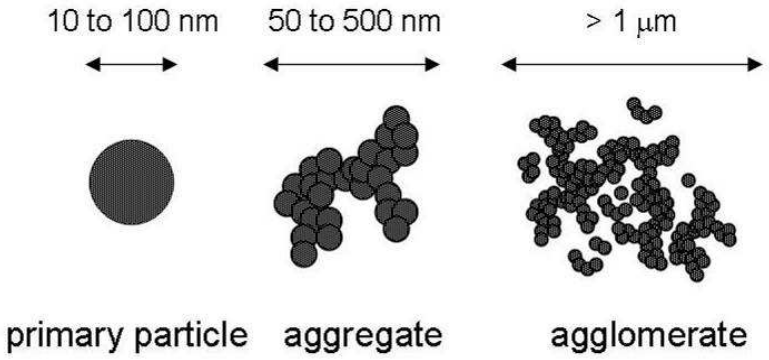

Figure 2.16. CB primary particles fused together to form aggregates and then agglomerates.

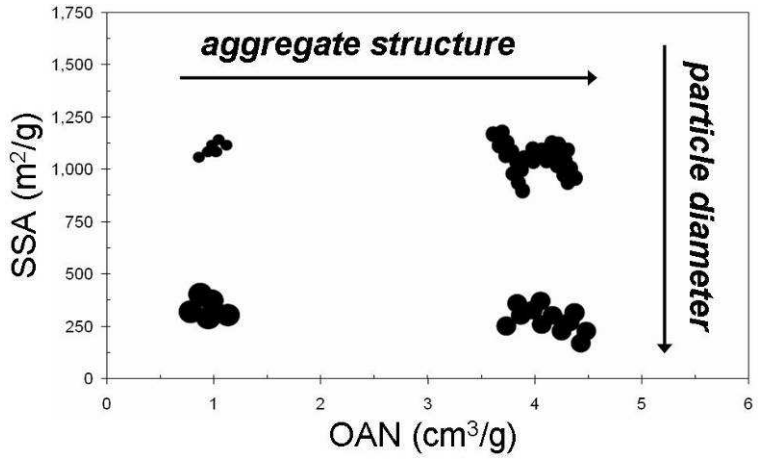

Figure 2.17. Scheme of the different CB conformations in relation to particle size and structure.

The particle size is typically determined by transmission electron microscope (TEM) measurements (see ASTM D-3849). Alternatively the specific surface area (SSA) could be measured by nitrogen adsorption measurements using the Brunauer-Emmet-Teller procedure (ASTM D 6556) or by the iodine number test (ASTM D 1510): small particles will confer a large surface area per unit weight. SSA measured with the BET method typically varies between 25 and 1500 m^2/g. Furthermore the following expression holds in the case of spherical particles with low porosity:

Equation 2.16

$$d_{BET} = \frac{6000}{S_{BET} \cdot \rho}$$

where d_{BET} is the average primary particle diameter in nm, S_{BET} the specific surface area determined by BET method in m^2/g and ρ the density in g/cm^3.

On the other side CB structure is evaluated by oil adsorption number (OAN), which represents the amount of oil (normally dibutyl phthalate, DBP) that can be absorbed by CB to reach a critical viscosity (ASTM D 2414). A higher value of OAN indicates a higher structure. OAN measured with DBP typically varies between 0.05 and 5 cm^3/g.

Moreover, CBs have to be evaluated by taking to account other factors such as the porosity, that in certain case can reach 30%, and the chemical groups on the surface introduced by the manufacturing process such as phenolic, quinolic and carboxyl chemisorbed complexes.

2.3.1.2 Carbon nanotubes

Since the discovery of carbon nanotubes (CNTs) in 1991 by Iijima [36], CNTs have been looked at with great interest in the field of the polymer composites because their unique physical, mechanical, electrical, thermal and optical properties [1, 37-41].

A carbon nanotube is a hexagonal network of carbon atoms rolled up into a seamless, hollow cylinder, with each end capped with half of a fullerene molecule (Figure 2.18). There are two main kinds of nanotube. Single-walled nanotubes (SWCNTs) are individual cylinders of 1-2 nm in diameter, which are actually a single molecule, and multi-walled nanotubes (MWCNTs) are a collection of several concentric graphene cylinders. The diameter, the chirality, and the form of the nanotube determine its properties.

The mechanical properties of various types of nanotubes have been extensively studied both by experimental and computational means. From a general point of view their modulus can be higher than 1 TPa and their tensile strength can reach 600 GPa with strain at break up to 40%. Moreover they can have the same electrical and thermal conductivity of the graphite (in-plane), i.e. 3000 $W \cdot m^{-1} \cdot K^{-1}$ and $5 \cdot 10^{-5}$ $\Omega \cdot cm$, and very low density, i.e. 1.3 g/cm^3. Nevertheless, these properties are achieved only in the case of individual SWCNT: the modulus of a ropes containing bundled SWCNT considerably decreases as the rope diameter increases because of the slippage occurring between the individual nanotubes within the rope (Figure 2.19). Moreover the MWCNTs have a lower modulus because only the outermost layers carry the load, and it could go down to 100 GPa.

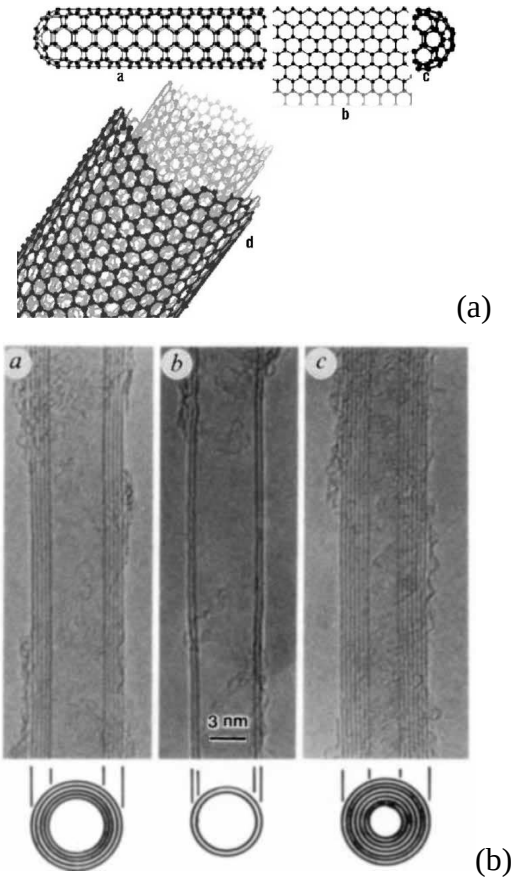

Figure 2.18. (a) Schematics of a single-walled carbon nanotube and a multiwalled carbon nanotube [2] and (b) TEM micrographs [36].

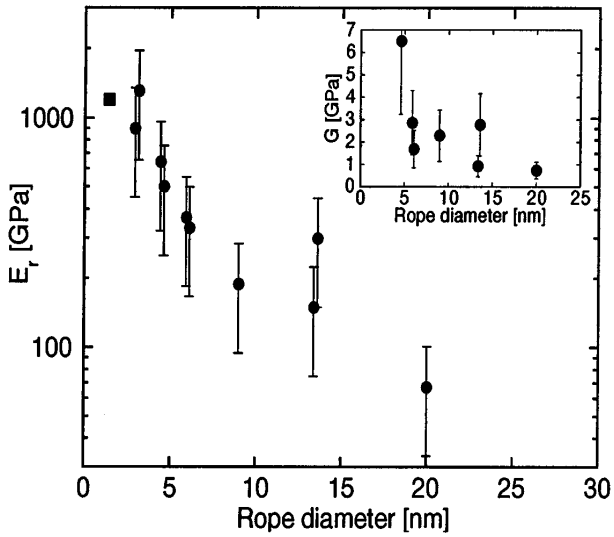

Figure 2.19. Tensile modulus and shear modulus (onset) of SWCNT as a function of rope diameter [42].

2.3.1.2.1 Carbon nanotubes based composites (1): pre-processing

The production of composites requires preliminary treatments to prepare the CNTs for the processing [1, 2, 28, 37]. In fact, most production processes generate a range of carbonaceous particles such as amorphous carbon, fullerenes, and nanocrystalline graphite. Moreover, metal

catalysts remain as a residue. The most common methods to remove unwanted by-products include thermal annealing in air or oxygen for selective etching of amorphous carbons [43-47], and acid treatment for eliminating catalyst residues [48]. Mechanical techniques like centrifugal separation, size exclusion chromatography and microfiltration [49-53] may be applied as well. Obviously all these techniques reduce the effective yield of the production process.

In addition a chemical functionalization, i.e. the addition of new functional groups, can be conducted on the CNTs to improve the nanotube-polymer interactions for processability and property enhancement. Several approaches have been employed to obtain surface modifications: doping with boron or nitrogen [54, 55], fluorination of the sidewalls at elevated temperatures [56], electrochemically reduction of aryl diazonium salts [57-59], plasma treatments [60, 61], addition of alkyl chains through reactions with sec-butyllithium [62], etc. However the most relevant treatments are the acid treatments. In fact, acid treatments with HNO_3, H_2SO_4, H_2O_2 or mixture oxidize the surface of CNT and introduce carboxylic acid, hydroxyl groups and so on [63-68]. Then the new functional groups can be used as linking for subsequent chemical reactions to attach new chemical groups on the CNT surface. Examples of this scheme are the reactions with thionyl chloride [69, 70], amines [71, 72], silane coupling agents [73, 74] and thiols [75].

2.3.1.2.2 Carbon nanotubes based composites (2): processing

Polymeric composites filled with CNTs are produced with either thermoplastic or thermoset matrices by using several processing methods such as melt-mixing, in-situ polymerization and solution processing. As for all nanocomposites, the main issues are the dispersion of the CNTs individually (i.e. the deagglomeration of bundles and ropes) and uniformly, their alignment, and the interfacial bonding.

Melt-mixing of CNTs into thermoplastic polymers using conventional processing techniques, such as extrusion, internal mixing, injection molding and blow molding [76-92], is particularly desirable, because of the speed, simplicity and availability of these processes in the plastics industry. Use of high-shear mixing and longer processing times may enhance dispersion, and when coupled with elongational flow, should yield aligned nanotubes as in the case of melt spinning and injection moulding [91, 92].

In-situ polymerization is a method used for directly improving dispersion and integration between the phases. Examples are intrinsically conducting polymers [2], thermosetting polymers as epoxy [93] and phenolic resins [94], and thermoplastic polymers as polystyrene [95], polyethylene [96] and polyamide [97, 98].

Solution-based methods provide an advantage through low viscosities, which facilitate mixing and dispersion of the CNTs. While sonication [99-102] is typically used to improve the filler dispersion, the effectiveness of the dispersion can be aided with surfactants such as SDS, Triton X-100 and NaBBs [103-105]. Even if these methods could be used with thermosetting polymers [106], they are used with thermoplastic polymers such as polyvinyl alcohol [99, 101, 102], polystyrene [30, 107], polymethyl methacrylate [100] and others. Moreover, a critical issue is the solvent removal: even if the evaporation during film casting maintained the good dispersion during the processing, in certain cases a rapid solvent can be useful to hinder reagglomeration phenomena of CNTs [100].

2.3.1.2.3 Carbon nanotubes based composites (3): mechanical properties

As mentioned ealier, CNTs possess remarkable properties: therefore the main challenge is to be able to exploit the mechanical properties in composites on a macroscale, combining the choice of materials with the appropriate processing method. This corresponds to have a good dispersion and a good load transfer between the matrix and the nanotubes.

Table 2.1. Examples of the percentage increase or decrease in modulus (E) and tensile strength (σ_R) of MWCNT filled polymer composites relative to the pure polymer.

Polymer matrix	MWCNT content	E	σ_R	References
Melt mixing				
LDPE	10 wt%	+89	+56	[108]
natural rubber	10 wt%	+12	n.a.	[109]
PC	8 wt%	–58	+78	[110]
polyurethane	5.6 wt%	+18	+78	[111]
PP	0.3 wt%	+33	+34	[112]
In-situ polymerization				
PET	2 wt%	+35	+290	[113]
nylon 1010	1 wt%	+27	n.a.	[97]
phenolic resin	2 wt%	+47	+87	[94, 114]
epoxy resin	8 wt%	–31	+67	[93]
Solution mixing				
PVOH	5 wt%	+140	+64	[101]
PVOH	1 vol%	+100	n.a.	[99, 115]
PVOH	1 wt%	+477	n.a.	[102]
PS	1 wt%	+42	+25	[30]
PS	5 wt%	+120	+57	[107]

Notes: n.a., not available; LDPE, low density polyethylene; PC, polycarbonate; PP, polypropylene; PET, poly(ethylene terephthalate); PVOH, poly(yinyl alcohol); PS, polystyrene.

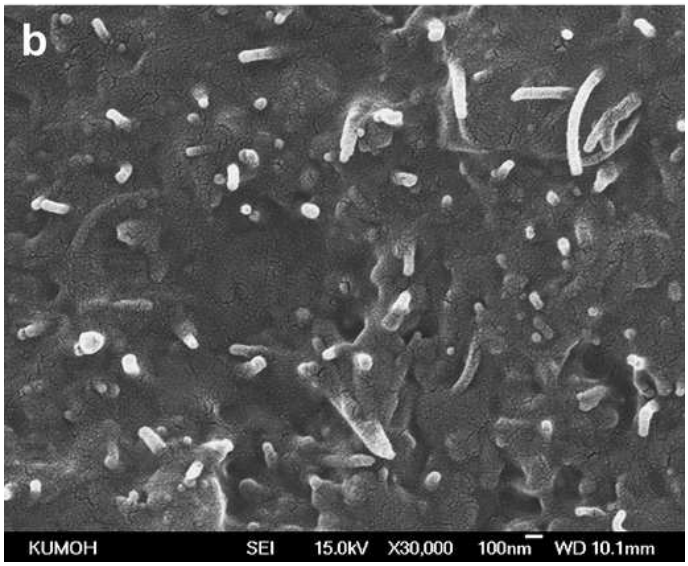

Figure 2.20. SEM micrographs of fracture surface of PET-MWCNT composites [113].

While a poor dispersion can induce an early failure and hence a reduction of the properties [91], a good dispersion can noticeably improve elastic modulus and strength. Table 2.1 shows some significant examples found in literature for MWCNT filled composites: from a general point of view, the best improvements were found in the case of solution mixing and in-situ polymerization

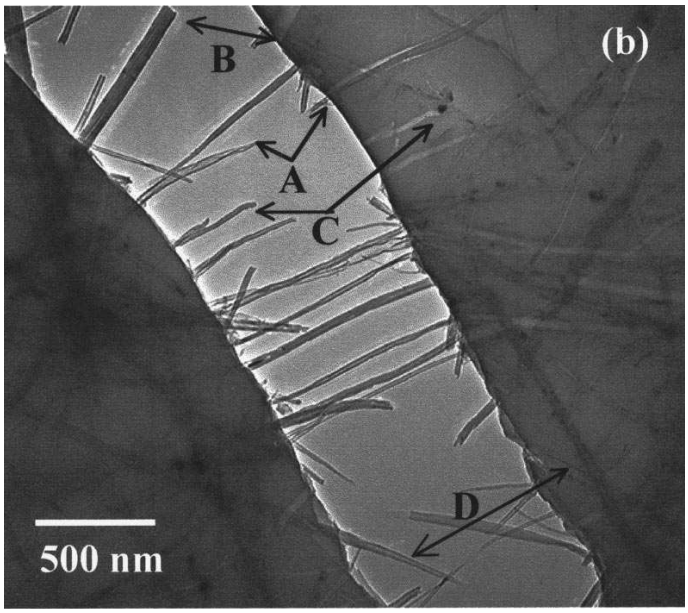

Figure 2.21. Fracture mechanisms in nanotube-based composites [30]

The improvement of the mechanical properties of CNT base composites is not related only to the efficiency of load transfer phenomena obtained with good interfacial interactions [113], as evidenced by Figure 2.20, where the CNTs are covered by a polymeric layer. Additional adsorption

energy mechanisms [30] can take place during the deformation process: Figure 2.21 shows nanotube pull-out phenomena, i.e. crack bridging by the nanotubes, as for conventional fibre composites [30].

2.3.2 Creep behaviour of nanocomposites

Several studies [116-129] show a drastic increase of the creep resistance for polymers filled with nanometric particles at low filler content, i.e. up to 5 wt%, if a good dispersion of the filler in the polymeric matrix is achieved (Figure 2.22). Otherwise the creep resistance decreases: this situation occurs over a critical filler fraction because the processing is no longer able to hinder agglomeration phenomena [118, 127]. For this reason compatibilizing agents [117, 119, 120] could be used to reduce the agglomeration tendency of the filler particles, because of the low interaction between filler and polymer. Moreover, it necessary to take into account other phenomena that the presence of the filler particles can induce: the reduction of the crystallinity or the crosslinking degree of the polymer matrix could induce a reduction of the creep resistance of the composites, despite the reinforcement effect of the nanofiller [121-123]. As for the other mechanical properties, the creep behaviour of nanocomposites could be further improved if a good filler-polymer interaction is achieved. Surface treatment of the filler [125, 126, 128] and cross-linking reactions induced between filler particles and polymer chains [129] are examples. In addition, other works [130-132] demonstrate that nanofillers could improve the creep behaviour more than micrometric fillers: Figure 2.22 shows, for example, the creep strain and strain rate of polypropylene (PP) filled with TiO_2 particles that have diameter of 21 and 300 nm.

While several works examine the creep behaviour of composites filled with plates and low aspect ratio nanoparticles, few papers about nanotube-filled nanocomposites are available in the literature [116, 124, 127]. In particular, Yang et al. [124] and Ganss et al. [116] investigated PP-MWCNT composites produced by melt mixing, while Zhang et al. [127] examined epoxy-SWCNT composites. From a general point of view, an improvement of the creep behaviour in terms of creep strain, strain rate and creep life was observed at higher and lower stress (in comparison to the tensile strength) if the filler had a good dispersion. Otherwise the creep resistance decreased in comparison to the polymeric matrix.

As mentioned before, the introduction of inorganic rigid filler particles, both in the case of micrometric and nanometric filler particles, improves the creep resistance of the composites. Moreover it is interesting to observe that the decrease in relative creep compliance of composites filled with micrometric filler is often closely approximated by the reciprocal of the relative elastic modulus of the same system as measured by stress-strain or dynamical mechanical tests as depicted

in Figure 2.23 [25, 133, 134]. This relation implies that the filler does not change the properties of the polymer in some manner.

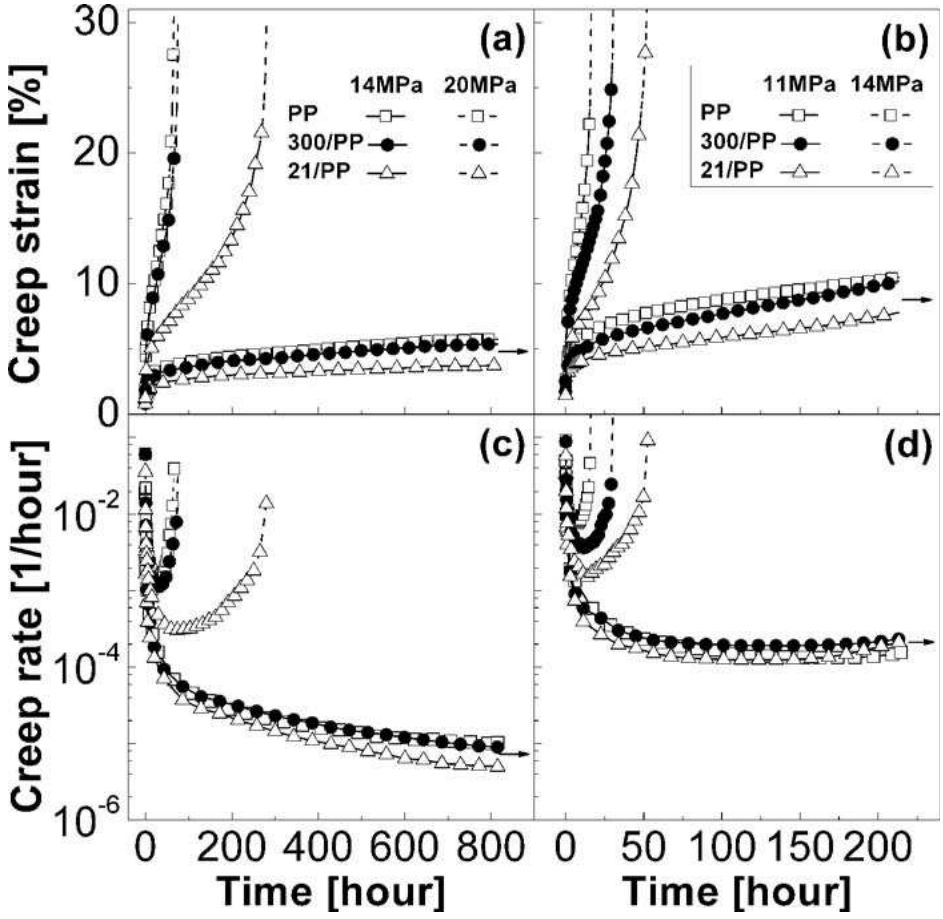

Figure 2.22. Creep curves for PP-TiO_2 composites at 23°C (a, c) and 50°C (b, d). In particular the data refers to PP and PP filled with TiO2 characterized by a diameter of 21 nm (21/PP) and of 300 nm (20/PP) [132].

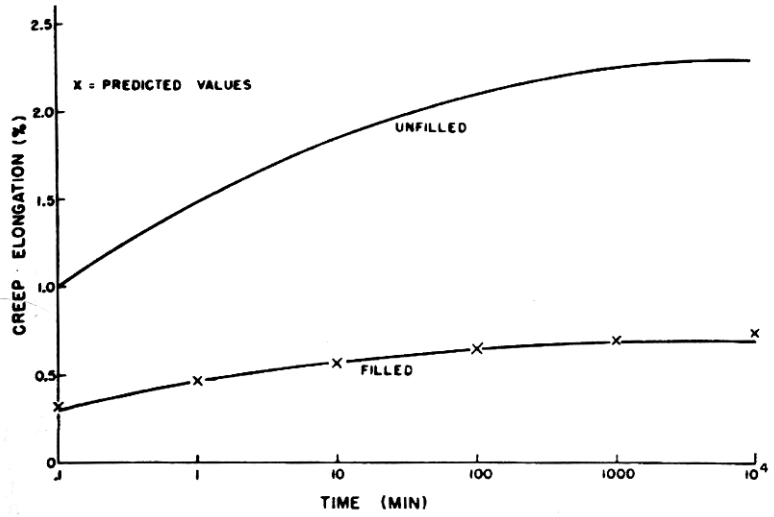

Figure 2.23. Creep of polyethylene unfilled and filled with kaolin: the predicted values are calculated from dynamical tests [25].

3 Experimental

3.1 Materials

3.1.1 Polymeric matrices

This work involved the use of several polymeric matrices. This list includes the following polymers:

- an *Eltex A4009* HDPE kindly supplied by BP Solvay (Solvay SA: Rue du Prince Albert 44, 1050 Bruxelles, Belgium), now Innovene, in the form of a fine powder. This HDPE had a melt flow rate of 0.8 g/10 min (evaluated at 190°C and 2.16 kg) and a density of 0.958 g/cm^3 at 23°C. This polymer was indicated as HDPE09 in following chapters;
- a *Plastene AD25* HDPE kindly supplied by Poliplast SpA (Via Agro Castello 9, 24020 Casnigo, Italy) in the form of a fine powder. This HDPE had a melt flow rate of 25 g/10 min (evaluated at 190°C and 2.16 kg) and a density of 0.954 g/cm^3 at 23°C. This polymer was indicated as HDPE25 in following chapters;
- a *Plastene BD70* LDPE kindly supplied by Poliplast SpA in the form of a fine powder. This LDPE had a melt flow rate of 70 g/10 min (evaluated at 190°C and 2.16 kg) and a density of 0.919 g/cm^3 at 23°C. This polymer was indicated as LDPE70 in following chapter;
- a *Fusabond E MB100D* maleated polyethylene kindly supplied by DuPont Srl (via Pontaccio 10, 20121 Milano, Italy). This modified polyethylene had a melt flow rate of 2.0 g/10 min (evaluated at 190°C and 2.16 kg), a density of 0.960 g/cm^3 at 23°C and a maleic anhydride content of 0.9 wt%. This polymer was indicated as MA-g-PE in following chapters;
- a *Mowiflex TC 232* plasticized partially hydrolyzed PVOH kindly supplied by Kuraray Specialities Europe GmbH (Building F821, Hoechst Industrial Park, 65926 Frankfurt am Main, Germany) in the form of pellets. This PVOH had a melt flow rate of 39 g/10 min (evaluated at 190°C and 21.6 kg). This polymer was indicated as PVOH89p in following chapters;

- a *Celvol 350* fully hydrolyzed PVOH kindly supplied by Celanese Corporation (1601 West LBJ Freeway, Dallas, Texas, USA) in the form of fine grains. This PVOH had a viscosity of 62-72 cP in form of a 4wt% aqueous solution at 20°C. This polymer was indicated as PVOH99 in following chapters;
- an *Edistir N 2560* PS kindly supplied by Polymeri Europa SpA (Piazza Boldrini 1, 20097 San Donato Milanese, Italy) in the form of pellets. This PS had a melt flow rate of 3.8 g/10 min (evaluated at 200°C and 5 kg) and a density of 1.05 g/cm^3 at 23°C. This polymer was indicated as PS in following chapters.

These materials are summarized in Table 3.1.

Table 3.1. List of the polymeric matrices.

Material code	Grade	Supplier
HDPE09	Eltex A4009	BP Solvay (Solvay SA)
HDPE25	Plastene AD25	Poliplast
LDPE70	Plastene BD70	Poliplast
MA-g-PE	Fusabond E MB100D	Dupont
PVOH89p	Mowiflex TC 232	Kuraray
PVOH99	Celvol 350	Celanese
PS	Edistir N 2560	Polimeri Europa

3.1.2 Inorganic fillers

This work involved the use of several inorganic fillers: Cu and Fe powders, CBs and MWCNTs. The following paragraphs are dedicated to present their characteristics.

3.1.2.1 Copper (Cu) and iron (Fe) powders

Micrometric copper (Cu) and iron (Fe) powders were used. In both cases two different dimensions of Cu and Fe powders were considered: a powder with a nominal characteristic dimension of 10 μm or less (but always in micrometer range) and a powder with a nominal characteristic dimension of 50 μm or more. The powders were kindly supplied by Sigma-Aldrich S.r.l. (Via Gallarate 154, 20151 Milano, Italy) and by Cerac Inc. (P.O. Box 1178, Milwaukee, Wisconsin, USA). Table 3.2 summarizes the details of all the used metallic powders.

Table 3.2. List of Cu and Fe powders.

Material Code	Grade	Supplier	Dimension
Cu10	32,645-3	Sigma-Aldrich	<10 μm
Cu45	C-1240	Cerac	-200+325 mesh (45-75 μm)
Fe15	I-1021	Cerac	325 mesh (<15 μm)
Fe45	I-1069	Cerac	-140+325 mesh (45-106 μm)

3.1.2.2 Carbon blacks (CBs)

Four different types of CBs were used, whose characteristic properties, such as the density determined by X-ray diffraction measurements, the specific surface area (SSA) determined by the Brunauer–Emmett–Teller method (ASTM D 6556-03), and the OAN determined with n-dibutyl phthalate (ASTM D 2414-04), are summarized in Table 3.3. All the materials were supplied in the form of a fine powders.

Table 3.3. List of CBs. D represents the average diameter of the primary particles as observed at TEM microscope.

Material Code	Grade	Supplier	Density [g/cm^3]	OAN [cm^3/g]	SSA [m^2/g]	D [nm]
CB105	Raven P-FE/B	Columbian Carbon Europa SRL (Via San Cassiano 140, 28069 San Martino Di Trecate, Italy)	1.92	0.98	105	30÷35
CB226	Conductex 975u	Columbian Carbon Europa SRL (see above)	1.94	1.69	226	20÷25
CB802	Ketjenblack EC300J	Akzo Nobel Chemicals SPA (Via Eliseo Vismara 80; 20020 Arese, Italy)	1.92	3.22	802	15÷20
CB1353	Ketjenblack EC600JD	Akzo Nobel Chemicals SPA (see above)	1.95	4.95	1353	10÷15

3.1.2.3 Multiwalled carbon nanotubes (MWCNTs)

Two types of MWCNTs have been considered in this work:

- First, a commercial masterbatch with the trademark *Graphistrength 100 P50* kindly supplied by Arkema SA (Paris la Defense, France) containing 50 wt% of MWCNTs in a polyacrylic carrier in the form of fine grains. The MWCNTs have an outer mean diameter of 10-15 nm and a length of 0.1-10 μm. This filler was indicated as pMWCNT in following chapters;

- second, MWCNTs *1240 XH* kindly supplied by Nanostructured & Amorphous Materials Inc. (820 Kristi Lane, Houston, TX 87544, USA) produced by catalytic chemical vapor deposition (CVD) in the form of fine powder. The MWCNTs have an outer mean diameter of 20-30 nm and a length of 0.5-2 μm. This filler was indicated as uMWCNT in following chapters.

These materials are summarized in Table 3.4.

Table 3.4. List of MWCNTs.

Material Code	Grade	Supplier	Diameter	Length
pMWCNT	Graphistrength 100 P50	Arkema	10-15 nm	0.1-10 μm
uMWCNT	1240 XH	NanoAmor	20-30 nm	0.5-2 μm

3.2 Composite preparation and characterization

In this work several types of composites were produced and several techniques were used to characterize them. For these reasons the description of composite preparation and characterization is divided in relation to the type of composites.

3.2.1 Cu and Fe powders based composites

The dried HDPE25, Cu10 and Cu45 powders were mixed and then melt-compounded with a twin screw extruder Thermo-Haake Polylab Rheomex PTW 16p corotating, intermeshing twin screw extruder with a screw diameter of 16 mm and a length-to-diameter ratio of 25, equipped with a rod capillary die (diameter = 5 mm). The barrel temperature profile was set at 130-155-160-170-170°C and the screw rotation speed at 20 rpm. The added filler fraction was assessed in a such a way to obtain a composite with a content up to about 50 vol%.

The grounded composite materials were processed in two ways. In the first case, all the materials produced were injection moulded by using a Morgan G-55T press in order to obtain a 100x60x2 mm^3 sheet. The barrel and nozzle temperatures were set at 190°C and the mould temperature at 50°C; the melting time was about 5 minutes, the clamping force of the mould 18 tons and injection pressure 140 psi. In the second case samples of the composites were compression moulded in an electrically heated hydraulic Carver press to obtain sheet dimensions of 200x200x0.5 mm^3. The hot press procedure involved preheating at 160 °C for 10 minutes followed by compressing for 30 seconds at the same temperature with a load of 10 tons, and subsequent cooling under pressure until room temperature was reached (at about 10°C/min). Only samples of the base matrices HDPE25 and LDPE70 and 1 vol% filled composites were produced with this technique.

The list of the sample produced is contained in Table 3.5. Notwithstanding, it is appropriate to observe that the work is divided into two parts:

- in the first part, the effects of the filler type (Cu and Fe powders), of the matrix type (HDPE and LDPE) and of the filler content were evaluated. In this case the composites produced by injection moulding were considered (see chapter 4.2);
- in second part, only the effect of the filler dimension was evaluated. In this case only the composites produced by compression moulding were considered, i.e. HDPE25-Cu10 and HDPE25-Cu45 composites (see chapter 4.3).

Table 3.5. List of the produced Cu and Fe powders based composites.

Composites	Injection moulding	Compression moulding
HDPE25	yes	yes
HDPE25-Cu10	up to 20 vol%	1 vol%
HDPE25-Cu45	up to 30 vol%	1 vol%
LDPE70	yes	-
LDPE70-Cu45	up to 50 vol%	-
LDPE70-Fe15	up to 30 vol%	-
LDPE70-Fe45	up to 30 vol%	1 vol%

The produced materials were analyzed with optical microscopy (OM), scanning electron microscopy (SEM), thermogravimetric analysis (TGA), differential scanning calorimetry (DSC), dynamic mechanical thermal analysis (DMTA), tensile tests and tensile creep tests. In particular the creep tests were conducted only on the HDPE25-Cu composites produced by compression moulding. Moreover SEM was conducted on the dry copper and iron powders.

3.2.1.1 SEM

The metallic powders were observed with a Philips XL-30 TMP ESEM scanning electron microscope (SEM) in order to evaluate their effective shapes and dimensions.

Moreover, the quality of the interaction between the filler particle and the polymeric matrix was evaluated by observing the fractured surface of the composites with a SEM Cambridge Stereoscan 200. The samples were immersed in liquid nitrogen for a minimum of 60 minutes and then fractured.

3.2.1.2 DSC

Differential scanning calorimetry (DSC) measurements were conducted with a Mettler DSC 30 calorimeter on the composite materials. In the case of the composites based on an HDPE25 matrix, a first heating ramp from 0°C up to 200°C was followed by a cooling stage from 200°C to 0°C, and by a second heating ramp up to 200°C. In the case of the composites based on LDPE70 matrix the reference temperatures were -20°C and 180°C. Both heating and cooling rates were fixed at 10°C/min, and all tests were conducted in nitrogen flushing at 100 ml/min. The crystallinity content of the composites was assessed by integrating the normalized area of the melting endothermic peak and dividing the heat involved by the reference value of a theoretical 100% crystalline HDPE (277.1 J/g) [135] and LDPE (140.6 J/g) [135].

3.2.1.3 TGA

Thermogravimetric analysis (TGA) was carried out on Mettler TG 50 at a heating rate of 10°C/min in nitrogen atmosphere (200 ml/min). Typically 30 mg samples of composite materials were placed into the alumina sample pan and heated from 30°C up to 600°C.

3.2.1.4 DMTA

Dynamic mechanical thermal analysis (DMTA) tests were carried out by using the MKII of Polymer Laboratories Ltd apparatus on the composite materials: the tests were performed at a frequency of 1 Hz by scanning temperature in the range from –130°C to +130°C at a heating rate of 3°C/min. The specimens consisted of strips with a nominal gauge length of 15 mm, and a width of 5 mm. The tests were carried out in tensile mode by applying a displacement amplitude of 32 μm corresponding to a strain amplitude of about 0.2%. The pre-load applied to perform the test was 0.1 MPa.

3.2.1.5 Tensile tests

An Instron tensile tester, model 4502, was used to measure tensile mechanical properties of the composite materials. The tests were conducted on 1BA specimens (with a gauge length of 30 mm) according to the standard ISO 527. The tensile modulus was determined by performing tests at a cross-head speed of 0.5 mm/min, while tensile strength and strain at yield and at break were measured at a cross-head speed of 50 mm/min. Five specimens were tested for every material.

3.2.1.6 Tensile creep tests

Tensile creep tests were conducted by using an Instron 4502 tensile tester on a strip sample with a gauge length of 60 mm and a width of 5 mm. The test were performed by applying a constant load, i.e. the stress, at a fixed temperature and monitoring the displacement, i.e. the deformation, for 3600 seconds. Before testing every, specimens was conditioned at the testing temperature for 15 minutes. The temperature was varied between 30°C and 90°C and the applied constant stress between 3 and 15 MPa.

3.2.2 CB based composites

The dried powders of HDPE09 and CBs (all the four types) were mixed and then melt-compounded with the twin screw extruder (see the chapter 3.2.1) equipped with a sheet die. The barrel temperature profile was set at 130-200-210-220-220°C and the screw rotation speed at 12 rpm. The extruder produced a continuous sheet with a section of 50x1.5 mm^2. The added filler fraction was assessed in a such a way to obtain a composite with a content of 0.5 and 1 vol%. For all the materials, repeated extrusions (up to 3 times) after grinding with a Piovan RN1515 granulator were performed.

Table 3.6 presents the list of the produced HDPE09-CB composites. It is appropriate to observe that the work can be divided in two parts:

- in the first part, the effects of the filler type and of the filler dispersion degree in the matrix were evaluated by considering only HDPE09-CB226 and HDPE09-CB1353 with a filler content of 1 vol% and extruded up to 3 times (see chapter 5.1);
- in second part, only the effect of the filler type was evaluated by considering all the HDPE09-CB composites with a filler content of 0.5 vol% and extruded up to 2 times (see chapter 5.2).

Table 3.6. List of the produced CB based composites

Composites	Filler content	Compression moulding
HDPE09	-	up to 3 extrusions
HDPE09-CB105	0.5 vol%	up to 2 extrusions
HDPE09-CB226	0.5 vol%	up to 2 extrusions
HDPE09-CB802	0.5 vol%	up to 2 extrusions
HDPE09-CB1353	0.5 vol%	up to 2 extrusions
HDPE09-CB226	1 vol%	up to 3 extrusions
HDPE09-CB226	1 vol%	up to 3 extrusions

The HDPE09-CB composites with a filler content of 1 vol% were analyzed with OM, transmission electron microscopy (TEM), SEM, TGA, DSC, DMTA, melt flow rate (MFI), rheological behaviour, gel permeation chromatography (GPC), tensile tests, essential work of fracture (EWF) and tensile creep tests. The HDPE09-CB composites with a filler content of 0.5 vol% were analyzed with OM, tensile tests and essential work of fracture (EWF) tests.

3.2.2.1 OM

The quality of the filler dispersion was evaluated by using a Zeiss Axiotech 100optical microscope (OM) equipped with a Leica DC 300 or Nikon Coolpix 4500digital camera. Thin slices with a thickness of about 10 μm were cut with a Leica RM 2035 microtome and then observed with microscope.

3.2.2.2 TEM

The quality of the filler dispersion was evaluated by using a Philips EM 400 T transmission electron microscope (TEM): ultrathin sections were cut with a Leica EM UC6cryo-ultramicrotome. Moreover, samples of the different CB were observed.

3.2.2.3 DSC

Differential scanning calorimetry (DSC) measurements were conducted on HDPE09 powders and on the composite materials. A first heating ramp from 0°C up to 200°C was followed by a cooling stage from 200°C to 0°C, and by a second heating ramp up to 200°C. Both heating and cooling rates were fixed at 10°C/min and all tests were conducted in nitrogen flushing at 100 ml/min. The crystallinity content of the composites was assessed by integrating the normalized area of the melting endothermic peak and dividing the heat involved by the reference value of a theoretical 100% crystalline HDPE (277.1 J/g) [135].

3.2.2.4 TGA

Thermogravimetric analysis (TGA) was carried out at a heating rate of 10°C/min in nitrogen atmosphere (200 ml/min). Typically 30 mg samples of composite materials were placed into the alumina sample pan and heated from 30°C up to 600°C.

3.2.2.5 MFI

The measurements of the melt flow index (MFI) were performed with a Dynisco LMI 4000melt indexer according to ASTM D 1238 standard: the tests were carried out at 220°C with a load of 5 kg for all the materials.

3.2.2.6 Rheology

The dynamic rheological behaviour of all the composites were measured in a rotational rheometer Rheometrics RDAII using small amplitude oscillatory shear flow between parallel plates under nitrogen atmosphere. The complex viscosity was obtained in a frequency range between 0.04 and 400 s^{-1} at 220°C. Dynamic strain sweeps were also performed on some samples to determine the strain range of linear response of each material.

3.2.2.7 GPC

Gel permeation chromatography (GPC) tests were performed with a Waters Sci. Chromatograph, model 150-CV on the HDPE09 samples, powder and extruded materials. The different samples were dissolved in 1, 2, 4 thriclorobenzene using 0.0125 wt% butylhydroxytoluene (BHT) as antioxidant; at the same initial concentration, and then injected at 135 ºC. The measurement was done in duplicate and sequentially to reduce the effect of changing the calibration curve. Furthermore, the measurements were repeated three timese for each sample. Molecular weight distributions (MWD) were assessed by using the Millenium software. From this, the number average molecular weight (M_n), the weight average molecular weight (M_w)and the index of polydispersity (*IP*) were calculated.

3.2.2.8 FTIR

Fourier Transform Infrared Spectroscopy (FTIR) were collected for all the composites materials with a spectrometer Thermo Nicolet. The tests were carried out in transmission mode on films (about 50 μm) produced by hot pressing.

3.2.2.9 DMTA

The dynamic mechanical thermal analysis (DMTA) tests were carried out on the composite materials in two modes: in the first case at a frequency of 1 Hz by scanning temperature in the range from –130°C to +130°C at a heating rate of 3°C/min, while in the second case at six frequencies (from 0.3 to 30 Hz) by scanning temperature in the range from –20°C to +130°C at a heating rate of 0.5°C/min. The specimens consisted of strips with a nominal gauge length of 15 mm and a width of

5 mm: the tests were carried out in tensile mode by applying a displacement amplitude of 32 μm that is a strain amplitude of about 0.2%. The pre-load applied to perform the test was 0.1 MPa.
These tests were performed only on HDPE09 extruded 1 and 3 times, HDPE09, HDPE09-CB226 1vol% and HDPE09-CB1353 1 vol% extruded 3 times. The goal was to analyze the effect of the multiple extrusion on HDPE09 and the effect of the filler type (with a good filler dispersion).

3.2.2.10 Tensile tests

Instron tensile tester, model 4502, was used to measure tensile mechanical properties of the composite materials. The tests were conducted on specimens 1BA (with a gauge length of 30 mm) according to the standard ISO 527. Tensile modulus was determined by performing test at cross-head speed of 0.5 mm/min, while tensile strength and strain at yield and at break at a cross-head speed of 50 mm/min. Five specimens were tested for every materials.

3.2.2.11 EWF

For EWF testing, rectangular coupons with a width W of 40 mm and an overall length of 100 mm were cut out from the extruded sheets. The coupons were then razor notched to produce a series of DENT specimens with varying ligament lengths L. After notching, each specimen was tested up to complete failure at an initial grips separation H of 60 mm and at a constant cross-head speed of 12 mm/min. The load–displacement curve for each specimen was recorded and the total work of fracture W_f, the maximum load F_{max}, the work for the yielding W_y and the work for the necking and subsequent fracture W_n were subsequently measured. The fracture surface of the DENT samples was observed with SEM and with a Leitz Wild stereoscopic microscope equipped with a digital camera.

3.2.2.12 Tensile creep tests

Tensile creep tests were conducted by using an Instron 4502 tensile tester on strip sample with a gauge length of 60 mm and a width of 5 mm. The test were performed by applying a constant load, and therefore the stress, at a fixed temperature and monitoring the displacement, and thus the deformation, for 3600 seconds. Before testing, every specimen was conditioned at the testing temperature for 15 minutes. The temperature was varied between 30°C and 90°C, and the applied constant stress between 3 and 15 MPa.
While all the materials underwent a reference test at 30°C and 3 MPa, the behaviour of some materials were investigated in more detail: HDPE09 extruded 1 and 3 times, HDPE09, HDPE09-

CB226 1vol% and HDPE09-CB1353 1 vol% extruded 3 times. The goal was to analyze the effect of the multiple extrusion on HDPE09 and the effect of the filler type (with a good filler dispersion).

3.2.3 MWCNT (Arkema) based composites

The dried powders or pellets of HDPE09, MA-p-PE and pMWCNT were mixed and then melt-compounded with a Thermo-Haake Polylab Rheomix 600 internal mixer. The temperature was set at 180°C and the rotation speed at 20 rpm for 5 minutes and then 100 rpm for 20 minutes. Samples of the composites were compression moulded to obtain sheet 200x200x0.5 mm^3. The hot press procedure involved preheating at 180 °C for 10 minutes followed by compressing for 30 seconds at the same temperature with a load of 10 tons, and subsequent cooling under pressure until to reach the room temperature (at about 10°C/min). The added MA-g-PE and pMWCNT fractions were assessed in a such a way to obtain the composite compositions as indicated in Table 3.7: it is appropriate to observe that the table indicate the effective MWCNT content in the composite materials and not the added pMWCNT fraction because pMWCNT is a masterbatch with only a partial content of MWCNTs. Moreover all the pMWCNT based composites were produced with an effective MWCNT content of 1 vol%.

Table 3.7. List of the produced pMWCNT based composites.

Material Code	**Polymeric matrix composition**		**Filler content**
	HDPE09 [vol%]	**MA-g-PE [vol%]**	**MWCNT [vol%]**
HDPE09-(MA-g-PE) blends			
HDPE09	100	-	-
HDPE09-(MA-g-PE) 5 vol%	95	5	-
HDPE09-(MA-g-PE) 10 vol%	90	10	-
HDPE09-(MA-g-PE) 20 vol%	80	20	-
HDPE09-(MA-g-PE)-pMWCNT composites			
HDPE09-pMWCNT 1 vol%	100	-	1
[HDPE09-(MA-g-PE) 5 vol%]-pMWCNT 1 vol%	95	5	1
[HDPE09-(MA-g-PE) 10 vol%]-pMWCNT 1 vol%	90	10	1
[HDPE09-(MA-g-PE) 20 vol%]-pMWCNT 1 vol%	80	20	1

It is appropriate to observe that the work can be divided in two parts:

- in the first part only the effects of pMWCNT on HDPE properties was evaluated. For this reason only HDPE09 and HDPE09-pMWCNT 1 vol% were considered (see chapter 0);

- in second part the effect of addition of the MA-g-PE was evaluated. For this reason the main topic of this part was the comparison between HDPE09-(MA-g-PE) blends and HDPE09-(MA-g-PE)-pMWCNT composites (see chapter 6.2).

The produced materials were analyzed with OM, TGA, DSC, DMTA, tensile tests and tensile creep tests: DMTA and the creep test were conducted only on HDPE09 and HDPE09-pMWCNT 1 vol% composites. Moreover, TEM, TGA, DSC and DMTA were conducted on the masterbatch pMWCNT.

3.2.3.1 OM

The quality of the filler dispersion was evaluated by optical microscopy: thin slices with a thickness of about 10 μm were cut with a microtome and then observed with microscope.

3.2.3.2 TEM

The MWCNTs of the masterbatch pMWCNT were observed with a TEM: for this reason a sample of pMWCNT was burned with a TGA in order to remove the polymeric carrier. Therefore the MWCNTs were dispersed in ethanol with the help of a sonication bath and a drop of the dispersion was put on a thin film of amorphous carbon. Once the ethanol was evaporated, the sample was observed at TEM.

3.2.3.3 DSC

In the case of DSC measurements on the composite materials a first heating ramp from 0°C up to 200°C was followed by a cooling stage from 200°C to 0°C and by a second heating ramp up to 200°C. In the case of the pMWCNT sample, the reference temperatures were -20°C and 250°C. Both heating and cooling rates were fixed at 10°C/min and all tests were conducted in nitrogen flushing at 100 ml/min.

3.2.3.4 TGA

TGA was carried out at a heating rate of 10°C/min in nitrogen atmosphere (200 ml/min). Typically 20 mg samples were placed into the alumina sample pan and heated from 30°C up to 600°C for the composites and up to 800°C for pMWCNT.

3.2.3.5 DMTA

The DMTA tests were performed at a frequency of 1 Hz by scanning temperature in the range from –130°C to +130°C at a heating rate of 3°C/min in the case of the composites and from room

temperature until the break at the same heating rate in the case of pMWCNT. The specimens consisted of strips with a nominal gauge length of 15 mm and a width of 5 mm: the tests were carried out in tensile mode by applying a displacement amplitude of 32 μm corresponding to a strain amplitude of about 0.2%. The pre-load applied to perform the test was 0.1 MPa.

The tested sample of pMWCNT was produced by compression moulding. The hot press procedure involved preheating at 180 °C for 10 minutes followed by compressing for 30 seconds at the same temperature with a load of 10 tons, and subsequent cooling under pressure until to reach the room temperature (at about 10°C/min).

3.2.3.6 Tensile tests

The tensile tests were conducted on specimens 1BA (with a gauge length of : 30 mm) according to the standard ISO 527. Tensile modulus was determined by performing test at cross-head speed of 0.5 mm/min, while tensile strength and strain at yield and at break at a cross-head speed of 50 mm/min. Five specimens were tested for every material.

3.2.3.7 Tensile creep tests

Tensile creep tests were conducted on strip samples with a gauge length of 60 mm and a width of 5 mm. The tests were performed by varying the temperature between 30°C and 90°C and the applied constant stress between 3 and 15 MPa. The displacement, and thereby the deformation, was monitored for 3600 seconds. Before the testing, every specimen was conditioned at the testing temperature for 15 minutes.

3.2.4 MWCNT (NanoAmor) based composites

In this chapter the work conducted on the uMWCNT of NanoAmor is described. This includes the treatment on uMWCNT, the characterization of the untreated and treated MWCNTs, the production and the characterization of the composites based on these MWCNTs.

3.2.4.1 MWCNT treatments

3.2.4.1.1 Oxidation of MWCNTs by nitric acid

A suspension of raw uMWCNT (about 0.5 g) and nitric acid (about 50 ml), i.e a concentration of 10 mg/ml, was added into a round-bottomed glass flask, and the MWCNTs were dispersed for 15 min in an Elma Transsonic T 460/H ultrasonic bath. Then the reaction flask equipped with reflux condenser and magnetic stirrer was mounted in a preheated oil bath at 130°C. After a fixed time (2,

6, 12 and 24 h) the suspension was extracted, cooled and centrifuged at 3500 rpm for 15 min, and the resulting yellow-brown solution was decanted. The wet powder was washed with distilled water, centrifuged (3500 rpm, 15 min) and decanted iteratively as long as the suspension reached a neutral pH. After the last centrifugation, the solid sample was dried in a oven under vacuum at 120°C for 12 h.

The samples produced with the treatment are indicated as oMWCNT in the following chapters.

3.2.4.1.2 Functionalization of MWCNT with silane coupling agents

The treatment was performed on oMWCNT characterized by an oxidation time of 24 h (see the previous chapter). Two types of silane were used: an octadecylsilane $CH_3(CH_2)_{17}SiH_3$ (molecular weight = 284.60) purchased from Sigma-Aldrich, indicated as ODS, and a phenyltrimethoxy silane $(CH_3O)_3Si–Ph$ (molecular weight = 198.29) with the commercial trademark Z-6124 purchased by Dow Corning, indicated as PMS. A suspension of oMWCNT (2 mg/ml), silane (25 μmol per each square meter of oMWCNT) and toluene in the case of ODS and ethanol in the case of PMS (50 ml) was added into a round-bottomed glass flask and the MWCNTs were dispersed for 15 min in an ultrasonic bath. Then two types of treatment were performed:

- the reaction flask equipped with reflux condenser and magnetic stirrer was mounted in a preheated oil bath at 80°C for 48 h. The treatment was performed only with ODS;
- an Hielscher UP400S tip sonicator was put into the reaction flask for 40 min at room temperature. The treatment was performed with ODS and PMS.

After the fixed time, the suspension was extracted and filtrated with a Teflon membrane (0.2 μm pores), washed with acetone (in the case of ODS) or ethanol (in the case of PMS) and dried in a oven under vacuum at 120°C for 12 h.

3.2.4.1.3 Characterization of MWCNTs

A Micromeritics AccuPyc 1330TC helium pycnometer was used to measure the density of the MWCNTs: the fill pressure was set to 19.5 psig and the equilibration rate to 0.0050 psig/min. Multiple measurements were employed to have a complete desorption of the nitrogen from the MWCNTs: the limiting density was assumed as the true density of the material.

TGA analysis was carried out at a heating rate of 10°C/min in nitrogen atmosphere and in air atmosphere (200 ml/min). Typically 10 mg samples were placed into the alumina sample pan and heated from 30°C up to 800°C.

TEM observations were performed to assess the morphology of the pristine and modified MWCNTs. Therefore the MWCNTs were dispersed in ethanol with the help of a sonication bath

and a drop of the dispersion was put on a thin film of amorphous carbon. Once the ethanol was evaporated, the sample was observed using a TEM.

The samples were observed and analyzed by SEM equipped an EDAX microanalysis system in order to detect the presence of residual catalysts and the relative content of carbon and oxygen.

FTIR spectra were collected with a Nicolet Magna 550 spectrometer in transmission mode on powdered samples in KBr pellets.

Nitrogen adsorption measurements at 77 K were carried out using a volumetric adsorption apparatus (Micromeritics ASAP 2010). Typically a sample of 0.1 g, that was previously dried at 150°C under a vacuum, was analyzed. The nitrogen adsorption isotherm curves were analyzed with Brunauer–Emmett–Teller method in order to determine the specific surface area and the pore size distribution.

3.2.4.2 MWCNT filled composites

3.2.4.2.1 HDPE09-MWCNT (extruder) composites

The dried powders of HDPE09 and uMWCNT were mixed and then melt-compounded with the twin screw extruder (see the chapter 3.2.1) equipped with a sheet die. The barrel temperature profile was set at 130-200-210-220-220°C and the screw rotation speed at 12 rpm. The extruder produced a continuous sheet with a section of 50x1.5 mm^2. The added filler fraction was assessed in a such a way as to obtain a composite with a content of 0.05, 0.25 and 0.5 vol%.

The quality of the filler dispersion was evaluated by optical microscopy: thin slices with a thickness of about 10 μm were cut with a microtome and then observed on a microscope.

TGA was carried out at a heating rate of 10°C/min in nitrogen atmosphere (200 ml/min). Typically 30 mg samples of composite materials were placed into the alumina sample pan and heated from 30°C up to 600°C.

DSC measurements were conducted on the composite materials. A first heating ramp from 0°C up to 200°C was followed by a cooling stage from 200°C to 0°C and by a second heating ramp up to 200°C. Both heating and cooling rates were fixed at 10°C/min and all tests were conducted in nitrogen flushing at 100 ml/min. The crystallinity content of the composites was assessed by integrating the normalized area of the melting endothermic peak and dividing the heat involved by the reference value of a theoretical 100% crystalline HDPE (277.1 J/g) [135].

Tensile tests were conducted on specimens 1BA (with a gauge length of 30 mm) according to the standard ISO 527 in order to measure the mechanical properties of the composite materials. Tensile modulus was determined by performing tests at a cross-head speed of 0.5 mm/min, while tensile

strength and strain at yield and at break at a cross-head speed of 50 mm/min. Five specimens were tested for every material.

DMTA tests were were performed on the composite materials at a frequency of 1 Hz by scanning temperature in the range from –130°C to +130°C at a heating rate of 3°C/min. The specimens consisted of strips with a nominal gauge length of 15 mm and a width of 5 mm: the tests were carried out in tensile mode by applying a displacement amplitude of 32 μm corresponding is a strain amplitude of about 0.2%. The pre-load applied to perform the test was 0.1 MPa.

3.2.4.2.2 HDPE09-MWCNT (mixer) composites

The dried powders or pellets of HDPE09 and uMWCNT were mixed and then melt-compounded with an internal mixer. More configurations were used to produce the composites materials: Table 3.8 presents a list of the temperature, rotation speed and time of processing. Samples of the composites were compression moulded to obtain sheet 200x200x0.5 mm^3. The hot press procedure involved preheating at 180 °C for 10 minutes followed by compressing for 30 seconds at the same temperature with a load of 10 tons, and subsequent cooling under pressure until to reach the room temperature (at about 10°C/min). The added uMWNCT fractions were assessed in a such a way to obtain the composite compositions as indicated in Table 3.8.

Table 3.8. List of the produced composite materials and corresponding processing conditions.

Material	Processing condition
HDPE09 HDPE09-uMWCNT 0.05 vol% HDPE09-uMWCNT 0.5 vol%	180°C 15 min @ 20 rpm
HDPE09 HDPE09-uMWCNT 0.05 vol% HDPE09-uMWCNT 0.5 vol%	180°C 5 min @ 20 rpm + 20 min @ 100 rpm
HDPE09 HDPE09-uMWCNT 0.5 vol%	135°C 5 min @ 20 rpm + 20 min @ 100 rpm

The quality of the filler dispersion was evaluated by optical microscopy: thin slices with a thickness of about 10 μm were cut with a microtome and then observed at microscope.

Thermogravimetric analysis (TGA) was carried out at a heating rate of 10°C/min in nitrogen atmosphere (200 ml/min). Typically 30 mg samples of composite materials were placed into the alumina sample pan and heated from 30°C up to 600°C.

Differential scanning calorimetry (DSC) measurements were conducted on the composite materials. A first heating ramp from 0°C up to 200°C was followed by a cooling stage from 200°C to 0°C and by a second heating ramp up to 200°C. Both heating and cooling rates were fixed at 10°C/min and all tests were conducted in nitrogen flushing at 100 ml/min. The crystallinity content of the composites was assessed by integrating the normalized area of the melting endothermic peak and dividing the heat involved by the reference value of a theoretical 100% crystalline HDPE (277.1 J/g) [135].

Tensile tests were conducted on specimens 1BA (with a gauge length of 30 mm) according to the standard ISO 527 in order to measure the mechanical properties of the composite materials. Tensile modulus was determined by performing test at cross-head speed of 0.5 mm/min, while tensile strength and strain at yield and at break at a cross-head speed of 50 mm/min. Five specimens were tested for every materials.

DMTA tests were were performed on the composite materials at a frequency of 1 Hz by scanning temperature in the range from –130°C to +130°C at a heating rate of 3°C/min. The specimens consisted of strips with a nominal gauge length of 15 mm and a width of 5 mm: the tests were carried out in tensile mode by applying a displacement amplitude of 32 μm that is a strain amplitude of about 0.2%. The pre-load applied to perform the test was 0.1 MPa.

Tensile creep tests were conducted on strip sample with a gauge length of 60 mm and a width of 5 mm. The test were performed at 30°C with an applied constant stress of 3 and 15 MPa: the displacement, i.e. the deformation, were monitored for 3600 seconds. Before the testing every specimens was conditioned at the testing temperature for 15 minutes.

3.2.4.2.3 PVOH-MWCNT (bath sonication) composites

The dried powders or grains of PVOH89p, PVOH99 and uMWCNT were compounded by solution mixing with the help of a sonication treatment. The MWCNTs were added to 50 g/l aqueous solution of PVOH in a such a way to obtain a filler fraction of 0.05 and 0.5 vol%, i.e. it was used dispersions of about 0.05 and 0.5 mg/ml, and dispersed for 1 h in an ultrasonic bath. The solutions were cast into a silicon mould and placed in a 60°C heated oven to allow evaporation of the solvent and the dried in a oven under vacuum at 110°C for 4 h. Table 3.10 presents the list of the produced materials.

The quality of the filler dispersion was evaluated by observing the produced films with an optical microscope.

Thermogravimetric analysis (TGA) was carried out at a heating rate of 10°C/min in nitrogen atmosphere (200 ml/min). Typically 30 mg samples of composite materials were placed into the alumina sample pan and heated from 30°C up to 600°C.

Differential scanning calorimetry (DSC) measurements were conducted on the composite materials. A first heating ramp from 0°C up to 240°C was followed by a cooling stage from 240°C to 0°C and by a second heating ramp up to 240°C. Both heating and cooling rates were fixed at 10°C/min and all tests were conducted in nitrogen flushing at 100 ml/min. The DSC curves was used to calculate the glass transition temperature and the crystallinity content that was assessed by integrating the normalized area of the melting endothermic peak and dividing the heat involved by the reference value of a theoretical 100% crystalline PVOH (161.4 J/g) [136].

DMTA tests were performed on the composite materials at a frequency of 1 Hz by scanning temperature in the range from –50°C to +200°C at a heating rate of 3°C/min. The specimens consisted of strips with a nominal gauge length of 15 mm and a width of 5 mm: the tests were carried out in tensile mode by applying a displacement amplitude of 32 μm that is a strain amplitude of about 0.2%. The pre-load applied to perform the test was 0.1 MPa.

3.2.4.2.4 PVOH-MWCNT (tip sonication) composites

The dried powders or grains of PVOH89p, uMWCNT, oMWCNT (with an oxidation time of 24 h) were compounded by solution mixing with the help of a cationic surfactant as SDS and of a sonication treatment. The MWCNTs were added to 100 g/l aqueous solution of PVOH in a such a way to obtain a filler fraction of 0.5 vol%, i.e. it was used dispersions of about 1 mg/ml, and dispersed for 15 min with a tip sonicator. Moreover a aqueous solution of PVOH with 1 g/l of sodium dodecyl sulfate (SDS, ≥96.0%, purchased by Sigma-Aldrich) was produced. The solutions were cast into a silicon mould and placed in a 60°C heated oven to allow evaporation of the solvent and the dried in a oven under vacuum at 110°C for 4 h. Table 3.9 presents the list of the produced materials.

The quality of the filler dispersion was evaluated by observing the produced films with an optical microscope.

Table 3.10. List of the produced PVOH-uMWCNT composites.

Material
PVOH89p
PVOH89p-uMWCNT 0.05 vol%
PVOH89p-uMWCNT 0.5 vol%
PVOH99
PVOH99-uMWCNT 0.05 vol%
PVOH99-uMWCNT 0.5 vol%

Table 3.9. List of the produced PVOH89p-MWCNT composites.

Material
PVOH89p
PVOH89p-uMWCNT 0.5 vol%
PVOH89p-oMWCNT 0.5 vol%
PVOH89p-SDS-uMWCNT 0.5 vol%

4 Results on copper- and iron-powder-based composites

This chapter is dedicated to Cu and Fe powders based composites: the paragraph 4.1 presents a brief characterization of the metallic powders. Afterwards the paragraph 4.2 deals with all the type of the composites produced by injection moulding (HDPE25-Cu10, HDPE25-Cu45, LDPE70-Cu45, LDPE70-Fe15 and LDPE70-Fe45) with different filler content, while the paragraph 4.3 with only HDPE25-Cu10 and HDPE25-Cu45 composites with 1 vol% of filler produced by compression moulding.

4.1 Cu and Fe powders

4.1.1 SEM

The main goal of the SEM observations of the metallic powders was to assess the effective particle shapes and dimensions and to compare these data to the datasheet of the suppliers. Figure 4.1 and Figure 4.2 show some examples of the acquired micrographs.

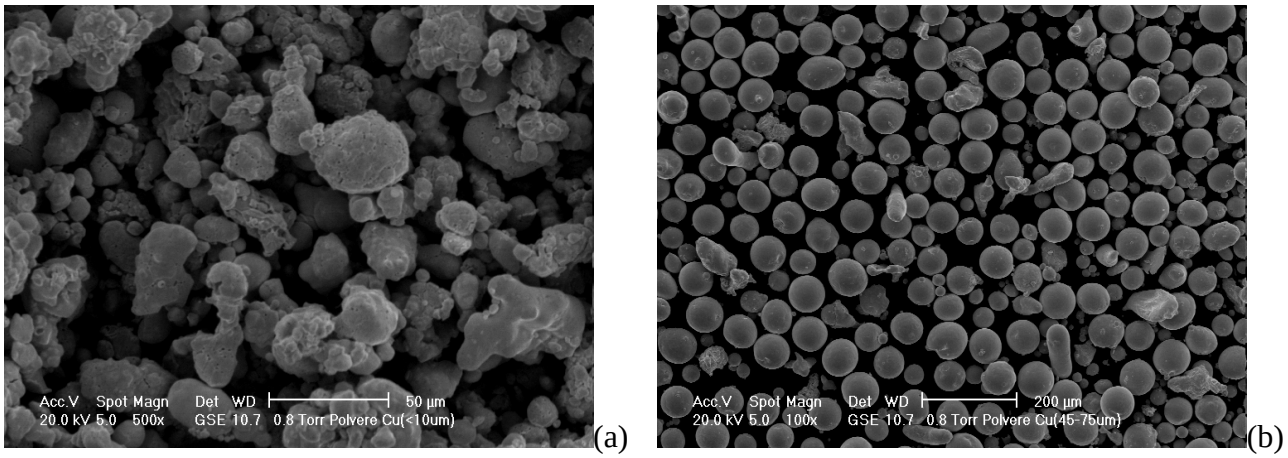

(a) (b)

Figure 4.1. SEM micrographs of Cu10 (a) and Cu45 (b).

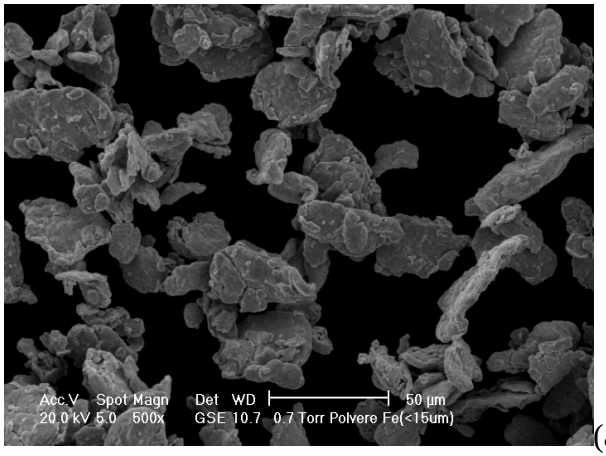

(a)

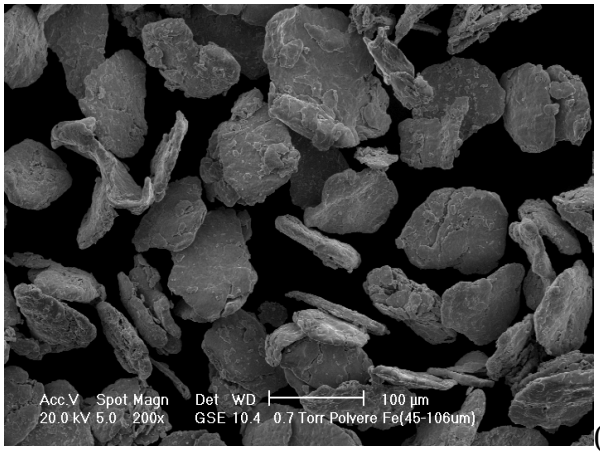

(b)

Figure 4.2. SEM micrographs of Fe15 (a) and Fe45 (b).

The powders of Cu10 had an irregular shape that only in first approximation was spherical: probably they were produced by reduction [137]. The particle dimensions were variable between 1 and 20 μm with a broad distribution. On the other hand the powder of Cu45 had perfectly spherical shape and they were probably produced by atomization [137]. In the case the particle had dimensions between 10 and 80 μm: nevertheless it is convenient to observe that the fraction of particle under 40 μm was very small.

The powders of Fe15 were plates with an irregular surface probably because they were produced by hydrogen reduction [137]. The plate width was variable between 10 and 50 μm and the thickness between 5 and 20 μm with a broad distribution: the most part of the plates were 20 μm large and 5 μm tick. Similarly the powders of Fe45 were plates with an irregular surface produced by hydrogen reduction [137]. In this case the plate width was variable between 40 and 200 μm and the thickness between 10 and 50 μm with a broad distribution: the most part of the plates were 100 μm large and 20 μm tick.

From a general point view these data are relatively in good agreement with the datasheet of the suppliers.

4.2 Cu and Fe powders base composites (injection moulding)

4.2.1 Extruder

Figure 4.3 shows the torque as a function of the filler content for all the type of composites during the extrusion process. The applied torque, that is in first approximation proportional to the melt viscosity, increased with the filler content: initially, i.e. at low filler content, with a linear trend and then, i.e. at high filler content, with an exponential trend. No difference was advisable between the

composites filled with particles of different dimension. Moreover it is appropriate to observe as the standard deviation of the measured torque increased with the filler content: as the filler content increased as the homogeneity of the composites was more difficult because the large difference between the densities of the polymer (0.954 g/cm^3 for HDPE09 and 0.919 g/cm^3 for LDPE70) and the density of the filler (8.96 g/cm^3 for Cu and 7.87 g/cm^3 for Fe).

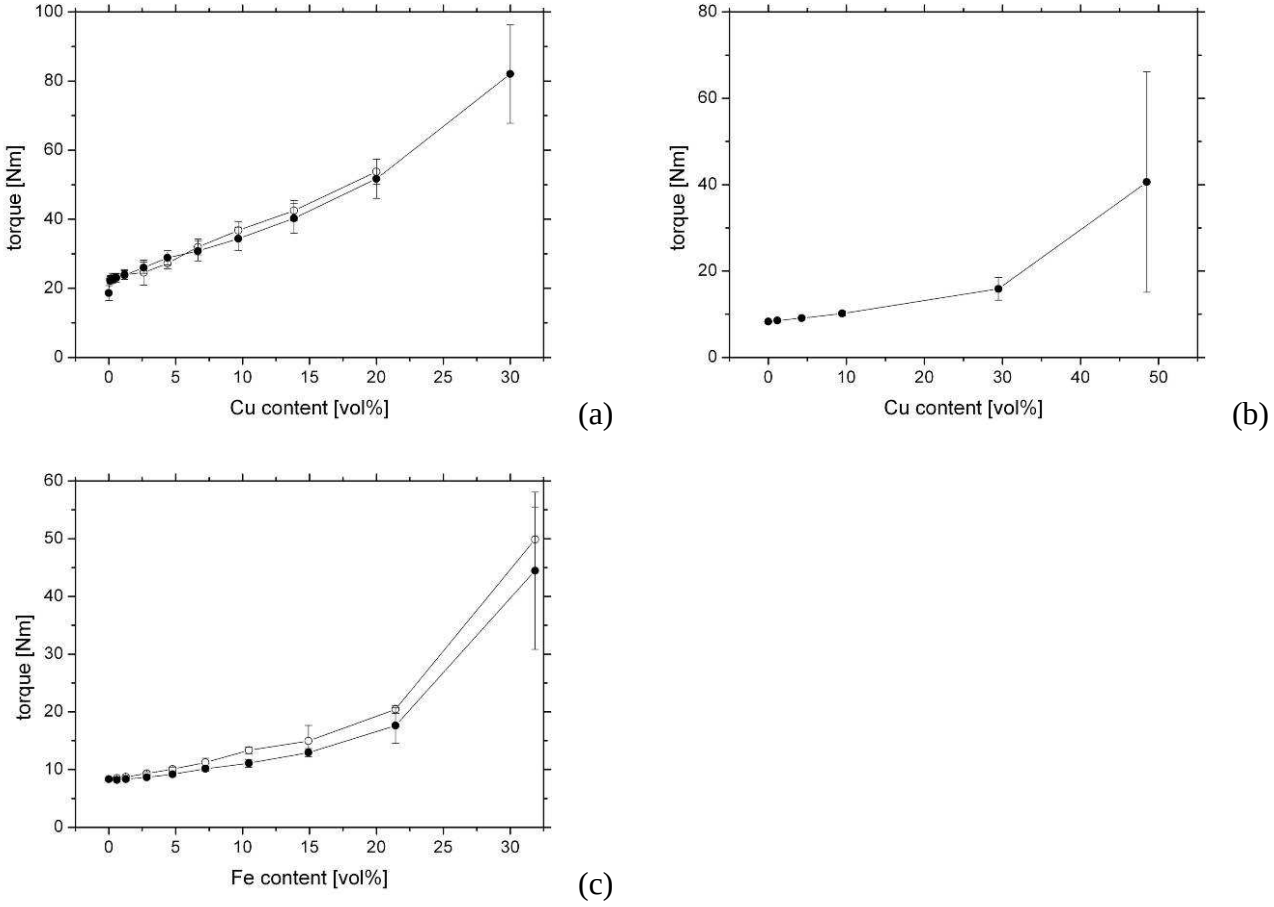

Figure 4.3. Torque as a function of the filler content for: (a) HDPE25-Cu10 (○) and HDPE25-Cu45 (●) composites; (b) LDPE70-Cu45 composites; and (c) LDPE70-Fe15 (○) and LDPE70-Fe45 (●) composites.

4.2.2 SEM

Samples of the produced composite materials were cryofractured in liquid nitrogen and then observed at SEM in order to evaluate the interaction between the polymeric matrix and the metallic particles. Figure 4.4 shows some examples of the acquired micrographs for HDPE25-Cu10 and HDPE25-Cu45 composites. In both the case there was no evident interaction between the polymer and the inorganic filler [138]: the filler particle surfaces were completely smooth and the cavity (where a particle was present before the cryofracture) were completely smooth too.

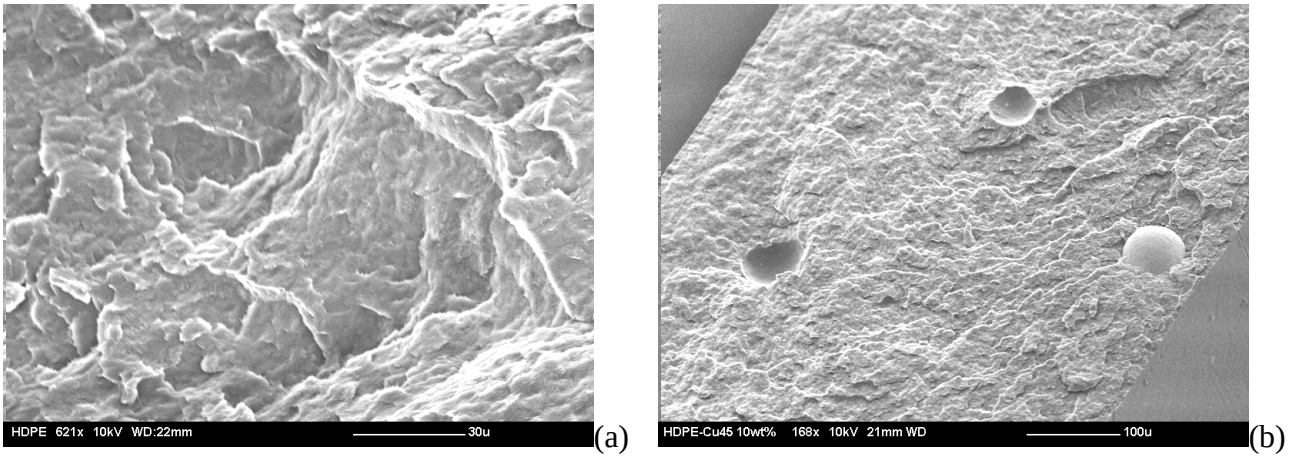

(a) (b)

Figure 4.4. SEM micrographs of the fractured surface of HDPE25-Cu10 (a) and HDPE25-Cu45 composites (b).

Figure 4.5 shows some examples of the acquired micrographs for LDPE70-Fe15 and LDPE70-Fe45 composites. In both the case there was evidence of a good interaction between the polymer and the inorganic filler [138]: the irregularity on the filler particle surfaces Figure 4.2 were covered by the polymer even after the fracture in the liquid nitrogen.

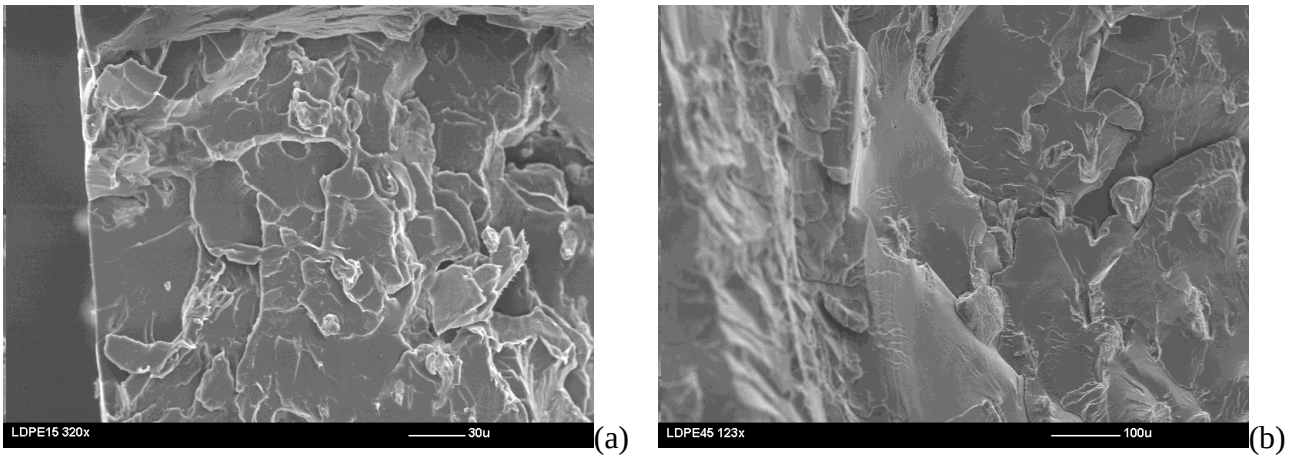

(a) (b)

Figure 4.5. SEM micrographs of the fractured surface of LDPE70-Fe15 and LDPE70-Fe45 composites.

4.2.3 DSC

The DSC analyses were conducted only on the base polyethylene matrices, HDPE and LDPE, and on the composites filled with 10 vol% of metallic powders, Cu and Fe, in order to evaluate the effect of the filler addition from a general point of view. The curves maintained the original shape of the curves of HDPE and LDPE: a broad exothermic peak related to the crystallization during the cooling stage and a broad endothermic peak related to the melting during the heating stage (Figure 4.6, Figure 4.7 and Figure 4.8).

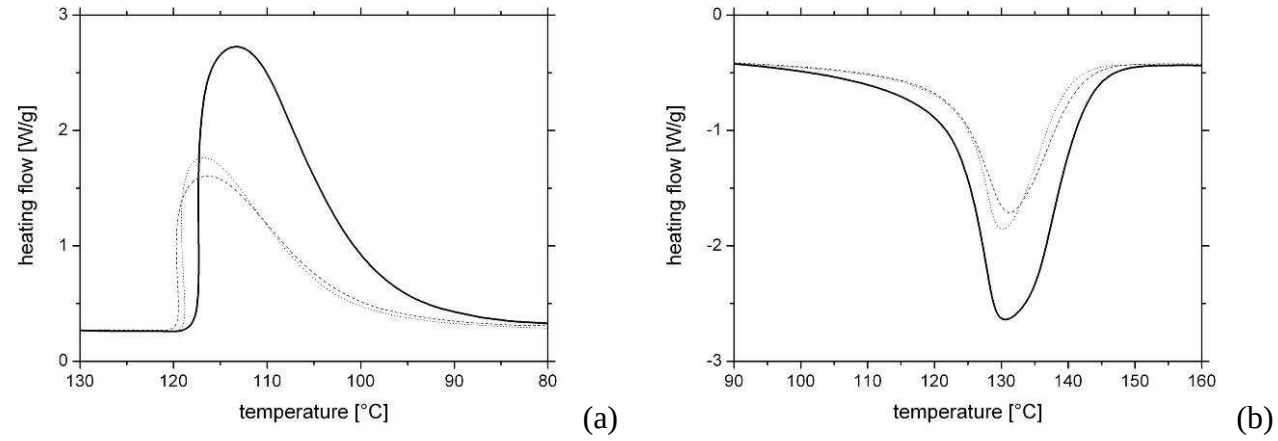

Figure 4.6. DSC curves of HDPE25 (—), HDPE25-Cu10 10vol% (···) and HDPE25-Cu45 10vol% (---) for the cooling stage (a) and the heating stage (b).

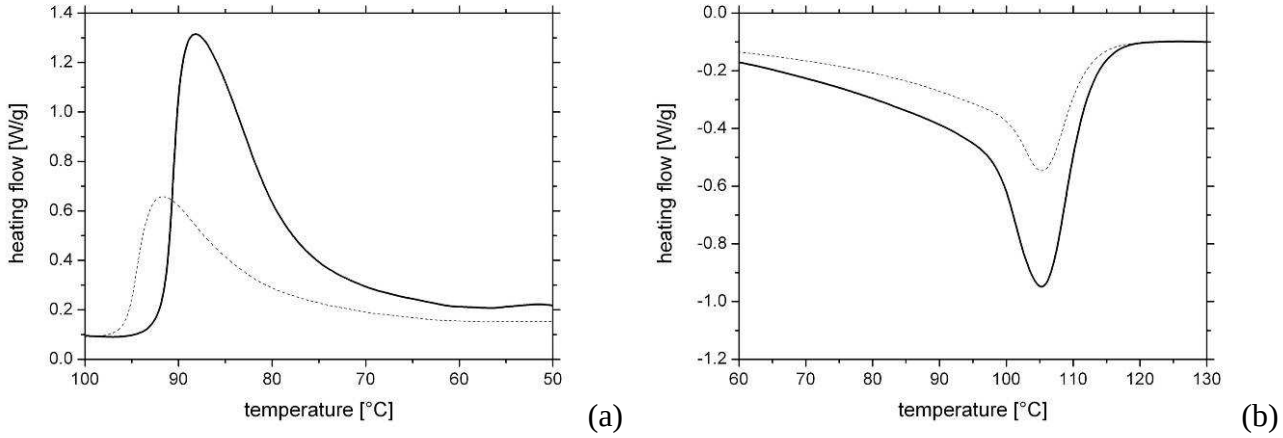

Figure 4.7. DSC curves of LDPE70 (—) and LDPE70-Cu45 10vol% (---) for the cooling stage (a) and the heating stage (b).

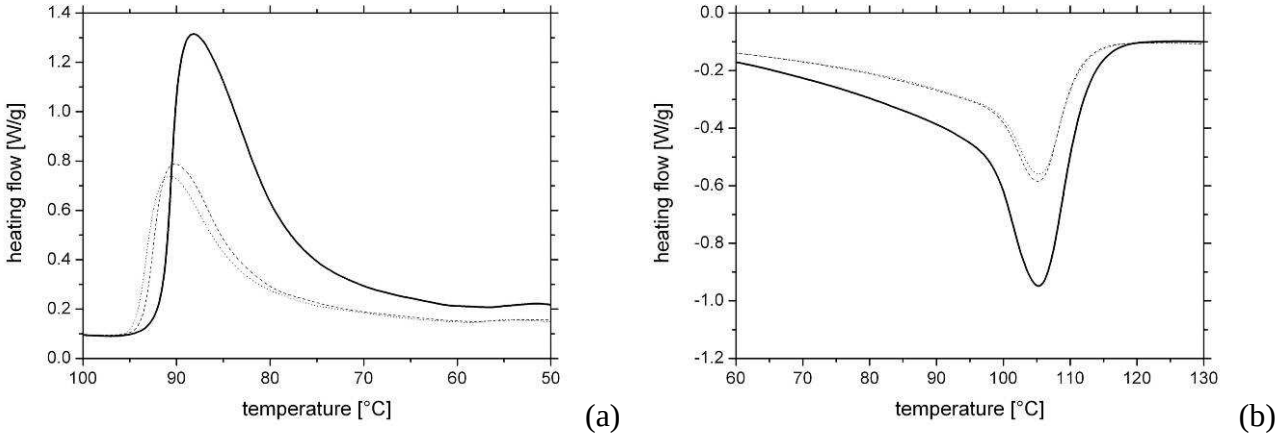

Figure 4.8. DSC curves of LDPE70 (—), LDPE70-Fe15 10vol% (···) and LDPE70-Fe45 10vol% (---) for the cooling stage (a) and the heating stage (b).

The results of these analyses are showed in Table 4.1: the data deal with the crystallization during the cooling stage and with the melting during the heating stage. The most evident effect was the nucleating effect of all the fillers: the crystallinity (from 2 to 4%), the onset and the peak temperatures of the crystallization (about 2°C) moved to higher values. On the other hand the melting temperature remained unchanged.

Table 4.1. Results of the analysis of the DSC curves: crystallinity (χ), melting (T_m) and crystallization (T_c) temperature, onset (T_{ON}) and endset (T_{END}) temperatures.

Material	Crystallization – Cooling (2nd scan)				Melting – Heating (3rd scan)			
	χ [wt%]	T_c [°C]	T_{ON} [°C]	T_{END} [°C]	χ [wt%]	T_m [°C]	T_{ON} [°C]	T_{END} [°C]
HDPE25	83.5	113.3	117.6	99.0	84.2	130.6	121.3	142.2
HDPE25-Cu10 10 vol%	86.8	116.8	118.9	102.6	86.9	130.2	122.6	139.4
HDPE25-Cu45 10 vol%	88.7	116.4	119.6	101.1	87.6	131.3	121.0	141.4
LDPE	87.9	88.2	91.8	75.8	87.2	105.3	93.1	112.6
LDPE70-Cu45 10 vol%	94.9	91.7	95.9	78.6	91.3	105.3	93.6	112.2
LDPE70-Fe15 10 vol%	91.1	90.8	94.5	80.9	91.7	105.3	94.4	111.5
LDPE70-Fe45 10 vol%	92.2	90.1	93.8	80.7	91.5	105.2	94.4	111.3

4.2.4 Tensile tests

The first observation about the tensile test on the produced composites was the different yielding phenomena. All the materials had a sharp yield in the stress-strain curves, but HDPE based composites had necking and whitened, while LDPE based composites had only necking and no whitening.

From Figure 4.9 to Figure 4.11 examples of stress-strain curves of all the composites (HDPE25-Cu10, HDPE25-Cu45, LDPE70-Cu45, LDPE70-Fe15 and LDPE70-Fe45) at different filler content are showed. Moreover the figures from Figure 4.12 to Figure 4.20 propose elastic modulus, stress and strain at yielding and at break for all the composites as a function of the filler content.

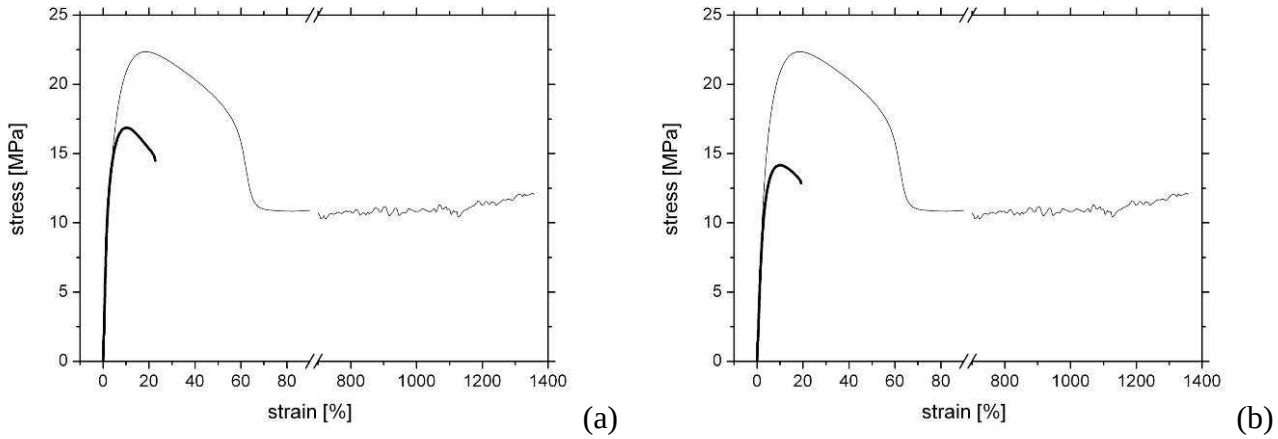

Figure 4.9. Examples of stress-strain curves of HDPE25-Cu10 (a) and HDPE25-Cu45 (b) composites at high filler content (thick line) in comparison to HDPE25 (thin line).

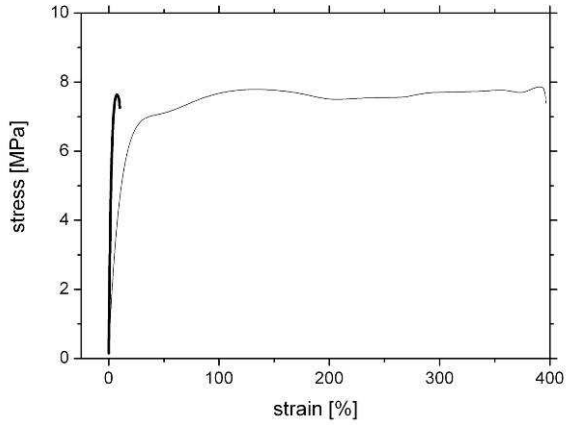

Figure 4.10. Examples of stress-strain curves of LDPE70-Cu45 composites at high filler content (thick line) in comparison to LDPE70 (thin line).

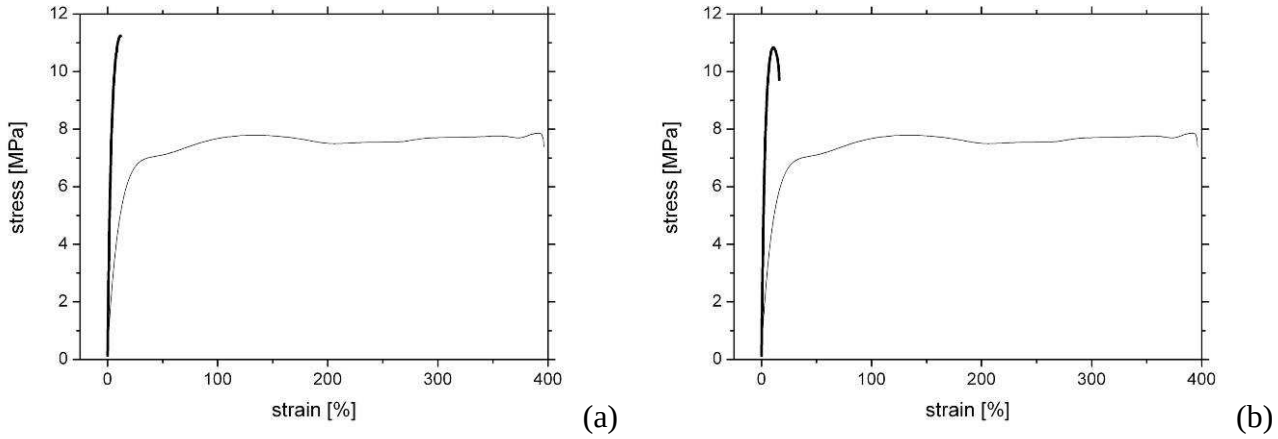

Figure 4.11. Examples of stress-strain curves of LDPE70-Fe15 (a) and LDPE70-Fe45 (b) composites at high filler content (thick line) in comparison to LDPE70 (thin line).

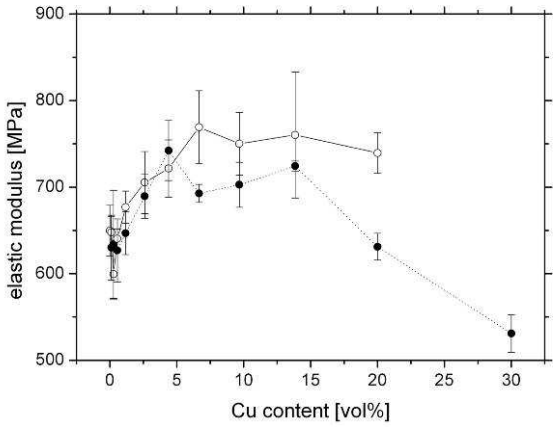

Figure 4.12. Elastic modulus as a function of the filler content for HDPE25-Cu10 (○) and HDPE25-Cu45 (●) composites.

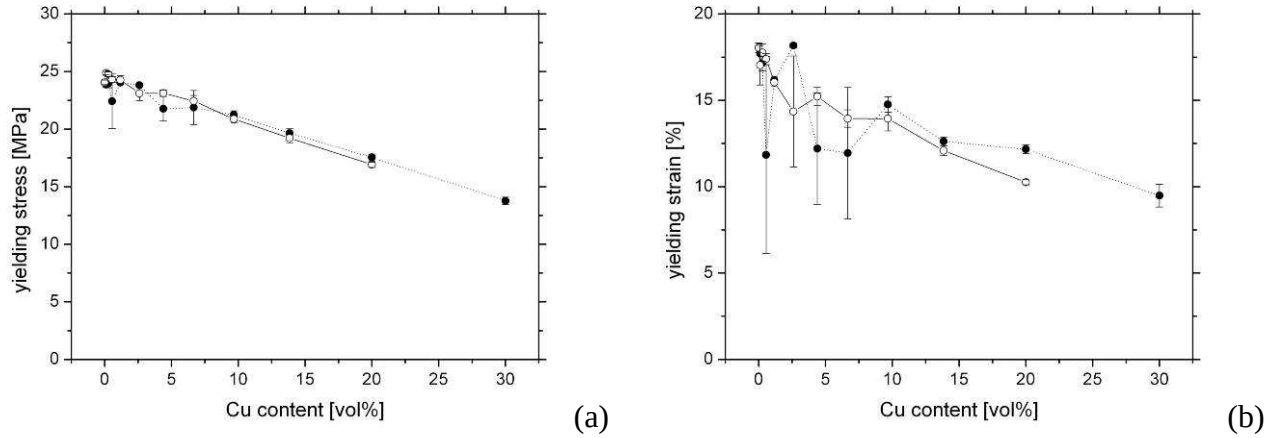

Figure 4.13. Yielding stress (a) and strain (b) as a function of the filler content for HDPE25-Cu10 (○) and HDPE25-Cu45 (●) composites.

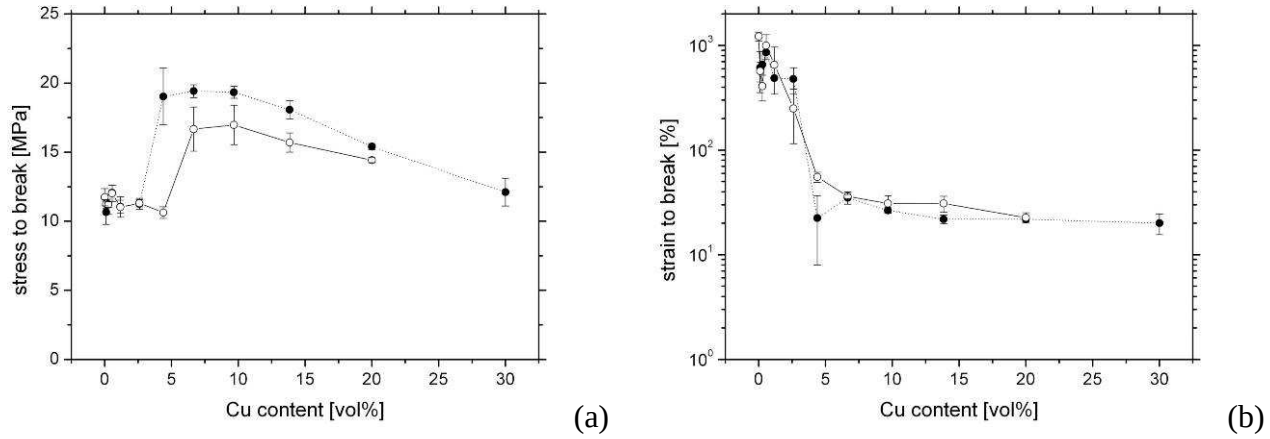

Figure 4.14. Stress (a) and strain at break (b) as a function of the filler content for HDPE25-Cu10 (○) and HDPE25-Cu45 (●) composites.

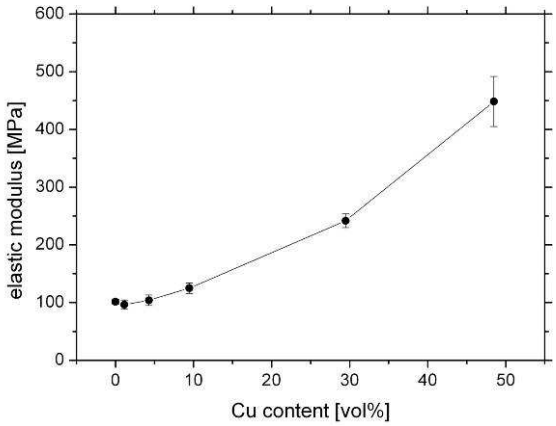

Figure 4.15. Elastic modulus as a function of the filler content for LDPE70-Cu45 composites.

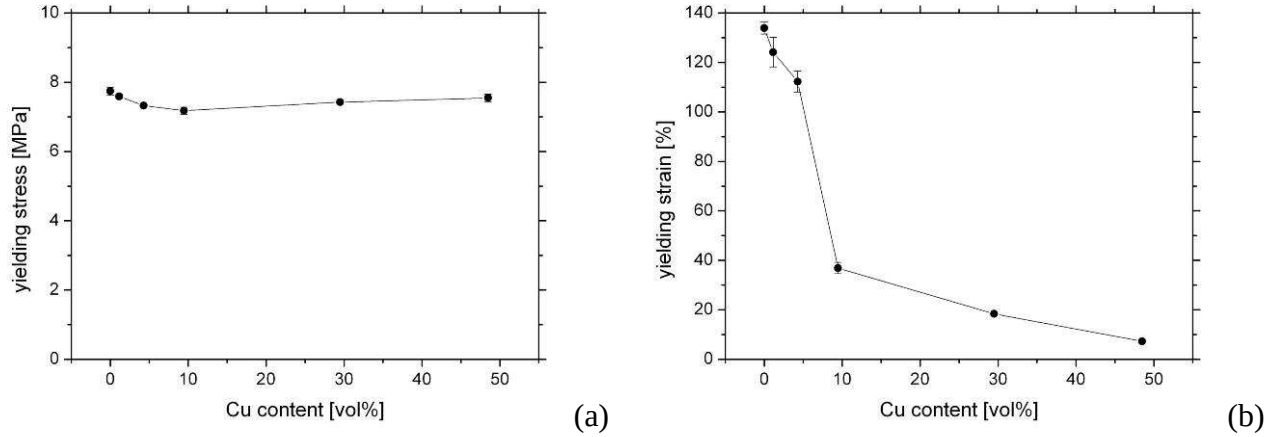

Figure 4.16. Yielding stress (a) and strain (b) as a function of the filler content for LDPE70-Cu45 composites.

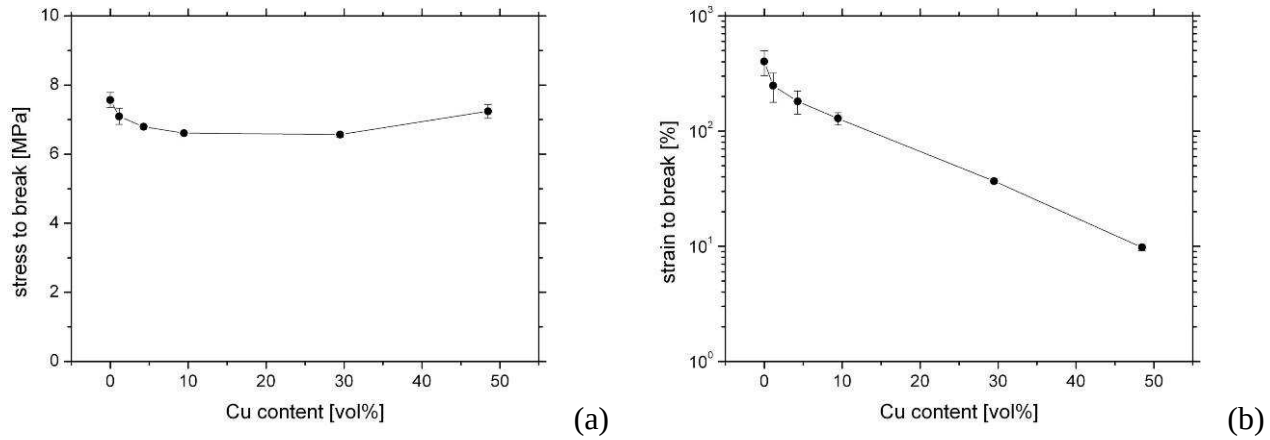

Figure 4.17. Stress (a) and strain at break (b) as a function of the filler content for LDPE70-Cu45 composites.

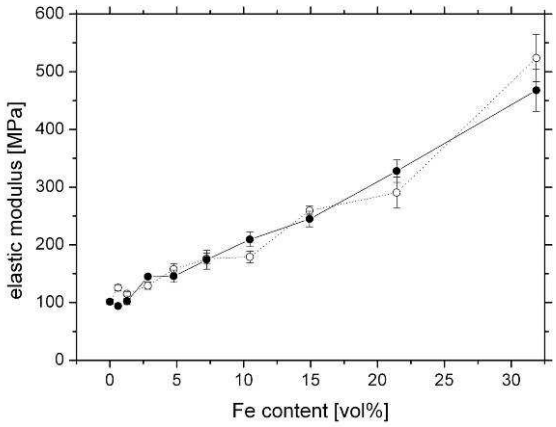

Figure 4.18. Elastic modulus as a function of the filler content for the filler content for LDPE70-Fe15 (○) and LDPE70-Fe45 (●) composites.

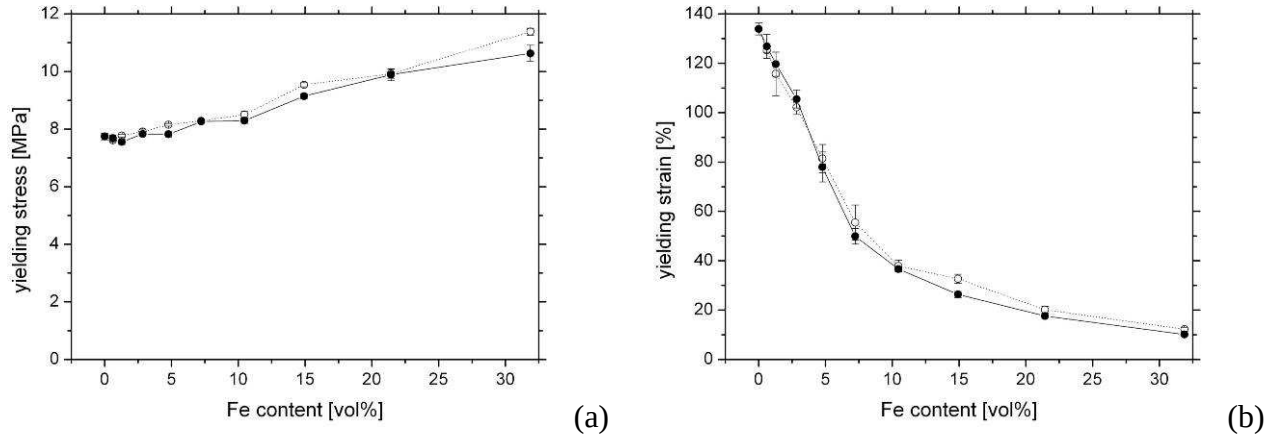

Figure 4.19. Yielding stress (a) and strain (b) as a function of the filler content for LDPE70-Fe15 (○) and LDPE70-Fe45 (●) composites.

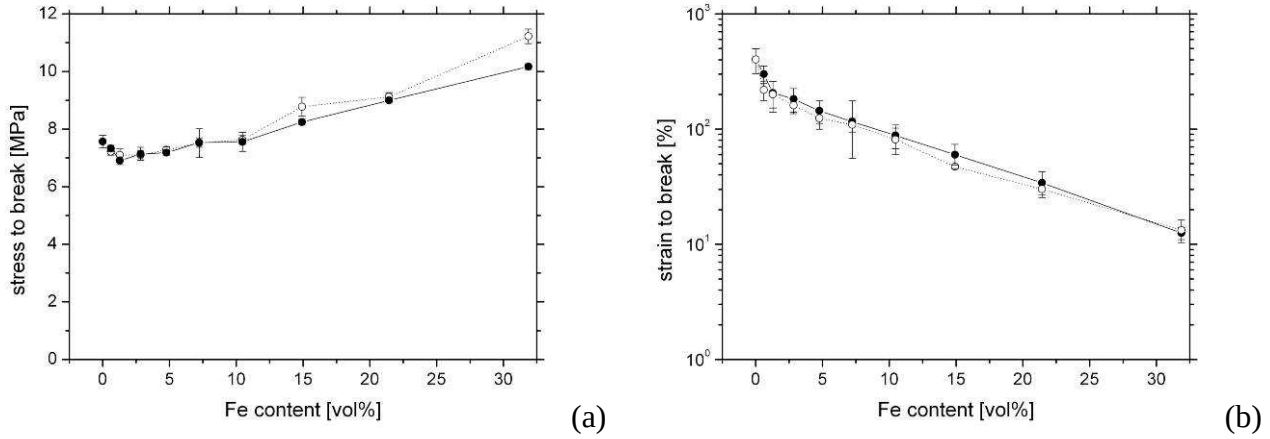

Figure 4.20. Stress (a) and strain at break (b) as a function of the filler content for LDPE70-Fe15 (○) and LDPE70-Fe45 (●) composites.

The evaluation of the effect of the filler type and content can be made with the help of the stress-strain curves or similarly with the help of the curves of the mechanical parameters. The main feature of the different composites can be summarized in the following topics:

- for all both HDPE25-Cu composites the elastic modulus increased until a filler content of 10 vol%. The following decrease is related to agglomeration phenomena [25]. The stress and the strain at yielding progressively decreased. The stress at break remained constant until a filler content of 5-10 vol% and then increased, while the strain at break decreased sharply from 1200% to 50% at a filler content of 5 vol% and then remained between 20% and 30% until a filler content of 30 vol%. No evident difference was present between HDPE25-Cu10 and HDPE25-Cu45 composites except the stress at break over the filler content of 5 vol%: in this case the Cu45 powder appeared to reduces the properties of the composites;
- for LDPE70-Cu45 composites the elastic modulus increased continuously until a filler content of 30 vol%, while the stress at yielding and the stress at break decreased slightly. The strain at yielding and the strain at break continuously decreased. Moreover two slope for both the strain at yielding;
- for LDPE70-Fe composites the elastic modulus, the stress at yielding and the stress at break increased continuously until a filler content of 30 vol%, while the strain at yielding and the strain at break continuously decreased. Moreover two slope for both the strain at yielding and the strain at break are detectable: the first had as reference strain the region at 7-10% and the second 1-2%. No evident difference between LDPE70-Fe15 and LDPE70-Fe45 composites was present: the properties at yielding and at break of LDPE70-Fe45 composites were lower than the ones of LDPE70-Fe15 composites but the difference was lower than the experimental errors.

4.2.5 DMTA

From Figure 4.21 to Figure 4.29 the DMTA curves of all the composites (HDPE25-Cu10, HDPE25-Cu45, LDPE70-Cu45, LDPE70-Fe15 and LDPE70-Fe45) are showed: these tests were conducted only on the base polyethylene matrices, HDPE and LDPE, and on the composites filled with 10 vol% of metallic powders, Cu and Fe, in order to evaluate the effect of the filler addition from a general point of view.

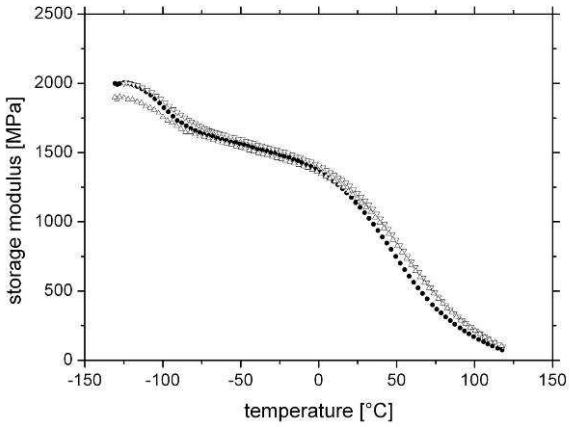

Figure 4.21. Storage modulus as a function of the temperature for HDPE25 (●), HDPE25-Cu10 10 vol% (▽) and HDPE25-Cu45 10 vol% (△).

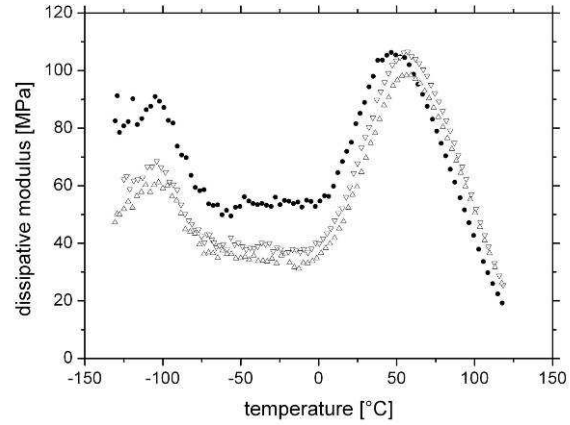

Figure 4.22. Dissipative modulus as a function of the temperature for HDPE25 (●), HDPE25-Cu10 10 vol% (▽) and HDPE25-Cu45 10 vol% (△).

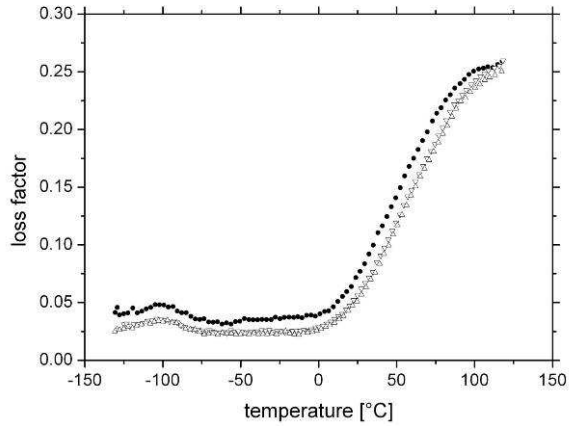

Figure 4.23. Loss factor as a function of the temperature for HDPE25 (●), HDPE25-Cu10 10vol% (▽) and HDPE25-Cu45 10vol% (△).

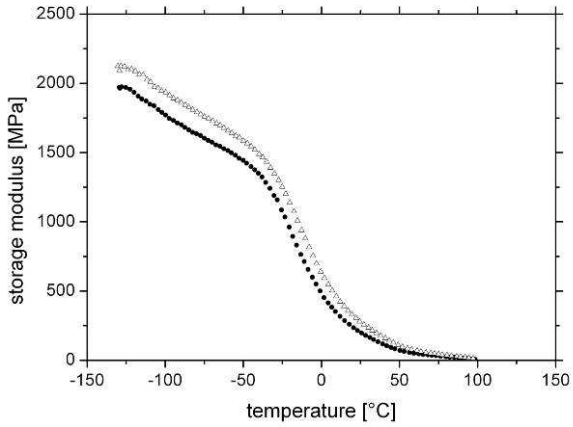

Figure 4.24. Storage modulus as a function of the temperature for LDPE70 (●) and LDPE70-Cu45 10 vol% (△).

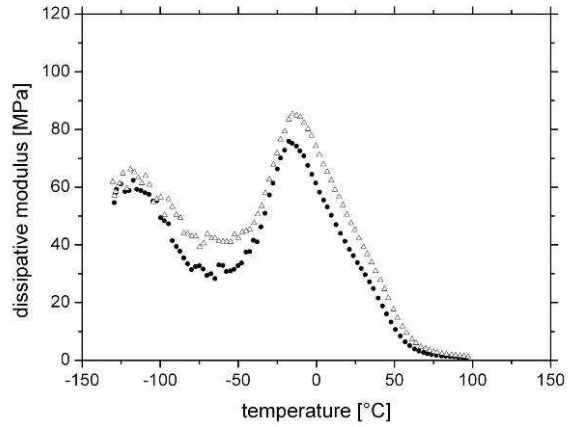

Figure 4.25. Dissipative modulus as a function of the temperature for LDPE70 (●) and LDPE70-Cu45 10 vol% (△).

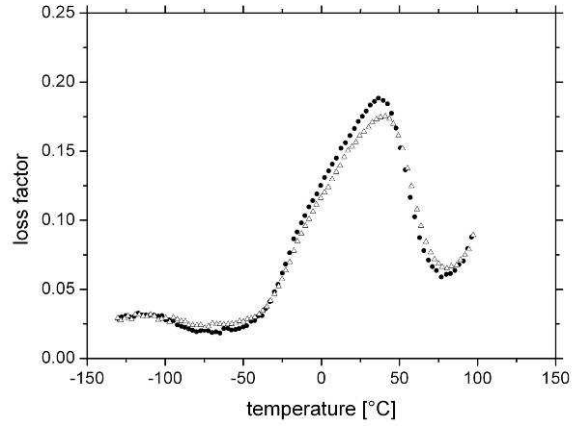

Figure 4.26. Loss factor as a function of the temperature for LDPE70 (●) and LDPE70-Cu45 10 vol% (△).

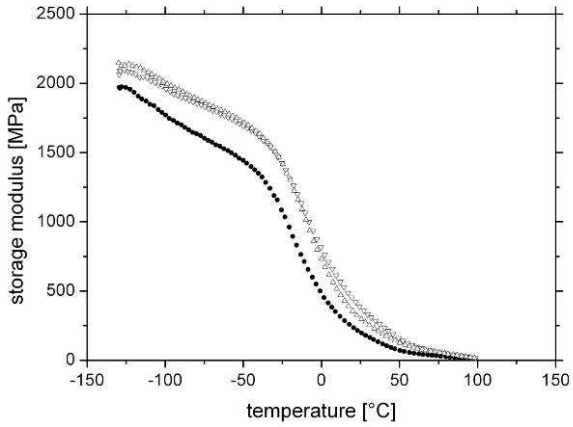

Figure 4.27. Storage modulus as a function of the temperature for LDPE70 (●), LDPE70-Fe15 10 vol% (▽) and LDPE70-Fe45 10 vol% (△).

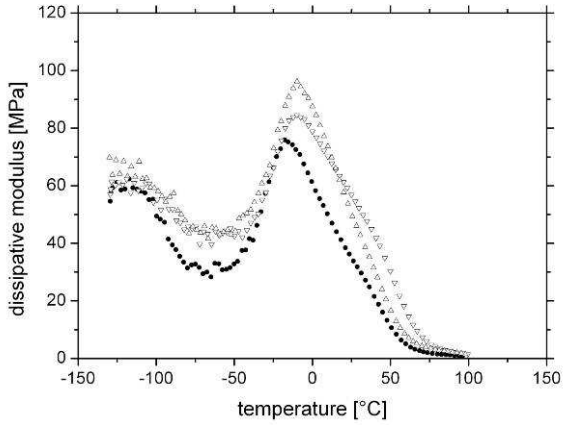

Figure 4.28. Dissipative modulus as a function of the temperature for LDPE70 (●), LDPE70-Fe15 10 vol% (▽) and LDPE70-Fe45 10 vol% (△).

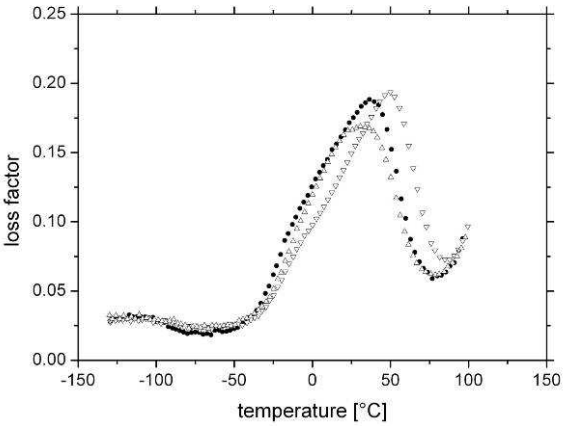

Figure 4.29. Loss factor as a function of the temperature for LDPE70 (●), LDPE70-Fe15 10 vol% (▽) and LDPE70-Fe45 10 vol% (△).

From a general point of view HDPE based composites presented two sharp drops of the storage modulus that corresponded to two peaks in terms of dissipative modulus and loss factor. The first phenomenon at low temperature (at about -100°C) was related to glass transition (γ-relaxation), while the second at high temperature (at about 50°C) to the α-relaxation. It is appropriate to observe that the loss factor increased without a peak because the increased mobility of the polymer chains when the polyethylene approached the melting: moreover the α-relaxation was evident as a shoulder in the loss factor curves. On the other hand in the case of LDPE based composites the dissipative modulus and the loss factor evidenced the β-relaxation too: moreover the α-relaxations was a peak as loss factor and a shoulder as dissipative modulus, while the β-relaxations vice versa, i.e. a peak as dissipative modulus and a shoulder as loss factor. Table 4.2 shows the relaxation temperatures for all the test materials.

Table 4.2. Relaxation temperatures calculated from DMTA test.

Material	**T_γ (T_g) [°C]**	**T_β [°C]**	**T_α [°C]**
HDPE25	-98.0	-	47.5
HDPE25-Cu10 10 vol%	-98.7	-	56.7
HDPE25-Cu45 10 vol%	-98.2	-	57.6
LDPE70	-111.4	-15.1	37.8
LDPE70-Cu45 10 vol%	-110.5	-12.4	41.7
LDPE70-Fe15 10 vol%	-109.5	-8.7	51.1
LDPE70-Fe45 10 vol%	-110.2	-9.5	32.9

In the case of HDPE25-Cu composites the γ-relaxation temperature remained constant at about -100°C, while the peak intensity of the loss factor decreased of about 25% for all both the composites. The literature reports the peak intensity decreases following a linear relationship with the filler volume fraction in the case of low filler-polymer interaction [25].On the other hand the α-relaxation moved up from 47°C for HDPE25 to 57°C (+10°C) for all both the composites. Moreover it is opportune to observe that the storage modulus was very similar for all the materials.
In the case of LDPE70-Cu45 composites the storage modulus increased of about 10% over all the temperature range. The γ-relaxation temperature remained constant at about -111°C: similarly the peak intensity of the loss factor remained constant for LDPE70 and LDPE70-Cu45 composites. On the other hand the β-relaxation moved up from -15°C for LDPE70 to 12°C for the composites and similarly the α-relaxation from 38°C for LDPE70 to 42°C for the composites with a reduction in all both the case of the intensity of the loss factor (about 7%). It is opportune to observe that in the

second case is a reduction of the peak intensity of the loss factor but not in the first one because the loss factor had only a shoulder.

In the case of LDPE70-Fe composites the storage modulus increased of about 10% over all the temperature range for all both the metallic powders. The γ-relaxation temperature remained constant at about -111°C and similarly the peak intensity of the loss factor for LDPE70 and LDPE70-Fe composites. On the other hand the β-relaxation moved up from -15°C for LDPE70 to 12°C for all both the composites with a reduction of the corresponding loss factor intensity (that in this case had a shoulder and not a peak). Moreover the decrease was of 15% in presence of Fe45 and of 22% in presence of Fe45. The effect of the Fe powders was more complicated on the α-relaxation: in the case of LDPE70-Fe45 composites the peak temperature shifted from 38°C for LDPE70 to 33°C with a reduction of the intensity of the loss factor (about 10%), while the peak temperature moved up from 38°C to 51°C and the peak intensity of the loss factor remained unchanged. 5

4.3 HDPE25-Cu composites (compression moulding)

4.3.1 TGA

Figure 4.30 shows the TGA and DTGA curves in temperature range where the degradation phenomena were more intense: Table 4.3 summarizes the characteristic parameters of these curves. The data evidenced no change for HDPE25-Cu10 and HDPE25-Cu45 composites in comparison to HDPE25 matrix. Moreover it is appropriate to observe that the residual fraction (about 10wt%) for the composites was in good agreement (by taking into account HDPE and Cu densities) with the filler fraction of 1vol%.

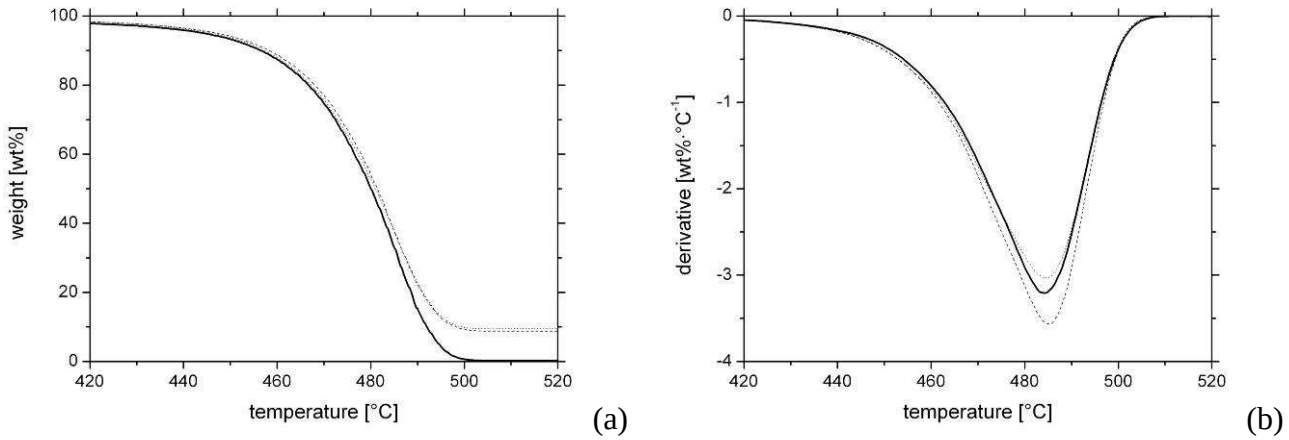

Figure 4.30. TGA (a) and DTGA (b) curves of HDPE25 (—), HDPE25-Cu10 (···) and HDPE25-Cu45 (---) composites.

Table 4.3. Results of the analysis of the TGA and DTGA curves: onset (T_{ON}), peak (T_{PEAK}) and endset (T_{END}) temperatures of the degradation and the residual fraction.

Material	T_{ON} [°C]	T_{PEAK} [°C]	T_{END} [°C]	Residual [wt%]
HDPE25	461.5	485.3	495.2	0.0
HDPE25-Cu10 1vol%	460.6	485.0	495.2	10.0
HDPE25-Cu45 1vol%	463.0	484.3	495.4	9.3

4.3.2 DSC

The DSC curves are showed in Figure 4.31: in the first case the crystallization during the cooling stage and in the second one the melting during the heating stage. In addition Table 4.4 contains the data elaborated from these DSC curves. In both the case the crystallinity did not change, while the peak temperatures during the crystallization and the melting were shifted for HDPE25-Cu10 and HDPE25-Cu45 composites in comparison to HDPE. In the case of the crystallization the peak temperatures increased of about 2°C even if the onset temperature did not change; on the other hand the peak temperature of the melting phenomena decreased of about 2°C.

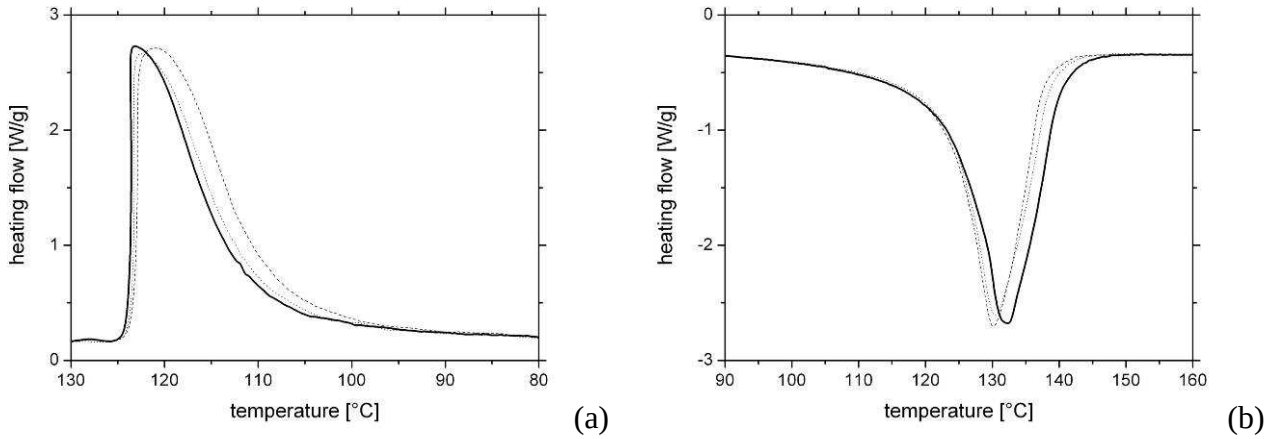

Figure 4.31. DSC curves of the crystallization phenomena during the cooling stage (a) and the heating stage (b) for HDPE25 (—), HDPE25-Cu10 (···) and HDPE25-Cu45 (---) composites.

Table 4.4. Results of the analysis of the DSC curves: crystallinity (χ), melting (T_m) and crystallization (T_c) temperature, onset (T_{ON}) and endset (T_{END}) temperatures.

Material	Crystallization – Cooling (2nd scan)				Melting – Heating (3rd scan)			
	χ [wt%]	T_c [°C]	T_{ON} [°C]	T_{END} [°C]	χ [wt%]	T_m [°C]	T_{ON} [°C]	T_{END} [°C]
HDPE25	74.0	120.6	122.3	105.2	72.2	132.2	124.0	143.5
HDPE25-Cu10 1vol%	73.9	122.2	122.3	105.5	72.6	130.6	124.0	143.5
HDPE25-Cu45 1vol%	70.6	123.2	122.6	105.1	71.2	130.2	124.5	143.1

4.3.3 Tensile tests

The most relevant result of the tensile tests were the effect of production process on HDPE09: the high ductility of HDPE25 dropped down in comparison to the samples produced by injection molding (see for comparison Figure 4.9 and Figure 4.32). HDPE25 sample produced by compression moulding had a strain to break of only 13.7%.

Regarding the filler addition, Table 4.5 summarizes the mechanical properties of composites: the observed deviations were limited in the experimental errors. In this way all the properties of HDPE25-Cu10 and HDPE25-Cu45 composites did not change in comparison to HDPE.

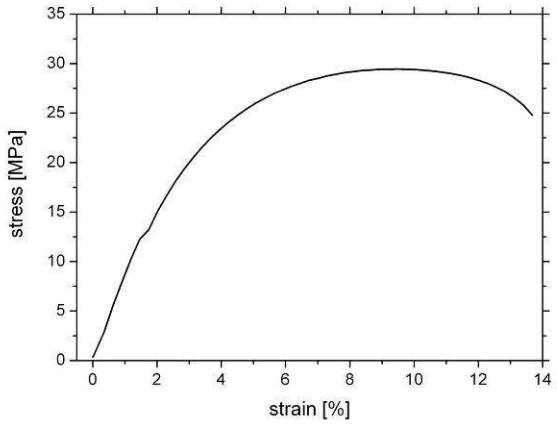

Figure 4.32. Example of the stress-strain curves of HDPE25.

Table 4.5. Mechanical properties of the HDPE25-Cu composites: elastic modulus (E), stress and strain at yielding (σ_Y and ε_Y) and at break (σ_R and ε_R).

Material	E [MPa]	σ_Y [MPa]	ε_Y [%]	σ_R [MPa]	ε_R [%]
HDPE25	795	29.1	9.6	25.0	13.7
HDPE25-Cu10 1vol%	844	29.5	10.0	28.6	13.2
HDPE25-Cu45 1vol%	829	28.4	8.2	28.4	8.3

4.3.4 DMTA

The results of the DMTA tests are showed in Figure 4.33, Figure 4.34 and Figure 4.35. The materials presented two sharp drops of the storage modulus that corresponded to two peaks in terms of dissipative modulus and loss factor. In particular the first phenomenon at low temperature was related to glass transition (γ-relaxation) that is -102.7°C for HDPE25: no meaningful change was observed for HDPE25-Cu10 (102.2°C) and HDPE25-Cu45 (102.5°C) composites. Moreover the intensity of the loss factor peak was only slightly reduced. On the other hand the phenomenon at higher temperatures was the α-relaxation: in this case the peak temperature passed from 41.0°C for HDPE25 to 48.8°C for HDPE25-Cu10 composites and to 43.2°C for HDPE25-Cu45 composites. Even if the dissipative modulus increased in correspondence of the α-relaxation, a small reduction of loss factor was advisable.

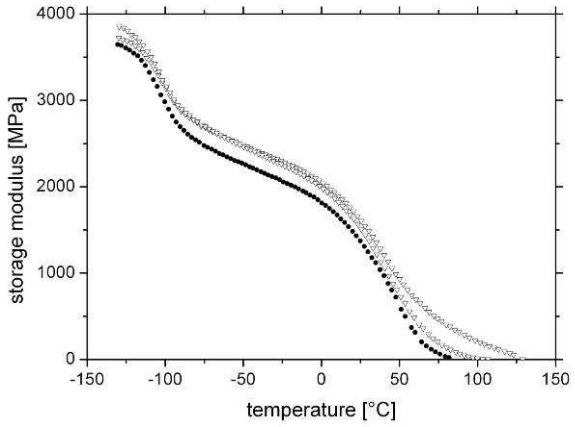

Figure 4.33. Storage modulus as a function of the temperature for HDPE25 (●), HDPE25-Cu10 (▽) and HDPE25-Cu45 (△) composites.

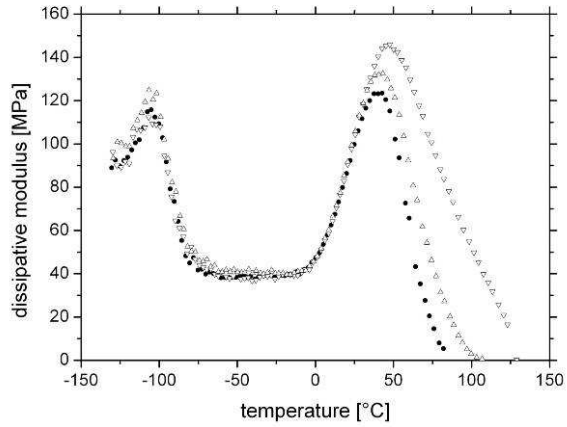

Figure 4.34. Dissipative modulus as a function of the temperature for HDPE25 (●), HDPE25-Cu10 (▽) and HDPE25-Cu45 (△) composites.

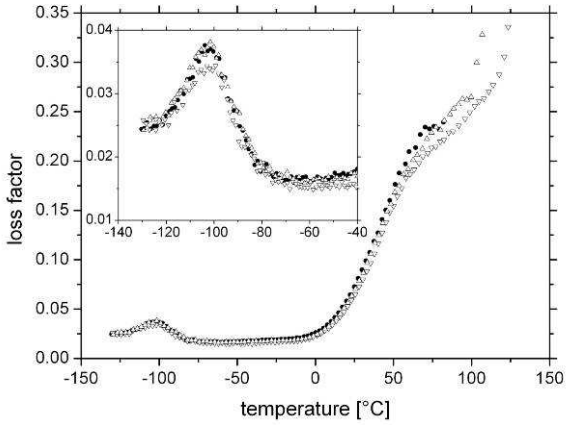

Figure 4.35. Loss factor as a function of the temperature for HDPE25 (●), HDPE25-Cu10 (▽) and HDPE25-Cu45 (△) composites. The inset shows a detail of the curves at low temperatures.

4.3.5 Tensile creep tests

From a general point of view the addition of both the copper powders, Cu10 and Cu45, resulted to substantially increase the creep resistance of HDPE matrix. This effect is detectable in the linear viscoelastic region (i.e. at low stresses or temperatures), and it becomes more and more evident in the non-linear viscoelastic or viscoplastic region (i.e. at high stresses or temperatures). Examples of this behaviour are proposed in Figure 4.36 and in Figure 4.37 where creep compliance and creep compliance rate of HDPE25-Cu composites at 30°C and 60°C are showed. Moreover it is possible to observe as the effect of filler addition differentiated only at high stress: at low stress level the two copper powders, Cu10 and Cu45, acted on HDPE25 creep properties by reducing the creep compliance in the same way. Only when the temperatures was 60°C and the applied stress 10 MPa, a sharp difference appeared: in particular the Cu45 induced an increase of the creep life of 37%, while Cu10 of 300%.

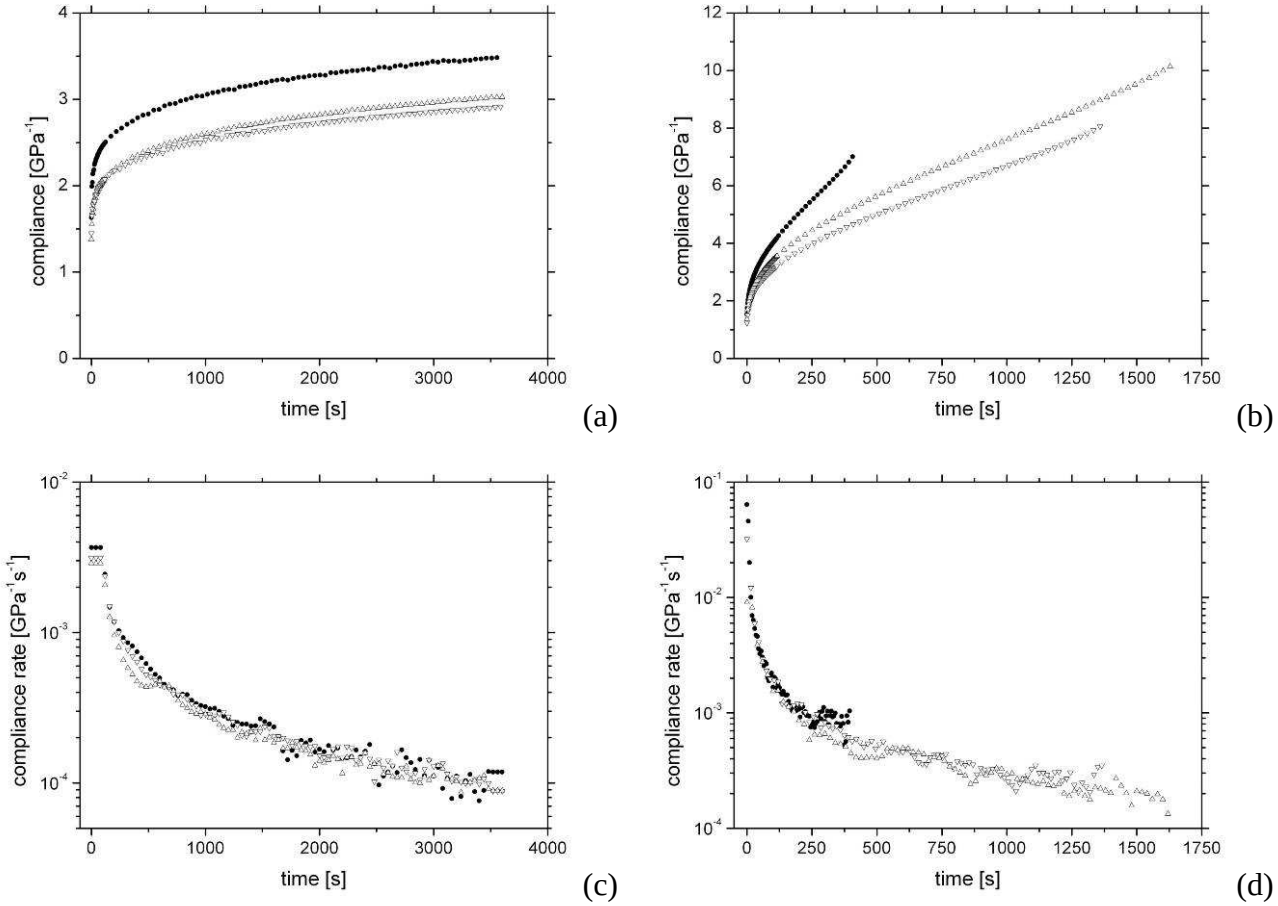

Figure 4.36. Creep compliace at 30°C (a, c) and creep compliance rate (b, d) as a function of time at 30°C with a stress of 3 MPa (a, b) and 15 MPa (c, d) for HDPE25 (●), HDPE25-Cu10 (▽) and HDPE25-Cu45 (△) composites.

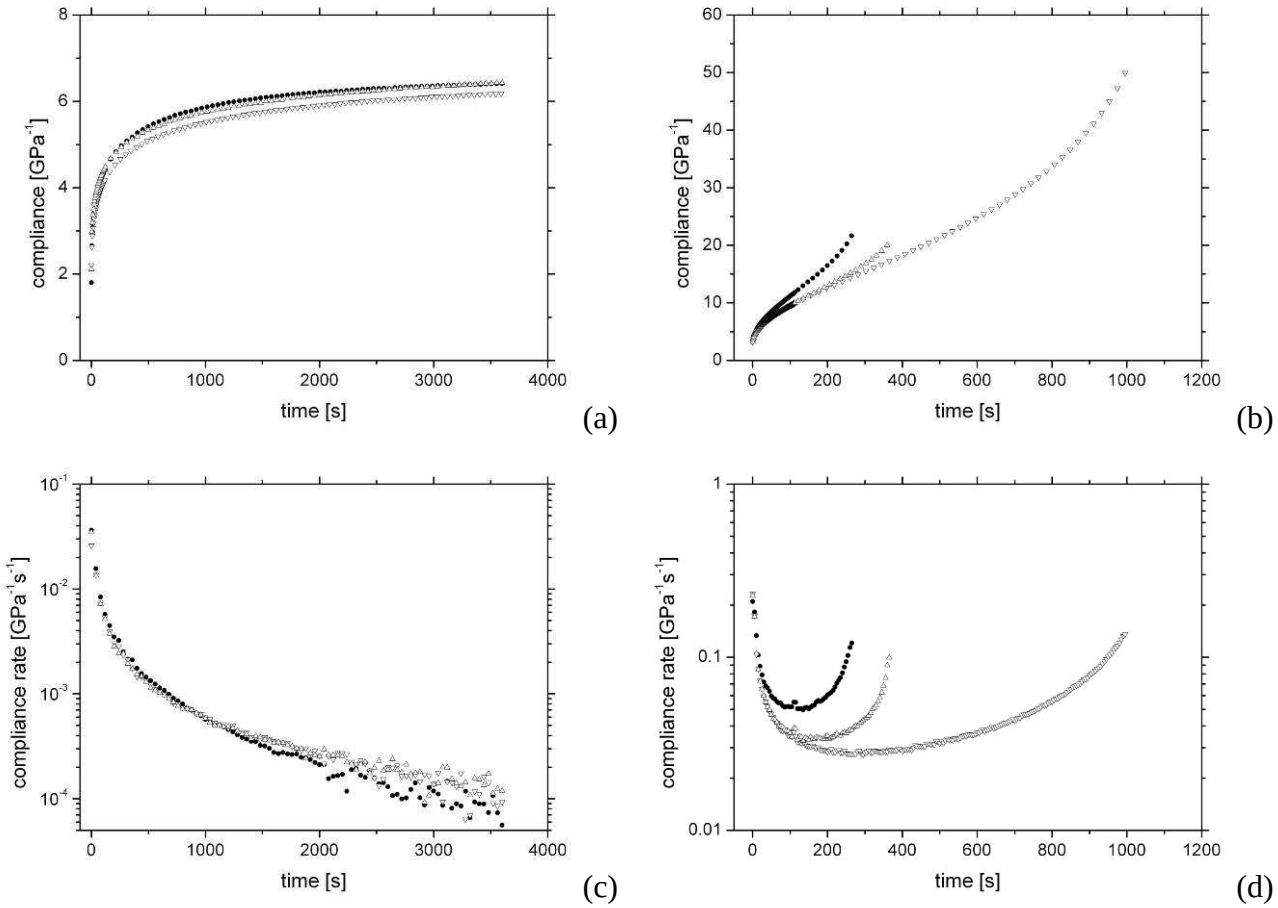

Figure 4.37. Creep compliace at 60°C (a, c) and creep compliance rate (b, d) as a function of time at 30°C with a stress of 3 MPa (a, b) and 10 MPa (c, d) for HDPE25 (●), HDPE25-Cu10 (▽) and HDPE25-Cu45 (△) composites.

Figure 4.38 shows the isochronous creep stress-strain curves at 30°C and 60°C for the tested materials. It is evident as the increased temperatures reduced the creep resistance of both the tested materials and mainly as the creep resistance increased for HDPE25-Cu composites comparison to HDPE25 especially when the applied stress increases.

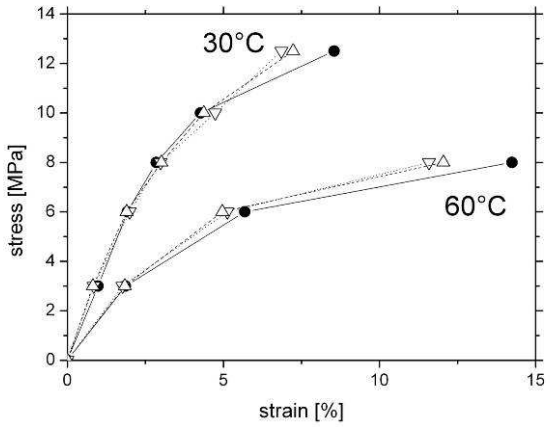

Figure 4.38. The isochronous creep stress-strain for HDPE25 (●), HDPE25-Cu10 (▽) and HDPE25-Cu45 (△) composites at 30°C and 60°C.

Figure 4.39 proposes the isochronous creep compliance curves at 2000 s and the related elastic and viscoelastic components. While the elastic components are the same for HDPE25 and for HDPE25-Cu composites, the viscoelastic components are sharply different. In particular the viscoelastic components of the compliance is reduced by about 14% for HDPE25-Cu composites in comparison to HDPE25 over 60°C.

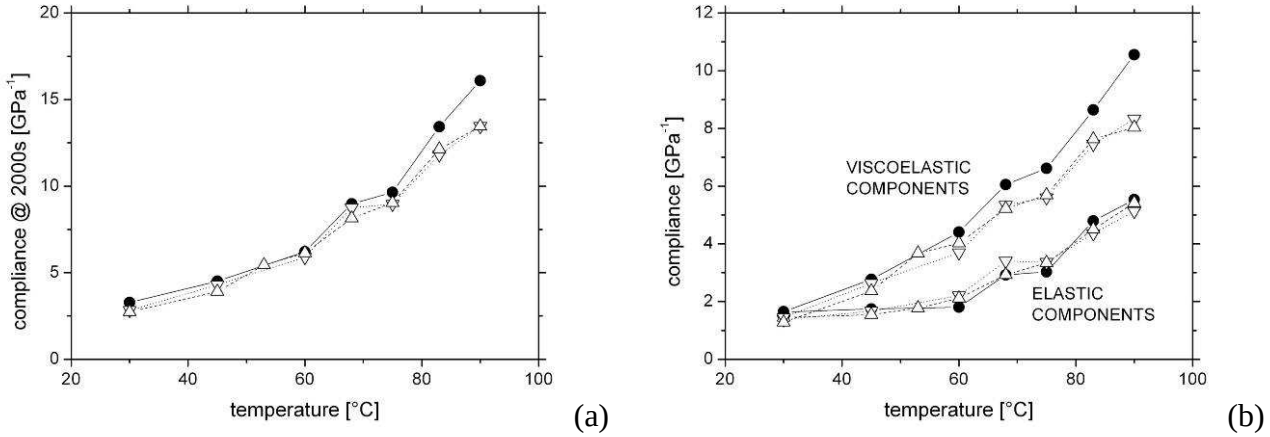

Figure 4.39. Isochronous compliance (a) and elastic and viscoelastic components of the isochronous compliance (b) at 2,000 s for HDPE25 (●), HDPE25-Cu10 (▽) and HDPE25-Cu45 (△) composites at 30°C and 60°C.

On the basis of a time-temperature superposition principle, short term creep performed in the linear-viscoelastic region (with an applied stress of 3 MPa) allowed to obtain creep compliance master curves for long term creep (Figure 4.40). Over the extended time period covered by the master curves, the creep compliance is reduced by about 18%, on average, for all both the composites.

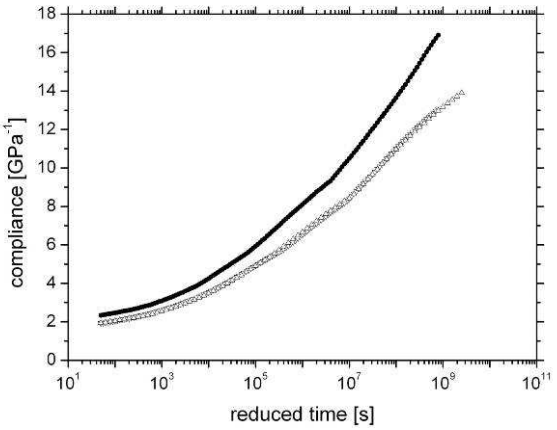

Figure 4.40. Creep compliance master curves obtained at 3 MPa and referred at 30°C for HDPE25 (●), HDPE25-Cu10 (▽) and HDPE25-Cu45 (△) composites.

Moreover the shift factor (Figure 4.41) calculated from the short term creep test to obtain the master curves as a function of the temperature was fitted with an Arrhenius law. In this way an activation energy for the relaxation phenomenon was determined: the values increased from (192±17) kJ/kmol for HDPE25 to (207±13) kJ/kmol for HDPE25-Cu10 composites and to (211±10) kJ/kmol for HDPE25-Cu45 composites.

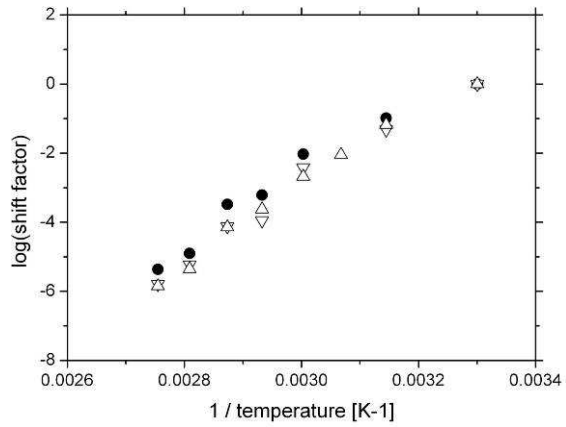

Figure 4.41. Shift factor as a function of the inverse of the absolute temperature for HDPE25 (●), HDPE25-Cu10 (▽) and HDPE25-Cu45 (△) composites.

The master curve data were used to calculate the creep compliance rate over the full time range. Figure 4.42 shows as HDPE25 and HDPE25-Cu composites had practically the same behaviour: the results are in agreement with the results at low stresses in linear viscoelastic region (as for example in Figure 4.36 and Figure 4.37). Moreover it was possible to fit the data with a power law which has the expression $dD/dt = 0.15 \cdot t^{-0.89}$ where the compliance is expressed in GPa^{-1} and the time in s.

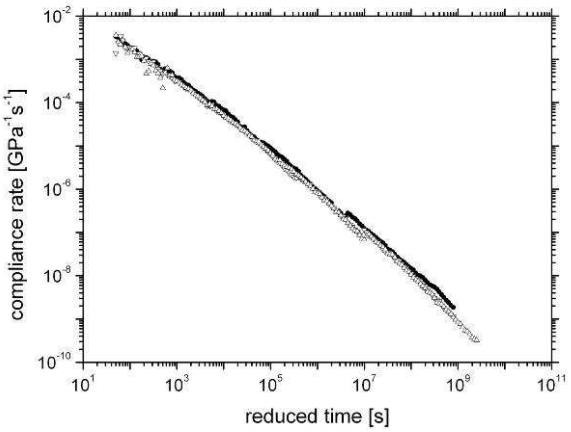

Figure 4.42. Creep compliance rate as a function of time in a log-log scale for HDPE25 (●), HDPE25-Cu10 (▽) and HDPE25-Cu45 (△) composites.

The master curve data were also used to calculate the retardation spectra over the full time range available: Figure 4.43 shows as the Cu addition reduced the spectrum intensity of HDPE25 by shifting apparently to higher retardation times.

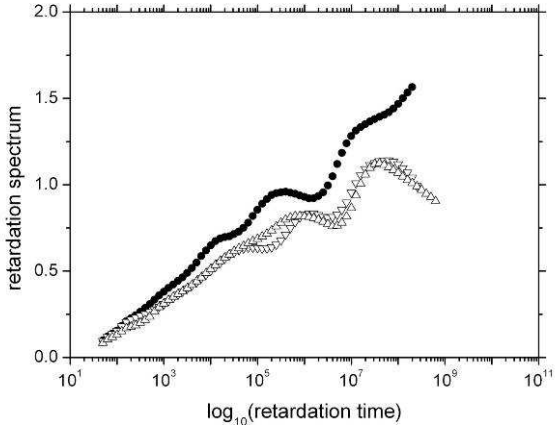

Figure 4.43. Retardation spectra as a function of the retardation time for HDPE25 (●), HDPE25-Cu10 (▽) and HDPE25-Cu45 (△) composites.

5 Results on carbon-black-based composites (CB)

This chapter is dedicated to the CB based composites: the paragraph 5.1 deals with HDPE09-CB composites with a filler content of 1 vol% extruded up to 3 times (HDPE09, HDPE09-CB226 1 vol% and HDPE09-CB1353 1 vol%), while the paragraph 5.2 with HDPE09-CB composites with a filler content of 1 vol% extruded 2 times (HDPE09, HDPE09-CB105 0.5 vol%, HDPE09-CB226 0.5 vol%, HDPE09-CB802 0.5 vol% and HDPE09-CB1353 0.5 vol%). In the following chapters the composites could be indicated without the filler content (e.g. HDPE09-CB226) where there is no problem of misunderstanding.

5.1 HDPE09-CB 1 vol% composites

5.1.1 Extruder

Table 5.1 shows the torque, the die pressure and the temperature of the melt during in the twin screw extruder during the production of HDPE09-CB composites. The presence of the filler induced a decrease: this effect is bigger in the case of the CB with the lower specific surface area, i.e CB226. In literature [139, 140] this behaviour was correlated with the lubricating effect of the CB at low filler. On the contrary the other parameters did not change.

5.1.2 OM

The observation of thin sections of the composite materials with an optical microscope was used to control the extent of filler agglomerates. The micrographs of Figure 5.1 evidenced an increasing degree of dispersion of the filler in the polymeric matrix through repeated extrusions: moreover the dispersion appeared more easy in the case of the CB with the lower specific surface area, i.e. CB226.

5.1.3 TEM

The observation of ultrathin sections of the composite materials with a TEM was used to assess the filler agglomeration in the polymeric matrix at the same dimension scale of the nanometric filler

particles. The micrographs of Figure 5.2 evidenced as multiple extrusions increased the degree of dispersion of the: the filler agglomerated broke up to reach the basic CB aggregates.

Table 5.1. Torque (M), die pressure (p) and melt temperature along the barrel (T_i) during the composites production with the twin screw extruder for HDPE09-CB composites at different numbers of extrusion (Extr.).

Material	Extr.	M [Nm]	P [bar]	T_1 [°C]	T_2 [°C]	T_3 [°C]
HDPE09	1	89.9	18.4	212.8	227.3	237.5
	2	79.5	18.5	212.4	226.6	236.7
	3	87.7	20.1	213.0	225.6	236.2
HDPE09-CB226 1 vol%	1	74.5	17.6	212.2	226.6	236.4
	2	71.6	18.2	212.0	226.4	236.1
	3	70.9	15.8	212.0	226.6	237.2
HDPE09-CB1353 1 vol%	1	86.3	17.4	212.6	226.1	236.0
	2	80.1	17.5	213.1	225.9	236.1
	3	81.6	18.3	212.5	226.1	235.9

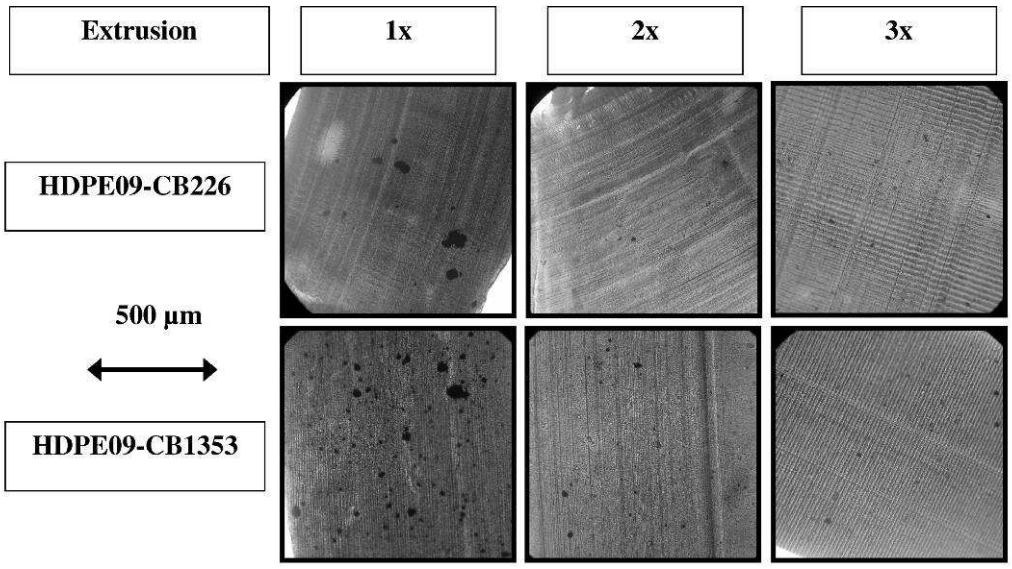

Figure 5.1. OM micrographs of thin sections of HDPE09-CB composites at different extrusions.

5.1.4 DSC

Figure 5.3 shows the DSC curves of HDPE09 powder and HDPE09 extruded 1 time as examples, while Table 2.1 contains the data elaborated from these DSC curves. While no evident effect was present between HDPE09 and HDPE09-CB composites, the only difference occurred between HDPE09 powder and HDPE09 extruded. As evidenced in Figure 5.2 the shape of the curves changed, the crystallinity decreased (about 7%) and on the other hand the melting temperature

increased (about 2°C): this fact is probably related to degradation phenomena that taken place during the extrusion.

5.1.5 TGA

Figure 5.4 shows an example of TGA and DTGA curves: the main degradation occurred between 440°C and 500°C as a single phenomenon as confirmed by DTGA curves. Figure 5.4 proposes the reference temperature of the degradation too: from a general point of view the number of extrusion did induced any change, while the CB increased the stability of the composites. The effect was more intense in the case of CB1353 (about 6°C) in comparison to CB226 (about 3°C).

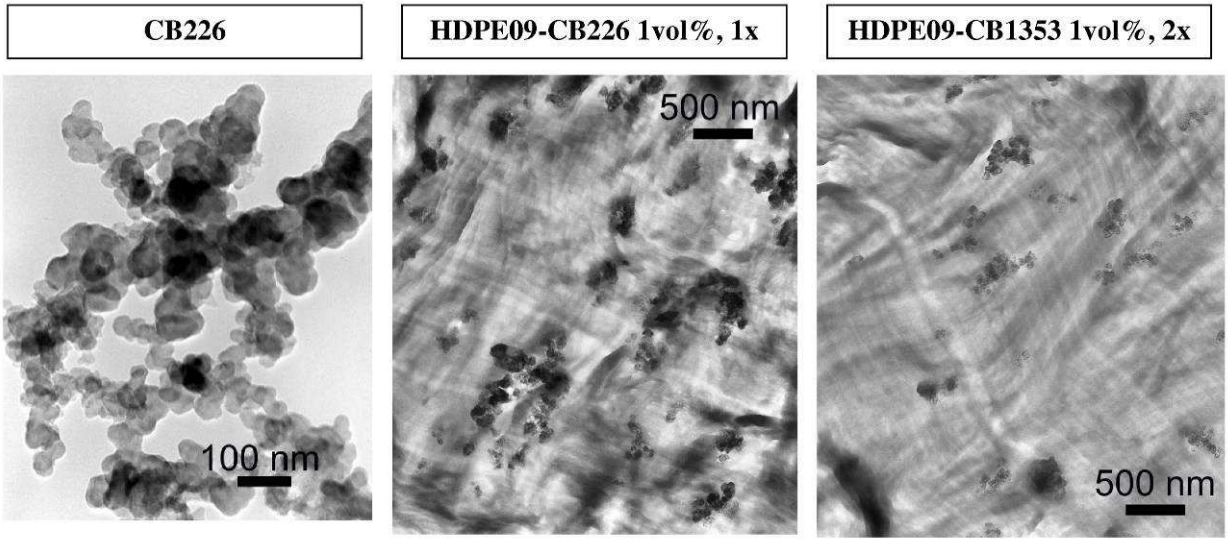

Figure 5.2. TEM micrographs of thin sections of HDPE09-CB composites at different extrusions.

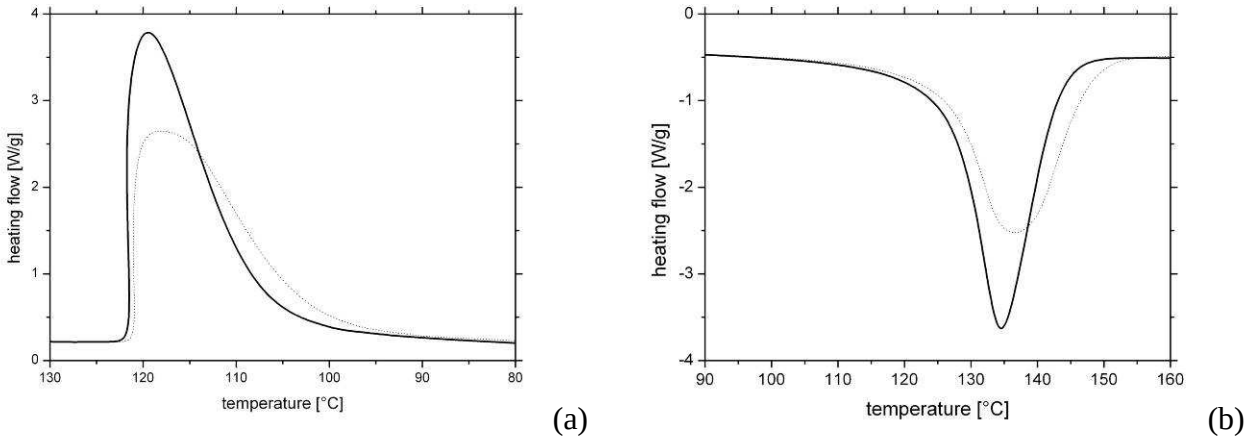

(a) (b)

Figure 5.3. DSC curves of the crystallization phenomena during the cooling stage (a) and the heating stage (b) for HDPE09 powder (—) and HDPE09 extruded 1 time (···).

Table 5.2. Results of the analysis of the DSC curves: crystallinity (χ), melting (T_m) and crystallization (T_c) temperature, onset (T_{ON}) and endset (T_{END}) temperatures.

Material	Extr.	Crystallization – Cooling (2nd scan)				Melting – Heating (3rd scan)			
		χ [wt%]	T_c [°C]	T_{ON} [°C]	T_{END} [°C]	χ [wt%]	T_m [°C]	T_{ON} [°C]	T_{END} [°C]
HDPE09	powder	81.0	119.4	121.6	108.3	81.3	134.6	126.0	142.8
HDPE09	1	74.4	118.1	121.1	102.8	74.4	136.7	125.2	147.3
	2	74.4	116.6	121.8	102.1	73.8	136.5	124.8	147.3
	3	73.3	116.8	122.9	100.9	73.3	136.4	124.2	147.5
HDPE09-CB226 1 vol%	1	73.8	116.4	121.6	102.8	73.4	137.3	125.1	147.4
	2	74.9	117.1	122.0	103.6	74.1	136.5	125.2	146.8
	3	74.0	117.5	122.5	103.1	73.7	136.0	124.9	147.1
HDPE09-CB1353 1 vol%	1	73.9	114.8	121.6	100.5	73.3	139.8	124.2	150.3
	2	73.7	117.5	122.1	103.9	73.1	136.3	125.3	146.7
	3	73.7	116.7	121.9	103.5	73.4	137.2	125.1	147.2

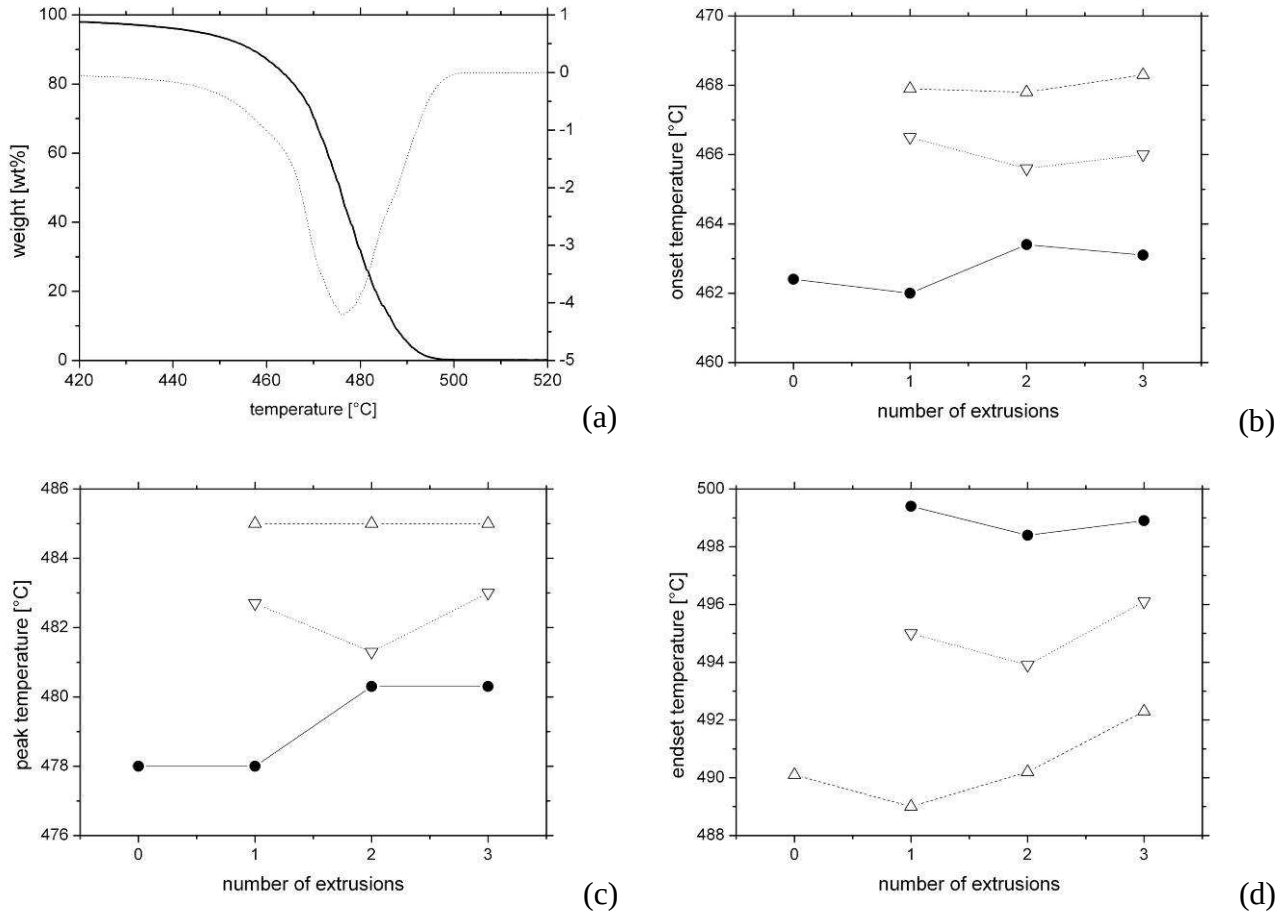

Figure 5.4. Example of TGA and DTGA curves for HDPE09 extruded 1 time (a) and the results of the analysis of these curves for all the HDPE09-CB composites as a function of the number of extrusions: onset (b), peak (c) and endset (d) temperatures of the degradation.

5.1.6 GPC

Figure 5.5 shows the molecular weight distribution (MWD) of HDPE09 at different number of extrusions: as the number of extrusion increased the width of the MWD decreased and in particular the lower and upper tail lost intensity.

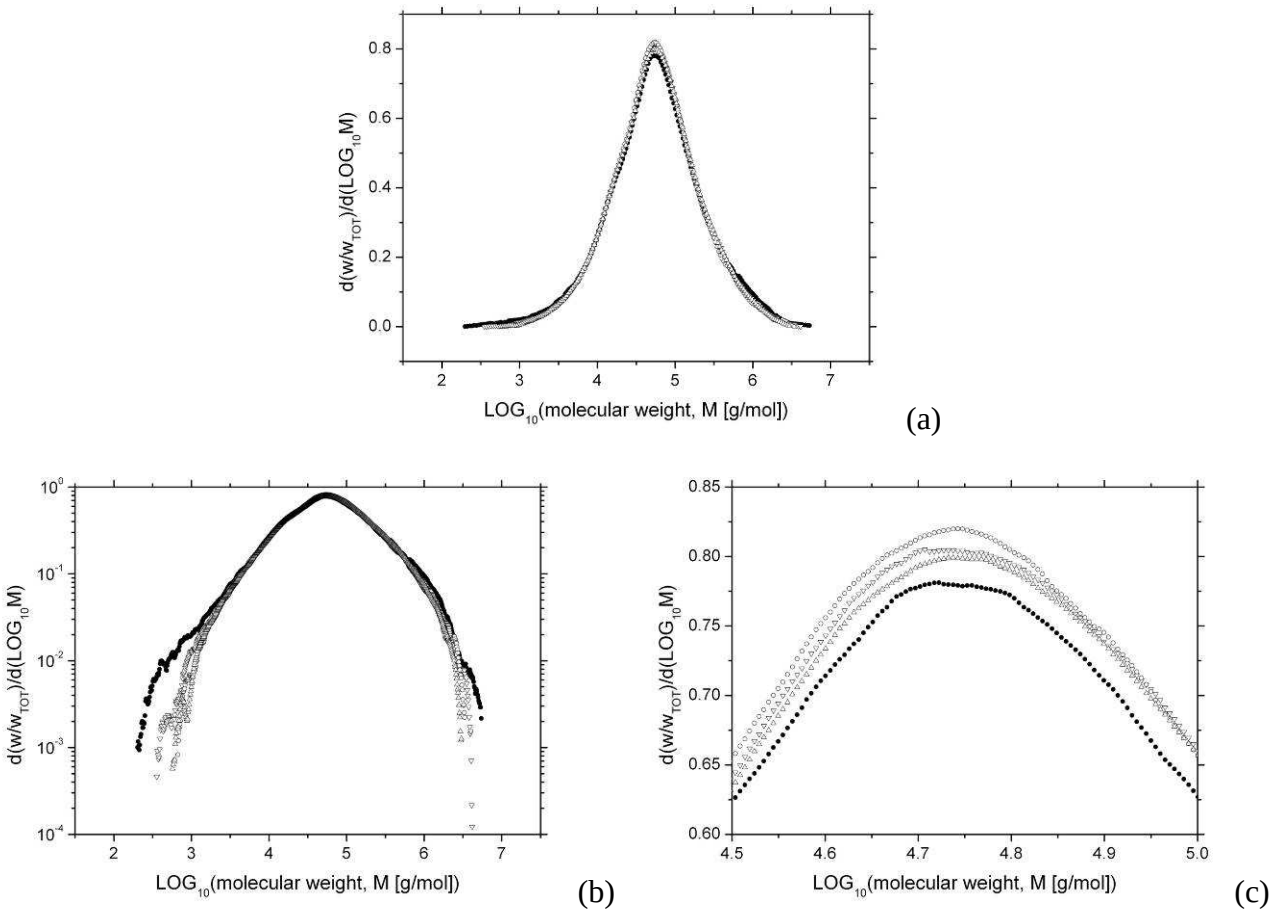

Figure 5.5. Molecular weight distribution of HDPE09 (a) with evidenced the details at upper and lower tails (b) and around the peak (c): powder (○), extruded 1 (●), 2 (▽) and 3 times (△).

Figure 5.6 shows the number average molecular weight (M_n), the weight average molecular weight (M_w)and the index of polydispersity (*IP*) as a function of the number of extrusions: the trends evidenced the decrease of the polymer chain weight (about 15% from the powder to the material extruded 3 time) and the narrowing of the MWD.

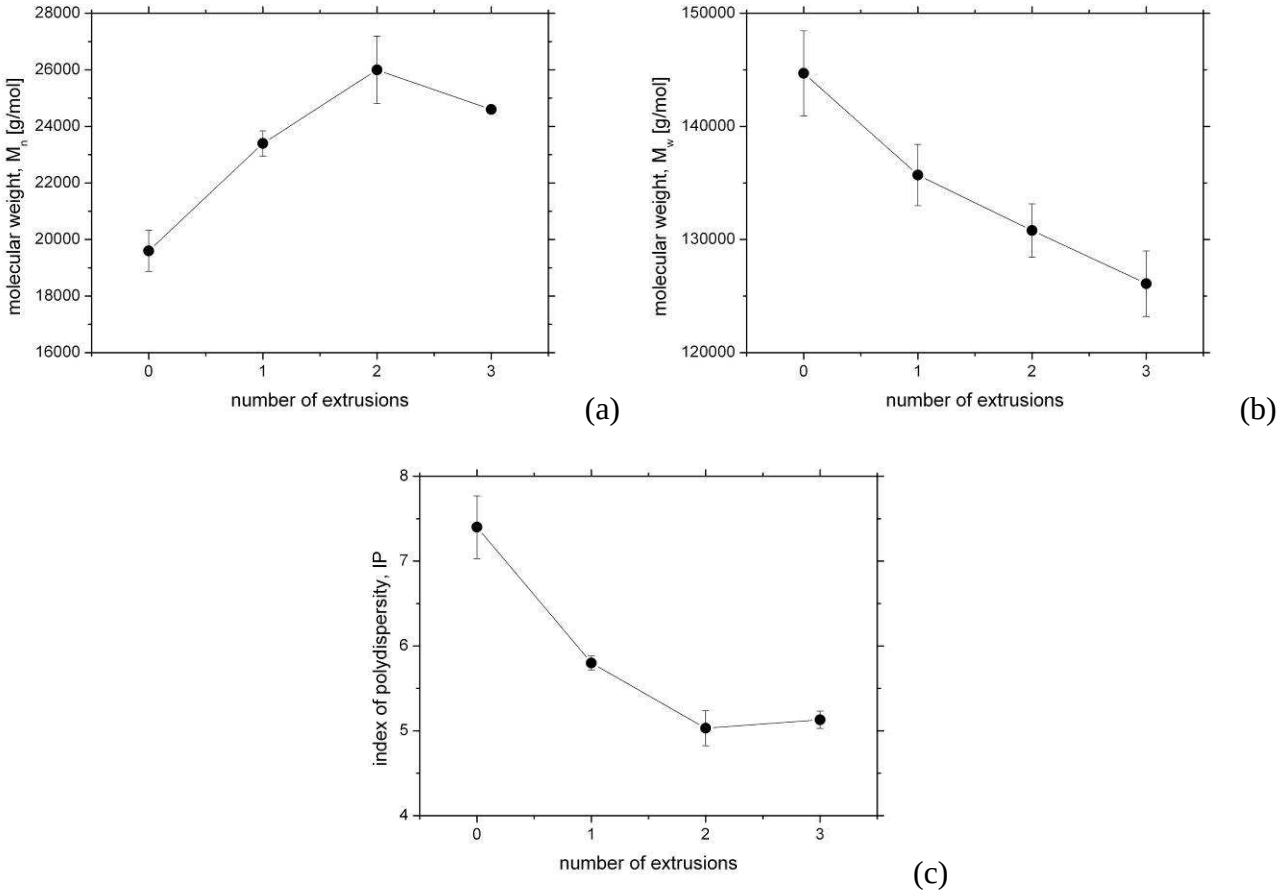

Figure 5.6. Number average molecular weight (a), weight average molecular weight (b) and index of polydispersity (c) as a function of the number of extrusions for HDPE09.

The polymer degradation was analyzed by using the chain scission distribution function (CSDF) approach [141, 142]. This function compares two MWD by calculating the number of chain scissions for all the molecular weights of the initial MWD to obtain the final MWD. Moreover the value of the CSDF represents the logarithm of number of chain scission occurred to a chain with a given initial molecular weight. Figure 5.7 shows the CSDF for every extrusion step: from powder to the material extruded 1 time and so on. More than the original MWDs, the CSDFs evidenced the details of the degradation phenomena: the main effect of the degradation induced by the extrusion process taken place during the first extrusion and then the phenomenon progressively lost intensity. Moreover the degradation affected with more intensity the lower molecular weight and the higher molecular weight. This behaviour induced the reduction of the IP and in particular the breaking of the longer chains caused the reduction of the weight average molecular weight.

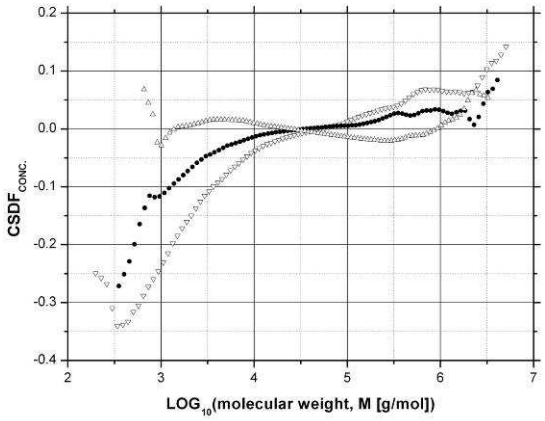

Figure 5.7. CSDF of HDPE09 for the 3 extrusion processes: from powder to the materials extruded 1 time (●), from 1 to 2 times (▽) and from 2 to 3 times (△).

5.1.7 MFI

Figure 5.8 shows the MFI as a function of the number of extrusions for HDPE09 and HDPE09-CB composites. The MFI of HDPE09 progressively decreased as the number of extrusions increased, while the MFI remained almost constant in the case of HDPE09-CB composites.

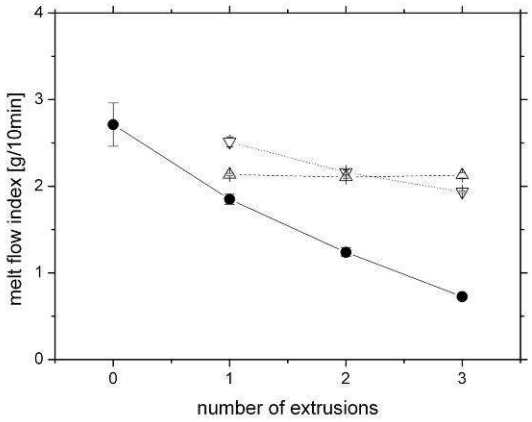

Figure 5.8. MFI as a function of the number of extrusions for HDPE09 (●), HDPE09-CB226 1 vol% (▽) and HDPE09-CB1353 1 vol% (△).

5.1.8 Rheology

Figure 5.9 shows the complex shear viscosity as a function of the shear rate for all the materials. The main effect was the progressive increasing of HDPE09 after every extrusion, while the viscosity of the HDPE09-CB composites decreased in comparison to HDPE09. No significant difference was presence between HDPE09-CB226 and HDPE09-CB1353 composites. Moreover all the materials had a pseudoplastic behaviour and the curves tended to superimpose each other. This results was in agreement with the MFI data.

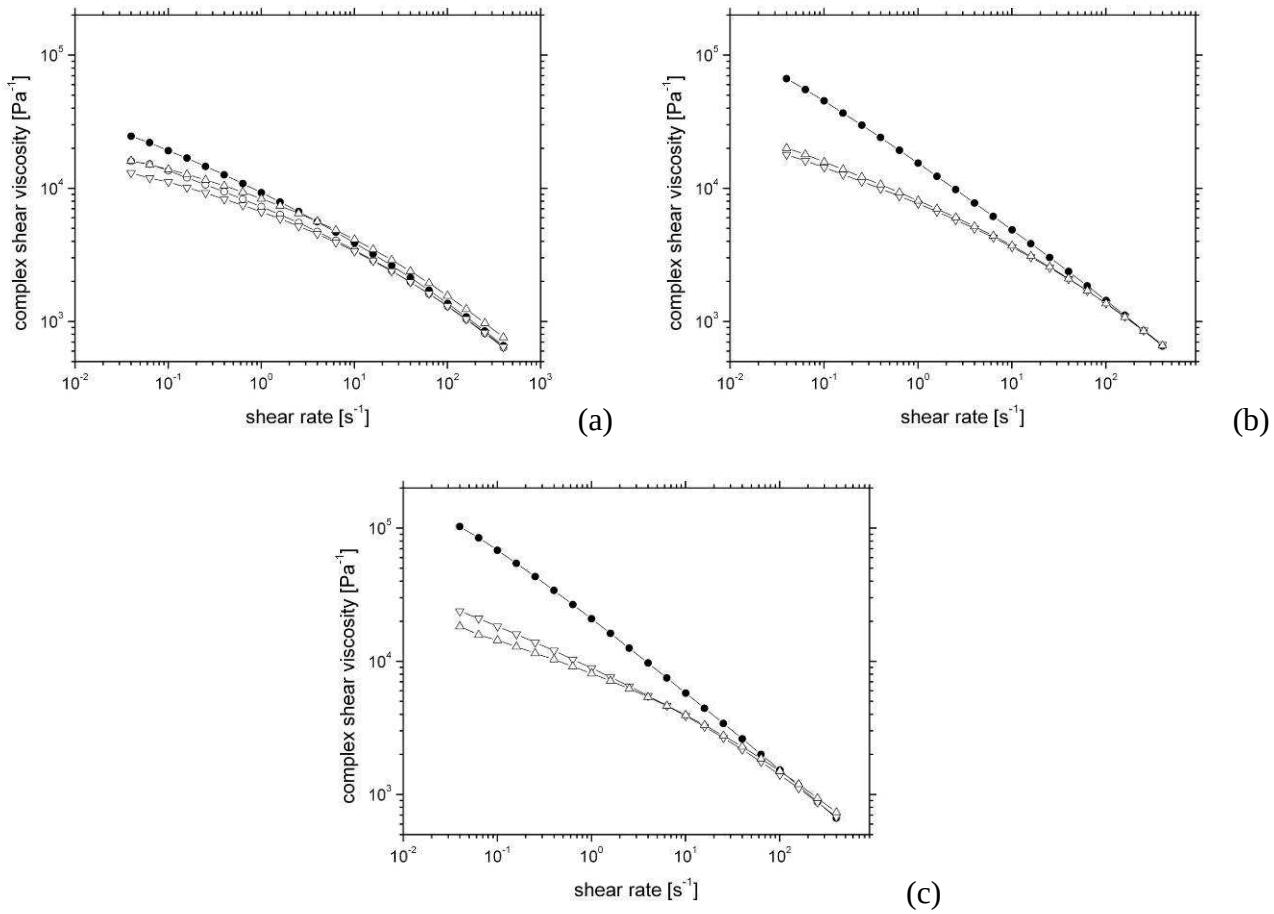

Figure 5.9. Complex shear viscosity as a function of the shear rate for HDPE09 powder(○), HDPE09 (●), HDPE09-CB226 1 vol% (△) and HDPE09-CB1353 1 vol% (△) extruded 1 (a), 2 (b) and 3 time (c).

5.1.9 IR

Figure 5.10 shows some examples of the infrared spectra acquired for the tested materials. From a general point of view the characteristic peaks of polyethylene were evident: C–H stretching (2916 and 2855 cm^{-1}), C–H bending (1492 and 1466 cm^{-1}) and $-(CH_2)_n-$ rocking (749 and 723 cm^{-1}). Moreover the slope of the spectra of HDPE09-CB composites was related with the presence of nanometric particles in the polymeric matrix that scattered the light.

The spectra evidenced the presence of a carbonyl group at 1720 cm^{-1} for all the materials, even for the base HDPE09 powder. The oxidation of the materials was investigated by observing the C=O peak at 1720 cm^{-1} and by normalizing the absorbance intensity to the intensity of the peaks a 1300 and 720 cm^{-1} which are related to skeletal C–C vibrations of the polyethylene chains. The results are presented in Figure 5.11. The main oxidation was induced on HDPE09 after the first extrusion, while then the intensity remained almost constant. Moreover the intensity increased for HDPE09-CB composites without any change with the number of extrusions: in particular the phenomenon was more intense in presence of CB1353.

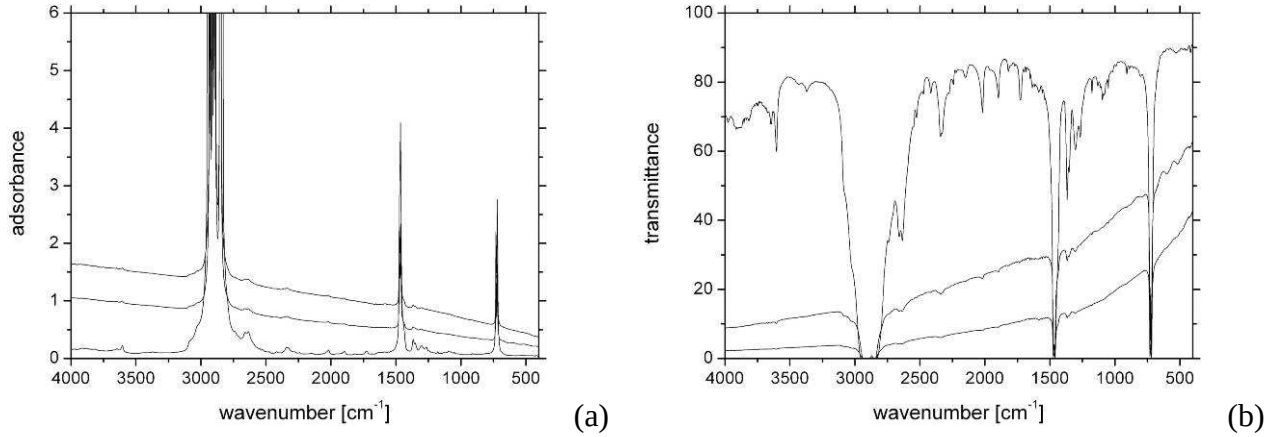

Figure 5.10. Examples of IR spectra in terms of absorbance (a) and transmittance (b) for HDPE09, HDPE09-CB226 1 vol% and HDPE09-CB1353 1 vol% extruded 3 times (from the bottom to the top in the case of the absorbance spectra and vice versa in the case of the transmittance).

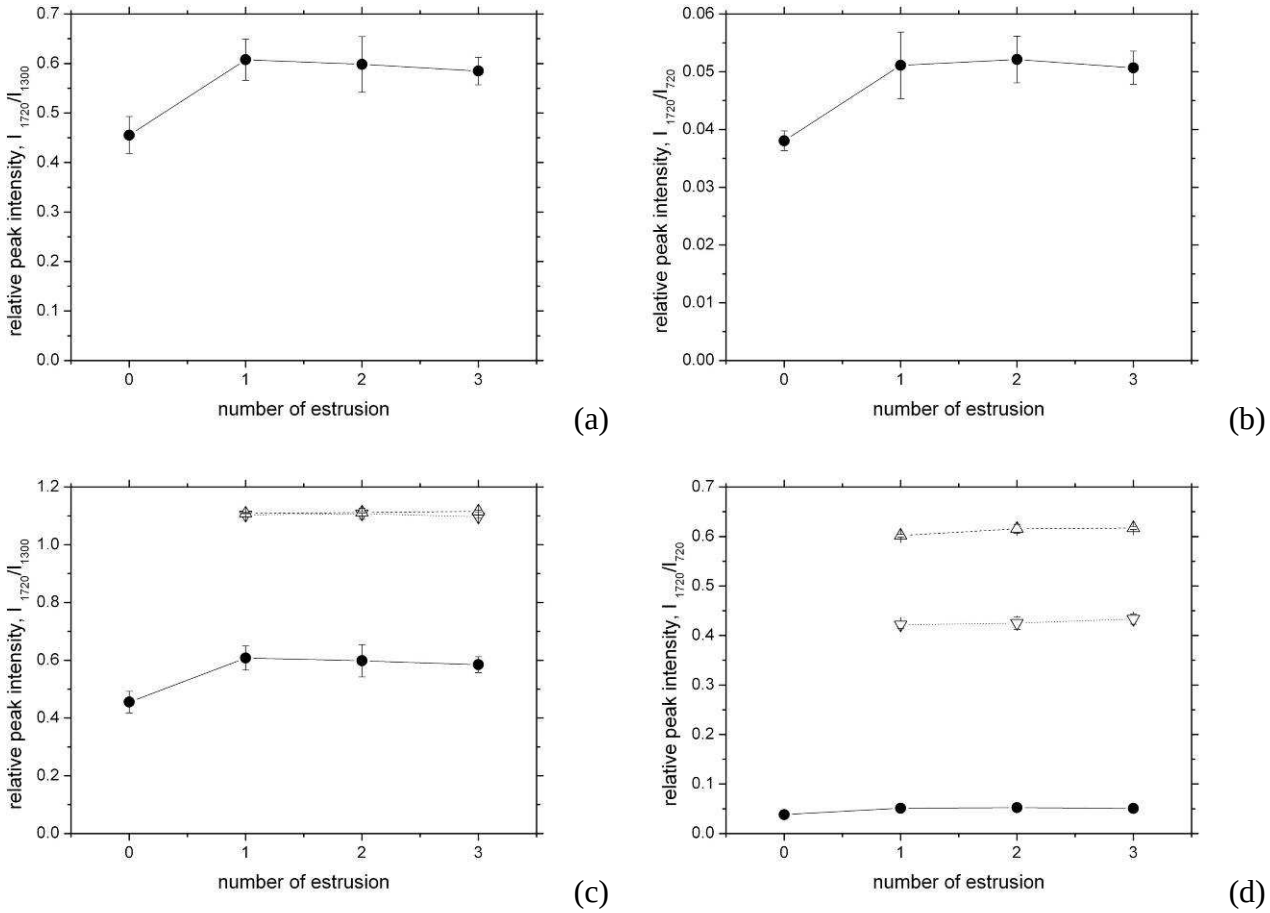

Figure 5.11. The relative intensity of the C=O peak (1720 cm^{-1}), respect to the peak at 1300 (a, c) and 720 cm^{-1} (b, d) as a function of the number of extrusions for HDPE09 (●), HDPE09-CB226 1 vol% (▽) and HDPE09-CB1353 1 vol% (△).

The spectra evidenced the peak at 1378 cm^{-1} that is characteristic of the methyl group, i.e. the ends of the main chains or branching. The intensity of this peak was normalized with the intensity of the peak at 1300 cm^{-1} that is related to the skeletal C–C vibrations. Figure 5.12 show the trends for all the materials as a function of the number of extrusions. While HDPE09-CB composites were not influenced, HDPE09 was characterized by a ratio that decreased after the first extrusion and then remained almost constant.

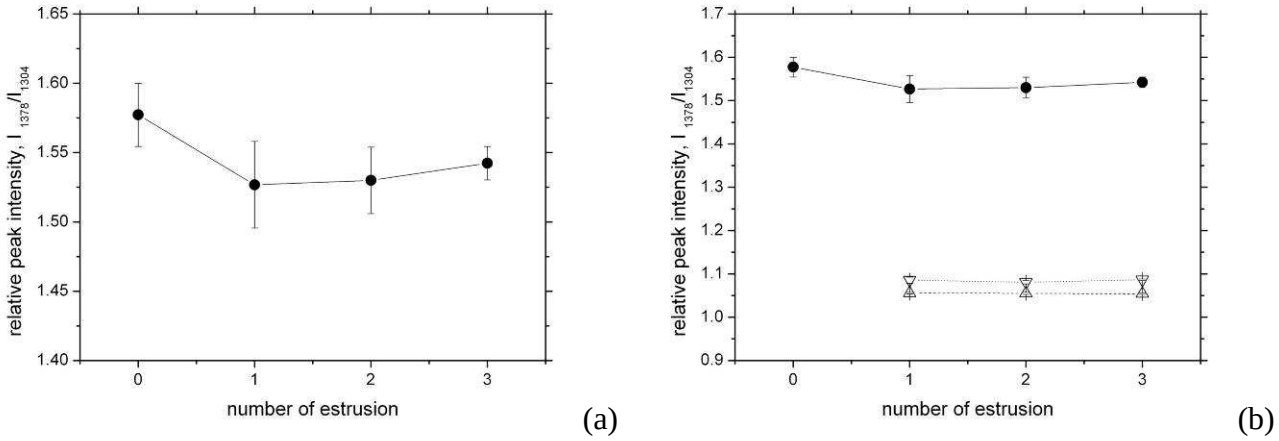

Figure 5.12. The relative intensity of the $-CH_3$ peak (1378 cm^{-1}), respect to the peak at 1300 cm^{-1} (b, d) as a function of the number of extrusions for HDPE09 (●), HDPE09-CB226 1 vol% (▽) and HDPE09-CB1353 1 vol% (△).

5.1.10 Tensile tests

Examples of the stress-strain curves are showed in Figure 5.13, while Figure 5.14, Figure 5.15 and Figure 5.16 present the results of the analyses of these curves (elastic modulus, stress and strain at yield and break). HDPE09 evidenced a very high ductility: after the sharp yielding the material had a long plastic plateau until to reach a strain hardening behaviour and the break over a strain of 2000%. While HDPE maintained the high ductility after 3 extrusions, the yielding stress decreased of 1 MPa: this fact was probably related to the degradation induced by the multiple extrusions. On the other hand the filler addition had two main effect: the increase of the yielding stress (1 MPa for HDPE09-CB226 and 2 MPa for HDPE-CB1353) and mainly the sharp decrease of the strain at break. This effect was more evident in the case of HDPE09-CB1353 composites. Moreover the multiple extrusions induced an increase for HDPE09-CB226 composites, while no change for HDPE09-CB1353 composites. With regard to the elastic modulus the difference between the different materials were lower than the experimental error: nevertheless it was advisable a general decreasing trends as the number of extrusions increased.

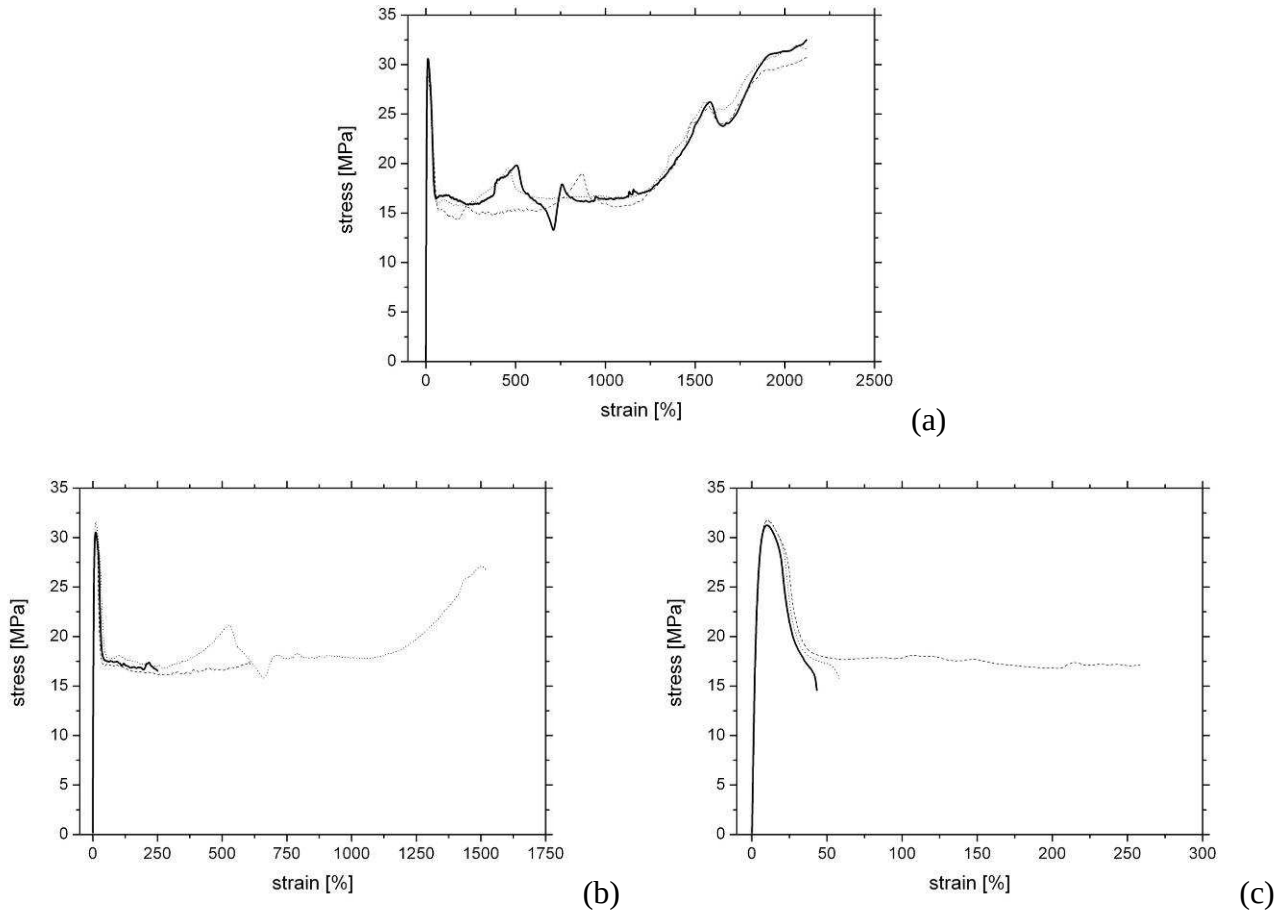

Figure 5.13. Examples of stress-strain curves of HDPE09 (a), HDPE09-CB226 1 1 vol% (b) and HDPE09-CB1353 1 vol% (c) extruded 1 (—), 2 (---) and 3 times (···).

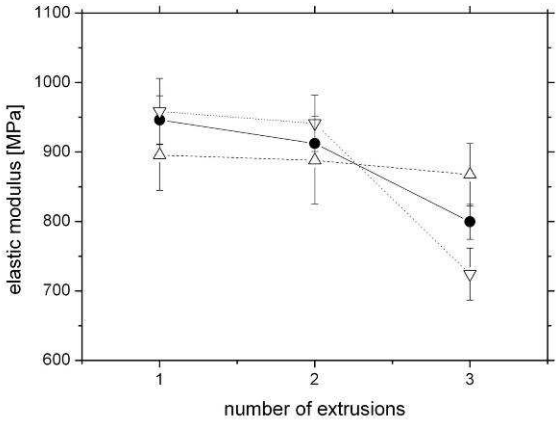

Figure 5.14. Elastic modulus as a function of the number of extrusions for HDPE09 (●), HDPE09-CB226 1 vol% (▽) and HDPE09-CB1353 1 vol% (△).

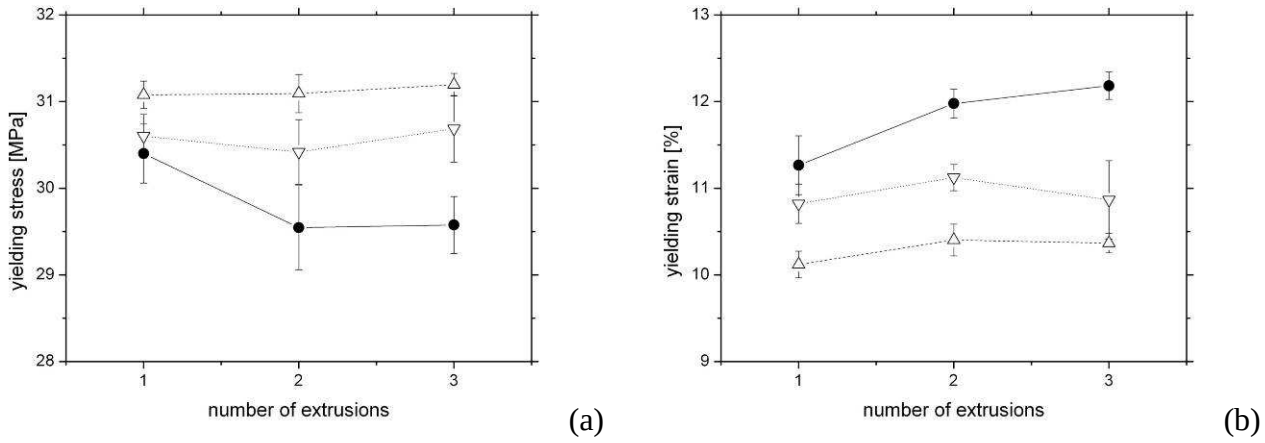

(a) (b)

Figure 5.15. Yielding stress (a) and strain (b) as a function of the number of extrusions for HDPE09 (●), HDPE09-CB226 1 vol% (▽) and HDPE09-CB1353 1 vol% (△).

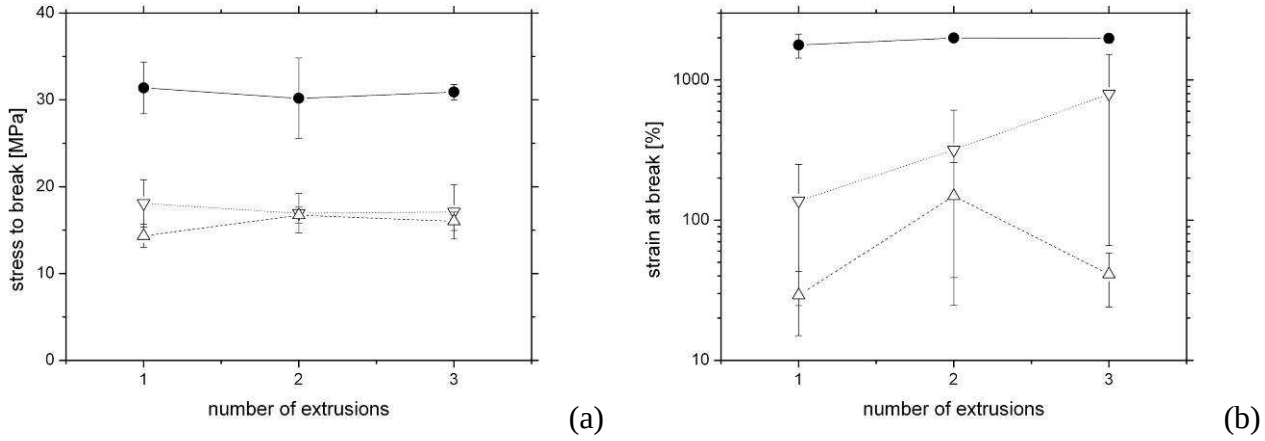

(a) (b)

Figure 5.16. Stress (a) and strain (b) at break as a function of the number of extrusions for HDPE09 (●), HDPE09-CB226 1 vol% (▽) and HDPE09-CB1353 1 vol% (△).

5.1.11 EWF

The load-displacement curves of the tensile test on the DENT samples at various ligament length and the specific work of fracture as a function of the ligament length for all the tested materials are presented in Figure 5.18, Figure 5.19 and Figure 5.20, while Figure 5.21 shows the yielding specific work and the propagation specific work as a function of the ligament length.

For all the materials, a similar trend of the load-displacement curve was observed. In the first part of the test the load increased rapidly and, after the peak, a slow drop in load occurred with a further increase of displacement until the fracture of the specimens. The last part of the curve is very smooth in the case of HDPE09, while it is more irregular for HDPE09-CB composites. The ductile behaviour is evidence if Figure 5.17 that proposes some pictures of the stretched samples during the tests. Moreover all the curves of the specific work of fracture as a function of the ligament length showed a good linear trend that was necessary to employ the EWF approach.

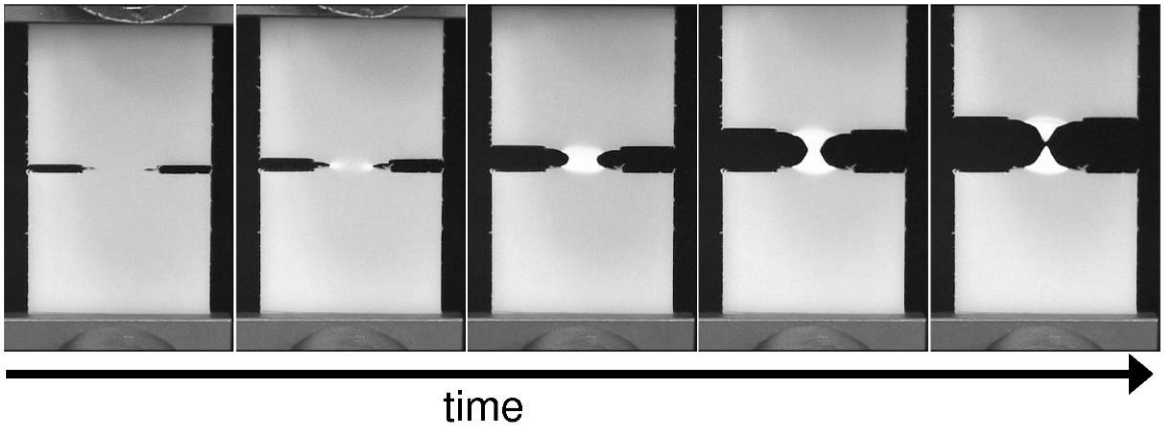

(a)

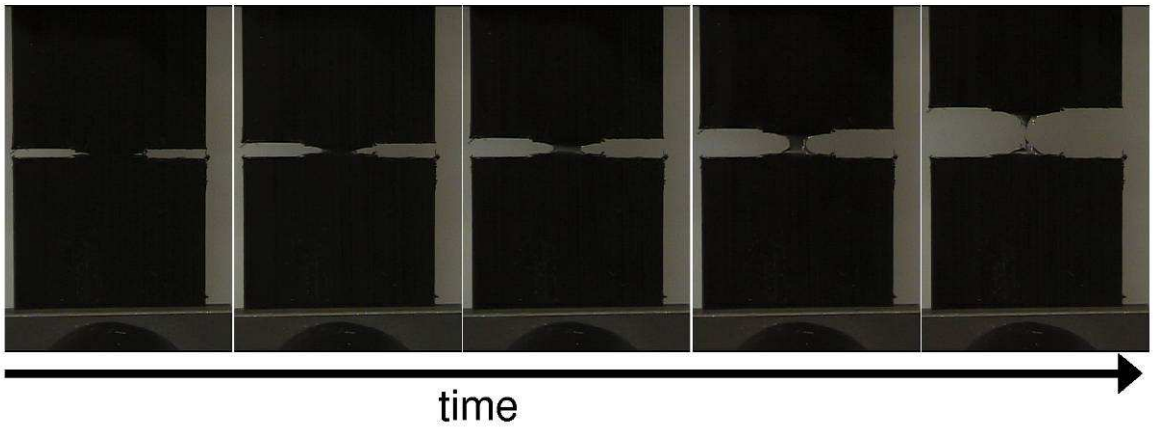

(b)

Figure 5.17. Examples of the stretching of DENT samples for HDPE09 (a) and HDPE09-CB226 1 vol% (b) extruded 1 time.

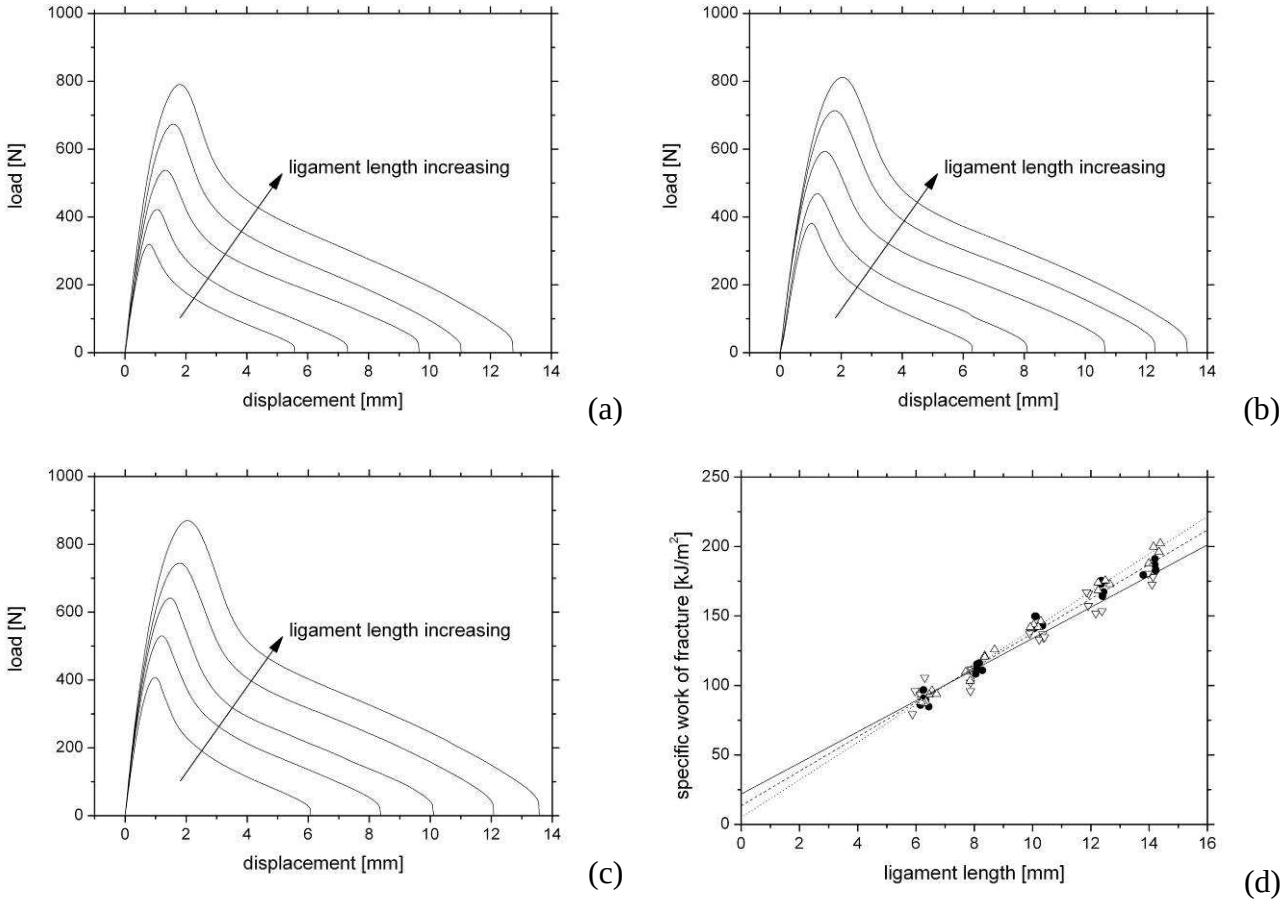

Figure 5.18. Examples of the load-displacement curves for HDPE09 extruded 1 (a), 2 (b) and 3 times (c) and the specific work of fracture as a function of the ligament length for HDPE09 extruded 1 (▽, —), 2 (●, ---) and 3 times (△,···).

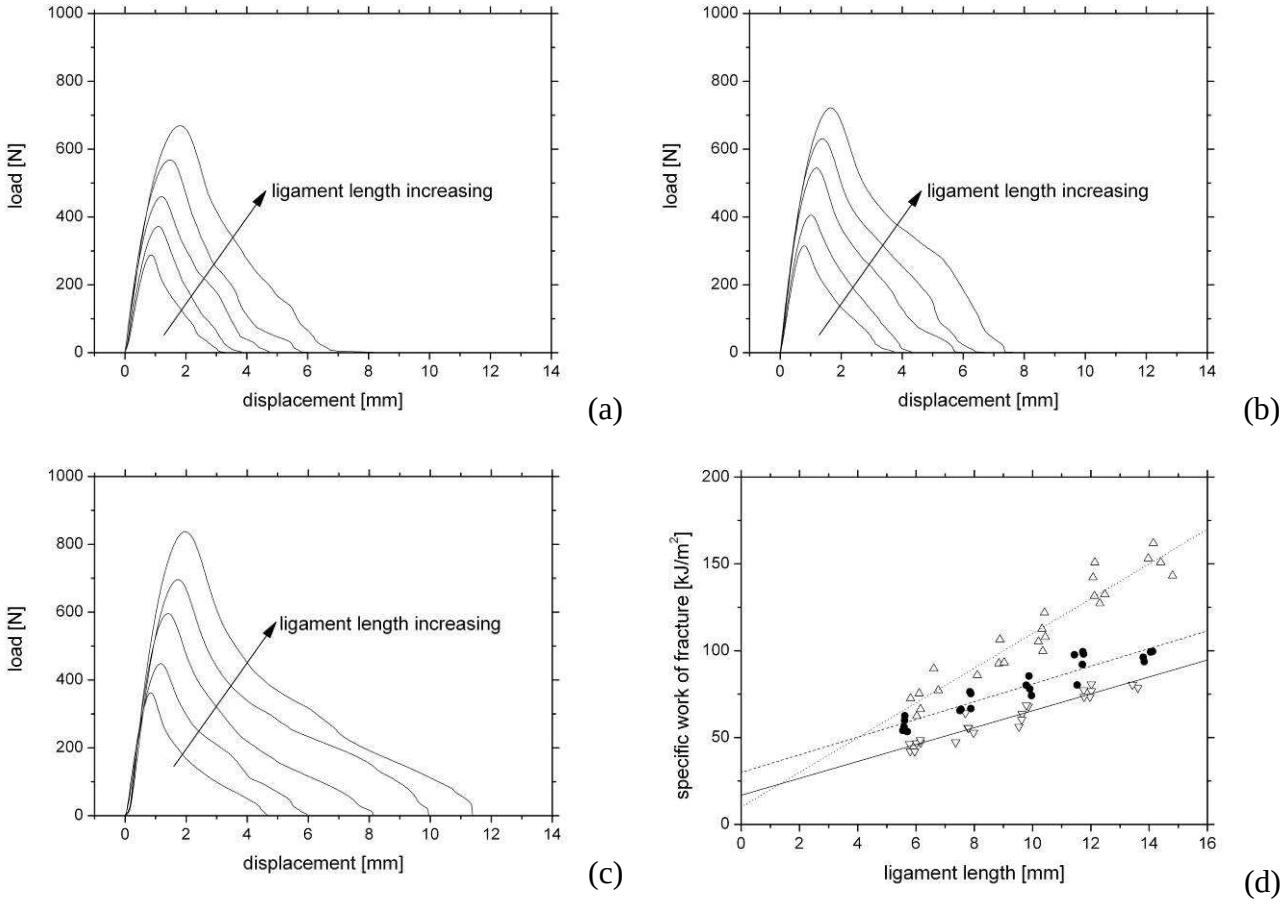

Figure 5.19. Examples of the load-displacement curves for HDPE09-CB226 1vol% extruded 1 (a), 2 (b) and 3 times (c) and the specific work of fracture as a function of the ligament length for HDPE09-CB226 1vol% extruded 1 (▽, —), 2 (●, ---) and 3 times (△,···).

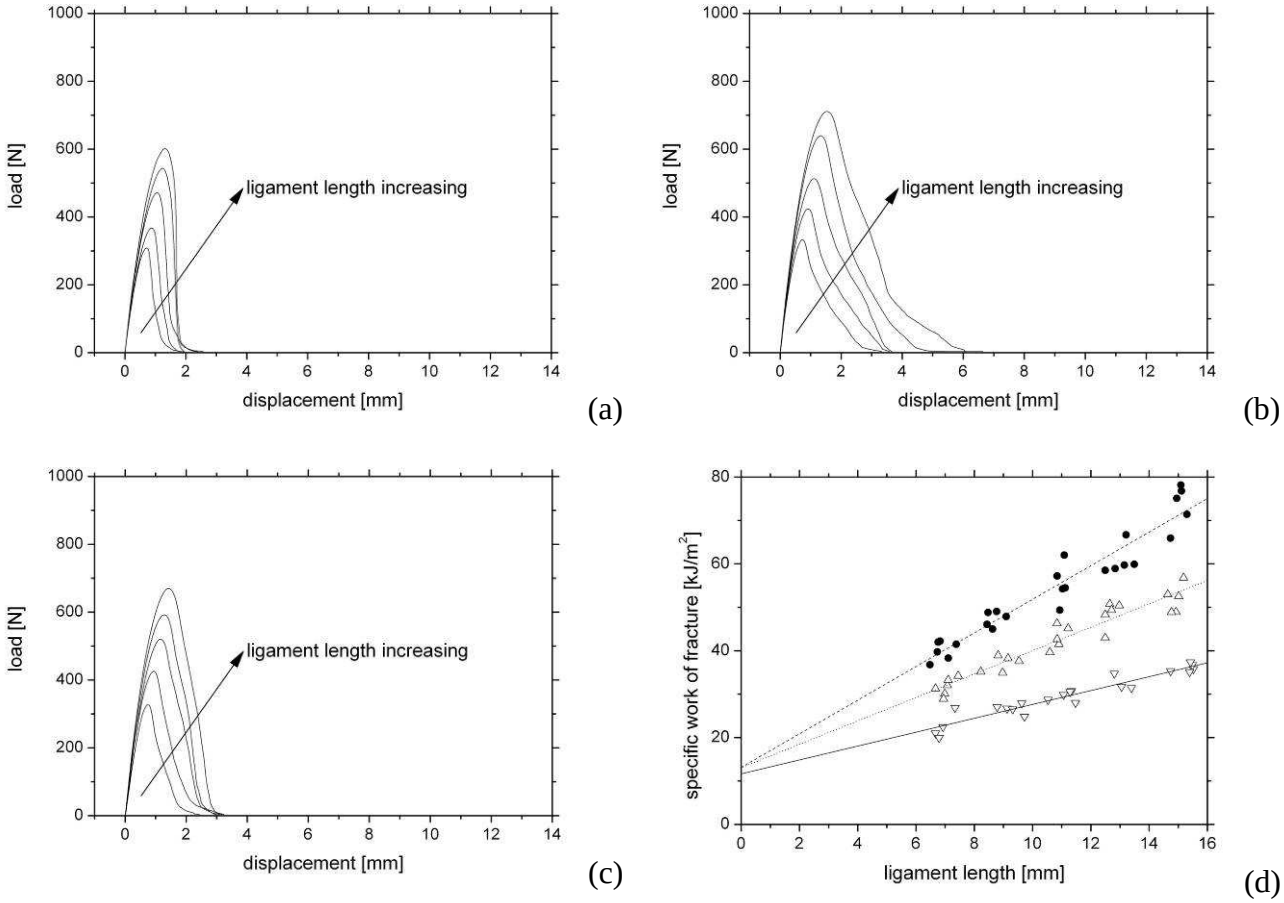

Figure 5.20. Examples of the load-displacement curves for HDPE09-CB1353 1vol% extruded 1 (a), 2 (b) and 3 times (c) and the specific work of fracture as a function of the ligament length for HDPE09-CB1353 1vol% extruded 1 (▽, —), 2 (●, ---) and 3 times (△,——).

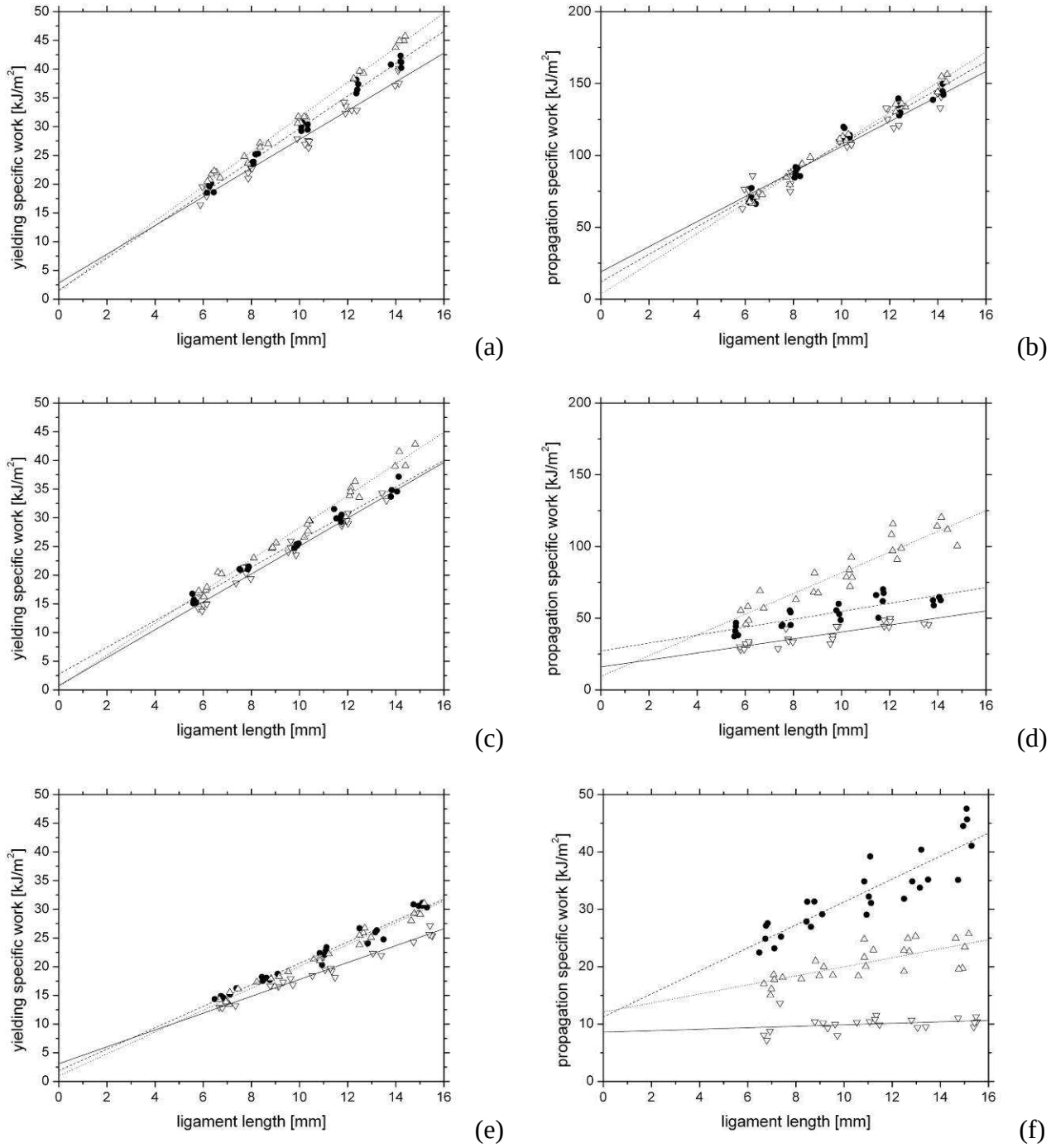

Figure 5.21. Specific work for yielding (a, c, e) and for propagation (b, d, f) for HDPE09 (a, b), HDPE-CB226 1vol% (c, d) and HDPE-CB1353 1vol% (e, f) extruded 1 (▽, —), 2 (●, ---) and 3 times (△,——).

The results of the data analysis performed by the EWF approach are summarized in Table 5.3, Table 5.4 and Table 5.5. EWF parameters clearly indicated that the fracture toughness of HDPE matrix degraded during the repeated extrusions. In fact, the specific essential work and his components decreased and the non-essential work and his components increased. Moreover, the initiation contribute was only about 10% of the essential and non-essential work of fracture

parameters: the crack propagation component undoubtedly represented the most important phenomenon of energy adsorption during the fracture of the sample.

In the case of the composites the situation was more complicated. For the CB226 based composites a beneficial effect on the specific essential work of fracture parameter could be observed only in the case of the second and third extrusions. At the same time, the non-essential work of fracture component (which is related to the energy required to plastically deform the outer process zone) was always reduced by the CB presence, independently of the number of extrusions, even if in third extrusion it became similar to HDPE09 matrix. In the case of the CB1353 based composites the essential work of fracture parameter markedly decreased after the first extrusion, but remained almost constant through the following extrusions. The non-essential work of fracture component showed a similar trend: after the first extrusion it drastically decreased, but it remained almost constant through the following extrusions. As a consequence a toughening effect was observed only after three consecutive extrusions. The analysis of the two contributes of the EWF parameters evidenced the same considerations of the global parameters.

Table 5.3. Essential work of fracture (w_e) and plastic work dissipation (βw_p).

Material	Extr.	w_e [kJ/m^2]		βw_p [MJ/m^3]		R^2
		mean	SD	mean	SD	
HDPE09	1	21.8	5.1	10.8	0.5	0.9560
	2	13.5	4.3	12.4	0.4	0.9772
	3	5.0	2.4	13.5	0.2	0.9934
HDPE09-CB226 1 vol%	1	16.8	3.0	4.9	0.3	0.9171
	2	29.9	4.0	5.1	0.4	0.8875
	3	9.9	6.7	10.0	0.6	0.9183
HDPE09-CB1353 1 vol%	1	11.6	1.3	1.6	0.1	0.9090
	2	13.1	2.6	3.9	0.2	0.9195
	3	13.1	1.8	2.7	0.2	0.9182

Table 5.4. Initiation terms of Essential work of fracture ($w_{e,ini}$) and plastic work dissipation ($\beta w_{p,ini}$).

Material	Extr.	$w_{e,ini}$ [kJ/m^2]		$\beta w_{p\ ini}$ [MJ/m^3]		R^2
		mean	SD	mean	SD	
HDPE09	1	2.8	0.9	2.5	0.1	0.9728
	2	1.5	0.6	2.8	0.1	0.9911
	3	1.5	0.5	3.0	0.1	0.9930
HDPE09-CB226 1 vol%	1	0.8	0.8	2.4	0.1	0.9753
	2	2.8	0.6	2.3	0.1	0.9859
	3	0.5	0.8	2.8	0.1	0.9829
HDPE09-CB1353 1 vol%	1	3.1	0.7	1.5	0.1	0.9670
	2	1.9	0.7	1.9	0.1	0.9742
	3	1.0	0.6	1.9	0.1	0.9816

Table 5.5. Propagation terms of Essential work of fracture ($w_{e,prop}$) and plastic work dissipation ($\beta w_{p,prop}$).

Material	Extr.	$w_{e,prop}$ [kJ/m^2]		$\beta w_{p,prop}$ [MJ/m^3]		R^2
		mean	SD	mean	SD	
HDPE09	1	19.0	4.6	8.7	0.4	0.9426
	2	12.0	4.1	9.6	0.4	0.9647
	3	3.5	2.3	10.5	0.2	1.0
HDPE09-CB226 1 vol%	1	16.0	2.9	2.4	0.3	0.7541
	2	27.1	3.9	2.8	0.4	0.7058
	3	9.4	6.4	7.2	0.6	0.8647
HDPE09-CB1353 1 vol%	1	8.6	1.1	0.1	0.1	0.1
	2	11.3	2.4	2.0	0.2	0.8
	3	12.1	1.6	0.8	0.1	0.5

The effect of the filler type and of the number of extrusions was evidenced by calculating the relative toughness, i.e. the ratio between the essential work of fracture of HDPE09-CB composites and the one of HDPE09 with the same number of extrusions. This ratio was calculated for initiation and propagation components too. The results are showed in Figure 5.22. In the case of HDPE09-CB226 composites the fracture toughness markedly increased in comparison to HDPE09 already after the second extrusion and remained constant after three extrusions. On the other hand the fracture toughness of HDPE09-CB1353 composites increased only after three extrusions, but the plateau was not still evident. These results could be related to the different evolution of the filler dispersion in the polymeric matrix for CB226 and CB1353. Moreover, while the initiation

components appeared almost constant, the propagation components had the same trend of the total relative toughness.

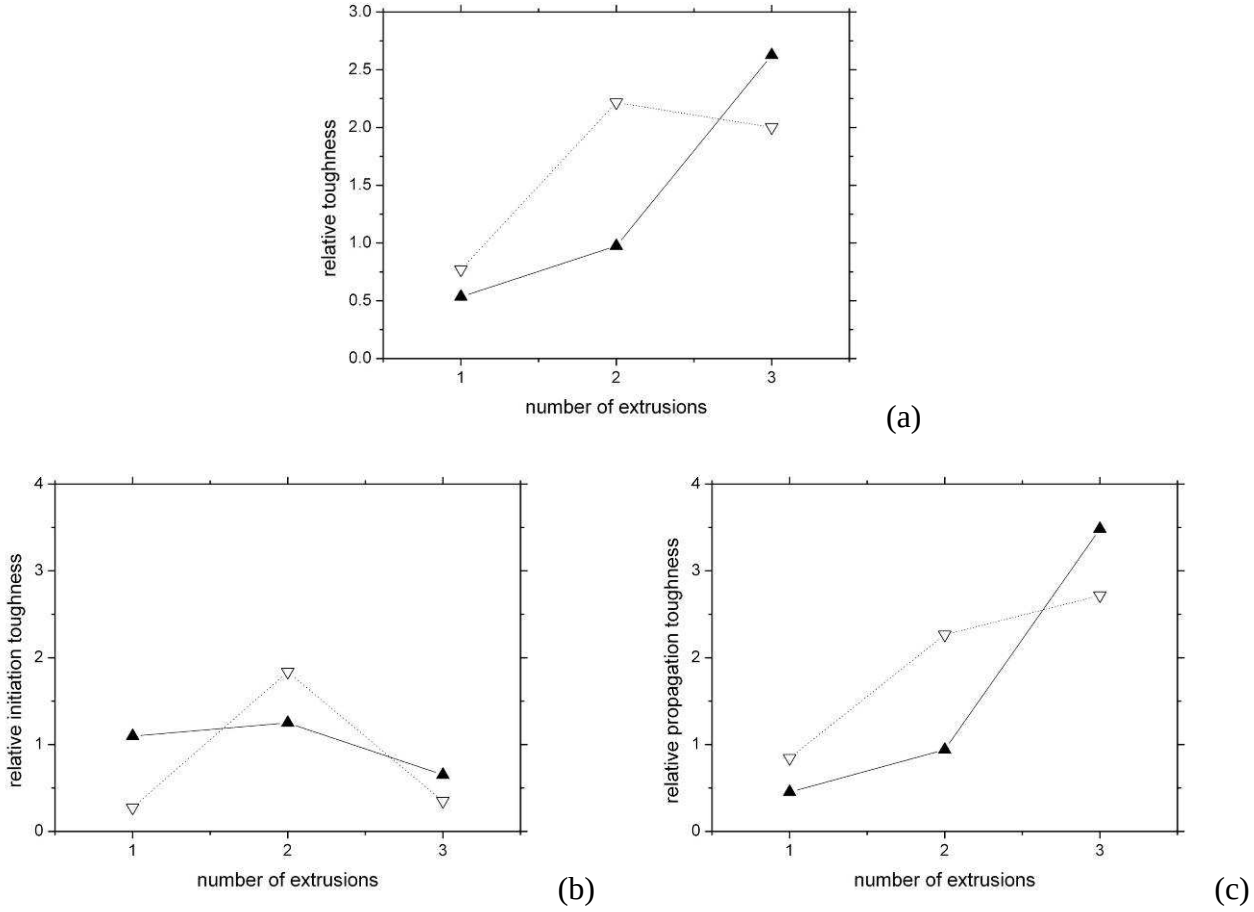

Figure 5.22. Relative toughness, relative initiation and propagation toughness for HDPE09-CB226 (▽) and HDPE09-CB1353 (▲) composites.

The tests were recorded with a digital video camera and the images analyzed in order to understand the fracture process. The crack propagation and the increasing of the yielded region were monitored during the test for HDPE09. These two parameter were compared to the load-displacement curve. The yielded area was monitored only for HDPE09 samples because the different refractive index of the yielded region, but not for HDPE09-CB composites for which no colour change was observed (Figure 5.17). The results of this analysis are presented in Figure 5.23. The image analysis evidenced that the peak of the load–displacement curves corresponded to the fully yielding of the ligament. In this way it was possible to verify an other basic hypothesis necessary to apply the EWF approach. Moreover it was possible to correlate the yielding region with the crack initiation ($w_{e,ini}$) and the necking and fracture region to the crack propagation ($w_{e,prop}$).

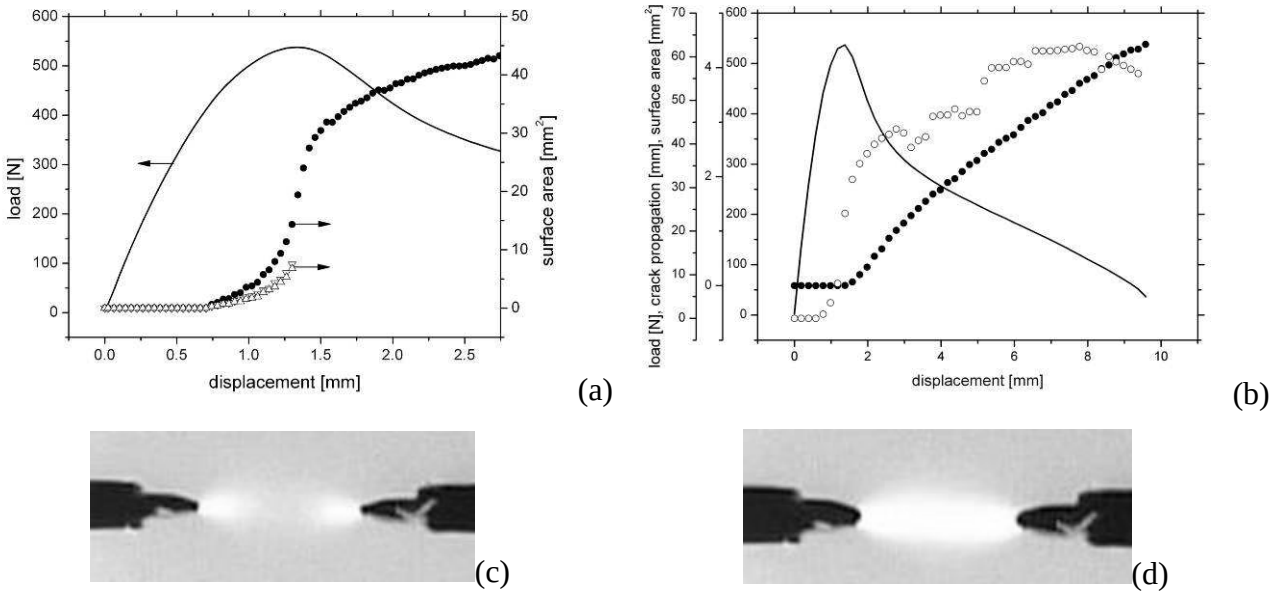

Figure 5.23. Results of the image analysis: yielded area and crack propagation during tensile test on DENT specimen (ligament length = 10 mm) for HDPE09 extruded 1 time.

Figure 5.24 shows the micrographs acquired with a stereoscopic microscope of the fracture surface near the initial crack tip of the DENT specimens (all with an initial ligament length of 10 mm). Microcavitation phenomena were observed for all the materials, but with different intensity in terms of dimensions and density. In particular the microcavitation decreased for HDPE09 as the number of extrusions increased, while the phenomenon was more intense for HDPE09-CB composites after every extrusion and in particular with CB1353.

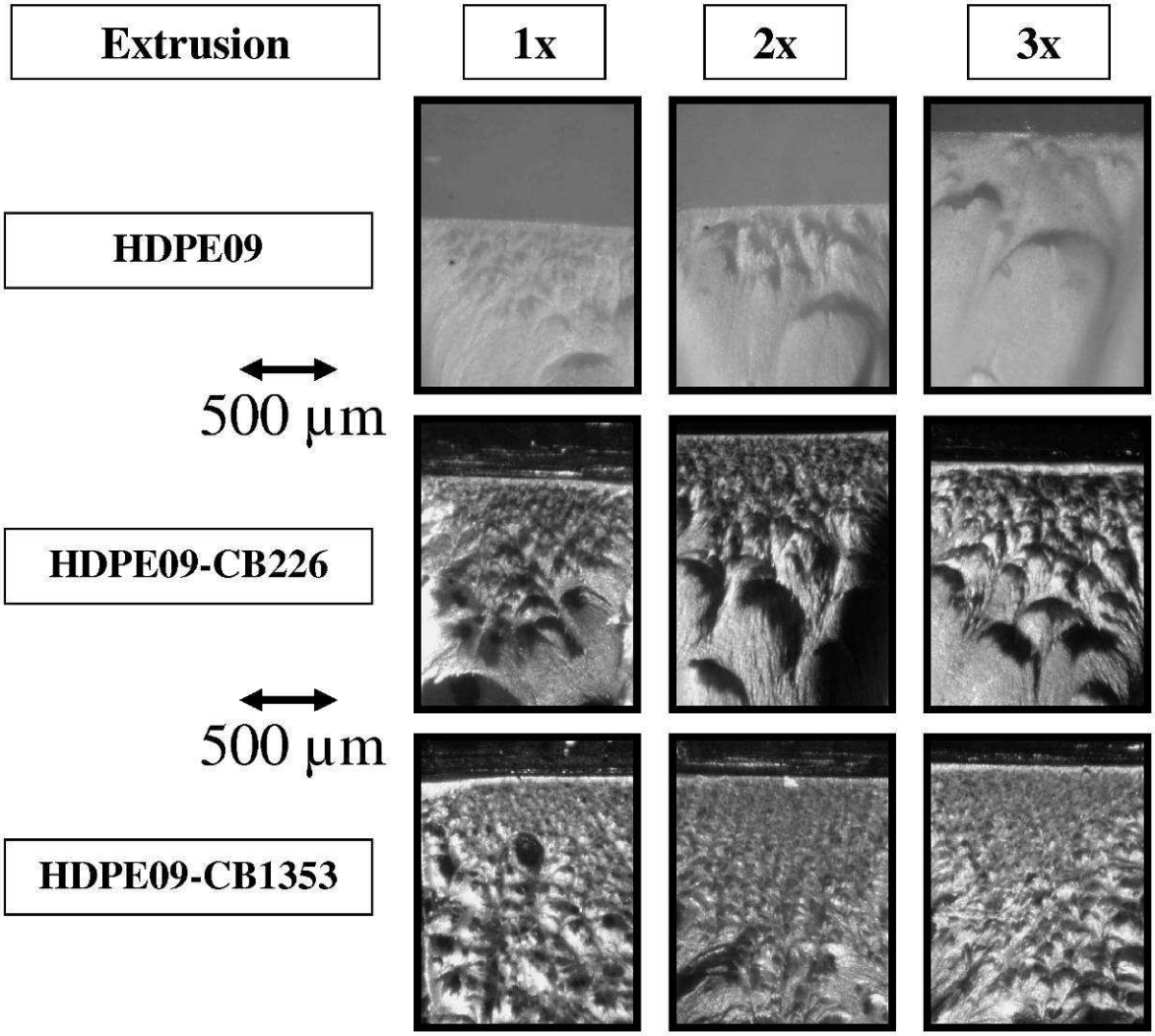

Figure 5.24. Micrographs acquired with a stereoscopic microscope of the fracture surface near the initial crack tip of the DENT specimens (all with an initial ligament length of 10 mm).

5.1.12 Tensile creep tests

From a general point of view the multiple extrusion induced a progressive reduction of the creep resistance of HDPE09, while CB resulted to substantially increase the creep resistance of the HDPE09 matrix with an effect stronger and stronger as the number of extrusion increased and as the specific surface area of CB increased (i.e. from CB226 to CB1353). Figure 5.25 shows the results of creep test at 30°C and 3 MPa for all the produced materials.

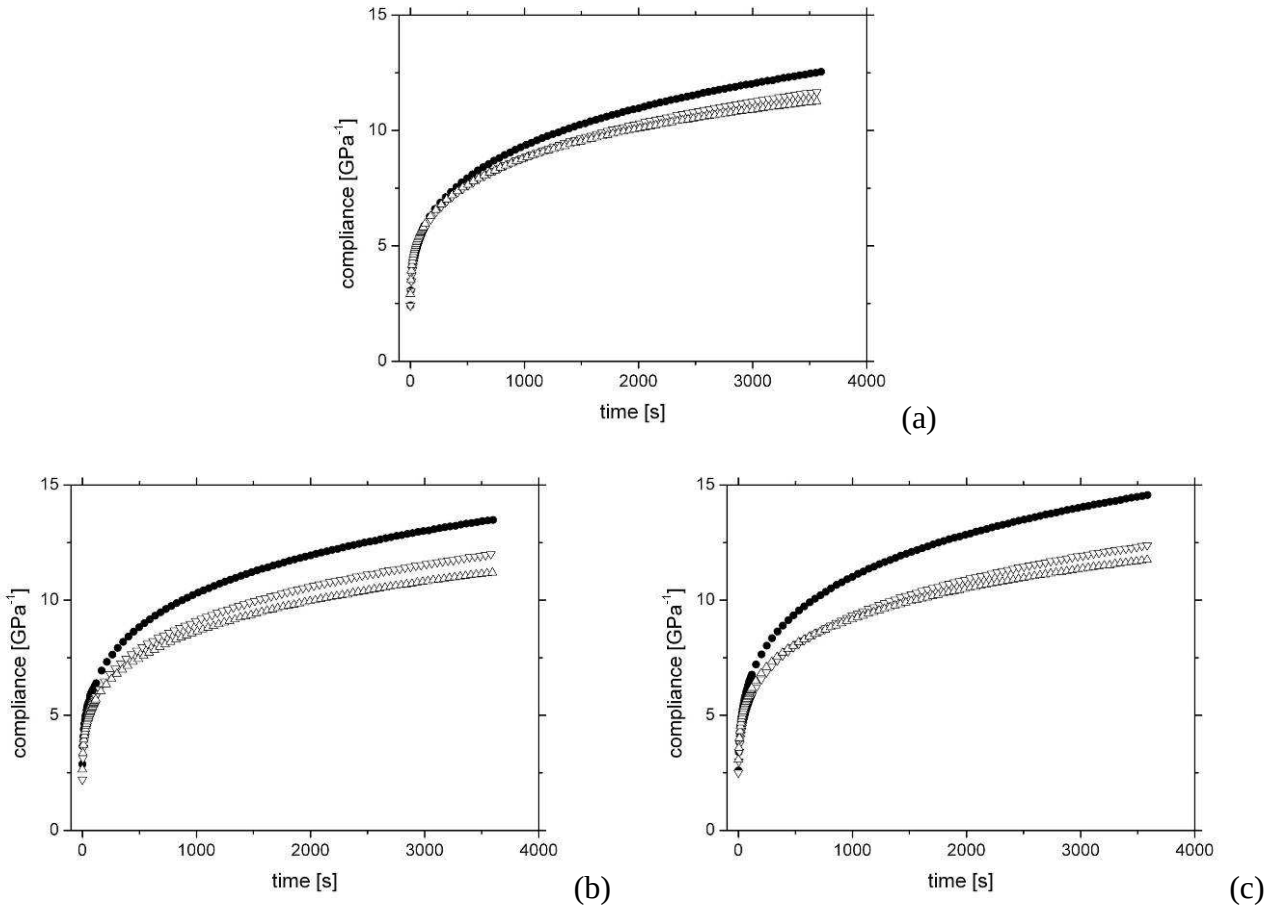

Figure 5.25. Creep compliance at 30°C and 10 MPa for HDPE09 (●), HDPE09-CB226 1 vol% (▽) and HDPE09-CB1353 1 vol% (△) extruded 1 (a), 2 (b) and 3 times (c).

While all the materials underwent a reference test at 30°C and 3 MPa, the behaviour of some materials were investigated in more detail: HDPE09 extruded 1 and 3 times, HDPE09, HDPE09-CB226 1vol% and HDPE09-CB1353 1 vol% extruded 3 times. The goal was to analyze the effect of the multiple extrusion on HDPE09 and the effect of the filler type (with a good filler dispersion). The effects on the creep resistance were detectable in the linear viscoelastic region (i.e. at low stresses or temperatures), and it became more and more evident in the non-linear viscoelastic or viscoplastic region (i.e. at high stresses or temperatures). Examples of this behaviour are proposed in Figure 5.26 and in Figure 5.27 where compliance and compliance rate of the tested materials at 30°C and 75°C are showed.

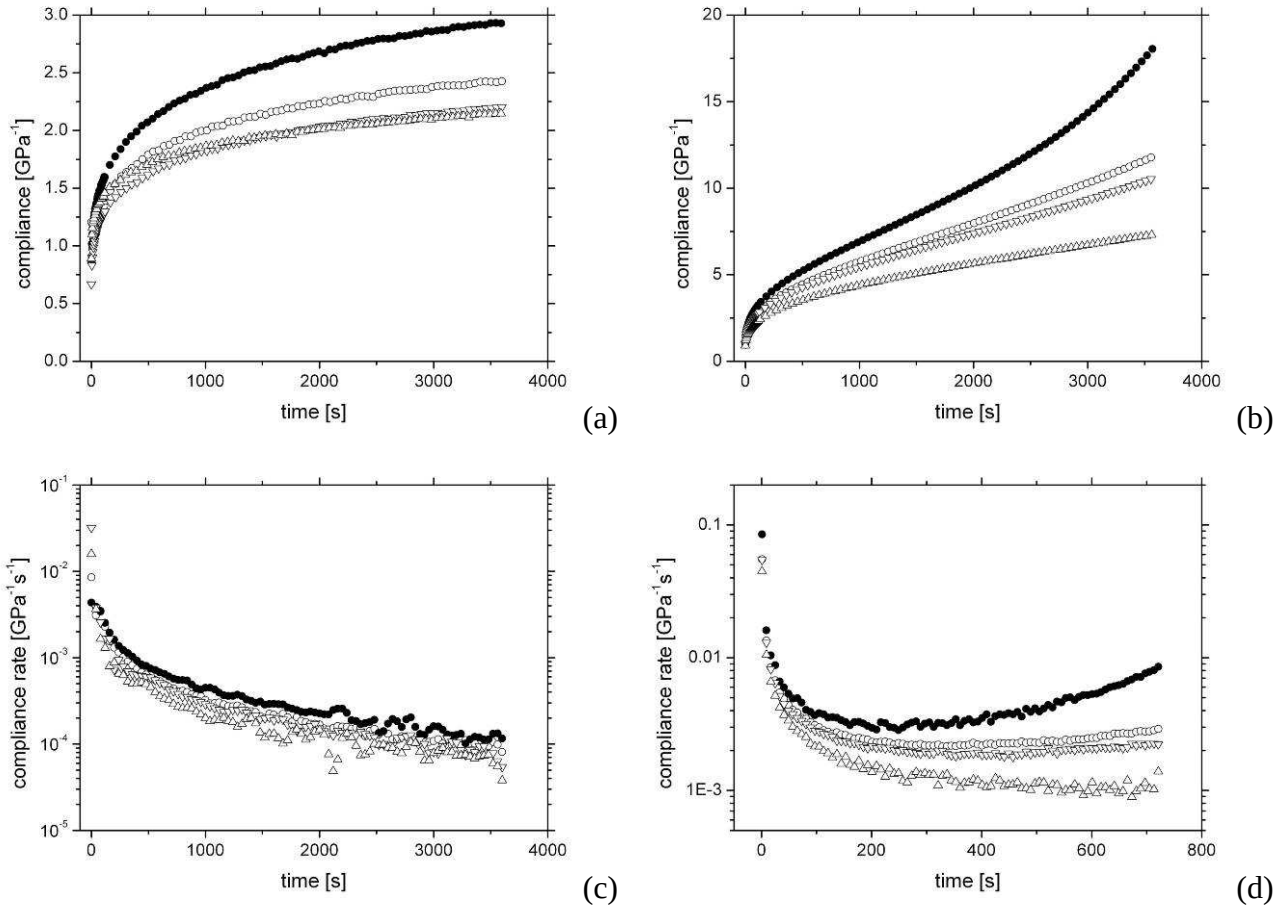

Figure 5.26. Creep compliance at 30°C (a, c) and creep compliance rate (b, d) as a function of time at 30°C with a stress of 3 MPa (a, b) and 15 MPa (c, d) for HDPE09 extruded 1 (○) and 3 times (●) and for HDPE09-CB226 1 vol% (▽) and HDPE09-CB1353 1 vol% (△).

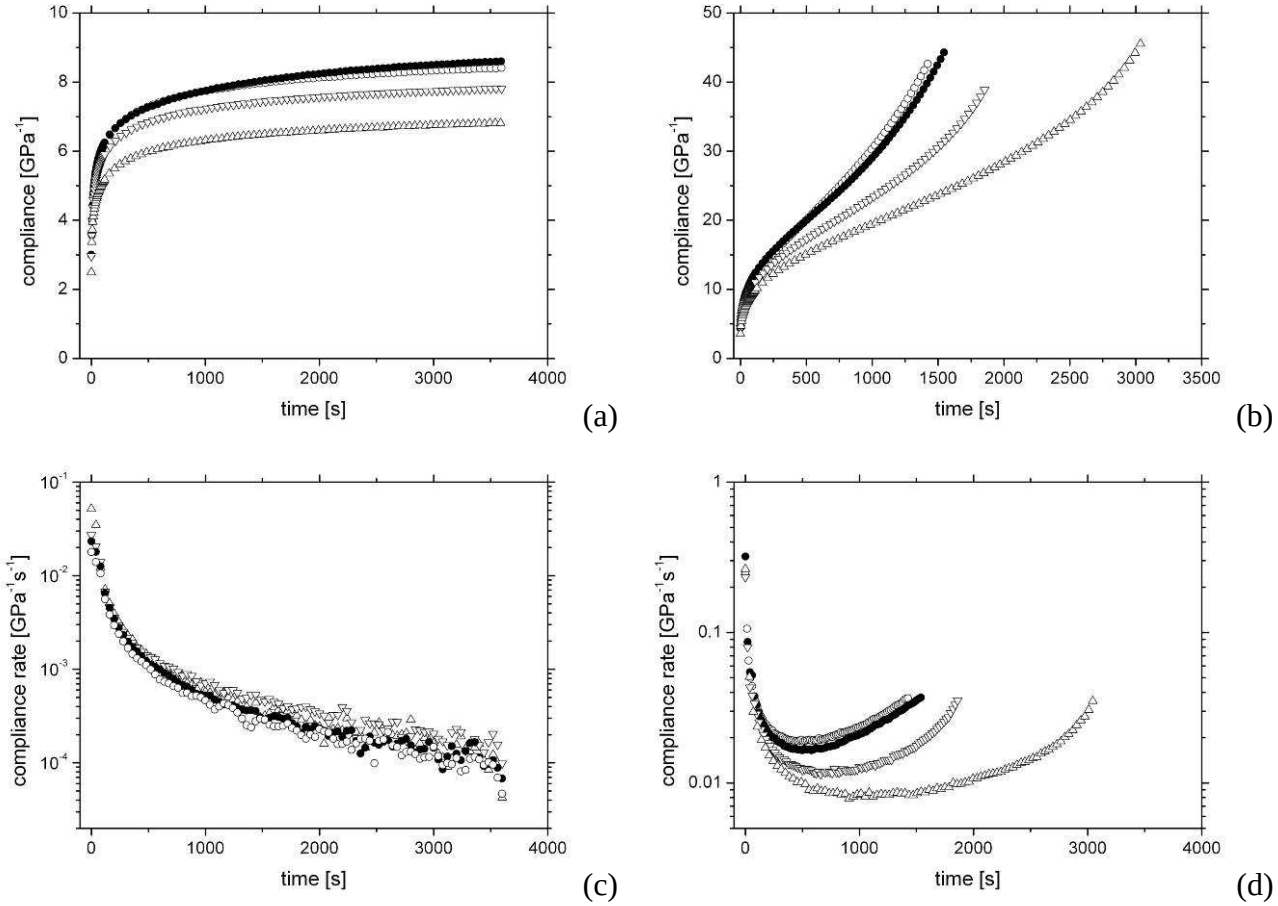

Figure 5.27. Creep compliance at 30°C (a, c) and creep compliance rate (b, d) as a function of time at 75°C with a stress of 3 MPa (a, b) and 8 MPa (c, d) for HDPE09 extruded 1 (○) and 3 times (●) and for HDPE09-CB226 1 vol% (▽) and HDPE09-CB1353 1 vol% (△).

The isochronous stress-strain curves at 30°C and 75°C for a creep time of 2000 are showed in Figure 5.28. It is evident as the increased temperatures reduced the creep resistance of both the tested materials and mainly as the creep resistance decreased for HDPE09 after 3 extrusion and increased for HDPE09-CB composites in comparison to HDPE09 especially when the applied stress increased. This effect was stronger for HDPE09-CB1353 composites in comparison to HDPE09-CB226 composites.

Figure 5.29 proposes the partitioning of the isochronous creep compliance at 2000 s in the related elastic (i.e. the creep compliance at 0 s) and viscoelastic components. While the elastic components are the same for all the materials, the viscoelastic components were sharply different. In particular the viscoelastic components of the compliance increased for HDPE09 after 3 extrusions but only for temperature lower than 60°C, while a sharp reduction was observed for all both HDPE09-CB composites in comparison to HDPE09 extruded 3 times. Moreover an average reduction of 12% for

HDPE09-CB226 composites and an average reduction of 24% for HDPE09-CB1353 composites were observed.

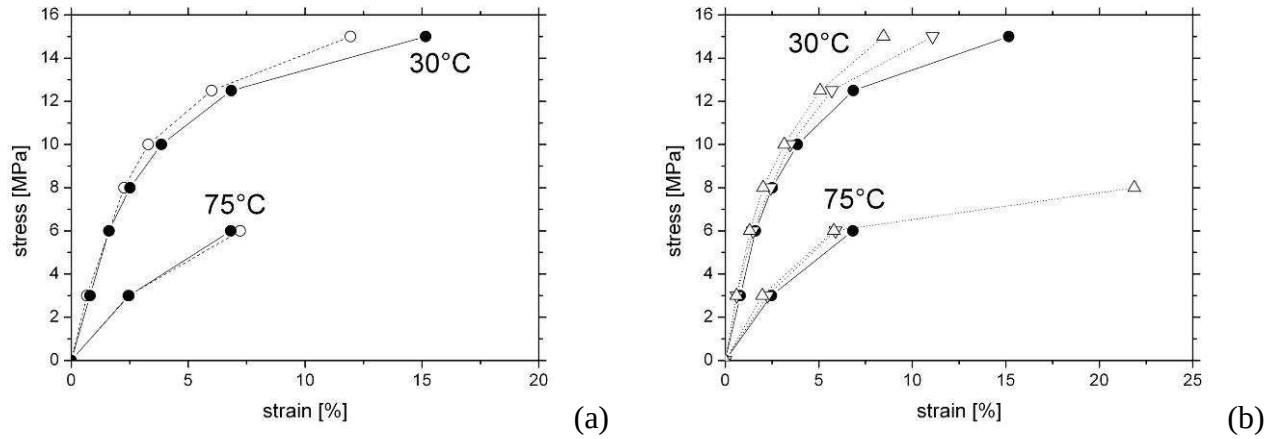

Figure 5.28. The isochronous stress-strain curves of HDPE09 extruded 1 (○) and 3 times (●) and of HDPE09-CB226 1 vol% (▽) and HDPE09-CB1353 1 vol% (△) for a creep time of 2000 s.

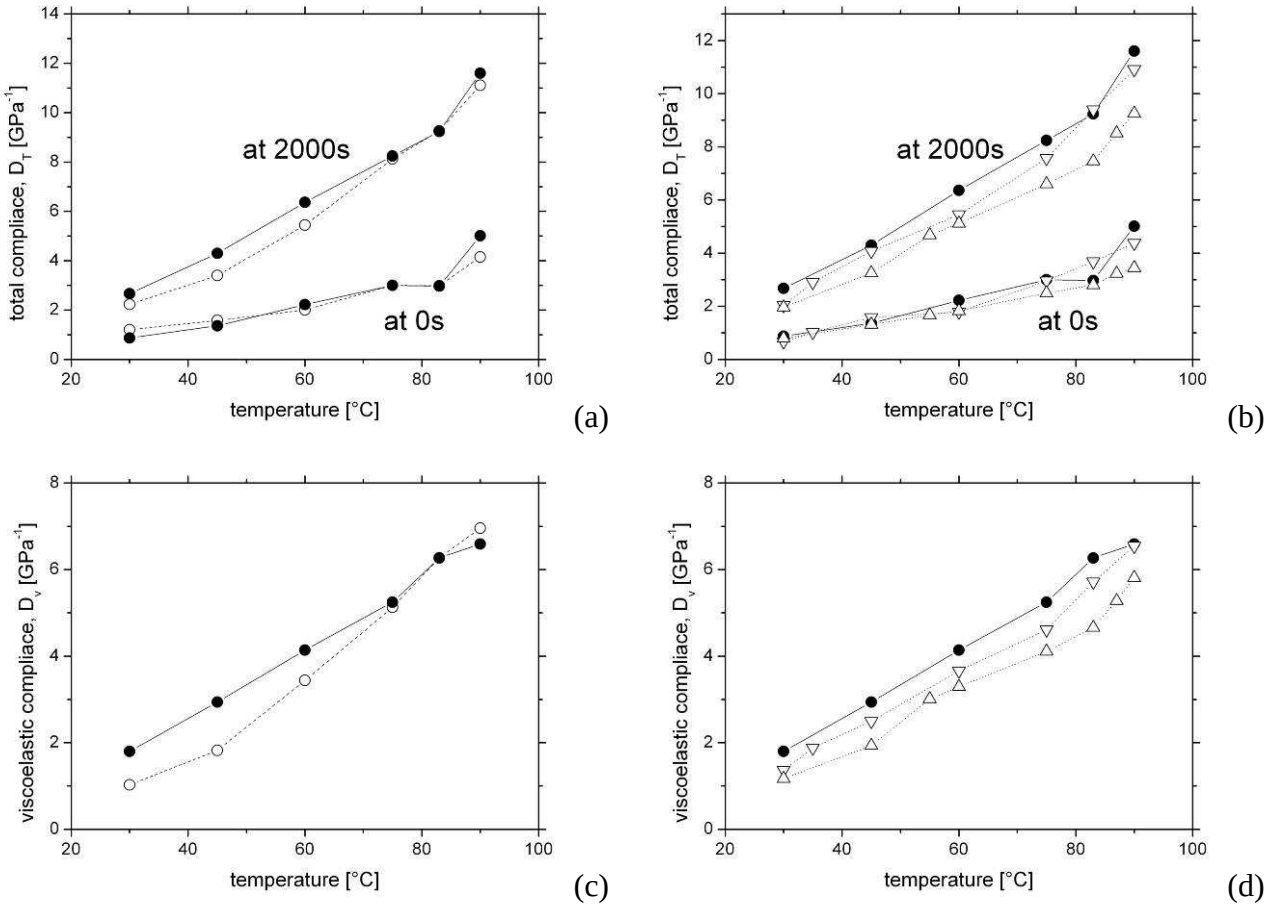

Figure 5.29. Isochronous compliance at 0 s and 2,000 s (a, b) and viscoelastic components of the isochronous compliance at 2,000 s for HDPE09 extruded 1 (○) and 3 times (●) and of HDPE09-CB226 1 vol% (▽) and HDPE09-CB1353 1 vol% (△).

On the basis of a time-temperature superposition principle, short term creep performed in the linear-viscoelastic region (with an applied stress of 3 MPa) allowed to obtain creep compliance master curves for long term creep at 30°C (Figure 5.30). Over the extended time period covered by the master curves, the creep compliance increased for HDPE09 of about 13% after 3 extrusion, while it was reduced by about 25% and 30%, on average, for HDPE09-CB226 and HDPE09-CB1353 composites, respectively.

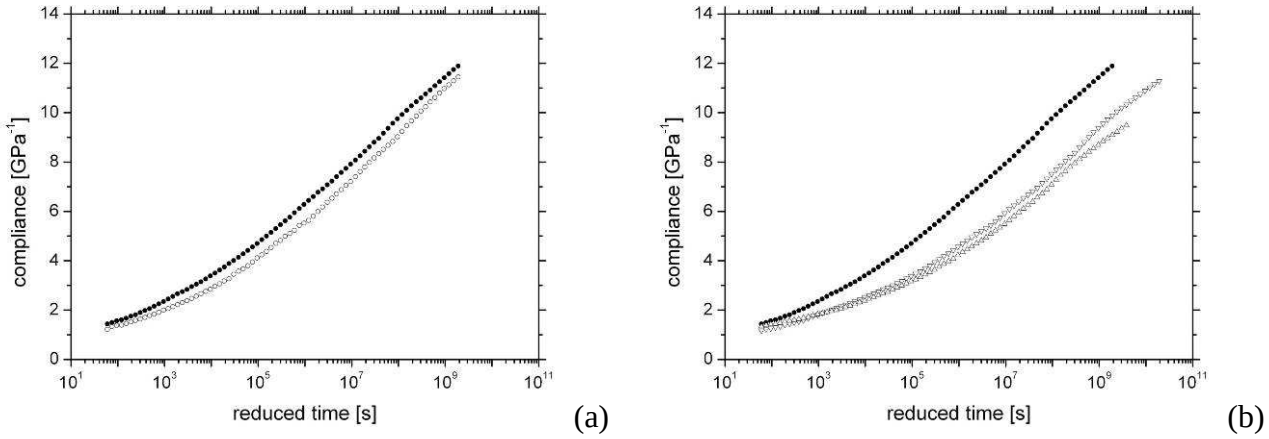

Figure 5.30. Creep compliance master curves obtained at 3 MPa and referred at 30°C for HDPE09 extruded 1 (○) and 3 times (●) and of HDPE09-CB226 1 vol% (▽) and HDPE09-CB1353 1 vol% (△).

Moreover the shift factor (Figure 5.31) calculated from the short term creep test to obtain the master curves as a function of the temperature was fitted with an Arrhenius law. In this way an activation energy for the relaxation phenomenon was determined: the values decreased after 3 extrusion from (203±10) kJ/kmol to (173±41) kJ/kmol, while increased for HDPE09-CB226 composites, (218±10) kJ/kmol, and for HDPE09-CB1353 composites, (206±6) kJ/kmol.

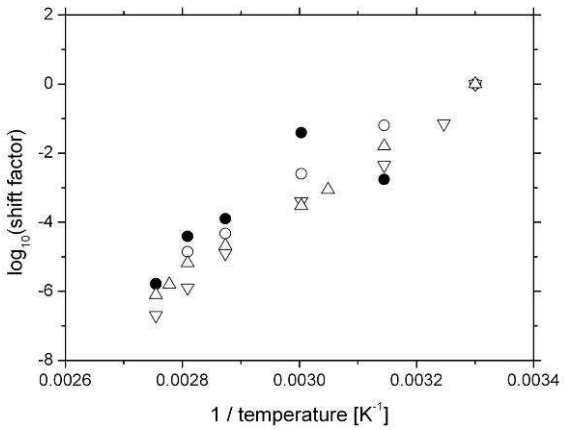

Figure 5.31. Shift factor as a function of the inverse of the absolute temperature for HDPE09 extruded 1 (○) and 3 times (●) and of HDPE09-CB226 1 vol% (▽) and HDPE09-CB1353 1 vol% (△).

The master curve data were used to calculate the creep compliance rate over the full time range. Figure 5.32 shows as all the materials had practically the same behaviour for time over 10^4 s: the main difference were present at low time where the results were congruent with the variations of the creep resistance and they were in agreement with the results at low stresses in linear viscoelastic region (as for example in Figure 5.26 and Figure 5.27). Moreover it was possible to fit the data with a power law which has the expression $dD/dt = 0.19 \cdot t^{-0.93}$ where the compliance is expressed in GPa^{-1} and the time in s.

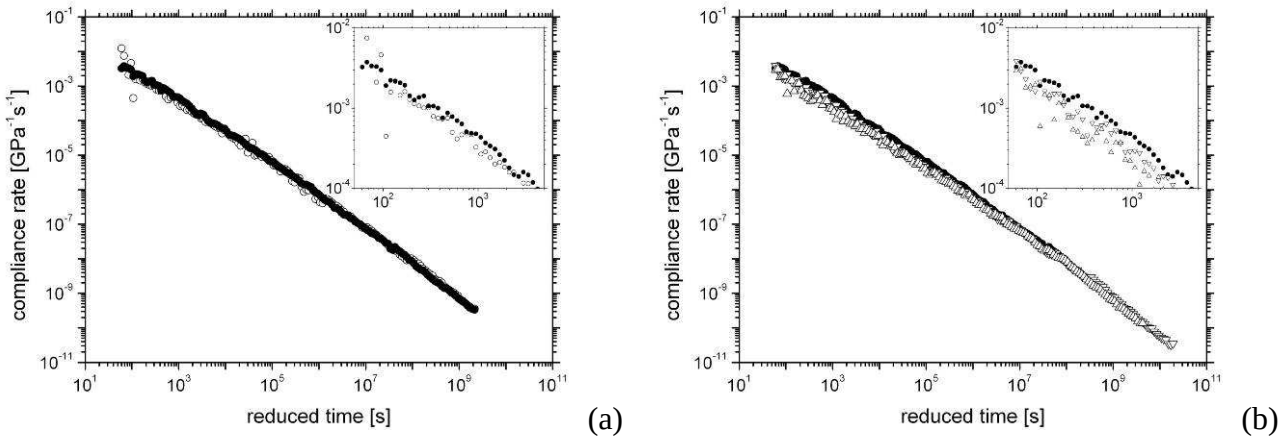

Figure 5.32. Creep compliance rate as a function of time in a log-log scale for HDPE09 extruded 1 (○) and 3 times (●) and of HDPE09-CB226 1 vol% (▽) and HDPE09-CB1353 1 vol% (△). The inset is a detail at short times.

The master curve data were also used to calculate the retardation spectra over the full time range available: Figure 5.33 shows as the multiple extrusions shifted the spectrum to lower retardation times, while CB to higher retardation times. This effect was slightly stronger in the case of CB1353 in comparison to CB226.

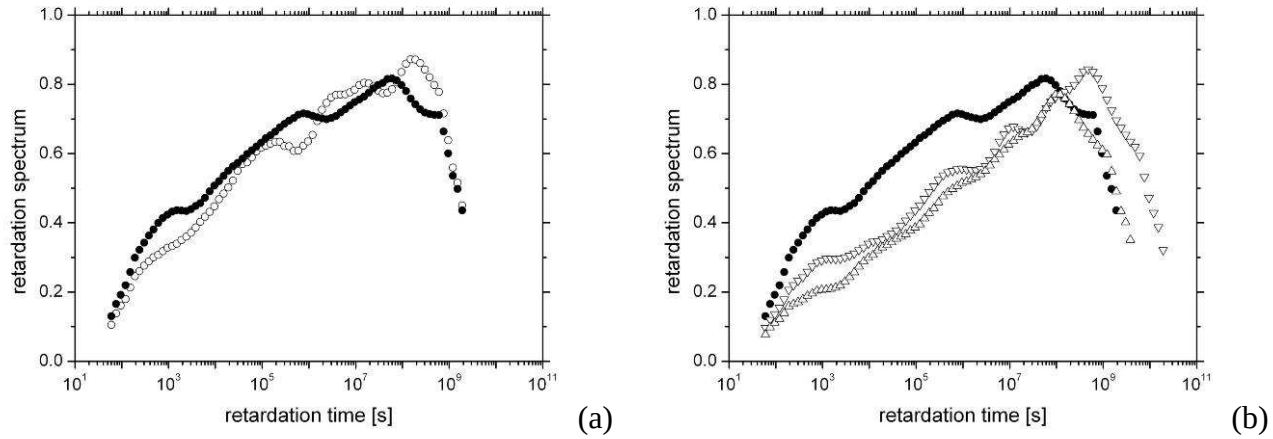

Figure 5.33. Retardation spectra as a function of the retardation time for HDPE09 extruded 1 (○) and 3 times (●) and of HDPE09-CB226 1 vol% (▽) and HDPE09-CB1353 1 vol% (△).

5.1.13 DMTA

The results of the DMTA tests at 1 Hz from -130°C are showed in Figure 5.34, Figure 5.35 and Figure 5.36. The materials presented two sharp drops of the storage modulus that corresponded to two peaks in terms of dissipative modulus and loss factor. In particular the first phenomenon at low temperature (about -100°C) was related to glass transition (γ-relaxation), while the phenomenon at higher temperatures (about 60°C) is the α-relaxation of the crystalline phase [12].

The glass transition temperature decreased of 10°C after 3 extrusions for HDPE09, while it increased of about 4°C in the case of HDPE09-CB composites. On the other hand the temperature of the α-relaxation increased of about 3°C after 3 extrusion for HDPE09, while it remained almost constant in presence of CB226 and increased of about 6°C for HDPE09-CB1353 composites. Table 5.6 summarizes the characteristic temperature of the glass transition and of the α- and γ-relaxation.

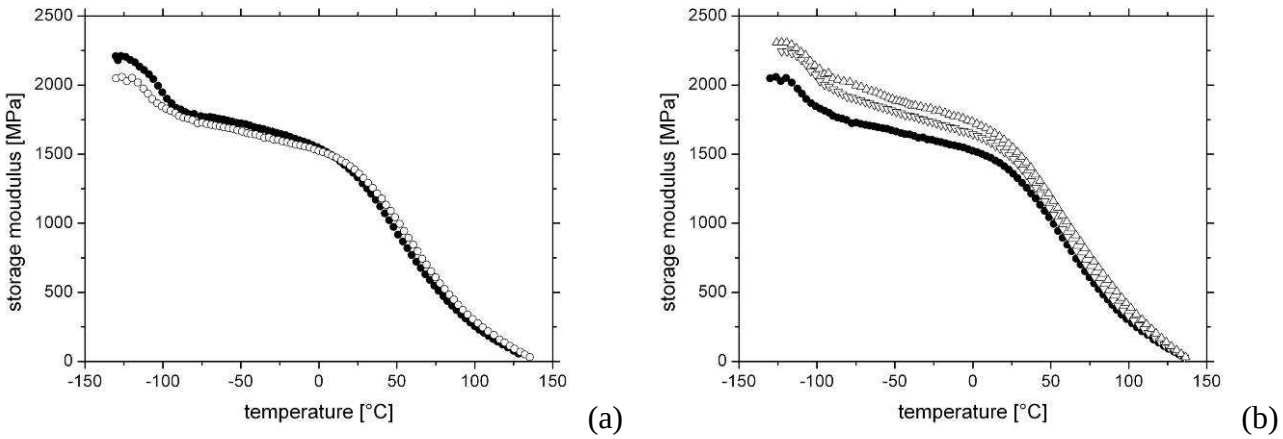

Figure 5.34. The storage modulus as a function of the temperature for HDPE09 extruded 1 (○) and 3 times (●) and of HDPE09-CB226 1 vol% (▽) and HDPE09-CB1353 1 vol% (△).

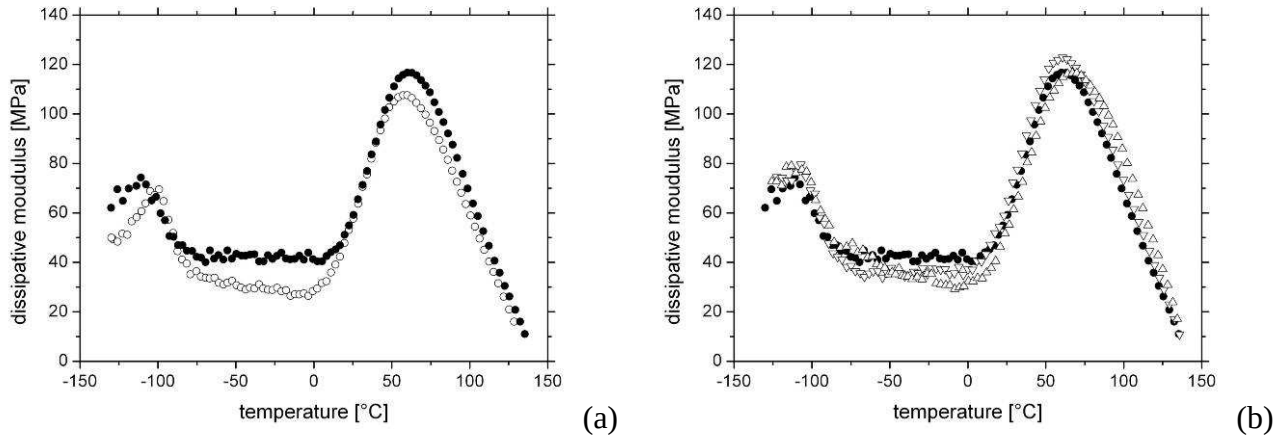

Figure 5.35. The dissipative modulus as a function of the temperature for HDPE09 extruded 1 (○) and 3 times (●) and of HDPE09-CB226 1 vol% (▽) and HDPE09-CB1353 1 vol% (△).

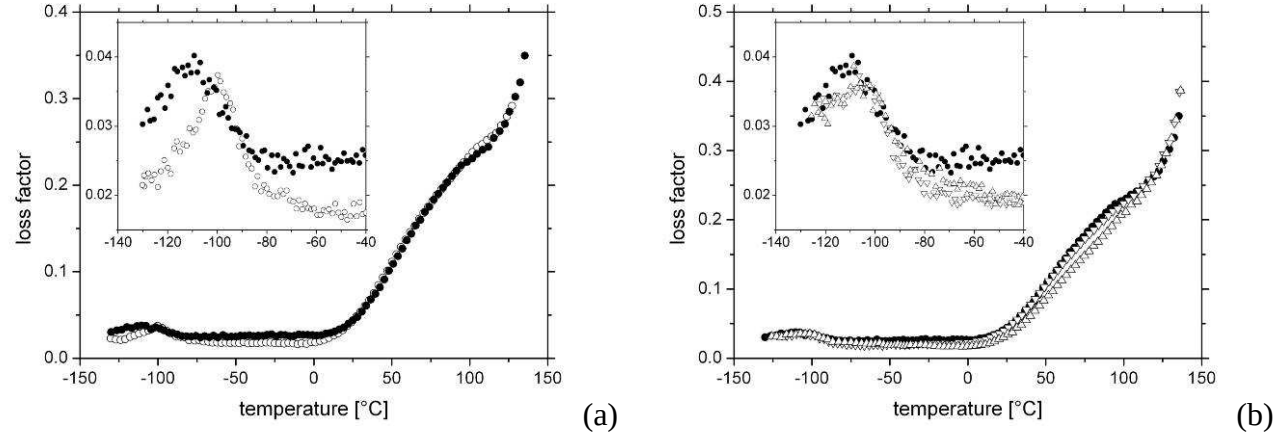

Figure 5.36. The loss factor as a function of the temperature for HDPE09 extruded 1 (○) and 3 times (●) and of HDPE09-CB226 1 vol% (▽) and HDPE09-CB1353 1 vol% (△).

Table 5.6. The temperature of the α- and γ-relaxations.

Material	**T_γ (T_g) [°C]**	**T_α [°C]**
HDPE09, 1x	-98.8	59.9
HDPE09, 3x	-108.9	62.9
HDPE09-CB226 1 vol%, 3x	-104.3	62.4
HDPE09-CB1353 1 vol%, 3x	-103.8	69.0

The data acquired with DMTA tests in multifrequency mode were elaborated on the basis of a time-temperature superposition principle in order to obtain the master curves of the modulus as function of the frequency at 30°C (Figure 5.37). Over the extended frequency range covered by the master curves, the modulus decreased of about 4% after 3 extrusion for HDPE09, while it increased of

about 5% and 13%, on average, for HDPE09-CB226 and HDPE09-CB1353 composites, respectively.

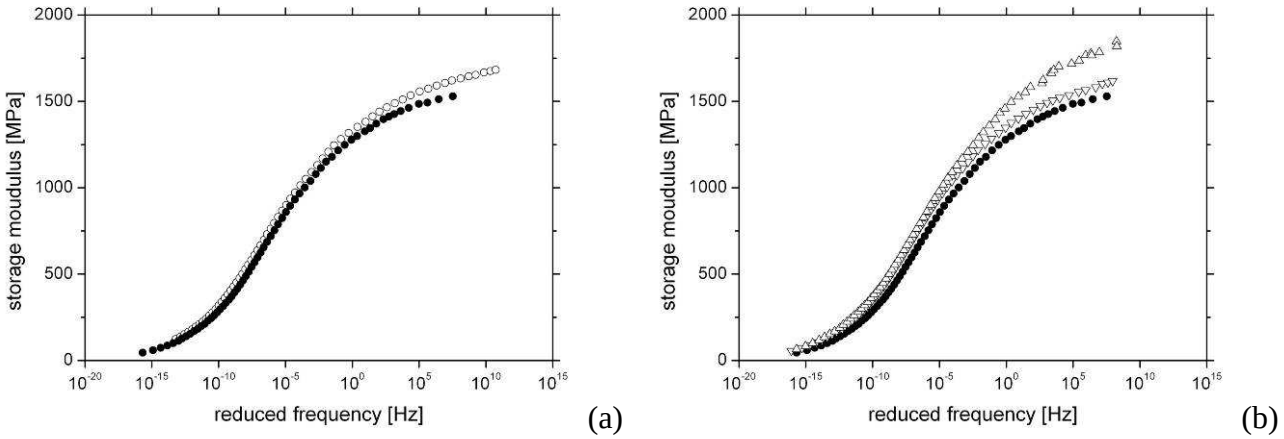

Figure 5.37. Master curves of the storage modulus referred at 30°C for HDPE09 extruded 1 (○) and 3 times (●) and of HDPE09-CB226 1 vol% (▽) and HDPE09-CB1353 1 vol% (△).

The shift factor (Figure 5.38) calculated to obtain the master curves as a function of the temperature was fitted with an Arrhenius law: in this way an activation energy at low and high temperature, i.e. under and over about 60°C where the α-relaxation taken place, was determined. Moreover Arrhenius equation was applied to calculate an activation energy E of the relaxation phenomena [143]: in particular the frequency f and the corresponding absolute temperature of the dissipative modulus peak T_{PEAK} was fitted with the following equation:

Equation 5.1

$$f = f_0 \exp\left(\frac{E}{R \cdot T_{PEAK}}\right)$$

where f_0 and E were fitting parameters. Table 5.7 contains the results of this analysis. From a general point of view the activation energy decreased after 3 extrusion for HDPE09, while increased for HDPE09-CB composites in comparison to HDPE09 after the same number of extrusions.

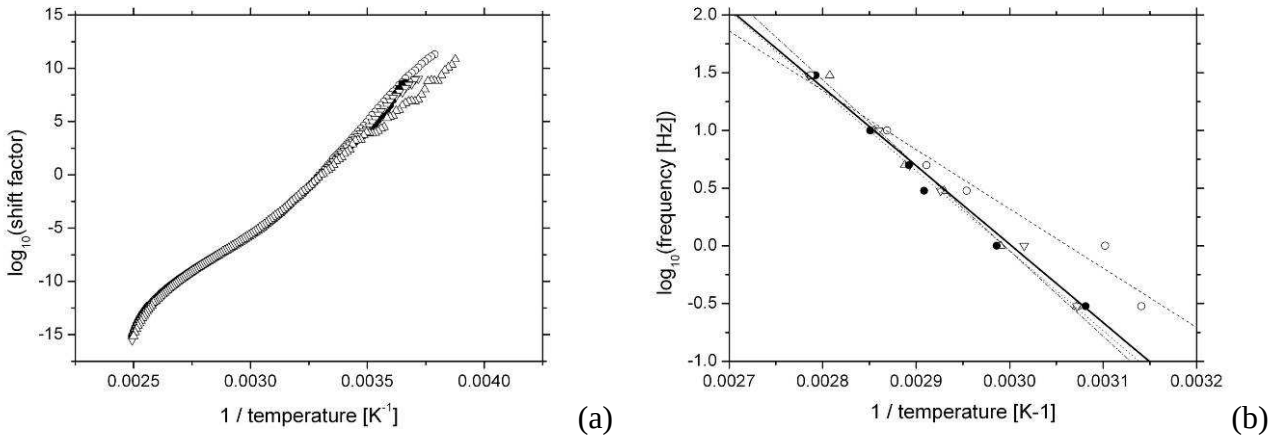

Figure 5.38. Shift factor as a function of the inverse of the absolute temperature (a) and Arrhenius plot (b) for HDPE09 extruded 1 (○) and 3 times (●) and of HDPE09-CB226 1 vol% (▽) and HDPE09-CB1353 1 vol% (△).

Table 5.7. Activation energy calculated from the shift factor at low (E_{low}) and high temperature (E_{high}) and from the Arrhenius plot (E_{Arr}).

Material	E_{low} [kJ/kmol]	E_{high} [kJ/kmol]	E_{Arr} [kJ/kmol]
HDPE09, 1x	460±3	269±1	142±6
HDPE09, 3x	372±5	259±1	130±5
HDPE09-CB226 1 vol%, 3x	424±7	264±1	133±7
HDPE09-CB1353 1 vol%, 3x	411±14	271±1	98±8

The master curve data were also used to calculate the retardation spectra over the full frequency range available: Figure 5.39 shows as the multiple extrusions induced a narrowing of the spectrum, while CB induced the shift of higher relaxation times.

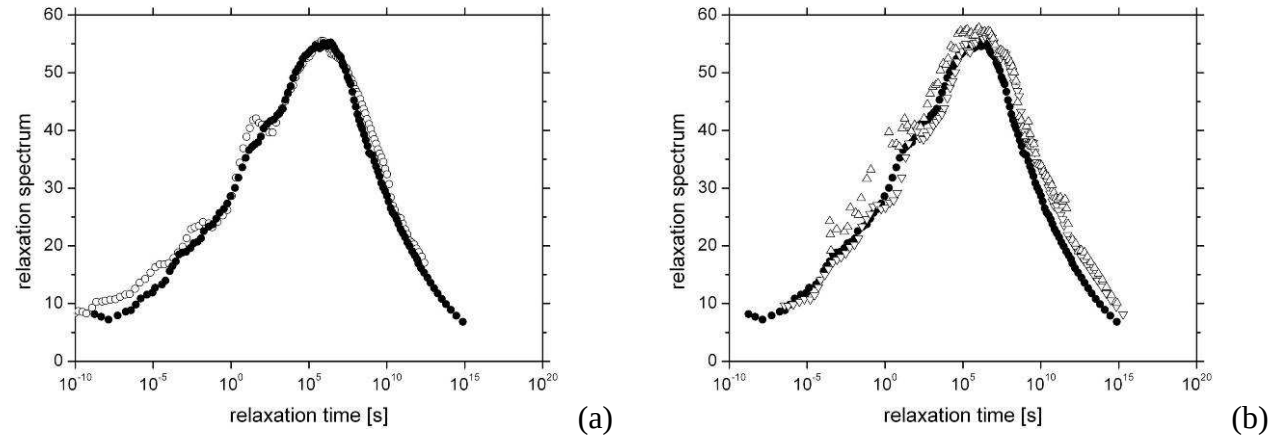

Figure 5.39. Relaxation spectra for HDPE09 extruded 1 (○) and 3 times (●) and of HDPE09-CB226 1 vol% (▽) and HDPE09-CB1353 1 vol% (△).

5.2 HDPE09-CB 0.5 vol% composites

5.2.1 Extruder

Table 5.8 shows the torque, the die pressure and the temperature of the melt during in the twin screw extruder during the production of HDPE09-CB composites. After the first extrusion the torque and the die pressure sharply decreased in presence of the filler: this effect became stronger as the specific surface area increased. As in the previous chapter (see 5.1.1) this behaviour was correlated with the lubricating effect of the CB at low filler content [139, 140].On the contrary the melt temperature did not change.

Table 5.8. Torque (M), die pressure (p) and melt temperature along the barrel (T_i) during the composites production with the twin screw extruder for HDPE09-CB composites at different numbers of extrusion (Extr.).

Material	Extr.	M [Nm]	P [bar]	T_1 [°C]	T_2 [°C]	T_3 [°C]
HDPE09	1	89.9	18.4	212.8	227.3	237.5
	2	79.5	18.5	212.4	226.6	236.7
HDPE09-CB105 0.5 vol%	1	56.5	12.6	211.6	226.9	237.1
	2	77.8	15.5	212.9	227.2	237.3
HDPE09-CB226 0.5 vol%	1	63.5	12.4	212.3	226.5	236.4
	2	73.8	16.4	211.9	226.1	235.9
HDPE09-CB802 0.5 vol%	1	64.5	15.2	212.6	226.2	236.2
	2	72.8	17.7	212.6	226.3	235.9
HDPE09-CB1353 0.5 vol%	1	69.0	14.9	212.7	226.4	236.7
	2	72.2	17.5	212.8	225.9	236.1

5.2.2 Tensile tests

Table 5.9 presents the results of the analyses of stress-strain curves of HDPE09-CB composites (elastic modulus, stress and strain at yield and break). The main effect was the drop of the ductility in presence of CB: the effect became stronger as specific surface area of CB increased, while it decreased from the first to the second extrusion. Moreover the filler induced generally an increase of about 1 MPa of the yielding stress.

Table 5.9. Mechanical properties of the HDPE09-CB composites: elastic modulus (E), stress and strain at yielding (σ_Y and ε_Y) and at break (σ_R and ε_R).

Material	Extr.	E [MPa]	σ_Y [MPa]	ε_Y [%]	σ_R [MPa]	ε_R [%]
HDPE09	1	946	30.4	11.3	31.4	1777
	2	912	29.5	12.0	30.2	1995
HDPE09-CB105 0.5 vol%	1	790	30.9	11.0	18.4	882
	2	751	30.9	11.3	21.6	967
HDPE09-CB226 0.5 vol%	1	822	31.5	11.0	24.1	1225
	2	750	30.8	11.3	28.6	1702
HDPE09-CB802 0.5 vol%	1	869	32.1	10.5	17.8	703
	2	746	31.1	11.3	21.1	1155
HDPE09-CB1353 0.5 vol%	1	879	31.8	10.5	16.6	162
	2	806	31.4	11.0	17.1	314

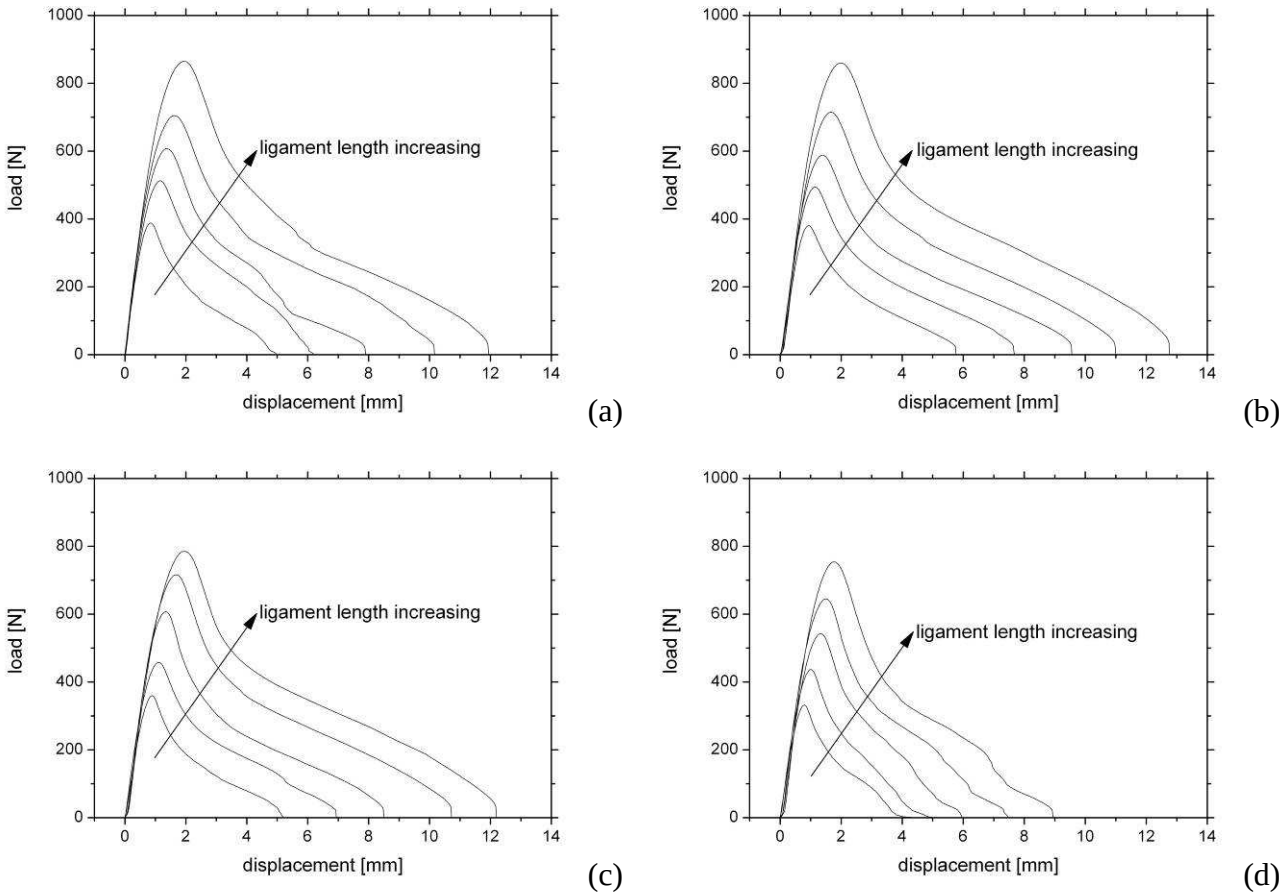

Figure 5.40. Examples of the load-displacement curves for HDPE09-CB105 0.5vol% extruded 2 (a), HDPE09-CB226 0.5vol% extruded 2 (b), HDPE09-CB802 0.5vol% extruded 2 (c) and HDPE09-CB1353 0.5vol% extruded 2 (d).

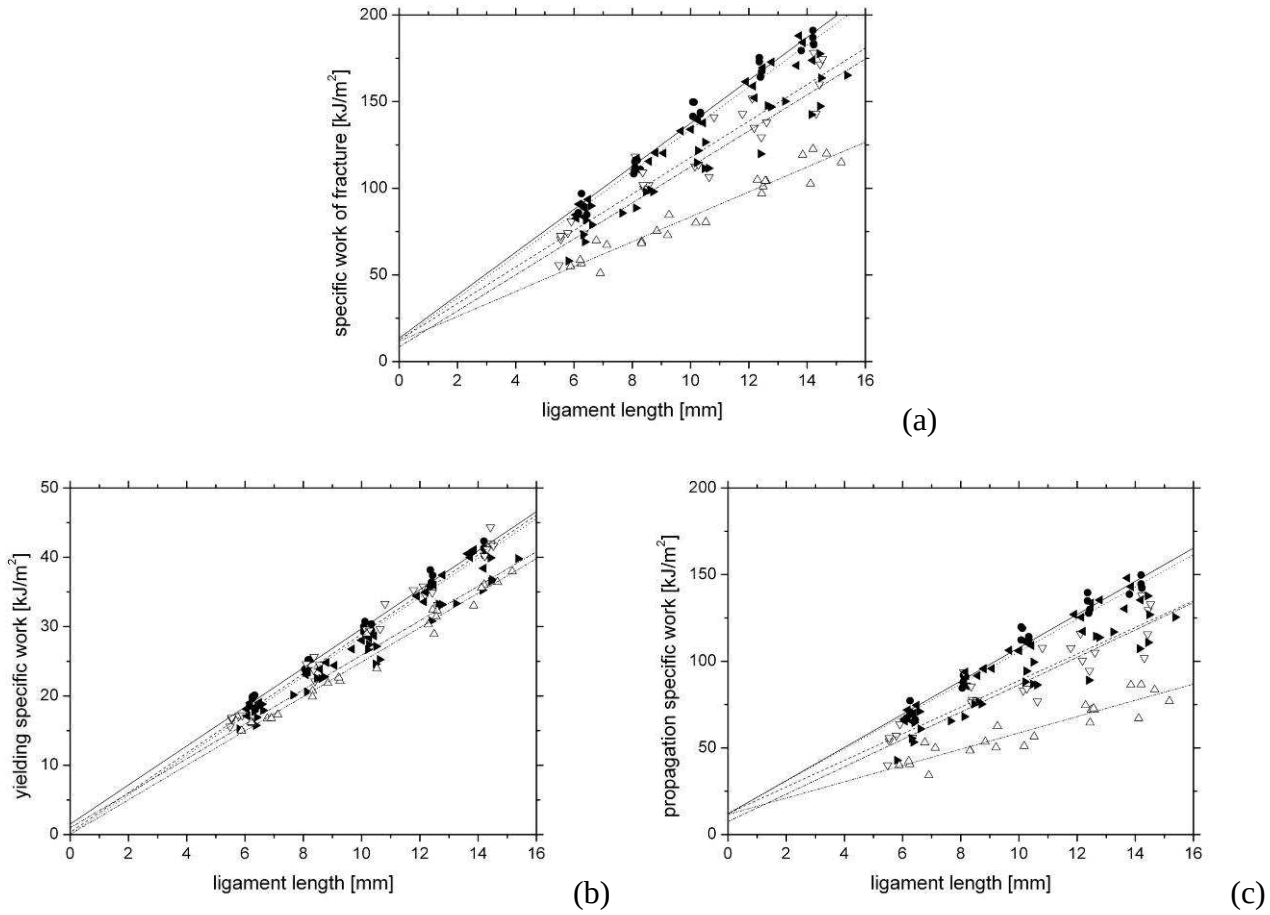

Figure 5.41. Specific work of fracture (a), initiation (b) and propagation (c) as a function of the ligament length for HDPE09 extruded 2 times (●), HDPE09-CB105 0.5vol% extruded 2 (▽), HDPE09-CB226 0.5vol% extruded 2 (◀), HDPE09-CB802 0.5vol% extruded 2 (▶) and HDPE09-CB1353 0.5vol% extruded 2 (△).

The results of the data analysis performed by the EWF approach are summarized in Table 5.10, Table 5.11 and Table 5.12. These results are plotted in Figure 5.42 as a function of the specific surface area of CB: unfortunately no clear trend was detectable because the experimental errors for the essential work of fracture and his components. Only the plastic work dissipation showed a clear trend with a peak at 226 m^2/g (i.e. for CB226): this trends was clearly evidenced by the work-ligament curves (Figure 5.41).

Figure 5.43 shows the micrographs acquired with a stereoscopic microscope of the fracture surface near the initial crack tip of the DENT specimens (all with an initial ligament length of 10 mm). Microcavitation phenomena were observed for all the materials, but with different intensity in terms of dimensions and density. In particular the microcavitation increased from HDPE09 to HDPE09-CB composites and as the specific surface area of CB increased.

Table 5.10. Essential work of fracture (w_e) and plastic work dissipation (βw_p).

Material	Extr.	w_e [kJ/m^2]		βw_p [MJ/m^3]		R^2
		mean	SD	mean	SD	
HDPE09	2	13.5	4.3	12.4	0.4	0.9772
HDPE09-CB105 0.5 vol%	2	12.4	7.3	10.5	0.7	0.9099
HDPE09-CB226 0.5 vol%	2	12.2	3.7	12.2	0.4	0.9801
HDPE09-CB802 0.5 vol%	2	8.5	6.1	10.4	0.6	0.9355
HDPE09-CB1353 0.5 vol%	2	11.7	4.4	7.2	0.4	0.9370

Table 5.11. Initiation terms of Essential work of fracture ($w_{e,ini}$) and plastic work dissipation ($\beta w_{p,ini}$).

Material	Extr.	$w_{e,ini}$ [kJ/m^2]		$\beta w_{p\ ini}$ [MJ/m^3]		R^2
		mean	SD	mean	SD	
HDPE09	2	1.5	0.6	2.8	0.1	0.9911
HDPE09-CB105 0.5 vol%	2	0.3	0.9	2.9	0.1	0.9815
HDPE09-CB226 0.5 vol%	2	0.0	0.7	2.8	0.1	0.9856
HDPE09-CB802 0.5 vol%	2	1.0	0.8	2.5	0.1	0.9795
HDPE09-CB1353 0.5 vol%	2	0.0	0.9	2.5	0.1	0.9755

Table 5.12. Propagation terms of Essential work of fracture ($w_{e,prop}$) and plastic work dissipation ($\beta w_{p,prop}$).

Material	Extr.	$w_{e,prop}$ [kJ/m^2]		$\beta w_{p,prop}$ [MJ/m^3]		R^2
		mean	SD	mean	SD	
HDPE09	2	12.0	4.1	9.6	0.4	0.9647
HDPE09-CB105 0.5 vol%	2	12.1	7.0	7.7	0.7	0.8525
HDPE09-CB226 0.5 vol%	2	12.2	3.5	9.3	0.3	0.9695
HDPE09-CB802 0.5 vol%	2	7.5	5.5	7.9	0.5	0.9103
HDPE09-CB1353 0.5 vol%	2	11.6	4.6	4.7	0.4	0.8538

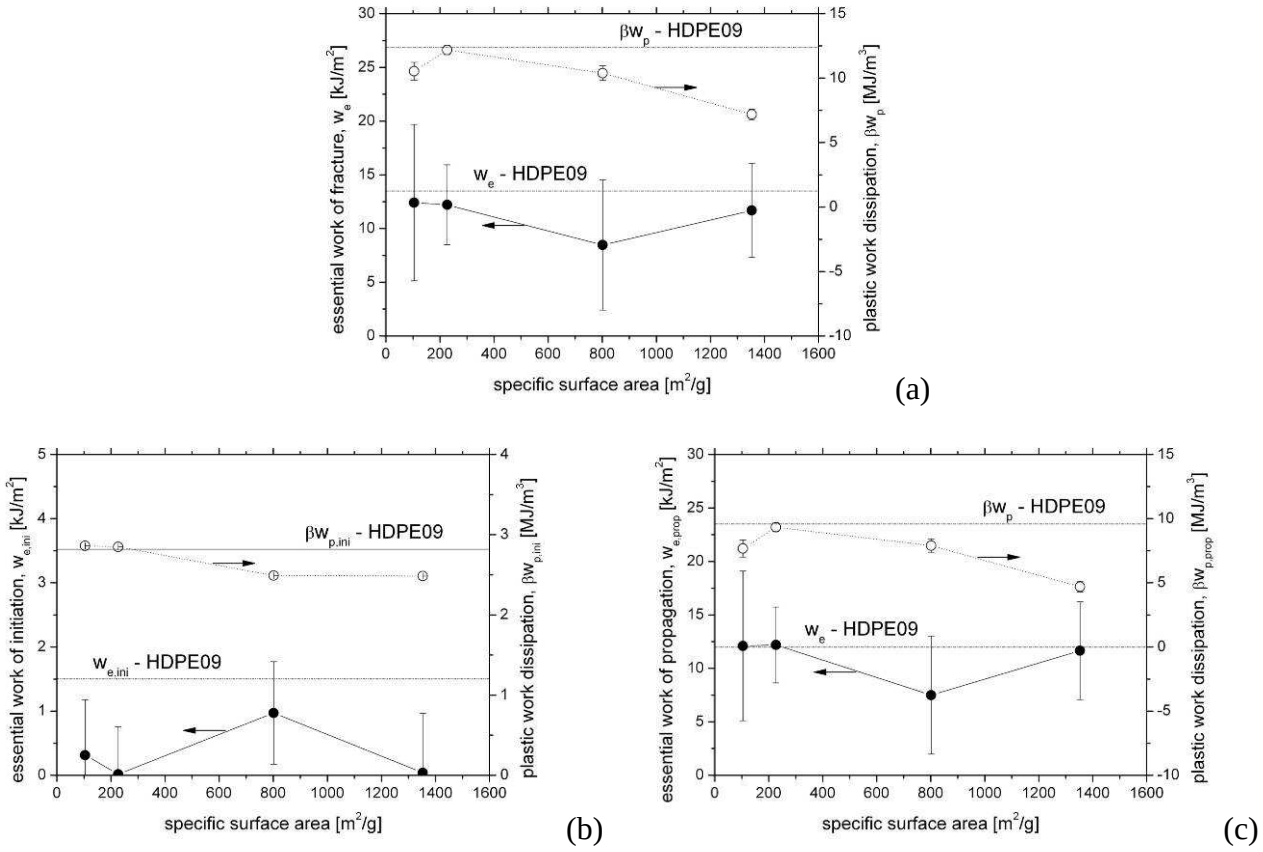

Figure 5.42. Essential work of fracture and plastic work dissipation (a) and initiation (b) and propagation (b) components as a function of the specific surface area of the CB.

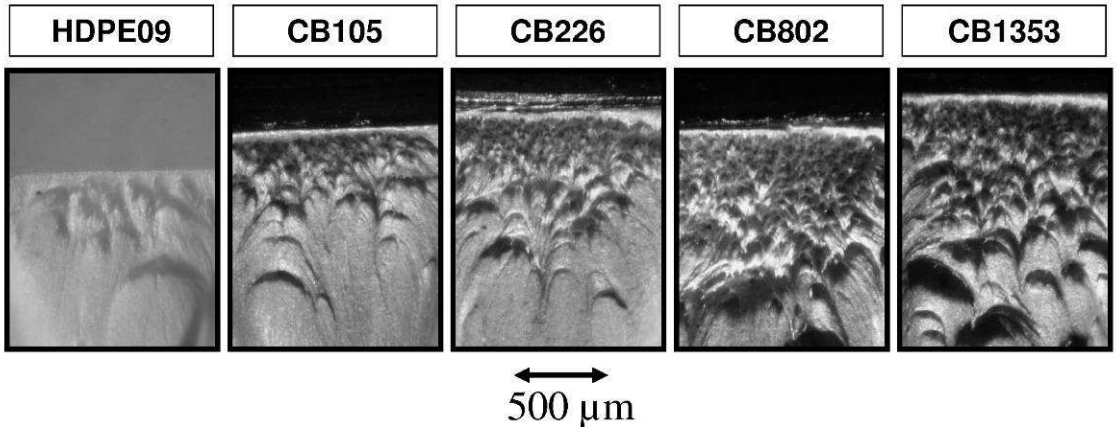

Figure 5.43. Micrographs acquired with a stereoscopic microscope of the fracture surface near the initial crack tip of the DENT specimens (all with an initial ligament length of 10 mm) for all the HDPE09-CB composites with 1 %vol filler.

6 Results on MWCNT (ARKEMA) based composites

This chapter is dedicated to the pMWCNT based composites: the paragraph 6.1 presents the results of characterization of the pMWCNT masterbatch. Afterwards the paragraph 0 deals with the HDPE09 and HDPE09-pMWCNT 1 vol% composites, while the paragraph 6.2 with the HDPE09-(MA-g-PE)-pMWCNT composites.

6.1 pMWCNT masterbatch

6.1.1 SEM

Figure 6.1 proposes some examples of the acquired micrographs of the masterbatch powders. The particles had a spherical shape with a diameter between 200 and 500 μm. Moreover MWCNTs were visible on the particle surface at high magnification inside some crack because the high filler content of this masterbatch (about 50 wt% as written in the datasheet).

6.1.2 TEM

Figure 6.2 shows some examples of TEM micrographs acquired for pMWCNT after TGA in nitrogen: the polymeric carrier was completely removed and the MWCNTs were perfectly visible. From a general point of view the MWCNTs had length from 200 nm to several microns and diameter between 10 and 20 nm. These data are in good agreement with the datasheet (see the chapter 3.1.2.3).

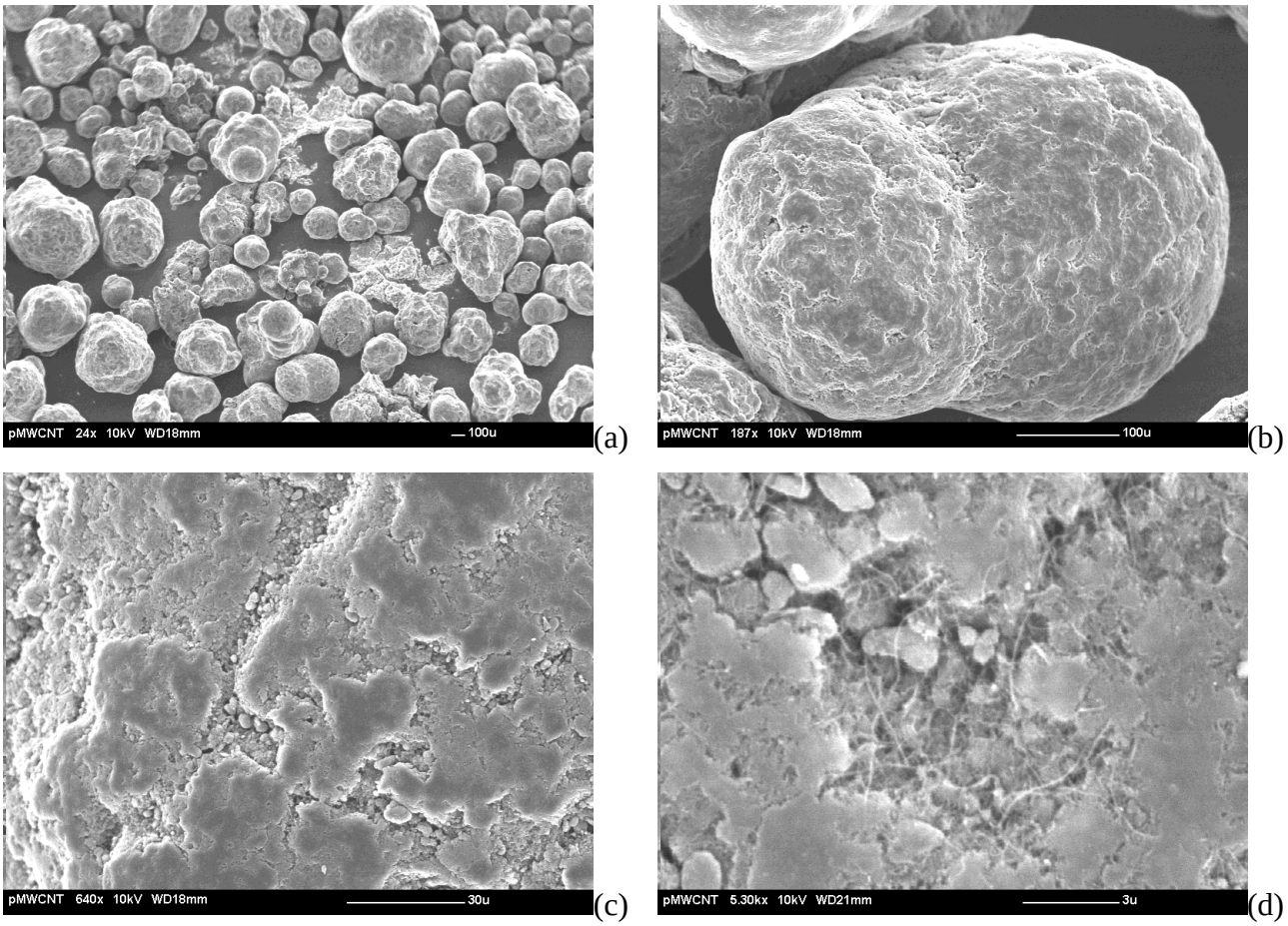

Figure 6.1. SEM micrographs of pMWCNT at different magnifications.

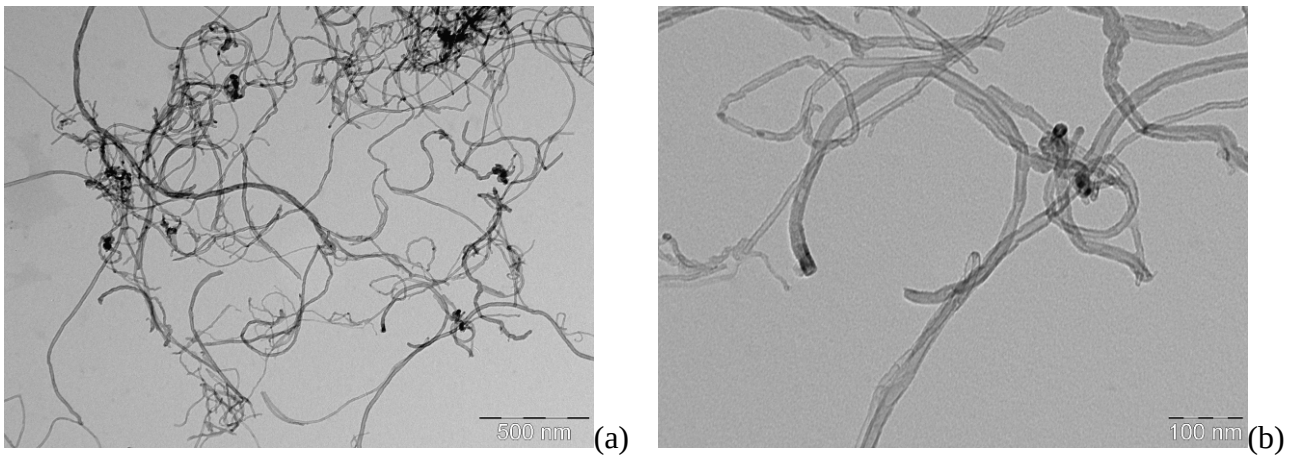

Figure 6.2. TEM micrographs of pMWCNT after TGA in nitrogen without the polymeric carrier.

6.1.3 TGA

Figure 6.3 shows the TGA curve and the corresponding DTGA curve: the main degradation phenomena taken place between 352°C and 455°C with two peaks at 387°C and 442°C in the

DTGA curve. These phenomena agree with literature because pMCWNT is a masterbatch containing 50 wt% of MWCNTs in a polyacrylic carrier: in fact it has been shown that polymers like polyacrylates degrade in several steps such as chain cleavage, end initiated depolymerisation and random scission in this temperature range [144-146]. Moreover it is advisable to observe that the residual fraction, i.e. 49.3wt%, is in good agreement with the value declared in the datasheet of the commercial product.

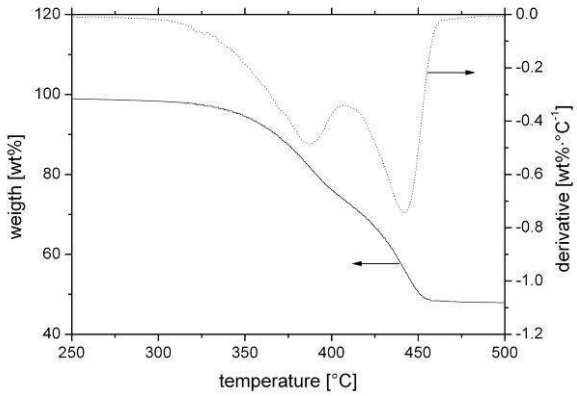

Figure 6.3. TGA curve and corresponding DTGA curve of pMWCNT.

6.1.4 DSC

Figure 6.4 shows the DSC curves of pMWCNT during the first heating stage and the second one: from -20 to 240°C the material did evidence no clear transition phenomenon. A glass transition was probably present at about 100°C, but the high filler content of the masterbatch reduced the intensity of the phenomenon.

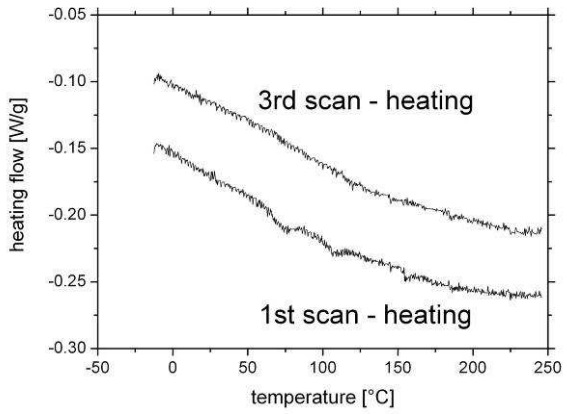

Figure 6.4. DSC curves of pMWCNT.

6.1.5 DMTA

The results of the DMTA tests are shown in Figure 6.5: the storage modulus decreased gradually from an initial plateau at about 2000 MPa and this was correlate with a relaxation phenomenon at 99.8°C as evidenced by a peak of the dissipative modulus. This data confirmed the not clear data obtained from DSC tests and it is in good agreement with the typical glass transition temperature of the polyacrylates.

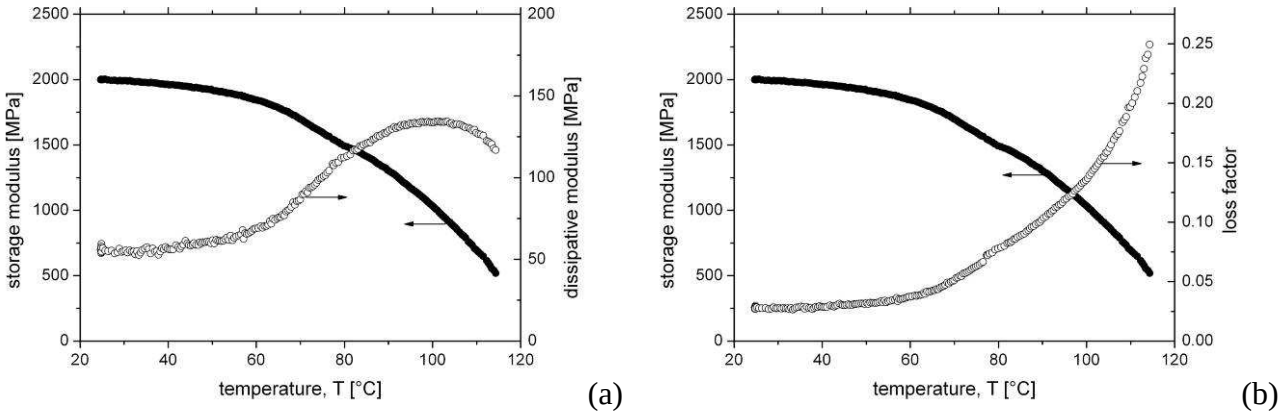

Figure 6.5. The storage modulus, the dissipative modulus and the loss factor as a function of the temperature for pMWCNT.

HDPE09-pMWCNT composites

6.1.6 Internal mixer

Figure 6.6 shows the torque and the temperature of the melt as a function of time during the composites production with the internal mixer. The curves evidenced as, when the mixture of polymer and filler powders was putted into the mixer chamber from room temperature to processing temperature, the torque (applied to maintain a constant speed rotation) increased until to reach a maximum that is related to the melting of the material. Similarly the temperature of the material inside the chamber decreased because the cold starting temperature of the material. After the melting of the material the torque decreased to a value related with the viscosity: similarly the temperature of the melt reached a plateau. The torque/temperature plateaus (which are linked) shifted up when the speed rotation was increased from 20 rpm to 100 rpm.

Table 6.1 contains the most significant data of the production process and evidences as the torque and temperature curves were very similar. The more interesting difference was the torque when the rotation speed was 100 rpm: in this case the torque increased from 13.7 Nm for HDPE09 to 15.4 Nm (+12%) for the HDPE09-pMWCNT composites.

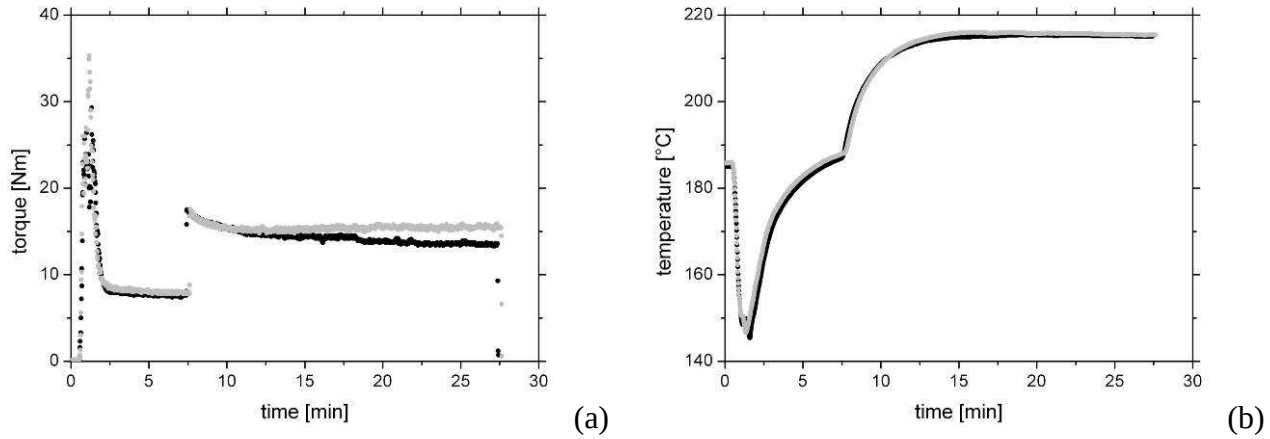

Figure 6.6. The torque (a) and the temperature of the melt (b) as a function of time during the composites production: HDPE09 (●) and HDPE09-pMWCNT 1vol% (●).

Table 6.1. Torque (M) and melt temperature (T) during the composites production in the internal mixer: the maximum/minimum value (MAX/MIN), at 20 rpm and at 100 rpm.

Material	M_{MAX} [Nm]	M_{20rpm} [Nm]	M_{100rpm} [Nm]	T_{MIN} [°C]	T_{20rpm} [°C]	T_{100rpm} [°C]
HDPE	29.3	7.6	13.7	145.4	186.9	215.4
HDPE-pMWCNT 1vol%	35.3	8.0	15.4	146.6	188.1	216.0

6.1.7 OM

Figure 6.7 shows an example of OM micrographs acquire for HDPE-pMWCNT composites: even if a relatively homogeneous dispersion was present, agglomerates of about 10 μm still remained in the composites.

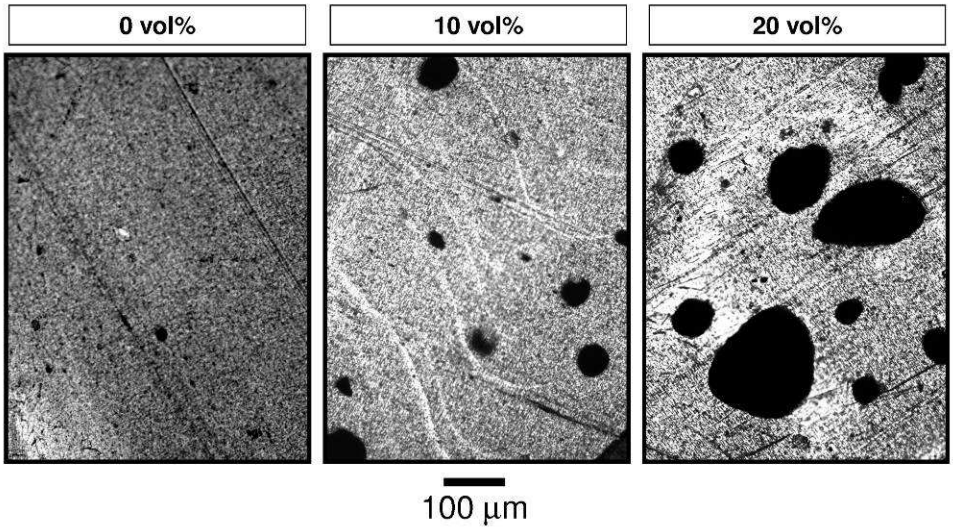

Figure 6.7. OM micrographs of HDPE09-(MA-g-PE)-pMWCNT composites with MWCNT content of 1 vol% at different MA-g-PE content.

6.1.8 SEM

The SEM observations had the main to assess the filler and masterbatch dispersion in HDPE09 matrix. For this reason samples of HDPE09 and HDPE09-pMWCNT 1 vol% were fractured in liquid nitrogen in order to have a brittle fracture with smooth surfaces. Figure 6.8 proposes some examples of the acquired micrographs at low and high magnifications.

The most significant result is the absence of evident agglomeration phenomena of MWNCTs and of the masterbatch: the irregularity of the fracture surface were very similar in both the case at low magnification. Moreover the surface evidenced ductile fracture phenomena at high magnification: Brough et al. [147] found that HDPE maintains a locally ductile behaviour even in the case of cryofracture because the thermal dissipation of the mechanical energy during the fracture process that causes locally the melting of the polymer. Nevertheless the morphology of the fracture surface changed from HDPE09 to HDPE09-pMWCNT 1 vol%: this fact is probably related to different mechanical properties of the materials.

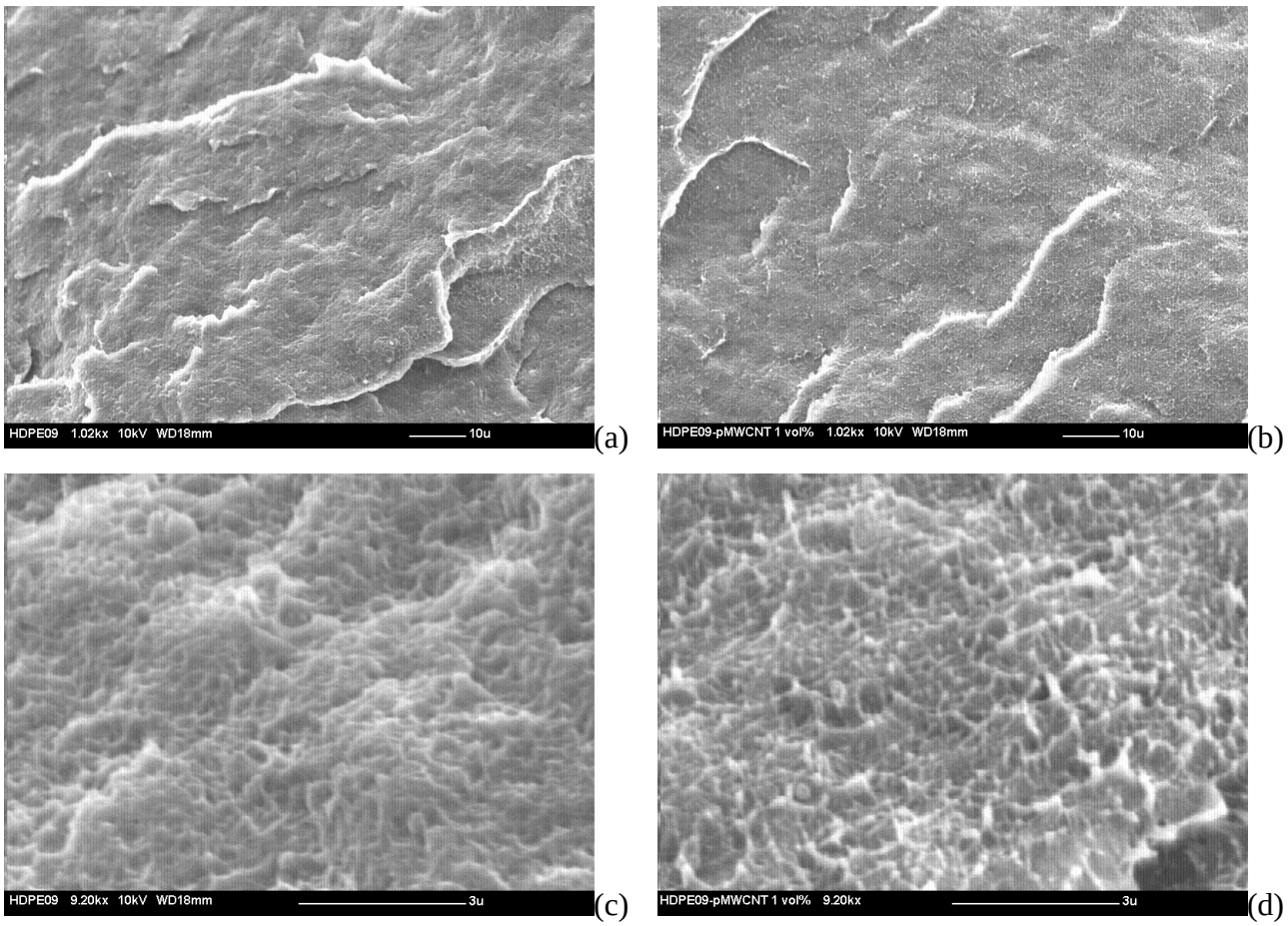

Figure 6.8. SEM micrographs at low and high magnifications of HDPE09 (a, c) and HDPE09-pMWCNT 1 vol% (b, d).

6.1.9 DSC

The DSC curves are showed in Figure 6.9: in the first case the crystallization during the cooling stage and in the second one the melting during the heating stage. In addition Table 6.2 contains the data elaborated from these DSC curves. In both the case a translation of the phenomenon to higher temperature was evident: the onset of the crystallization moved from 122.3°C for the base matrix to 123.5°C for the composites and the endset of the melting from 143.5°C to 145.5°C. Moreover the shape of the curves changed and the crystallinity increased of about 2%, while the peak temperature of melting/crystallization remained almost unchanged.

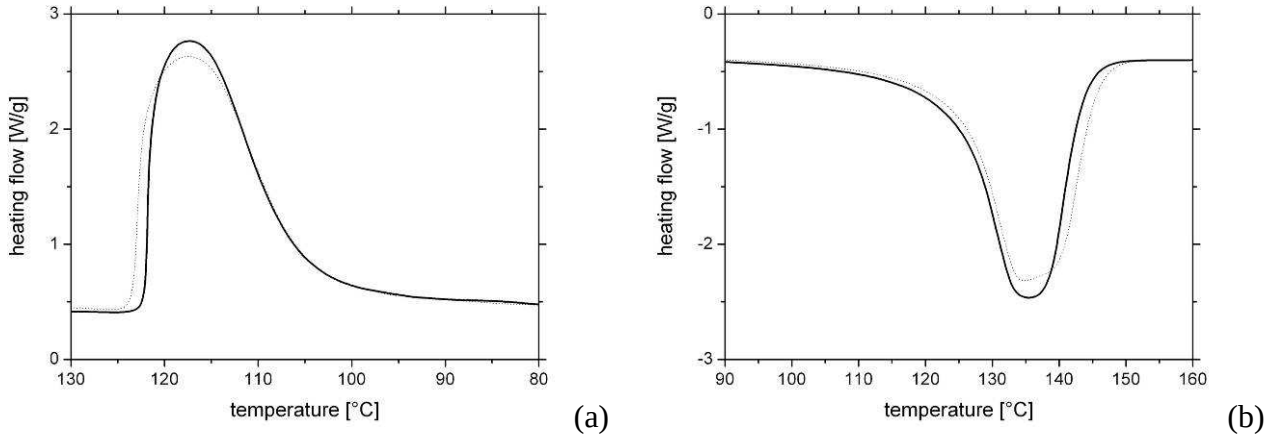

Figure 6.9. DSC curves of the crystallization phenomena during the cooling stage (a) and the heating stage (b): HDPE09 (—) and HDPE09-pMWCNT 1vol% (···).

Table 6.2. Results of the analysis of the DSC curves: crystallinity (χ), melting (T_m) and crystallization (T_c) temperature, onset (T_{ON}) and endset (T_{END}) temperatures.

Material	Crystallization – Cooling (2nd scan)				Melting – Heating (3rd scan)			
	χ [wt%]	T_c [°C]	T_{ON} [°C]	T_{END} [°C]	χ [wt%]	T_m [°C]	T_{ON} [°C]	T_{END} [°C]
HDPE09	70.2	117.2	122.3	105.5	70.4	135.6	123.9	143.5
HDPE09-pMWCNT 1vol%	72.2	117.4	123.5	104.7	72.0	134.8	124.6	145.5

6.1.10 TGA

Figure 6.10 shows the TGA curves and the DTGA curves of the tested materials in temperature range where the degradation phenomena were more intense: Table 6.3 summarizes the characteristic parameters of these curves. The data evidenced a slightly increased stability of the HDPE09-pMWCNT composites in comparison to HDPE09 matrix. The main difference was related to the peak intensity of the DTGA, that is reduced by 15%, and to the translation of the end of the

degradation of about 4°C. Moreover it is advisable to observe that the residual fraction of HDPE09-pMWCNT composites is in good agreement with the value expected for a filler fraction of 1 vol%.

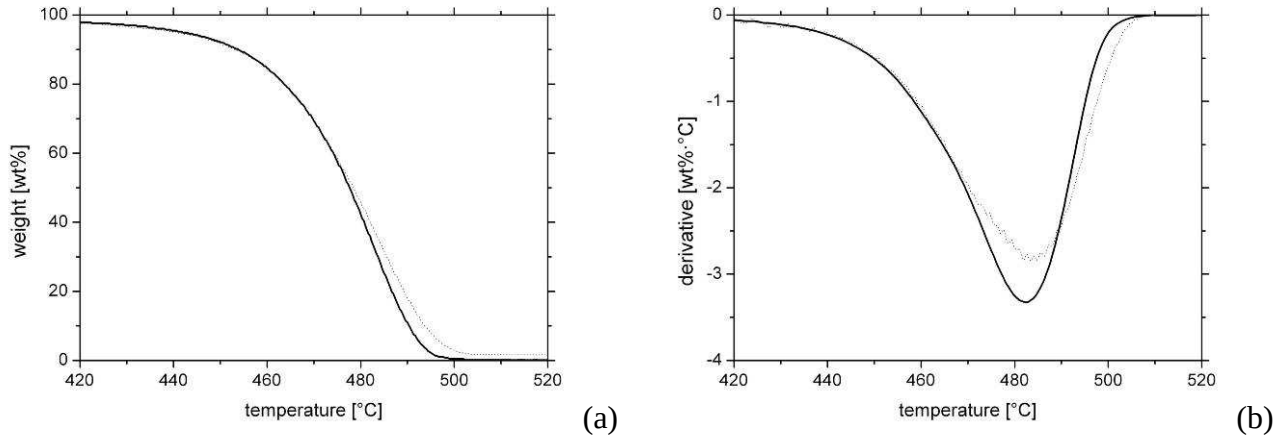

Figure 6.10. TGA and DTGA curves of HDPE09 (—) and HDPE09-pMWCNT 1vol% (···).

Table 6.3. The results of the analysis of the TGA and DTGA curves: onset (T_{ON}), peak (T_{PEAK}) and endset (T_{END}) temperatures of the degradation and the residual fraction.

Material	T_{ON} [°C]	T_{PEAK} [°C]	T_{END} [°C]	Residual [wt%]
HDPE09	458.6	482.7	493.9	0.0
HDPE09-pMWCNT 1vol%	455.2	483.7	496.4	1.79

6.1.11 Tensile tests

The most evident effect of the filler addition on the mechanical properties (Table 6.4) was the loss of most part of the plastic deformation of HDPE09: strain at break dropped from 1200% to 20%. On the other hand the elastic modulus increased by 20% (from 740 to 890 MPa) and the strength by 9% (from 27.8 to 30.3 MPa). This fact is depicted in Figure 6.11 where some examples of the stress-strain curves of HDPE09 and HDPE09-pMWCNT composites are presented.

Table 6.4. Mechanical properties of the HDPE09-pMWCNT composites: elastic modulus (E), stress and strain at yielding (σ_Y and ε_Y) and at break (σ_R and ε_R).

Material	E [MPa]	σ_Y [MPa]	ε_Y [%]	σ_R [MPa]	ε_R [%]
HDPE09	741	27.8	10.6	25.6	1200
HDPE09-pMWCNT 1vol%	887	30.3	10.7	25.5	20.0

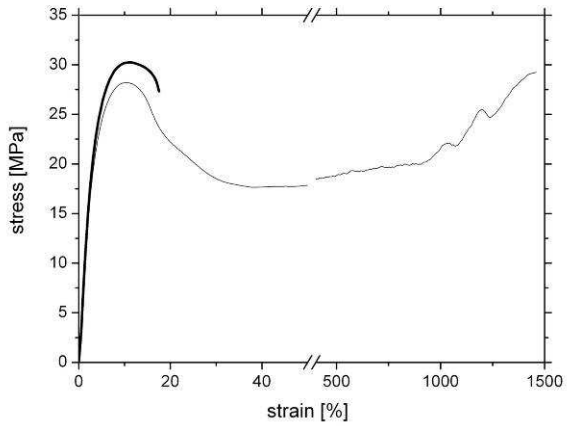

Figure 6.11. Examples of stress-strain curves of HDPE09 (—) and HDPE09-pMWCNT 1vol% (···).

6.1.12 DMTA

The results of the DMTA tests are showed in Figure 6.12, Figure 6.13 and Figure 6.14. The materials presented two sharp drops of the storage modulus that corresponded to two peaks in terms of dissipative modulus and loss factor. In particular the first phenomenon at low temperature was related to glass transition (γ-relaxation) that is -102.4°C for HDPE09 and -100.9°C for HDPE09-pMWCNT composites. On the other hand the phenomenon at higher temperatures is the α-relaxation: in this case the peak temperature passed from 53.9°C for HDPE09 to 55.5°C for the HDPE09-pMWCNT composites. For both the relaxations the difference was limited to an increase of 2°C.

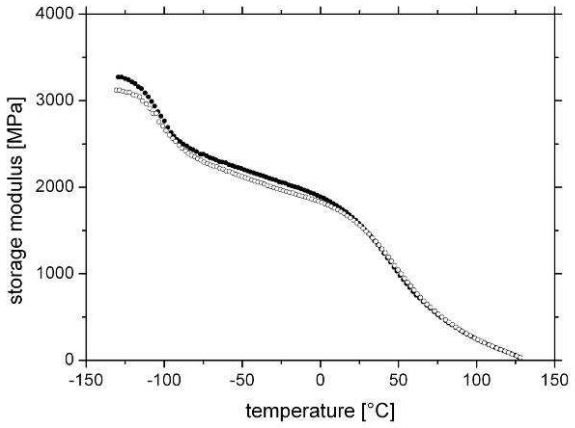

Figure 6.12. The storage modulus as a function of the temperature for HDPE09 (●) and HDPE09-pMWCNT 1vol% (○).

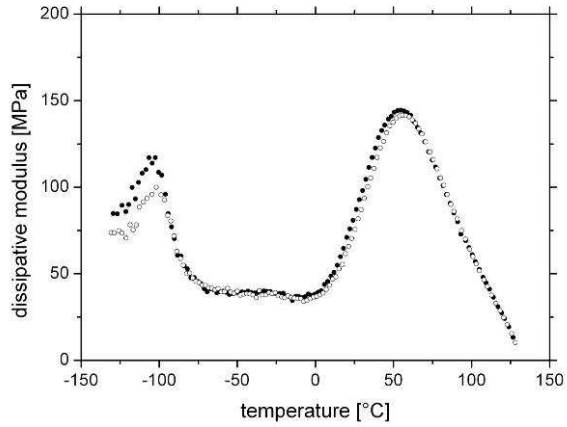

Figure 6.13. The dissipative modulus as a function of the temperature for HDPE09 (●) and HDPE09-pMWCNT 1vol% (○).

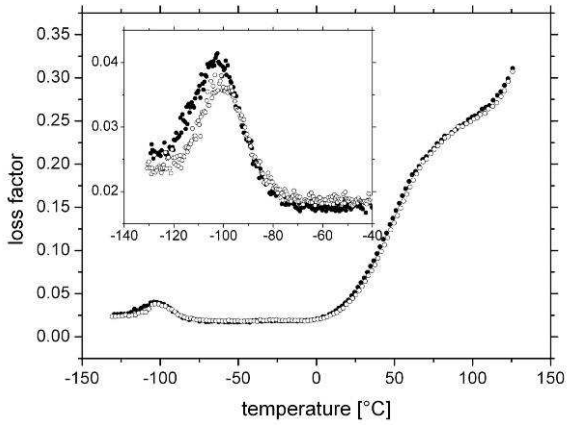

Figure 6.14. The loss factor as a function of the temperature for HDPE09 (●) and HDPE09-pMWCNT 1vol% (○). The inset shows a detail of the curves at low temperatures.

6.1.13 Tensile creep tests

From a general point of view MWCNTs resulted to substantially increase the creep resistance of the HDPE matrix. This effect was detectable in the linear viscoelastic region (i.e. at low stresses or temperatures), and it became more and more evident in the non-linear viscoelastic or viscoplastic region (i.e. at high stresses or temperatures). Examples of this behaviour are proposed in Figure 6.15 and in Figure 6.16 where compliance and compliance rate of HDPE09 and HDPE09-pMWCNT 1vol% at 30°C and 75°C are showed.

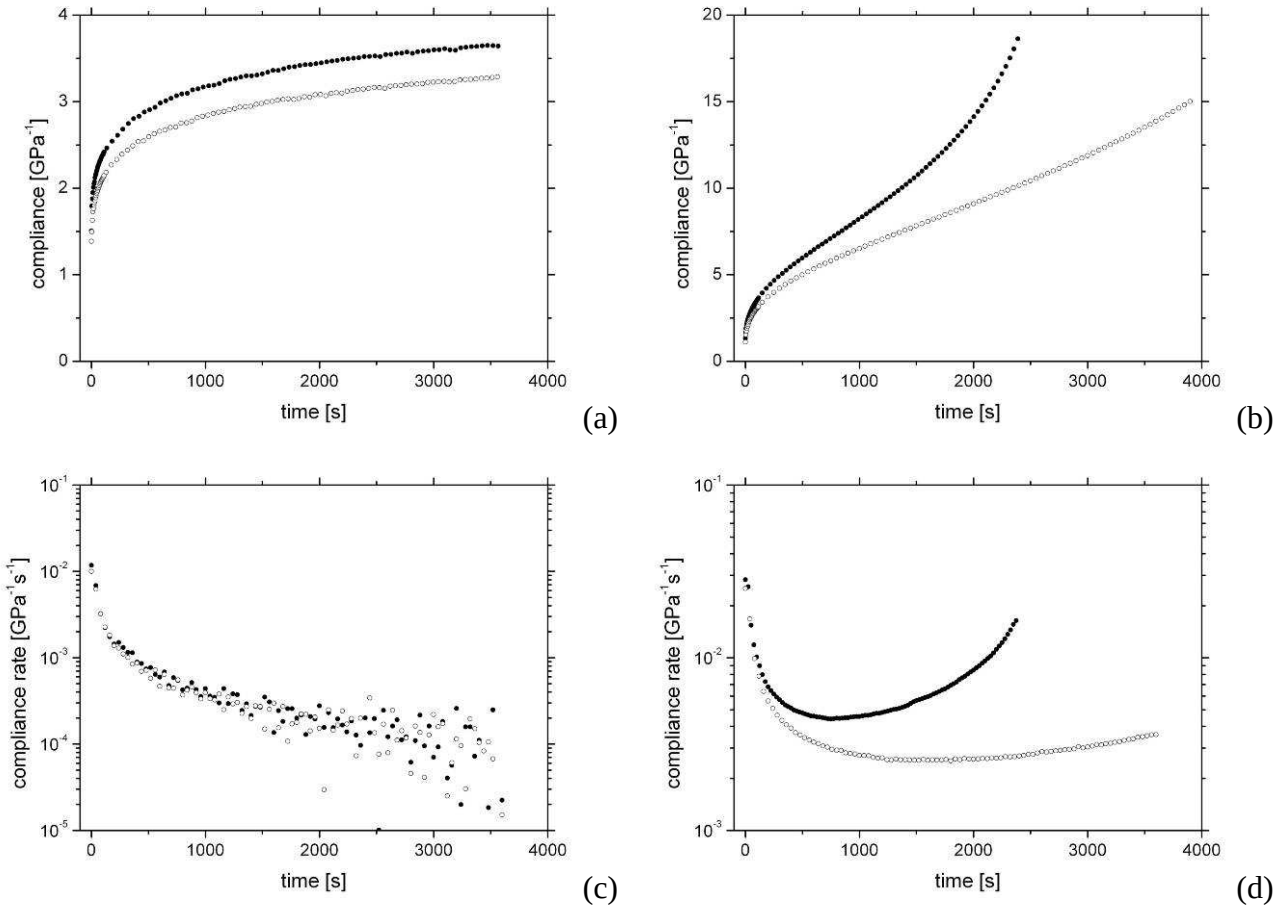

Figure 6.15. Creep compliance at 30°C (a, c) and creep compliance rate (b, d) as a function of time at 30°C with a stress of 3 MPa (a, b) and 15 MPa (c, d) for HDPE09 (●) and HDPE09-pMWCNT 1vol% (○).

The isochronous stress-strain curves at 30°C and 75°C for a creep time of 2000 are showed in Figure 6.17. It is evident as the increased temperatures reduced the creep resistance of both the tested materials and mainly as the creep resistance increased for HDPE09-pMWCNT composites in comparison to HDPE09 especially when the applied stress increased.

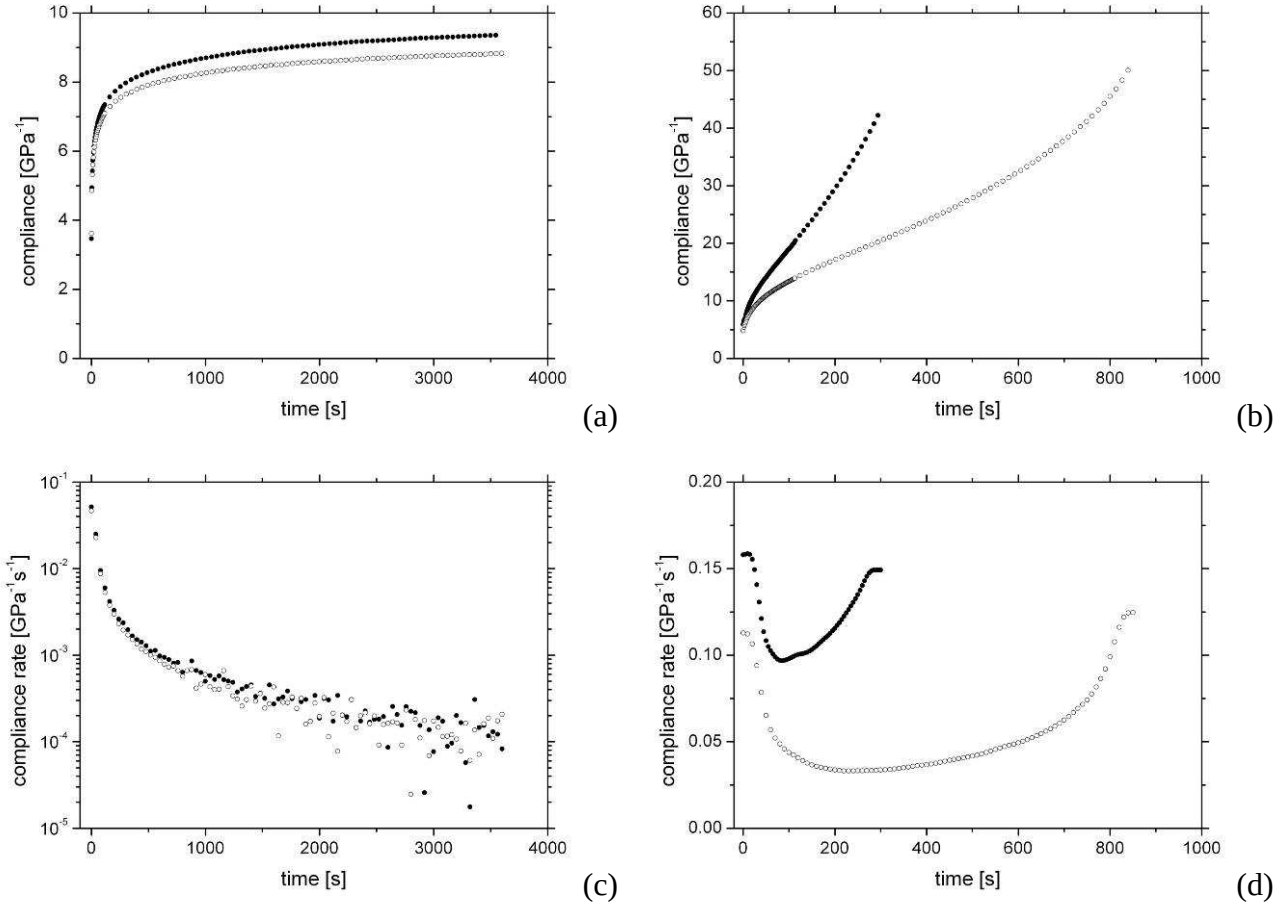

Figure 6.16. Creep compliance at 75°C (a, c) and creep compliance rate (b, d) as a function of time at 30°C with a stress of 3 MPa (a, b) and 15 MPa (c, d) for HDPE09 (●) and HDPE09-pMWCNT 1vol% (○).

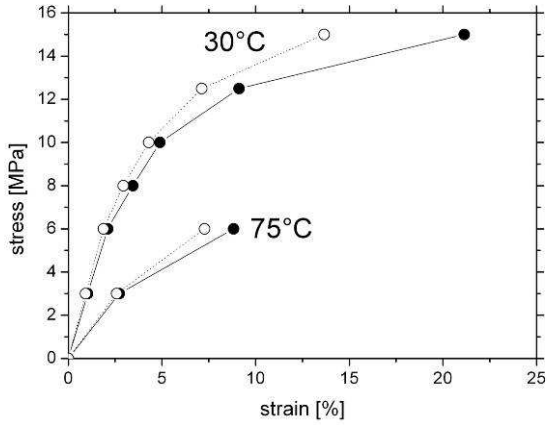

Figure 6.17. The isochronous stress-strain curves for HDPE (●) and HDPE-pMWCNT 1vol% (○) at 30°C and 75°C for a creep time of 2000 s.

Figure 6.18 proposes the isochronous creep compliance curves at 2000 s and the related elastic and viscoelastic components. While the elastic components are the same for HDPE09 and for HDPE09-pMWCNT 1vol%, the viscoelastic components are sharply different. In particular the viscoelastic

components of the compliance is reduced by about 10% for HDPE09-pMWCNT composites in comparison to HDPE09.

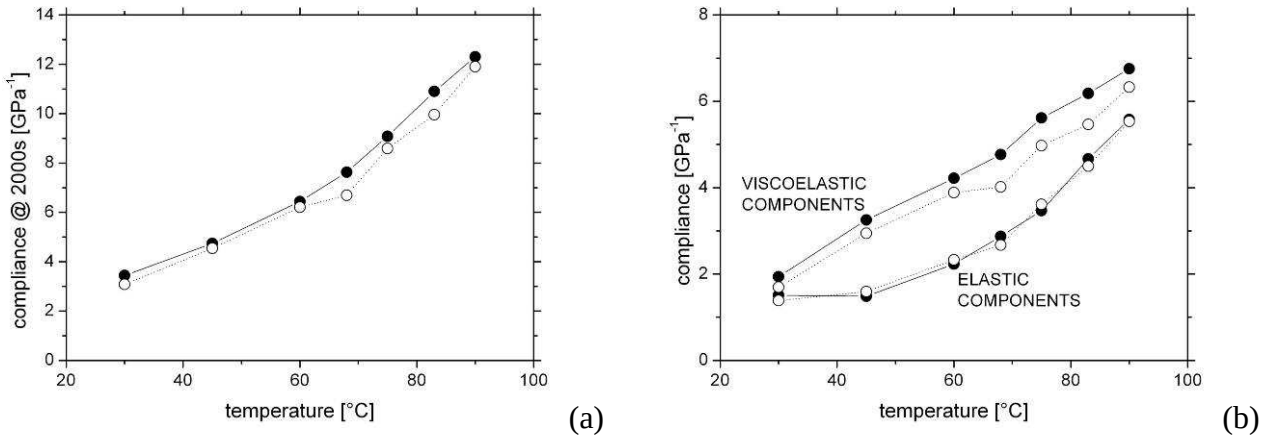

Figure 6.18. Total isochronous compliance (a) and elastic and viscoelastic components of the isochronous compliance at 2,000 s for HDPE09 (–●–) and HDPE09-pMWCNT 1vol% (··○··).

On the basis of a time-temperature superposition principle, short term creep performed in the linear-viscoelastic region (with an applied stress of 3 MPa) allowed to obtain creep compliance master curves for long term creep (Figure 6.19Figure 6.19.). Over the extended time period covered by the master curves, the creep compliance is reduced by about 12%, on average.

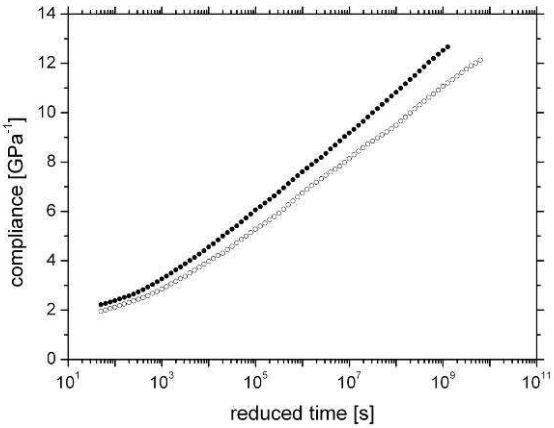

Figure 6.19. Creep compliance master curves obtained at 3 MPa and referred at 30°C for HDPE09 (●) and HDPE09-pMWCNT 1 vol% (○).

Moreover the shift factor (Figure 6.20) calculated from the short term creep test to obtain the master curves as a function of the temperature was fitted with an Arrhenius law. In this way an activation energy for the relaxation phenomenon was determined: the values increased from (196±16) kJ/kmol for HDPE09 to (213±18) kJ/kmol for HDPE09-pMWCNT composites.

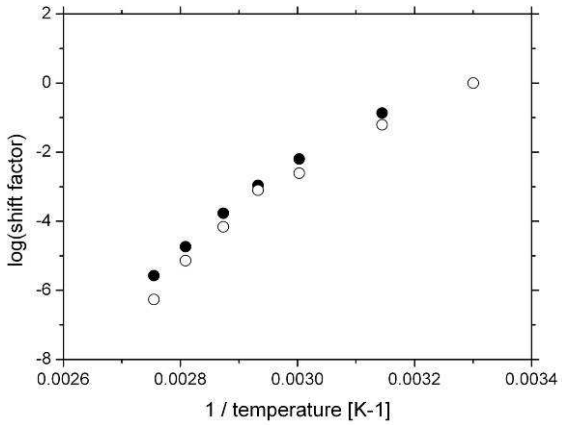

Figure 6.20. Shift factor as a function of the inverse of the absolute temperature for HDPE09 (●) and HDPE09-pMWCNT 1 vol% (○).

The master curve data were used to calculate the creep compliance rate over the full time range. Figure 6.21 shows as HDPE09 and HDPE09-pMWCNT composites have practically the same behaviour: the results are in agreement with the results at low stresses in linear viscoelastic region (as for example in Figure 6.15 and Figure 6.16). Moreover it was possible to fit the data with a power law which has the expression $dD/dt = 0.32 \cdot t^{-0.96}$ where the compliance is expressed in GPa^{-1} and the time in s.

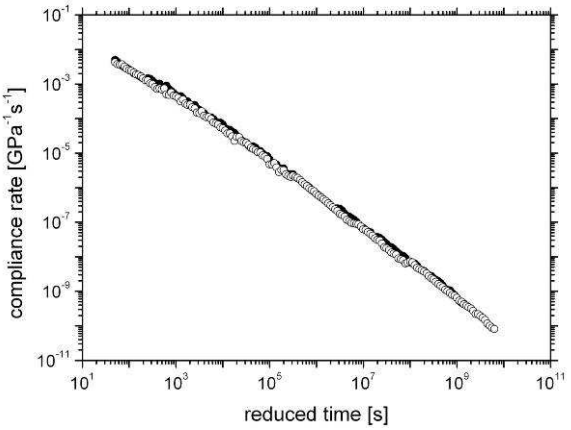

Figure 6.21. Creep compliance rate as a function of time in a log-log scale for HDPE09 (●) and HDPE09-pMWCNT 1 vol% (○).

The master curve data were also used to calculate the retardation spectra over the full time range available: Figure 6.22 shows as the MWCNT addition shifts the spectrum of HDPE09 to higher retardation times.

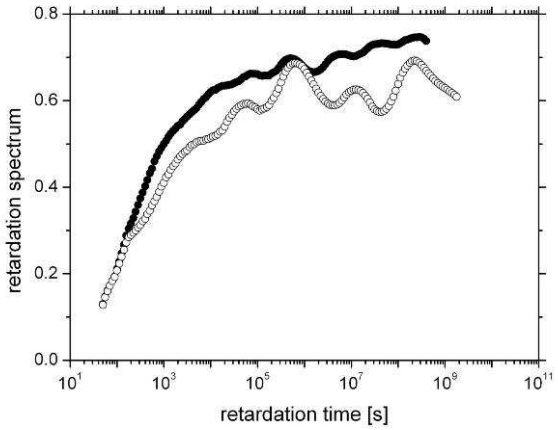

Figure 6.22. Retardation spectra as a function of the retardation time for HDPE09 (●) and HDPE09-pMWCNT 1 vol% (○).

6.2 HDPE09-(MA-g-PE)-pMWCNT composites

6.2.1 Internal mixer

Figure 6.23 shows the torque and the temperature of the melt as a function of the MA-g-PE content for the HDPE09-(MA-g-PE) blends and for the HDPE09-(MA-g-PE)-pMWCNT composites. While no difference was present in the case of the melt temperatures, the torque at 20 and 100 rpm increased of 5-10% for the HDPE09-(MA-g-PE)-pMWCNT composites in comparison to the corresponding matrices, i.e. the HDPE09-(MA-g-PE) blends. Moreover the torque values were only slightly affected by the MA-g-PE content.

It's convenient to observe that, even if the maximum torque values are reported, only qualitative evaluations are possible because the peak torque is very sensitive on the way in which the chamber of the internal mixer is filled.

6.2.2 OM

Figure 6.7 shows examples of OM micrographs acquire for HDPE-(MA-g-PE)-pMWCNT composites to evaluate the MWCNT dispersion in relation to MA-g-PE content. The relatively homogeneous dispersion of the composites without MA-g-PE, even if agglomerates of about 10 μm still remained, worsened as MA-g-PE content increased with bigger and bigger black agglomerates (over 100 μm) related to MWCNTs.

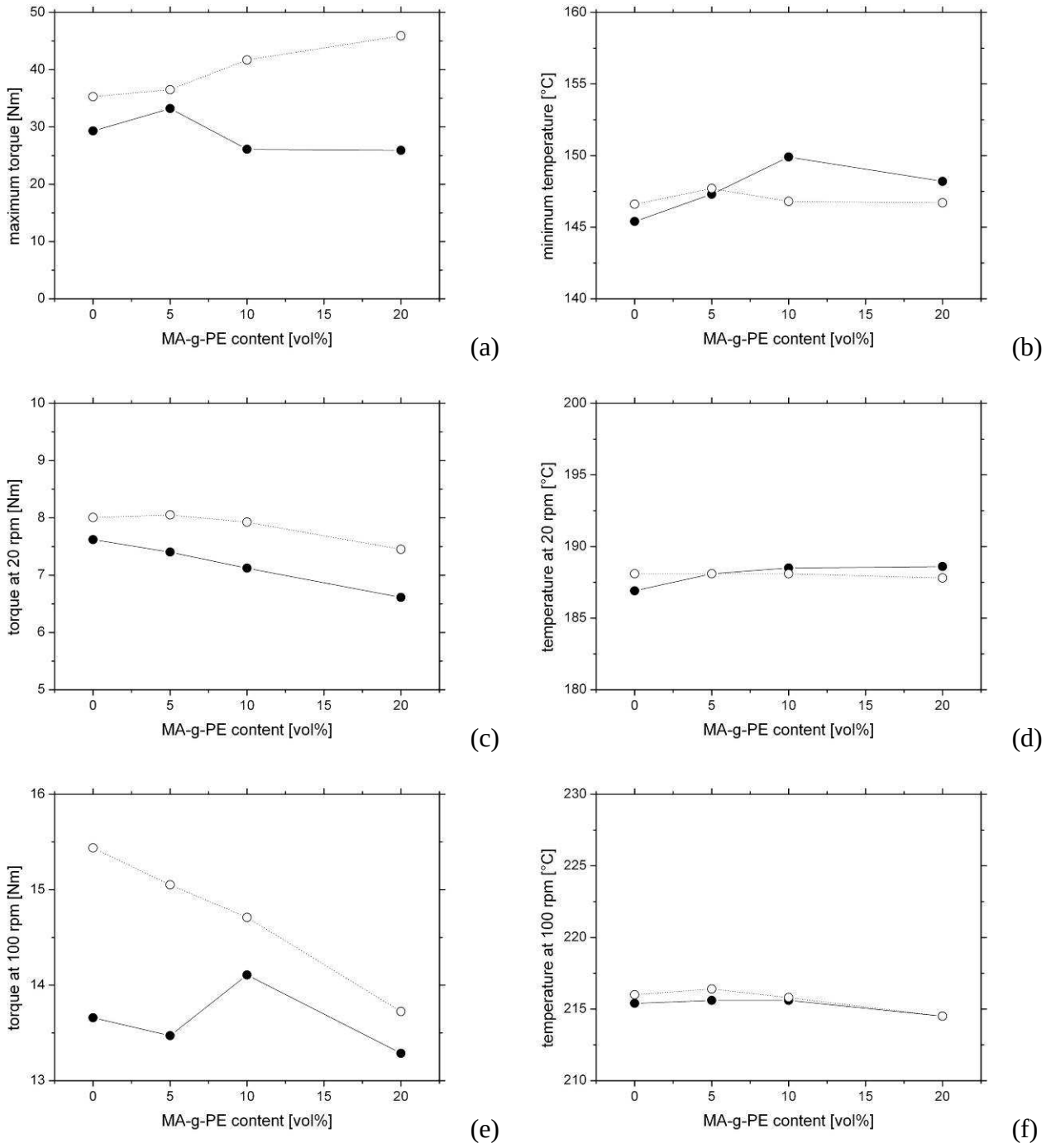

Figure 6.23. Torque (M) and melt temperature (T) during the composites production in the internal mixer: the maximum (a) and minimum (b), at 20 rpm (c, d) and at 100 rpm (e, f) for the HDPE09-(MA-g-PE) blends and the HDPE09-(MA-g-PE)-pMWCNT composites as a function of the MA-g-PE content.

6.2.3 DSC

Figure 6.24 presents the results of the DSC analyses by comparing the effect of the MA-g-PE content on the HDPE09-(MA-g-PE) blends and on the HDPE09-(MA-g-PE)-pMWCNT composites. While the crystallinity and the melting temperature did evidence no change, the crystallization temperature increased of 2°C with MA-g-PE content over 10 vol%. Moreover the

most interesting effect of the MWCNTs was related to the onset temperature of the crystallization that moved up of about 1°C for all the HDPE09-(MA-g-PE)-pMWCNT composites in comparison the corresponding HDPE09-(MA-g-PE) base matrix.

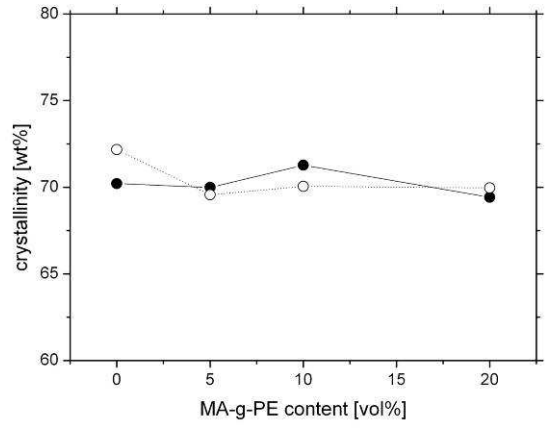

(a)

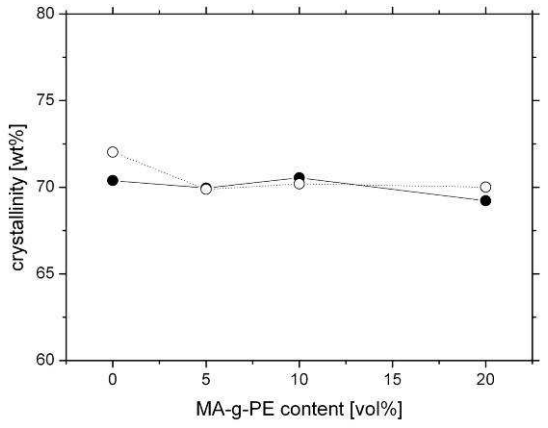

(b)

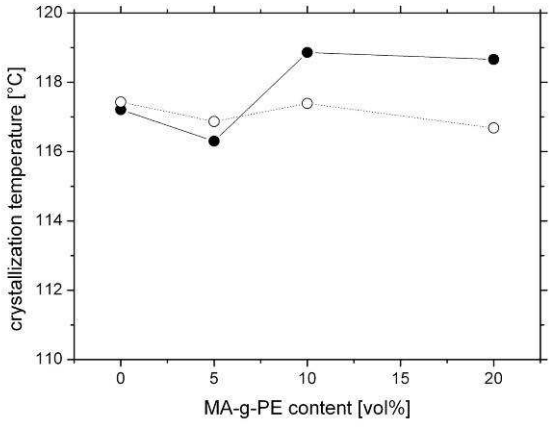

(c)

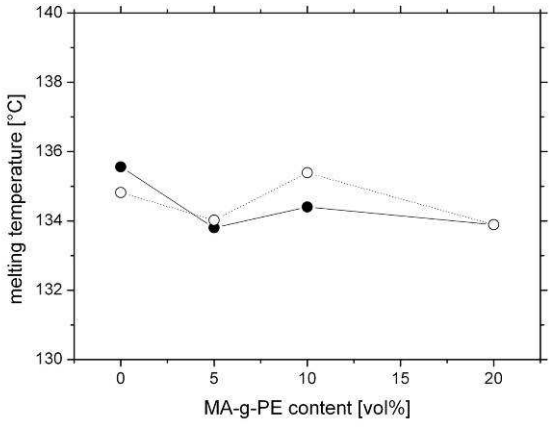

(d)

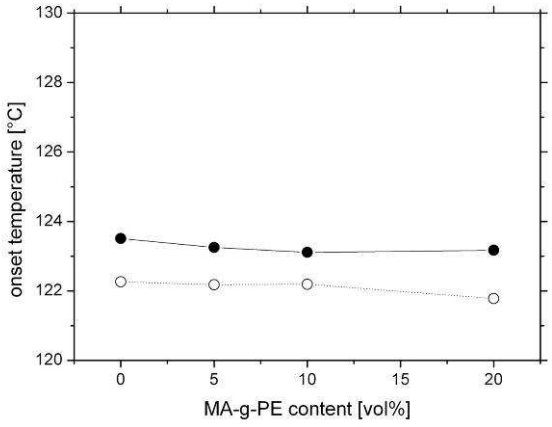

(e)

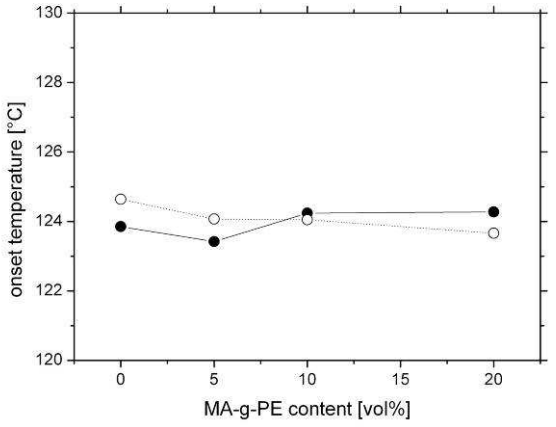

(f)

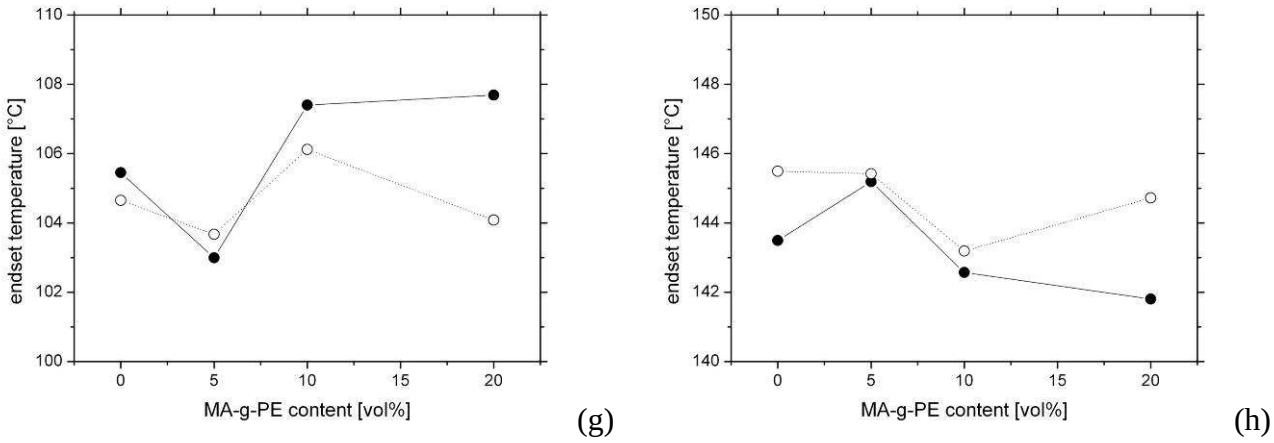

Figure 6.24. Results of the analysis of the DSC curves: crystallinity, melting and crystallization temperature, onset and endset temperatures for the HDPE09-(MA-g-PE) blends and the HDPE09-(MA-g-PE)-pMWCNT composites as a function of the MA-g-PE content.

6.2.4 TGA

The results of the analysis of the TGA and DTGA curves of the blends and of the composites are presented in Figure 6.25. These data evidenced three different trends that could be ascribed to the use of a masterbatch to disperse the MWCNTs in HDPE09. The onset temperature of the degradation decreased of about 4°C for all the HDPE09-(MA-g-PE)-pMWCNT composites in comparison to the HDPE09-(MA-g-PE) base matrix. This fact is related to the lower onset temperature of pMWNCNT (see 6.1.3) because (MA-g-PE) had the same onset temperature of HDPE09 (i.e. 458.2°C). On the other hand the endset temperature increased in presence of MWCNTs for the composites of about 2°C: in this case pMWCNT (455.2°C) and MA-g-PE (488.9°C) have no direct effect because the endset temperature were lower, i.e. the degradation phenomena were already finished. Moreover the peak temperature remained almost unchanged at about 483°C.

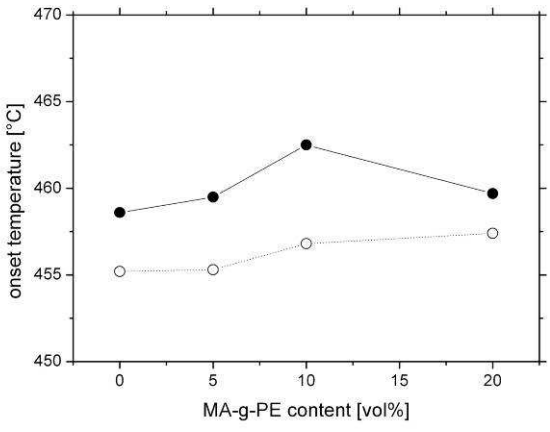

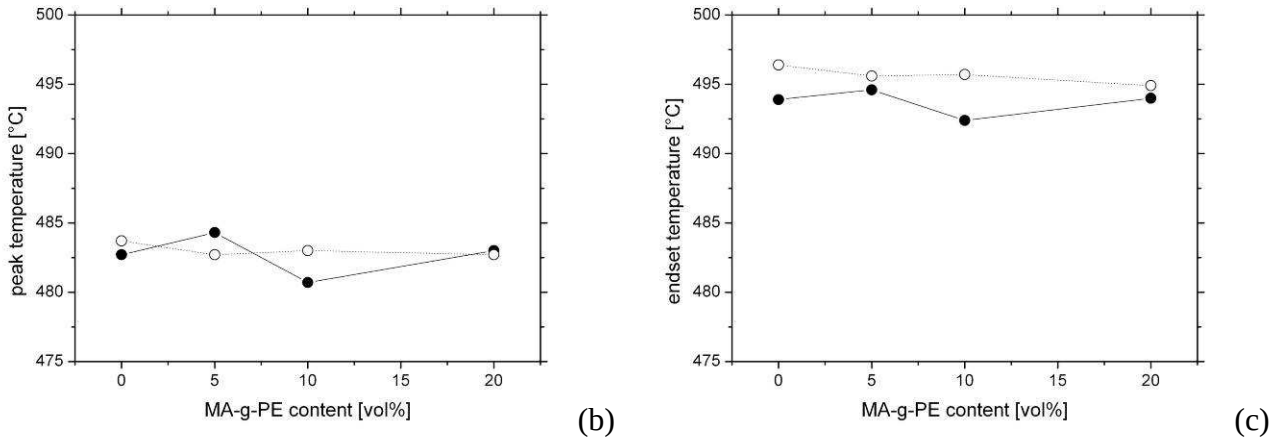

Figure 6.25. The results of the analysis of the TGA and DTGA curves: onset (T_{ON}), peak (T_{PEAK}) and endset (T_{END}) temperatures of the degradation and the residual fraction as a function of the MA-g-PE content for the HDPE09-(MA-g-PE) blends and the HDPE09-(MA-g-PE)-pMWCNT composites.

6.2.5 Tensile tests

As showed in the paragraph 6.1.11, the most evident effect of the filler addition on the mechanical properties (Figure 6.26, Figure 6.27 and Figure 6.28) was the loss of most part of the plastic deformation of the base matrices HDPE09-(MA-g-PE): strain at break dropped from 1000% or more to 15-20%.

While the stress to break (Figure 6.28) was not affected by the presence of MA-g-PE and of pMWCNT, the behaviour of the elastic modulus (Figure 6.26) and of the yielding stress (Figure 6.27) was more complex. All both the elastic modulus and the yielding stress showed a maximum with a MA-g-PE content of 10 vol% for the HDPE09-(MA-g-PE)-pMWCNT composites, on the other hand they decreased progressively in the case of the HDPE09-(MA-g-PE) blends which are the corresponding matrices.

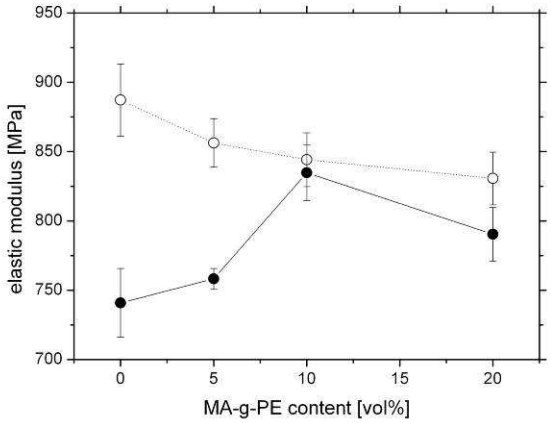

Figure 6.26. Elastic modulus as a function of the MA-g-PE content for the HDPE09-(MA-g-PE) blends and the HDPE09-(MA-g-PE)-pMWCNT composites.

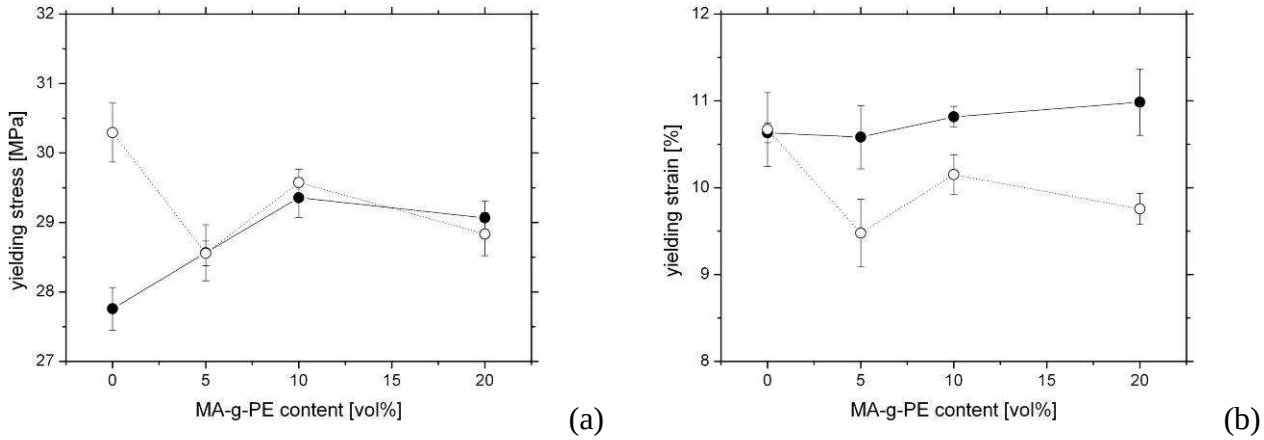

(a) (b)

Figure 6.27. Yielding stress (a) and strain (b) as a function of the MA-g-PE content for the HDPE09-(MA-g-PE) blends and the HDPE09-(MA-g-PE)-pMWCNT composites.

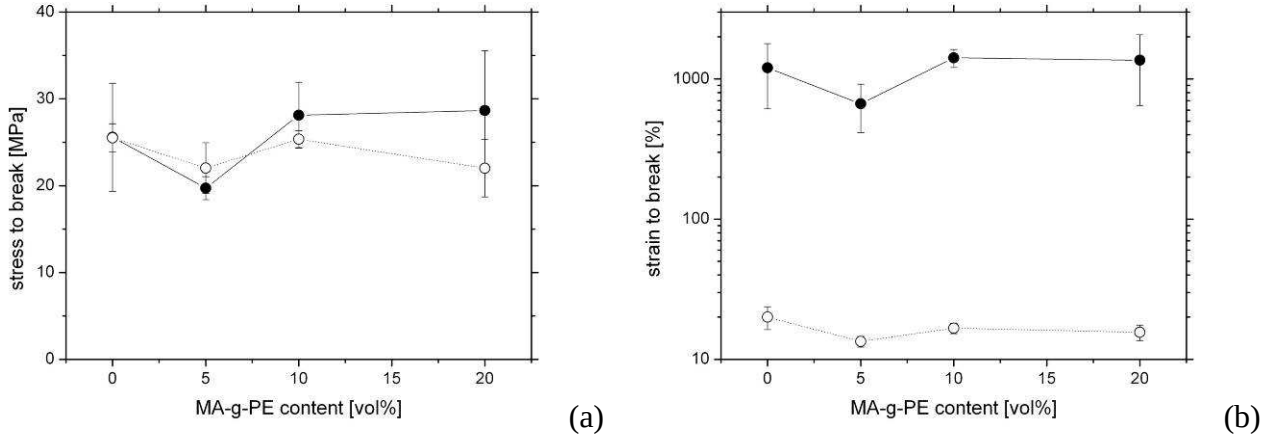

(a) (b)

Figure 6.28. Stress (a) and strain (b) at break as a function of the MA-g-PE content for the HDPE09-(MA-g-PE) blends and the HDPE09-(MA-g-PE)-pMWCNT composites.

7 Results on MWCNT (NANOAMOR) based composites

7.1 MWCNT treatments

7.1.1 SEM

Figure 7.1 proposes some examples of the acquired micrographs of uMWCNT powders as received from the supplier: the MWCNTs were in form of agglomerates with different dimensions. Even after the oxidation treatment in HNO_3, the MWCNTs remained in form of agglomerates (Figure 7.2).

7.1.2 Oxidation of MWCNTs by nitric acid

Figure 7.3 shows the residual mass of MWNCTs after the oxidation treatment in HNO_3 as a function of the treatment time. The residual mass decreased as the time increased because the oxidation: HNO_3 progressively destroyed the amorphous carbon and the graphitic layers of MWCNTs and induced the formation of hydroxyl and carbonyl groups [148]. The trend was in first approximation an exponential decay in good agreement with the literature [66].

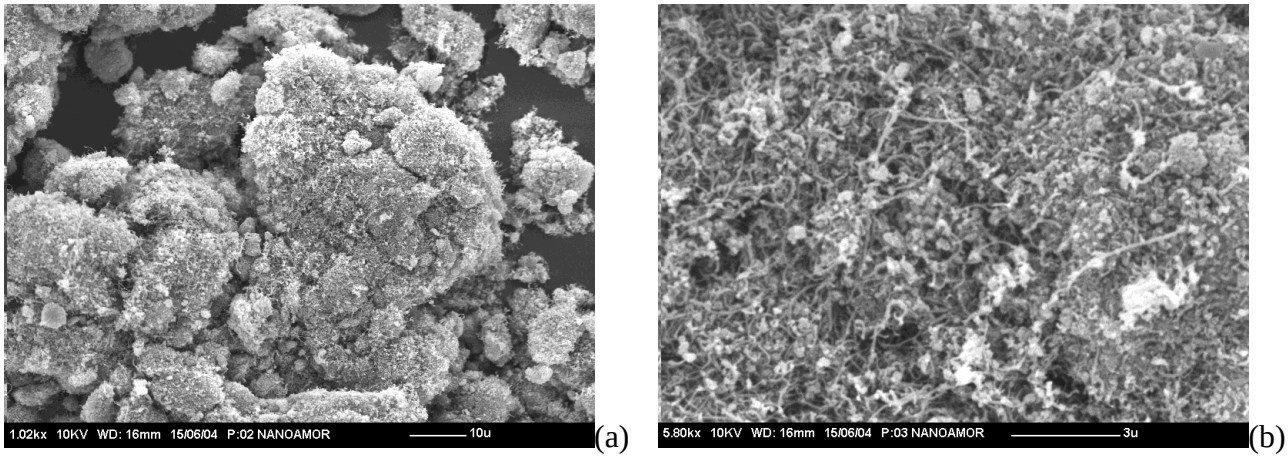

(a) (b)

Figure 7.1. SEM micrographs of uMWCNT powders.

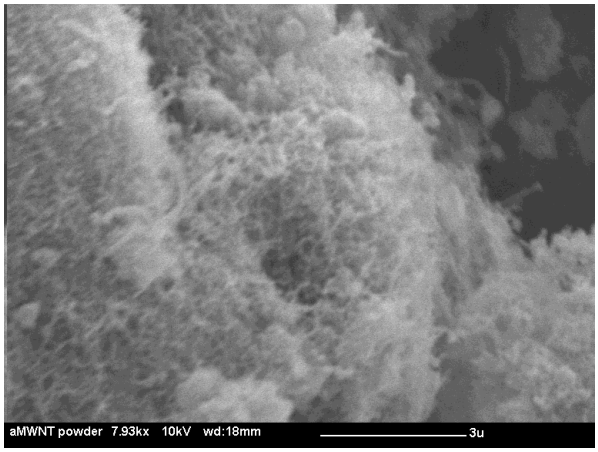

Figure 7.2. SEM micrograph of oMWCNT powders.

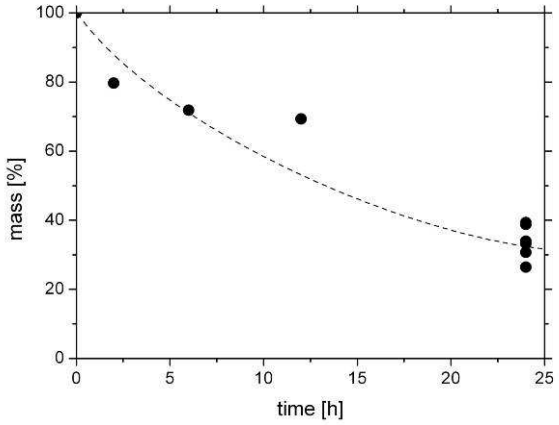

Figure 7.3. Residual mass of MWNCTs after the oxidation treatment in HNO_3 as a function of the treatment time.

7.1.3 TEM

Figure 7.4 and Figure 7.5 show the TEM micrographs of uMWCNT and oMWCNT treated for 24 h. The sample of uMWCNT evidenced not only MWCNTs, but a large amount of impurity too, i.e. amorphous carbon, residual catalyst particles and nanofibers. Moreover these MWCNTs had a broad distribution of the diameters (over 20 nm) and an high length (several microns) that induced an high agglomeration. On the other hand the sample of oMWCNT did have no impurity, short lengths (no more than 2-3 μm) and diameters between 25 and 55 nm. The oxidation treatment induced a reduction of the impurity content and a cutting of the MWCNTs [149]: in this way the agglomeration was reduced too as evidenced by the same preparation method of the samples for the TEM observations.

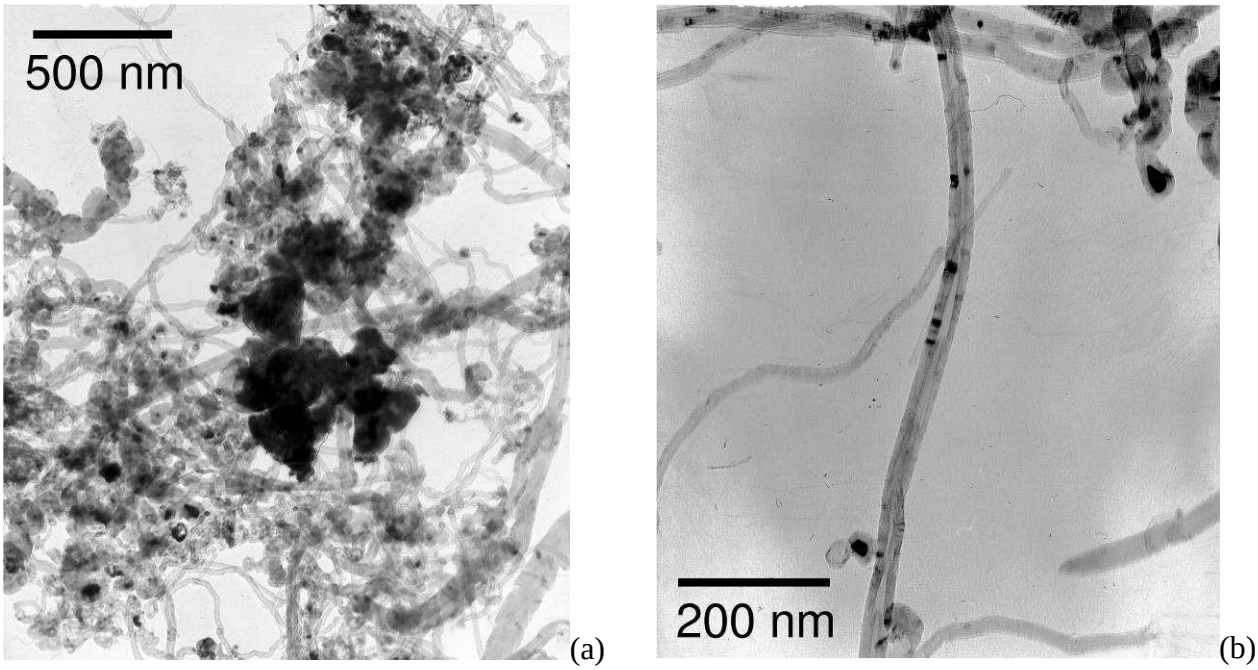

(a) (b)

Figure 7.4. TEM micrographs of uMWCNT at different magnifications.

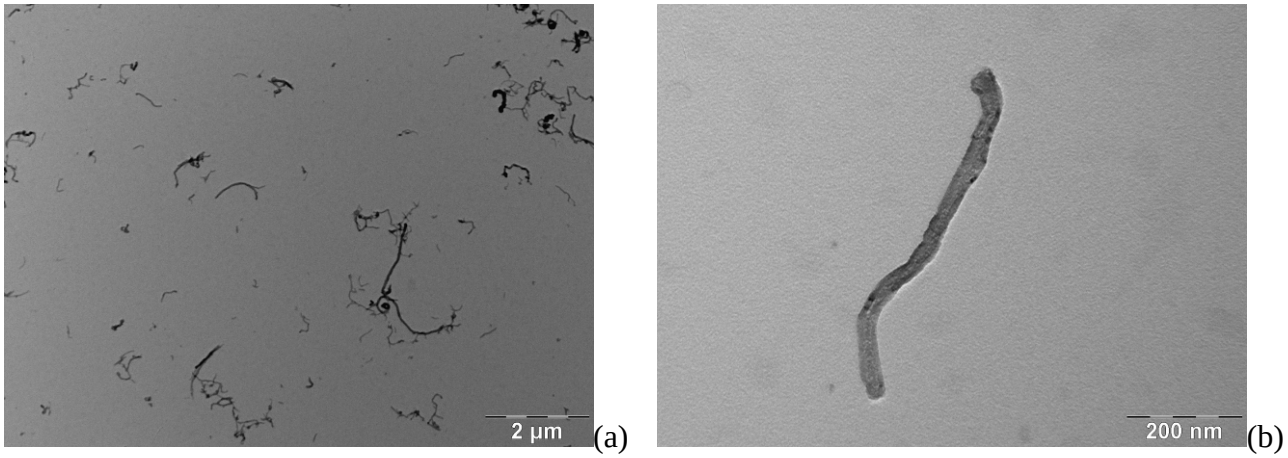

(a) (b)

Figure 7.5. TEM micrographs of oMWCNT at different magnifications.

7.1.4 EDAX

EDAX microanalysis was used to asses the effect of the oxidation treatment on the MWCNTs. The ratio of the peak intensity for Ni and O to C were used to have a semi-quantitative evaluation of the Ni and O content: the results for uMWCNT and oMWCNT (treated for 24 h) are presented in Figure 7.6. The data evidenced that the oxidation treatment induced a drastic reduction of the Ni content, i.e. the residual catalyst, and an increase of the O content. In particular the O content could indicate the increase of functional groups on the MWCNT surface [150].

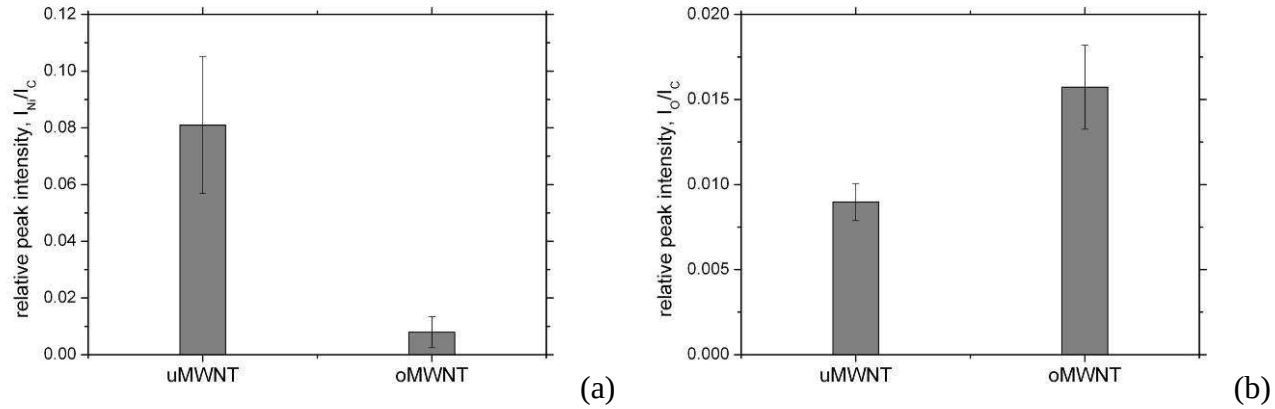

Figure 7.6. Comparison of the relative content of Ni (a) and O (b) for uMWCNT and oMWCNT (treated fo 24 h).

7.1.5 IR

Figure 7.7 shows the infrared spectra of uMWCNT and oMWCNT (treated for 24 h). At first glance the oxidation treatment introduced new peaks, i.e. new functional groups, in comparison to the untreated MWCNTs. In both the samples the peaks of CH_2 stretching (2918 and 2843 cm^{-1}), of OH stretching (3446 cm^{-1}) and bending (1382 cm^{-1}) and of C=C stretching in aromatic rings (1158 cm^{-1}) were detectable. On the other hand the treatment introduced the peaks of C=O stretching (1710 cm^{-1}), of C=O bending in aromatic (1198 cm^{-1}) and aliphatic structures (1182 cm^{-1}) and of C–O stretching (1024 cm^{-1}). In conclusion the spectra evidenced that mainly the formation of carboxylic group –COOH on the surface of MWCNTs, even if isolated carbonyl and hydroxyl groups could be present.

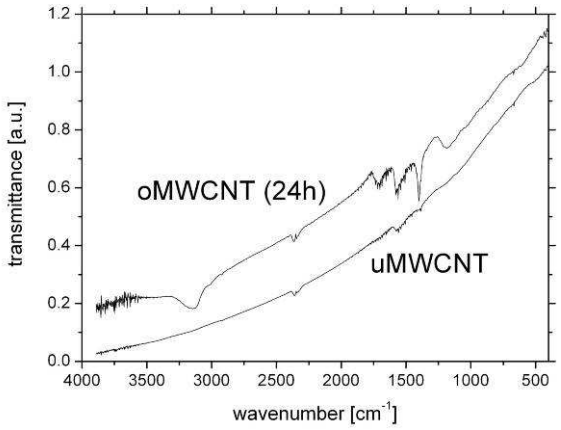

Figure 7.7. Infrared spectra of uMWCNT and oMWCNT (treated fo 24 h).

7.1.6 Nitrogen adsorption measurements

The nitrogen adsorption measurements was used to determine the values of the specific surface area: uMWCNT had 82.7 m^2/g, while oMWCNT (treated for 24 h) 107 m^2/g. This fact could be

related to the purification effect of the oxidation treatment: HNO_3 destroyed the impurities (i.e. amorphous carbon, residual catalyst particles and nanofibers) that had low specific surface area. Moreover Figure 7.8 shows the pore size distribution: the oxidation treatment had a complex effect on the particle size distribution because the peak started from a narrow peak at 24 nm to a broad peak from 24 to 64 nm.

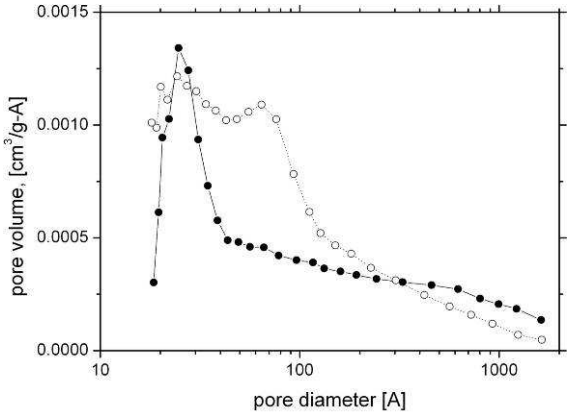

Figure 7.8. Pore size distribution for uMWCNT (●) and oMWCNT treated for 24 h (○).

7.1.7 TGA

Figure 7.9 shows the comparison of TGA analyses for uMWCNT and oMWCNT (treated for 24 h): the oxidation treatment had a stabilization effect and induced a new peak degradation. The TGA tests conducted in air atmosphere evidenced a shift of the onset temperature from 548°C to 624°C (+76°C) and of the maximum degradation rate from 599°C to 689°C (+90°C) after the oxidation treatment for 24 h. This fact could be related to the purification effect of the HNO_3 treatment (see the paragraph 7.1.6). Moreover the TGA tests conducted in nitrogen atmosphere evidenced a new degradation phenomenon between 210 and 260°C and a more drastic weight drop under 100°C. The oxidation treatment induced the formation of hydroxyl and carboxyl groups on the MWCNT surface: these groups was responsible for the more intense humidity adsorption (2 wt%) and for the degradation phenomena (with a peak at 250°C and a mass drop of 1.9 wt%). Moreover by assuming only carboxylic acid on MWCNT surface (that infrared spectra evidenced as the main group), a surface density of 4.0 μmol/m^2 (i.e 2.4 group/nm^2) for this group on MWCNTs was obtained in good agreement with the literature [68, 74, 151].

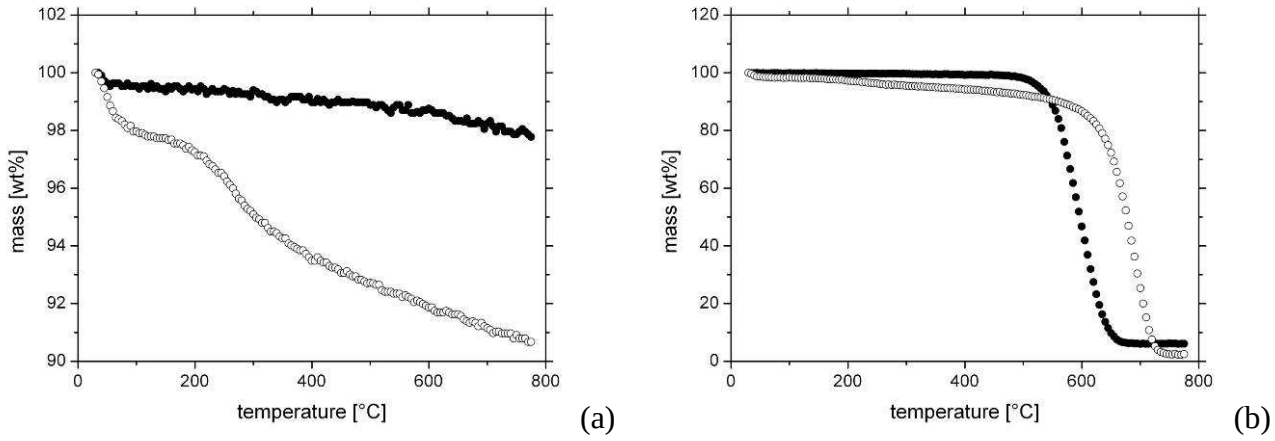

Figure 7.9. TGA curves for for uMWCNT (●) and oMWCNT treated for 24 h (○) in nitrogen (a) and air (b) atmosphere.

Figure 7.10 show the comparison of TGA analyses for uMWCNT, oMWCNT (treated for 24 h) and oMWCNT subjected to the treatment with the silane coupling agents: in all the case no significant difference was observable after the silane treatment in comparison to oMWCNT. The addition of silane on the filler surface had to introduce a new degradation peak between 400 and 600°C [152, 153], but it was completely absent: it is possible that the high carboxyl group content in comparison to the hydroxyl group reduced the effect of the treatment [73, 74].

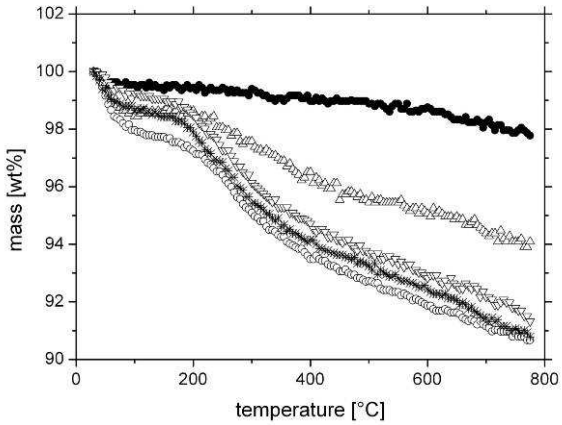

Figure 7.10. TGA curves in nitrogen atmosphere.for for uMWCNT (●), oMWCNT treated for 24 h (○), oMWCNT treated at 80°C for 48 h with ODS (△) and at room temperature for 40 min under sonicarion with ODS (▽) and PMS (∗).

7.1.8 Pycnometer

Pycnometric measurements were used to determine the density of uMWCNT. Multiple measurements were employed to have a complete desorption of the nitrogen from the MWCNTs: the limiting density was assumed as the true density of the material (Figure 7.11). After about 200

measurements, i.e. about 8 h, uMWCNT reached a limiting density of ***(2.15±0.02) g/cm^3***: this value is in good agreement with the literature for MWCNTs [99, 115]. This value was used to convert the weight fraction to the volume fraction.

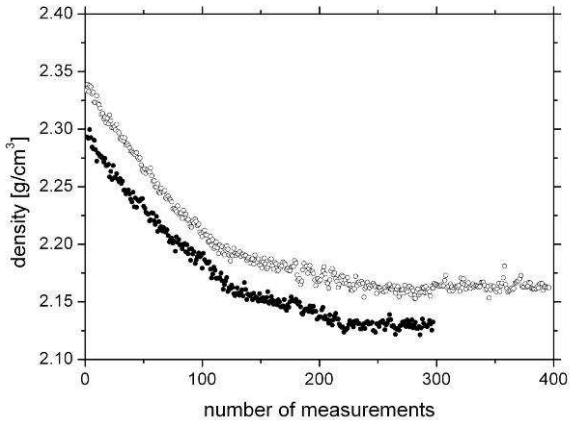

Figure 7.11. Density as a function of the number of measurements for uMWCNT in the pycnometric tests.

7.2 MWCNT filled composites

7.2.1 HDPE09-MWCNT (extruder) composites

7.2.1.1 Extruder

Table 7.1 shows the torque, the die pressure and the temperature of the melt during in the twin screw extruder during the production of HDPE09-CB composites. The presence of the filler induced an increase of the torque and the die pressure for all the composites of 5-10% without a specific trend. On the contrary the other parameters did not change.

Table 7.1. Torque (M), die pressure (p) and melt temperature along the barrel (T_i) during the composites production with the twin screw extruder for HDPE09-uMWCNT composites.

Material	M [Nm]	P [bar]	T_1 [°C]	T_2 [°C]	T_3 [°C]
HDPE09	70.0	13.9	212.8	226.2	236.2
HDPE09-uMWCNT 0.05 vol%	77.0	14.7	212.5	226.1	236.1
HDPE09-uMWCNT 0.25 vol%	73.5	14.4	212.4	226.4	236.2
HDPE09-uMWCNT 0.5 vol%	75.1	14.5	212.3	226.3	236.2

7.2.1.2 OM

The observation of thin sections of the composite materials with an optical microscope was used to control the extent of filler agglomerates. The micrographs of Figure 7.12 evidenced the presence of agglomerates for all the composites produced. From a general point of view the dimension of this agglomerates appeared independent on the filler content (up to about 20 μm), while the quantity of these agglomerates increased with the filler content. This fact demonstrated as the process was no able to break down the agglomerates probably because the energy was not enough [154-157].

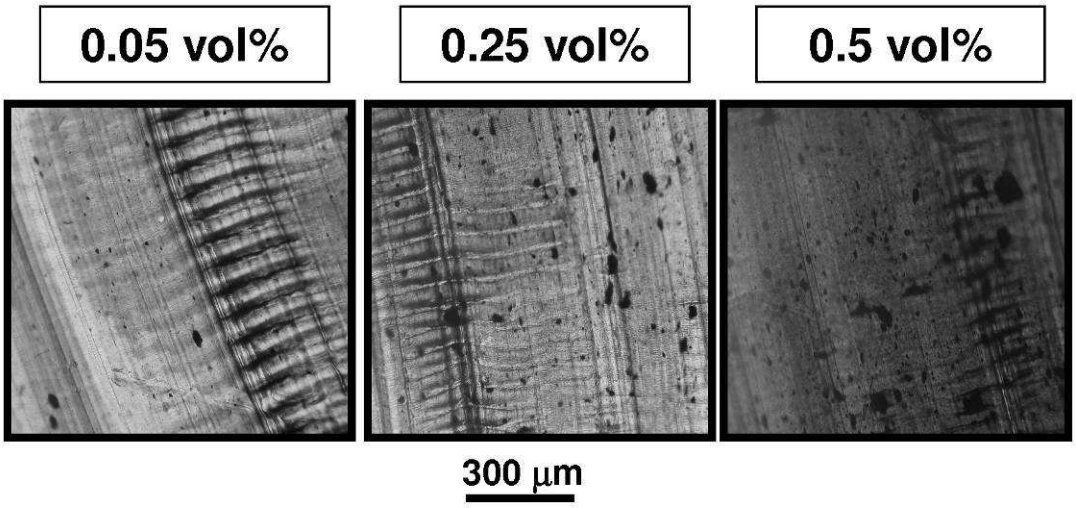

Figure 7.12. OM micrographs of HDPE09-uMWCNT composites.

7.2.1.3 DSC

Figure 7.13 shows the DSC curves of HDPE09-uMWCNT, while Table 7.2 contains the data elaborated from these DSC curves. The main effect was related to the crystallization phenomena: the onset temperature translated to higher temperature (about 1-2°C). The MWCNTs acted as a nucleating agent: however the crystallinity and the melting phenomena did not evidence any change.

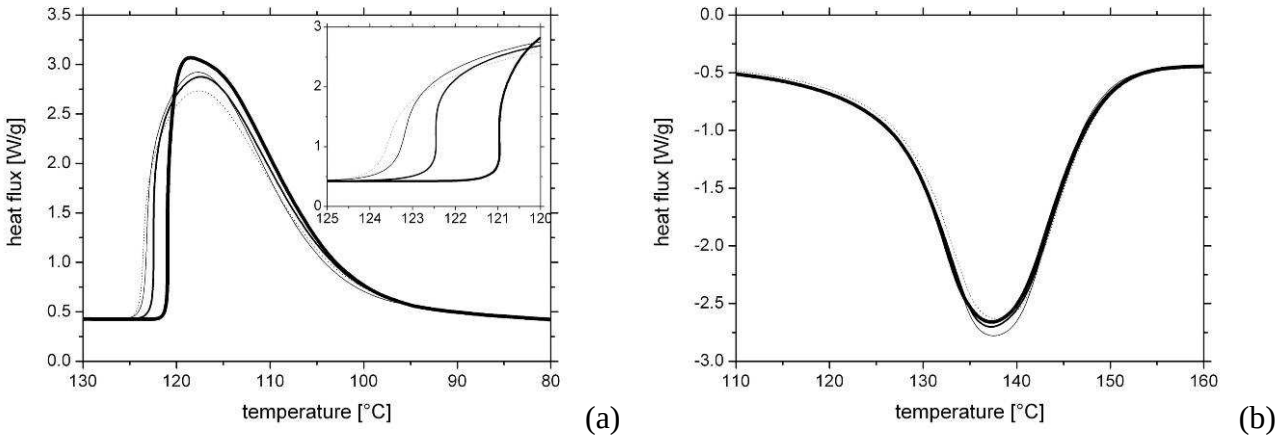

Figure 7.13. DSC curves of the crystallization phenomena during the cooling stage (a) and the heating stage (b) for HDPE09, HDPE09-uMWCNT 0.05, 0.25 and 0.5 vol% (decreasing thickness of the line). The inset of the cooling stage curves (a) shows a detail of the crystallization onset.

Table 7.2. Results of the analysis of the DSC curves: crystallinity (χ), melting (T_m) and crystallization (T_c) temperature, onset (T_{ON}) and endset (T_{END}) temperatures.

Material	Crystallization Cooling (2nd scan)				Melting Heating (3rd scan)			
	χ [wt%]	T_c [°C]	T_{ON} [°C]	T_{END} [°C]	χ [wt%]	T_m [°C]	T_{ON} [°C]	T_{END} [°C]
HDPE09	80.2	118.5	121.2	102.1	82.4	137.3	125.3	148.0
HDPE09-uMWCNT 0.05 vol%	81.5	117.4	122.8	102.2	83.1	137.3	125.2	148.2
HDPE09-uMWCNT 0.25 vol%	82.4	117.8	123.7	103.4	83.8	137.5	125.6	147.5
HDPE09-uMWCNT 0.5 vol%	81.7	117.6	124.2	102.1	82.3	137.9	125.6	148.3

7.2.1.4 TGA

Table 7.3 summarizes the reference temperatures of the degradation phenomenon as evidenced in TGA and DTGA curves. From a general point of view the degradation is not significantly by the filler addition.

Table 7.3. The results of the analysis of the TGA and DTGA curves: onset (T_{ON}), peak (T_{PEAK}) and endset (T_{END}) temperatures of the degradation.

Material	T_{ON} [°C]	T_{PEAK} [°C]	T_{END} [°C]
HDPE09	426.0	479.7	507.7
HDPE09-uMWCNT 0.05 vol%	426.7	480.3	508.3
HDPE09-uMWCNT 0.25 vol%	428.7	465.7	507.0
HDPE09-uMWCNT 0.5 vol%	428.0	476.0	512.3

7.2.1.5 Tensile tests

The most evident effect of the filler addition on the mechanical properties (Table 7.4) was the loss of most part of the plastic deformation of HDPE09: strain at break dropped from 2500% to 100-200%. On the other hand the elastic modulus did not change, while the yield stress decreased by about 1 MPa after the filler addition.

Table 7.4. Mechanical properties of the HDPE09-uMWCNT composites: elastic modulus (E), stress and strain at yielding (σ_Y and ε_Y) and at break (σ_R and ε_R).

Material	E [MPa]	σ_Y [MPa]	ε_Y [%]	σ_R [MPa]	ε_R [%]
HDPE09	860	31.1	13.8	33.8	2545
HDPE09-uMWCNT 0.05 vol%	910	30.2	14.2	1.0	175
HDPE09-uMWCNT 0.25 vol%	890	30.5	13.9	5.0	85
HDPE09-uMWCNT 0.5 vol%	880	30.3	13.9	4.9	97

7.2.1.6 DMTA

The results of the DMTA tests are showed in Figure 7.14, Figure 7.15 and Figure 7.16. The materials presented two sharp drops of the storage modulus that corresponded to two peaks in terms of dissipative modulus and loss factor. In particular they were related to glass transition (γ-relaxation) that was at -101°C for HDPE09 and the α-relaxation that was at 63°C for HDPE09. The reference temperature did not change significantly for HDPE09-uMWCNT composites.

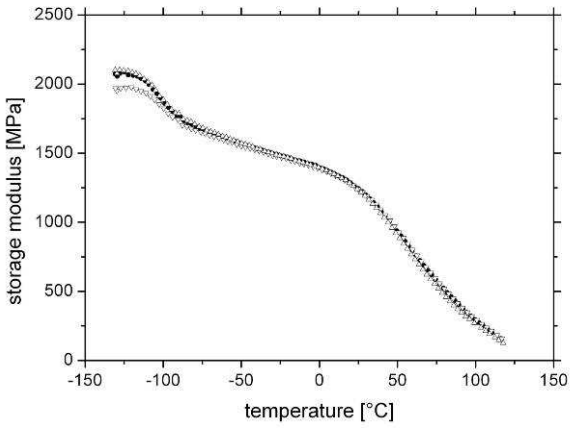

Figure 7.14. Storage modulus as a function of the temperature for HDPE09 (●), HDPE09-uMWCNT 0.05 (▽) and 0.5 vol% (△).

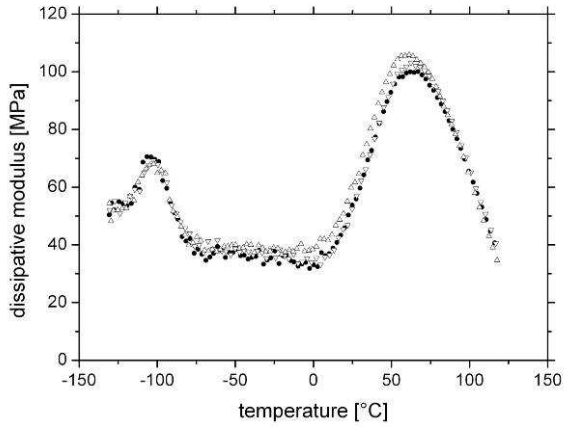

Figure 7.15. Dissipative modulus as a function of the temperature for HDPE09 (●), HDPE09-uMWCNT 0.05 (▽) and 0.5 vol% (△).

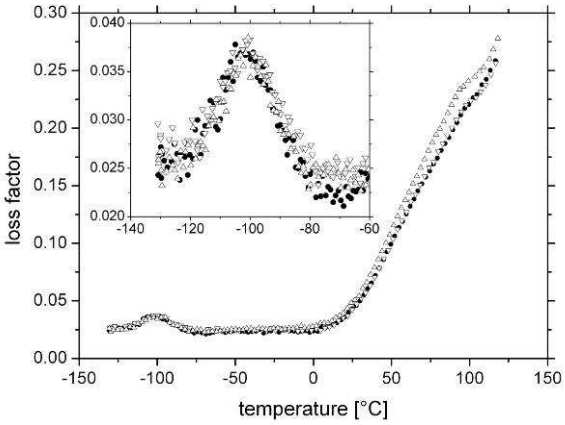

Figure 7.16. Loss factor as a function of the temperature for HDPE09 (●), HDPE09-uMWCNT 0.05 (▽) and 0.5 vol% (△).

7.2.2 HDPE09-MWCNT (mixer) composites

7.2.2.1 Internal mixer

Table 7.5 contains the most significant data of the production process of the composites with the internal mixer. From a general point of view the filler addition did not significantly affect the torque applied by the internal mixer. The torque increased only in the case of the composites produced a 135°C in comparison to the ones at 180°C because the viscosity of HDPE increases as the temperature decreases.

7.2.2.2 OM

The observation of thin sections of the composite materials with an optical microscope was used to control the extent of filler agglomerates. The micrographs of Figure 7.17 evidenced the presence of

agglomerates for all the composites produced. From a general point of view the dimension of this agglomerates was bigger in the case of the processing at 180°C and 20 rpm for 15 min, while it was relatively better in the case of the processing at 125°C. However agglomerates with dimensions of 20-30 μm were present in all the composites (with a filler content of 0.05 and 0.5 vol%). This fact demonstrated as the process was no able to break down the agglomerates probably because the energy was not enough [154-157] even if the processing parameters was changed to obtain the maximum viscosity of the polymer.

Table 7.5. Torque (M) and melt temperature (T) during the composites production in the internal mixer: the maximum/minimum value (MAX/MIN), at 20 rpm and at 100 rpm.

Material	M_{MAX} [Nm]	M_{20rpm} [Nm]	M_{100rpm} [Nm]	T_{MIN} [°C]	T_{20rpm} [°C]	T_{100rpm} [°C]
135°C, 20+100rpm, 5+20min						
HDPE09	90.8	11.6	16.1	121.3	144.7	177.8
HDPE09-uMWCNT 0.5 vol%	96.6	9.9	15.6	121.9	144.7	178.5
180°C, 20rpm, 15min						
HDPE09	26.3	7.6	n.a.	147.3	192.2	n.a.
HDPE09-uMWCNT 0.05 vol%	25.7	6.7	n.a.	149.5	191.5	n.a.
HDPE09-uMWCNT 0.5 vol%	31.9	7.1	n.a.	148.8	192.2	n.a.
180°C, 20+100rpm, 5+20min						
HDPE09	42.8	7.4	12.7	144.0	189.7	217.0
HDPE09-uMWCNT 0.05 vol%	30.8	7.1	12.0	147.3	189.4	215.2
HDPE09-uMWCNT 0.5 vol%	31.8	7.4	13.8	147.8	188.3	217.6

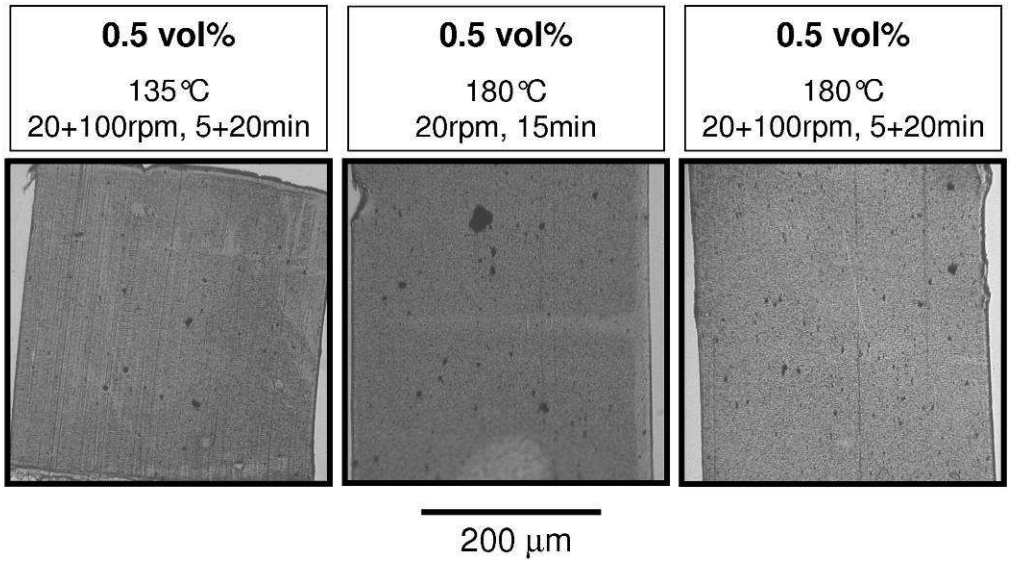

Figure 7.17. OM micrographs of HDPE09-uMWCNT composites produced with the internal mixer in different processing conditions.

7.2.2.3 DSC

Table 7.6 presents the data elaborated from the DSC curves. These data evidence three main topics: first of all the onset temperature of the crystallization increased of about 1°C in the case of the composites that underwent to a more intensive mixing at 135°C and 180°C (20+100 rpm for 5+20 min) in comparison to the composites that underwent to a no so intensive mixing (20 rpm for 15 min). Thes effect was evident mainly for the composites filled with 0.5 vol%. On the other hand the melting temperature increased up to 4°C in the case of the composites with intensive mixing (20+100 rpm for 5+20 min), while of only 1°C in the case of the other composites. Moreover the crystallinity change only in the case of the composites produced at 180°C with a reduced mixing (20 rpm for 15 min).

Table 7.6. Results of the analysis of the DSC curves: crystallinity (χ), melting (T_m) and crystallization (T_c) temperature, onset (T_{ON}) and endset (T_{END}) temperatures.

Material	Crystallization Cooling (2nd scan)				Melting Heating (3rd scan)			
	χ [wt%]	T_c [°C]	T_{ON} [°C]	T_{END} [°C]	χ [wt%]	T_m [°C]	T_{ON} [°C]	T_{END} [°C]
135°C, 20+100rpm, 5+20min								
HDPE09	73.0	116.0	122.3	103.3	73.0	133.7	124.1	145.5
HDPE09-uMWCNT 0.5 vol%	74.8	119.4	124.4	108.1	74.5	136.4	124.6	144.2
180°C, 20rpm, 15min								
HDPE09	70.7	116.0	122.2	104.8	70.8	134.1	123.9	144.3
HDPE09-uMWCNT 0.05 vol%	73.9	117.0	122.7	104.6	73.9	134.6	124.4	145.6
HDPE09-uMWCNT 0.5 vol%	74.0	116.2	123.7	102.7	74.5	135.2	124.7	147.4
180°C, 20+100rpm, 5+20min								
HDPE09	71.2	116.6	122.0	104.7	70.9	133.5	123.8	144.2
HDPE09-uMWCNT 0.05 vol%	71.6	116.3	122.3	103.5	71.1	134.3	123.7	145.2
HDPE09-uMWCNT 0.5 vol%	71.0	116.3	123.6	102.9	70.6	138.2	124.1	145.4

7.2.2.4 TGA

Table 7.7 summarizes the reference temperatures of the degradation phenomenon as evidenced in TGA and DTGA curves. From a general of view the degradation is not significantly affected by the filler addition in the case of the composites produced at 135°C; on the other hand the processing at 180°C with a reduced mixing decreased the thermal stability (5°C), while the processing at 180°C with an intensive mixing increased the thermal stability (8°C).

Table 7.7. The results of the analysis of the TGA and DTGA curves: onset (T_{ON}), peak (T_{PEAK}) and endset (T_{END}) temperatures of the degradation.

Material	T_{ON} [°C]	T_{PEAK} [°C]	T_{END} [°C]
135°C, 20+100rpm, 5+20min			
HDPE09	463.9	482.3	493.7
HDPE09-uMWCNT 0.5 vol%	464.8	480.7	494.8
180°C, 20rpm, 15min			
HDPE09	467.3	490.3	500.0
HDPE09-uMWCNT 0.05 vol%	459.1	482.0	495.0
HDPE09-uMWCNT 0.5 vol%	465.9	482.7	495.2
180°C, 20+100rpm, 5+20min			
HDPE09	456.0	481.3	491.8
HDPE09-uMWCNT 0.05 vol%	465.8	485.3	495.8
HDPE09-uMWCNT 0.5 vol%	464.2	479.0	494.3

7.2.2.5 Tensile tests

The most evident effect of the filler addition on the mechanical properties (Table 7.8) was the loss of most part of the plastic deformation of HDPE09: strain at break dropped from 1800% to 100% or lower. On the other hand the elastic modulus increased of about 10% only of intensive mixing (20+100 rpm for 5+20 min), while the yield stress increased by about 1 MPa after the filler addition.

Table 7.8. Mechanical properties of the HDPE09-uMWCNT composites: elastic modulus (E), stress and strain at yielding (σ_Y and ε_Y) and at break (σ_R and ε_R).

Material	E [MPa]	σ_Y [MPa]	ε_Y [%]	σ_R [MPa]	ε_R [%]
135°C, 20+100rpm, 5+20min					
HDPE09	713	29.4	11.1	31.0	1800
HDPE09-uMWCNT 0.5 vol%	827	30.6	10.8	19.0	34.1
180°C, 20rpm, 15min					
HDPE09	844	28.8	11.2	19.1	380
HDPE09-uMWCNT 0.05 vol%	832	29.1	11.4	17.7	53.7
HDPE09-uMWCNT 0.5 vol%	824	29.6	11.4	17.9	40.4
180°C, 20+100rpm, 5+20min					
HDPE09	733	27.8	11.0	29.6	1600
HDPE09-uMWCNT 0.05 vol%	829	29.0	12.2	22.4	835
HDPE09-uMWCNT 0.5 vol%	819	30.2	11.1	19.9	23.8

7.2.2.6 DMTA

The results of the DMTA tests are showed in Figure 7.18, Figure 7.19 and Figure 7.20. The materials presented two sharp drops of the storage modulus that corresponded to two peaks in terms of dissipative modulus and loss factor. In particular they were related to glass transition (γ-relaxation) that was at -101°C for HDPE09 and the α-relaxation that was at 53°C for HDPE09 with an intensive mixing (20+100 rpm for 5+20 min) and 47°C with a reduced mixing (20 rpm for 15 min).

These reference temperature did not change significantly for HDPE09-uMWCNT composites (Table 7.9).

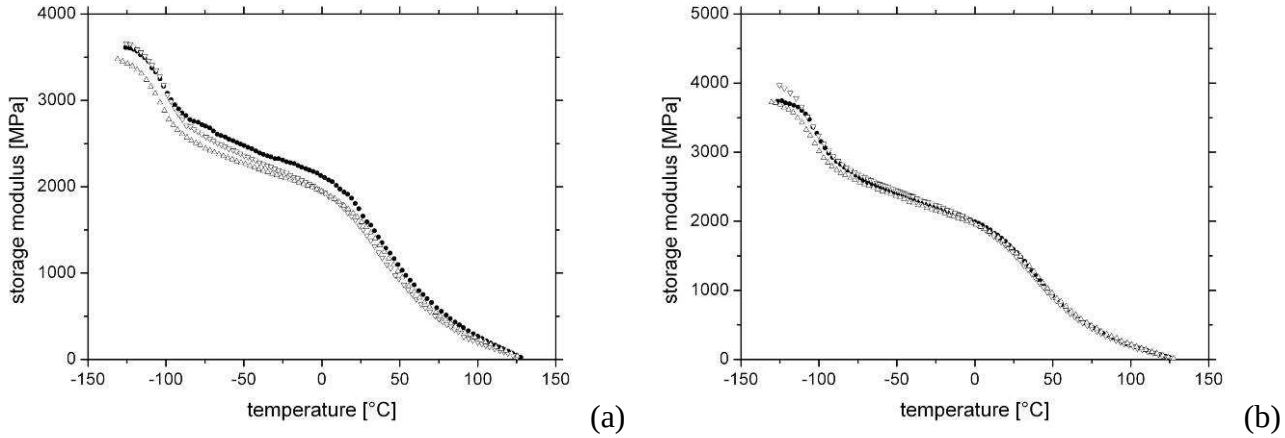

Figure 7.18. Storage modulus as a function of the temperature for HDPE09 (●), HDPE09-uMWCNT 0.05 (▽) and 0.5 vol% (△) for the composites produced at 180°C in the case of (a) low mixing (20 rpm for 15 min) and (b) high mixing (20+100 rpm for 5+20 min).

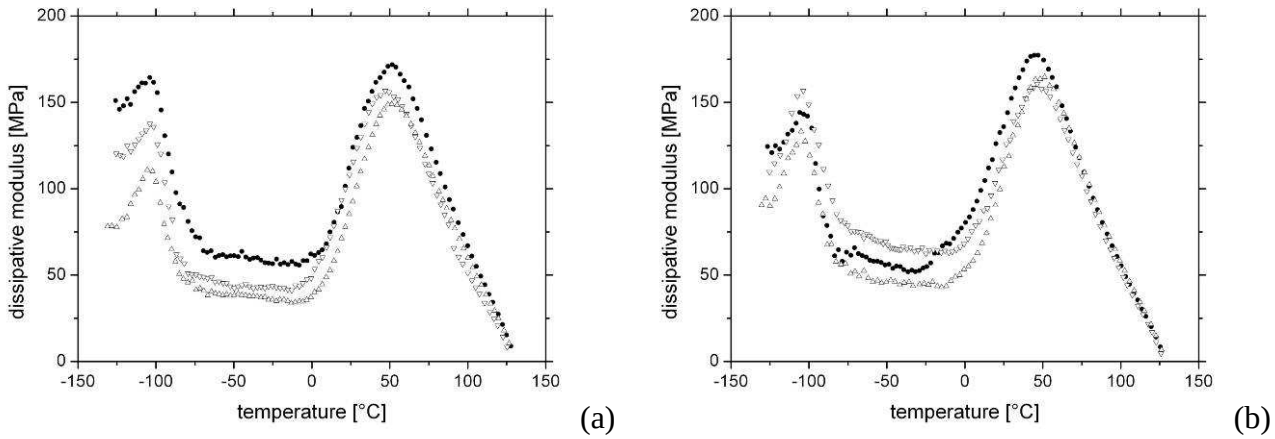

Figure 7.19. Dissipative modulus as a function of the temperature for HDPE09 (●), HDPE09-uMWCNT 0.05 (▽) and 0.5 vol% (△) for the composites produced at 180°C in the case of (a) low mixing (20 rpm for 15 min) and (b) high mixing (20+100 rpm for 5+20 min).

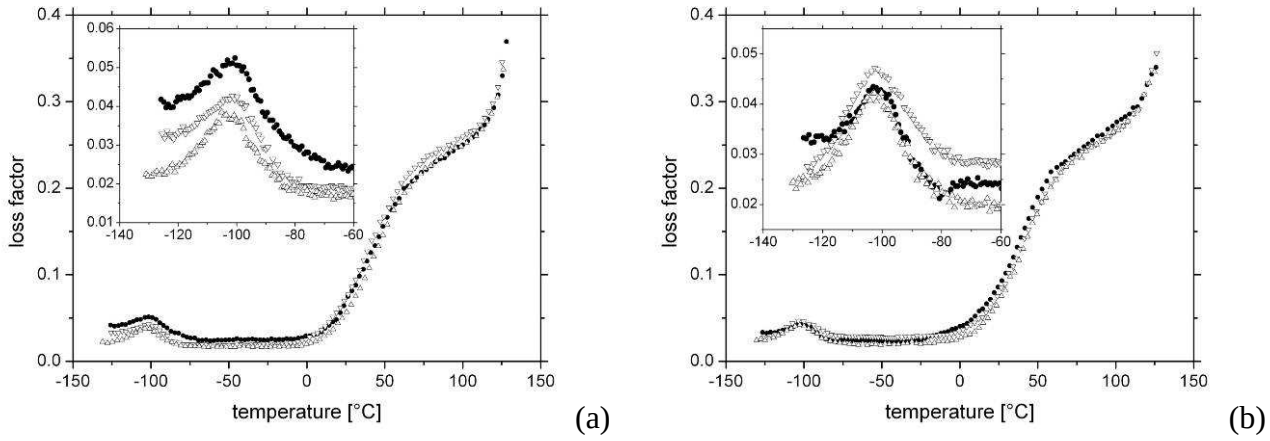

Figure 7.20. Loss factor as a function of the temperature for HDPE09 (●), HDPE09-uMWCNT 0.05 (▽) and 0.5 vol% (△) for the composites produced at 180°C in the case of (a) low mixing (20 rpm for 15 min) and (b) high mixing (20+100 rpm for 5+20 min). The inset is a detail of the loss factor at low temperature.

Table 7.9. The temperature of the α- and γ-relaxations.

Material	**T_γ (T_g) [°C]**	**T_α [°C]**
180°C, 20rpm, 15min		
HDPE09	52.7	101.8
HDPE09-uMWCNT 0.05 vol%	48.3	101.1
HDPE09-uMWCNT 0.5 vol%	53.1	102.1
180°C, 20+100rpm, 5+20min		
HDPE09	47.1	102.1
HDPE09-uMWCNT 0.05 vol%	47.9	101.4
HDPE09-uMWCNT 0.5 vol%	49.9	101.5

7.2.2.7 Tensile creep tests

From a general point of view MWCNTs resulted to have a different effect on the creep resistance of the HDPE matrix with relation to the applied constant stress. While the creep resistance substantially increased in the non-linear viscoelastic or viscoplastic region (i.e. at high stresses or temperatures), it was not changed (processing at 135°C) or even worsened (processing at 180°C) in the linear viscoelastic region (i.e. at low stresses or temperatures). Examples of this behaviour are proposed in Figure 7.21 and in Figure 7.22 where compliance and compliance rate of HDPE09-uMWCNT composites at 30°C are showed.

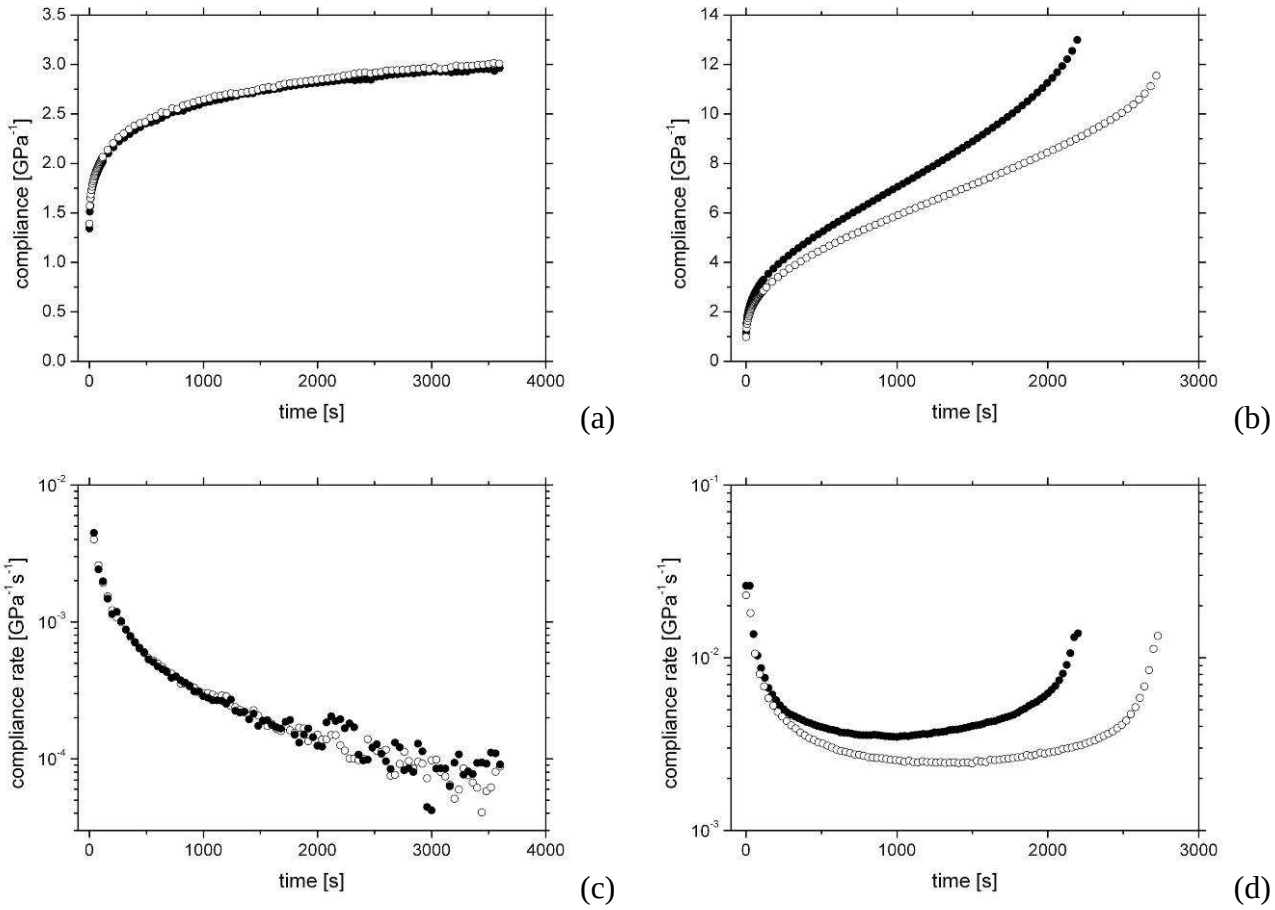

Figure 7.21. Creep compliance at 30°C (a, c) and creep compliance rate (b, d) as a function of time at 30°C with a stress of 3 MPa (a, b) and 15 MPa (c, d) for HDPE09 (●) and HDPE09-uMWCNT 0.5 vol% (○) produced with a processing at 135°C.

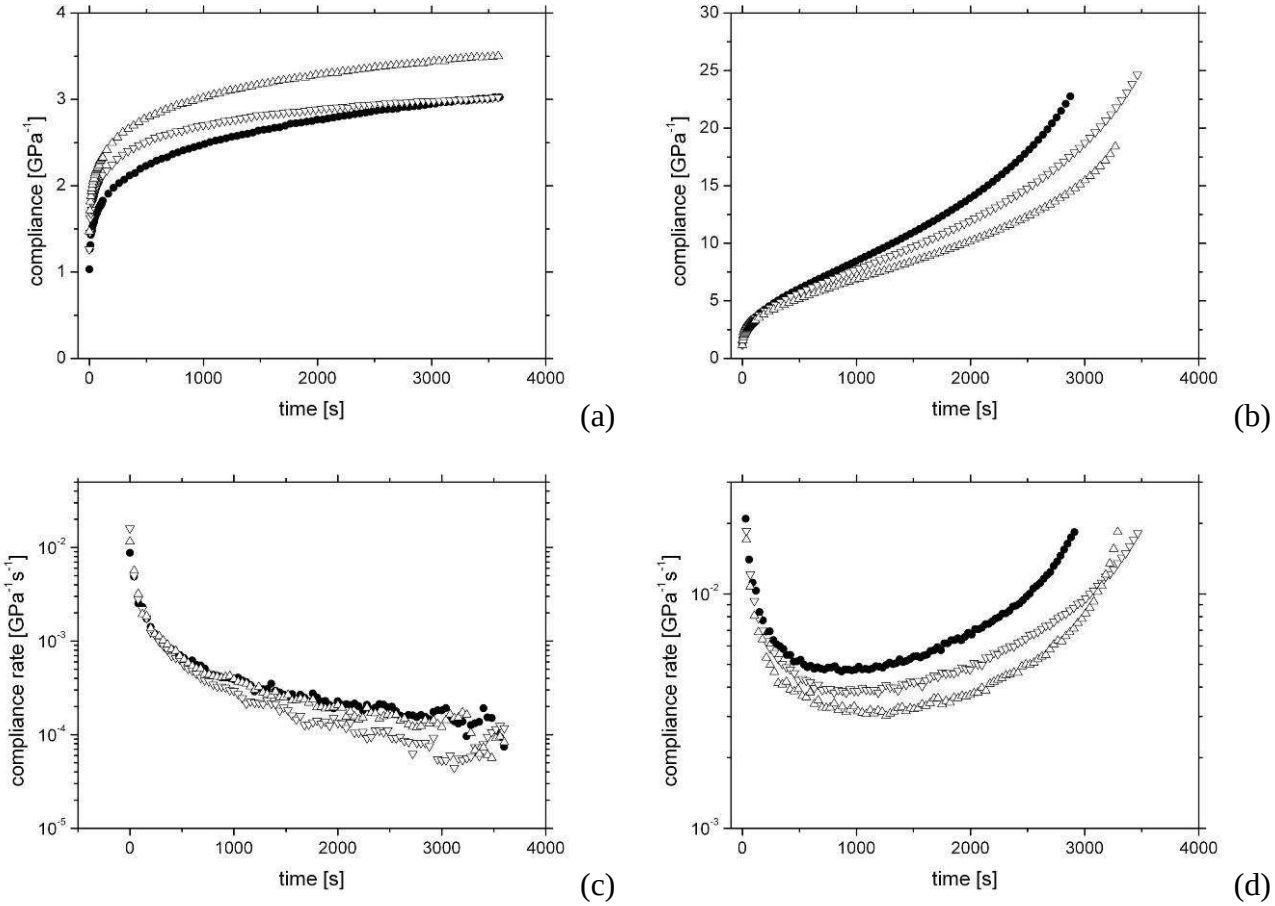

Figure 7.22. Creep compliance at 30°C (a, c) and creep compliance rate (b, d) as a function of time at 30°C with a stress of 3 MPa (a, b) and 15 MPa (c, d) for HDPE09 (●), HDPE09-uMWCNT 0.05 vol% (▽) and HDPE09-uMWCNT 0.5 vol% (△) produced with a processing at 180°C and 20+100 rpm for 5+20 min.

7.2.3 PVOH-MWCNT (bath sonication) composites

7.2.3.1 OM

The observation of thin sections of the composite materials with an optical microscope was used to control the extent of filler agglomerates. The micrographs of Figure 7.23 evidenced the presence of agglomerates for all the composites produced. From a general point of view the dimension of this agglomerates was up to 50 μm and the phenomenon was more strong in the case on higher filler content: no relevant difference was evident between the two type of the polymeric matrices.

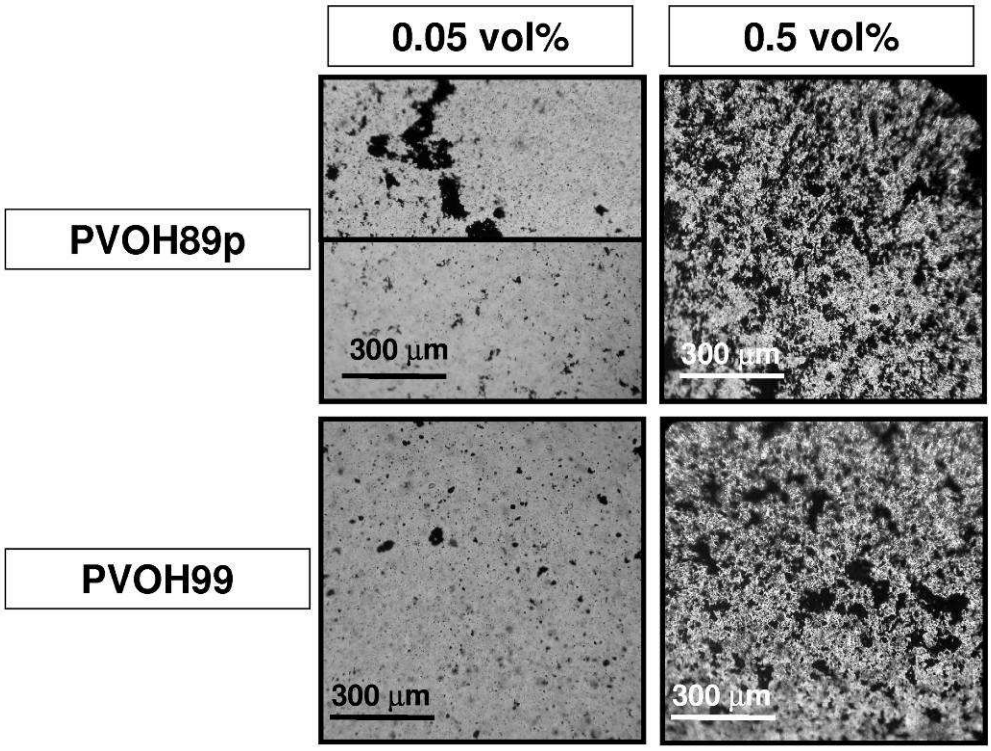

Figure 7.23. OM micrographs of PVOH89p-uMWCNT and PVOH99-uMWCNT composites.

7.2.3.2 DSC

The DSC curves are showed in Figure 7.24: in the first case the crystallization during the cooling stage and in the second one the melting during the heating stage. For all the materials the main phenomena was a glass transition between 50 and 100°C and a melting/crystallization over 150°C. Table 7.10 contains the data elaborated from these DSC curves. From a general point of view uMWCNT did have no significant effect on crystallinity and glass transition temperature in the case of PVOH99-uMWCNT, while the glass transition temperature shifted to lower values (up to 9°C) in the case of PVOH89p-uMWCNT. Moreover uMWCNT acted as nucleating agents by changing the shape of crystallization DSC curve for PVOH99-uMWCNT composites, while non clear effect was present for PVOH89p-uMWCNT composites.

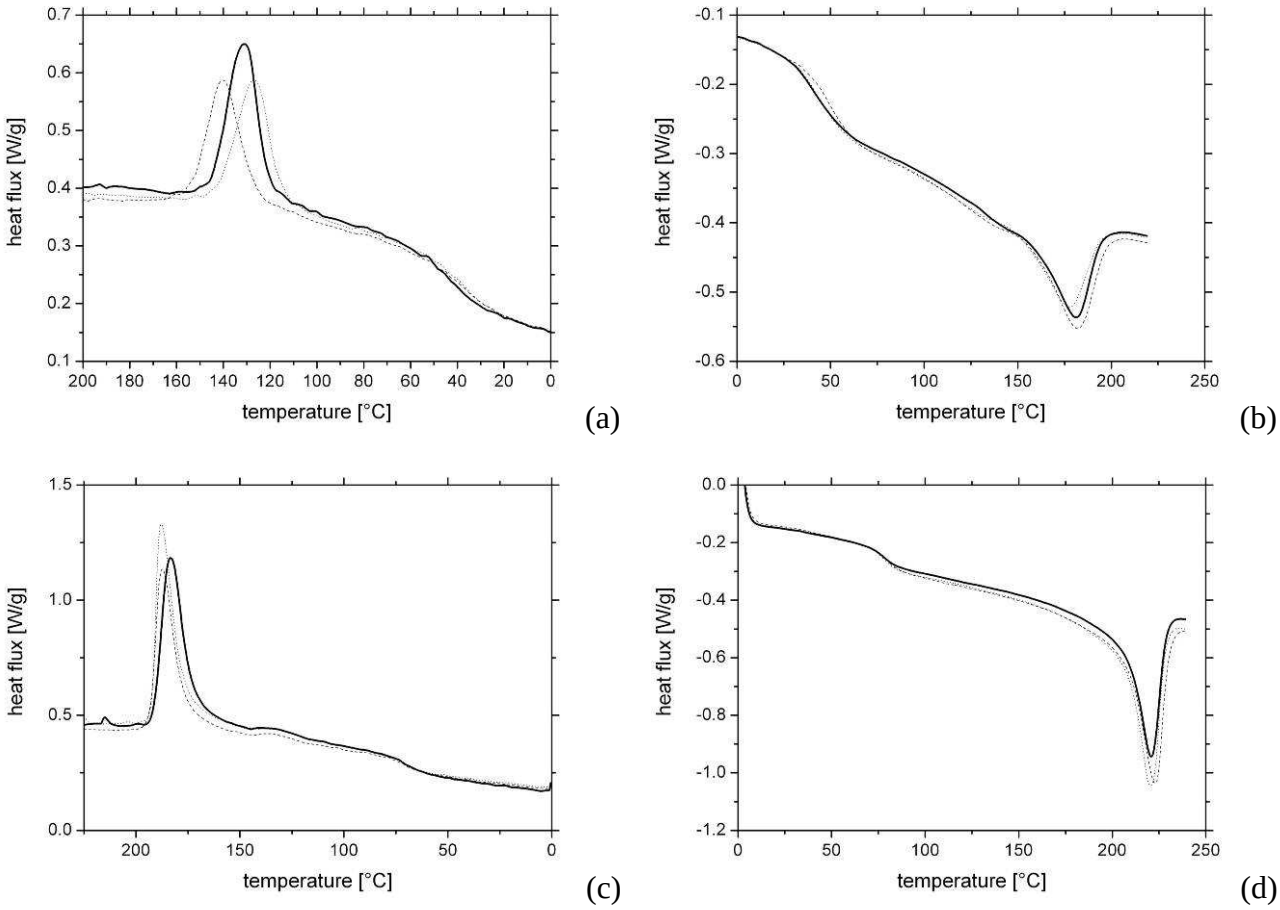

Figure 7.24. DSC curves of (a, b) PVOH89p (—, tick), PVOH89p-uMWCNT 0.05 vol% (—, thin) PVOH89p-uMWCNT 0.5 vol% (---) and of (c, d) of PVOH99 (—, tick), PVOH99-uMWCNT 0.05 vol% (—, thin), PVOH99-uMWCNT 0.5 vol% (---) composites for the cooling stage (a, c) and the heating stage (b, d).

Table 7.10. Results of the analysis of the DSC curves: glass temperature (T_g), crystallinity (χ), melting (T_m) and crystallization (T_c) temperature.

Material	Cooling (2nd scan)			Heating (3rd scan)		
	T_g [°C]	χ [wt%]	T_c [°C]	T_g [°C]	χ [wt%]	T_m [°C]
PVOH89p	51.1	17.9	130.8	49.7	18.5	181.4
PVOH89p-uMWCNT 0.05 vol%	38.5	16.4	126.6	42.3	15.6	177.8
PVOH89p-uMWCNT 0.5 vol%	44.1	17.0	140.0	40.4	17.2	180.8
PVOH99	72.6	41.5	183.5	78.7	41.0	222.8
PVOH99-uMWCNT 0.05 vol%	73.6	41.5	187.7	78.0	41.3	220.4
PVOH99-uMWCNT 0.5 vol%	71.2	37.0	187.3	77.5	37.1	220.7

7.2.3.3 TGA

Figure 7.25 shows examples of TGA curves and DTGA curves for PVOH89p and PVOH99, while Table 7.11 summarizes the reference temperatures for all the materials tested. From a general point

of view there were two distinct and well-separated weight drops at 300-450°C and 450-550°C for all both the PVOH, while only PVOH89p had an additional peak at about 200°C. From the literature [146, 158] the main reactions for the degradation phenomena under 450°C are the dehydration and the eliminations of residual acetate groups (randomly inserted between hydroxyl groups), while at higher temperature chain-scission reactions dominate. For what concern the composites the peak temperature of the degradation shifted to higher temperature (up to 25°C), while the onset temperature was non affected by the filler addition.

Moreover TGA curves did not evidence residual water release in the range of 100-150°C.: in relation to the sensitivity of the measurement technique the moisture content of the cast and dried materials was lower than 0.1 wt%.

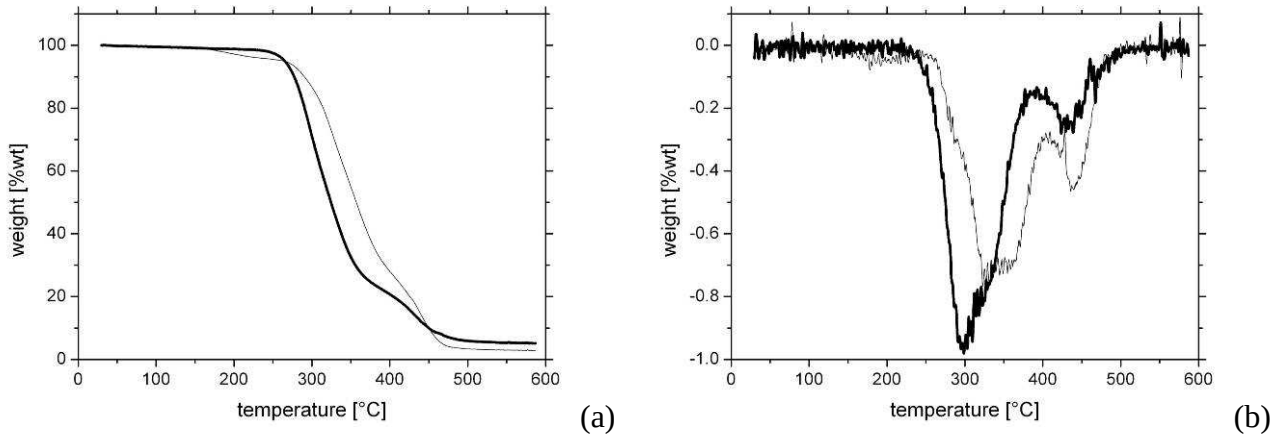

Figure 7.25. TGA (a) and DTGA (b) curves of PVOH89p (thick line) and PVOH99 (thin line).

Table 7.11. The results of the analysis of the TGA and DTGA curves: onset (T_{ON}), peak (T_{PEAK}) and endset (T_{END}) temperatures of the degradation.

Material	T_{ON} [°C]	T_{PEAK} [°C]	T_{END} [°C]
PVOH89p	244.7	327.3	508.7
PVOH89p-uMWCNT 0.05 vol%	239.0	328.0	510.0
PVOH89p-uMWCNT 0.5 vol%	249.0	345.3	507.7
PVOH99	226.3	298.7	531.0
PVOH99-uMWCNT 0.05 vol%	228.0	327.7	521.3
PVOH99-uMWCNT 0.5 vol%	226.7	299.7	511.0

7.2.3.4 DMTA

The results of the DMTA tests are showed in Figure 7.26, Figure 7.27 and Figure 7.28. The materials presented a sharp drops of the storage modulus that corresponded to the glass transition,

i.e. the γ-relaxation. Moreover the dissipative modulus and the loss factor evidenced several relaxation phenomena for all the materials: the α- and β-relaxations at about 120°C and 150°C related to the mobility of the crystalline phase, the γ-relaxation at 50-70°C related to the mobility of the amorphous phase (i.e. the glass transition) and the ε-relaxation at 0°C for PVOH89p and -50°C for PVOH99 related to the adsorbed moisture.

The data of Table 7.12 evidenced as the MWCNTs did not change the glass transition temperature in the case of PVOH99-uMWCNT composites, while the glass transition temperature decreased of about 6°C in the case of PVOH89-uMWCNT composites. Moreover it is interesting to observe the effect of the filler on the magnitude of the storage modulus. As evidenced in TABLE the modulus increase of about 4% for the composites filled with 0.05 vol% and of about 20% for the composites filled with 0.5 vol%.

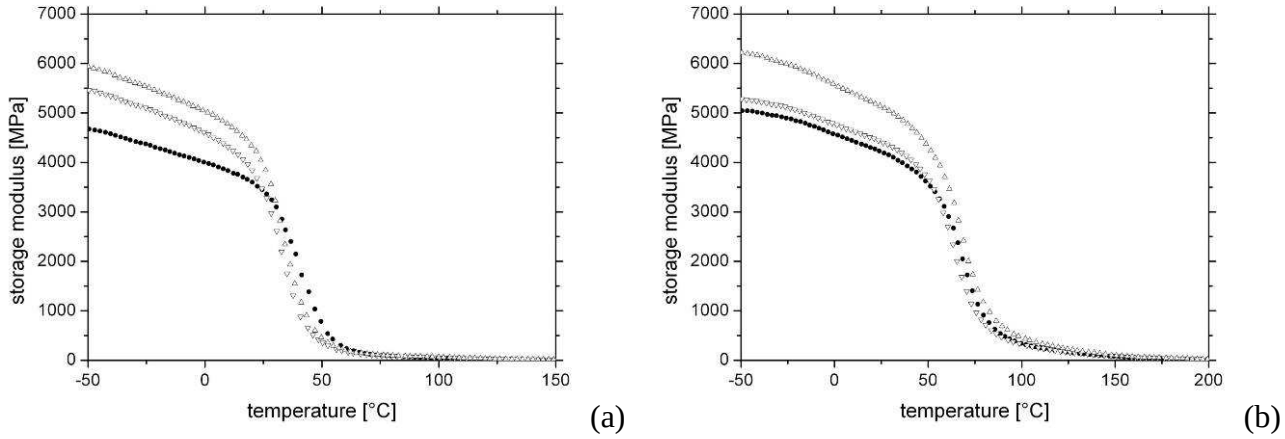

Figure 7.26. Storage modulus as a function of the temperature for (a) PVOH89p (●), PVOH89p-uMWCNT 0.05 vol% (▽) PVOH89p-uMWCNT 0.5 vol% (△) and of (b) of PVOH99 (●), PVOH99-uMWCNT 0.05 vol% (▽), PVOH99-uMWCNT 0.5 vol% (△) composites.

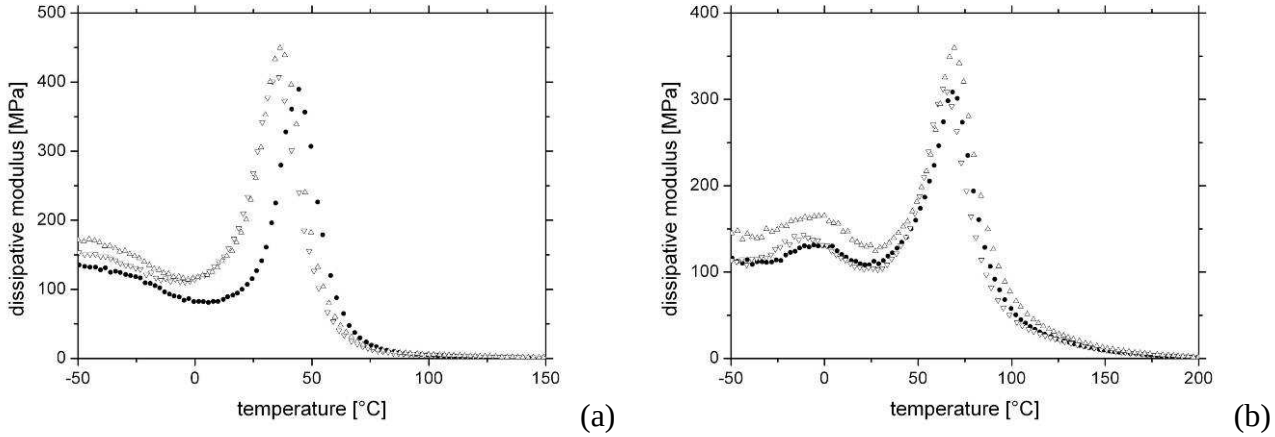

Figure 7.27. Dissipative modulus as a function of the temperature for (a) PVOH89p (●), PVOH89p-uMWCNT 0.05 vol% (▽) PVOH89p-uMWCNT 0.5 vol% (△) and of (b) of PVOH99 (●), PVOH99-uMWCNT 0.05 vol% (▽), PVOH99-uMWCNT 0.5 vol% (△) composites.

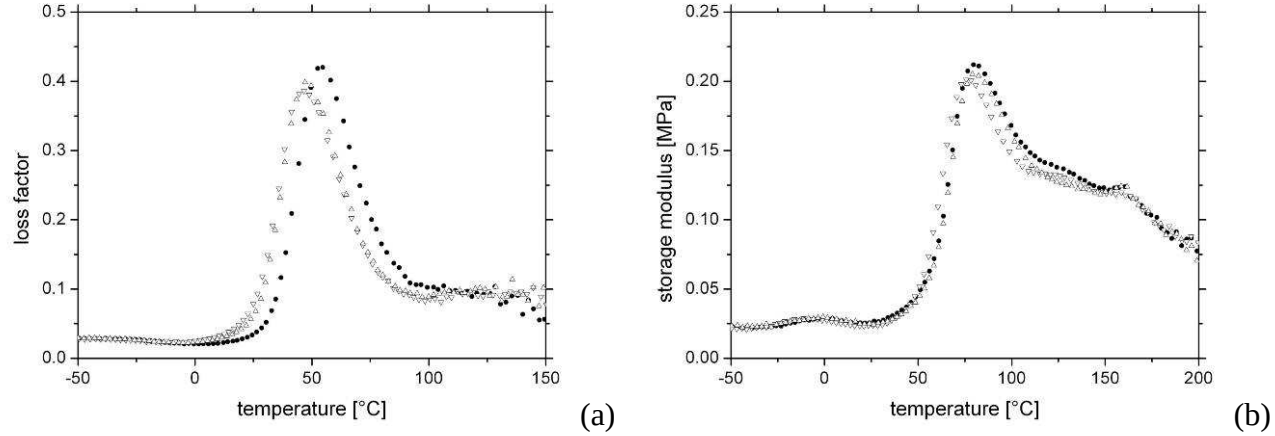

Figure 7.28. Loss factor as a function of the temperature for (a) PVOH89p (●), PVOH89p-uMWCNT 0.05 vol% (▽) PVOH89p-uMWCNT 0.5 vol% (△) and of (b) of PVOH99 (●), PVOH99-uMWCNT 0.05 vol% (▽), PVOH99-uMWCNT 0.5 vol% (△) composites.

Table 7.12. Glass transition temperature and relative change of the storage modulus at room temperature (RT) and at -50°C for PVOH-uMWCNT composites.

Material	**T_g [°C]**	**E' @ -50 [%]**	**E' @ RT [%]**
PVOH89p	54.3		
PVOH89p-uMWCNT 0.05 vol%	47.7	+17	+3.5
PVOH89p-uMWCNT 0.5 vol%	48.4	+27	+18
PVOH99	80.9		
PVOH99-uMWCNT 0.05 vol%	76.3	+4.4	+4.8
PVOH99-uMWCNT 0.5 vol%	80.8	+23	+21

7.2.4 PVOH-MWCNT (tip sonication) composites

7.2.4.1 OM

The observation of thin sections of the composite materials with an optical microscope was used to control the extent of filler agglomerates. The micrographs of Figure 7.29 evidenced the presence of agglomerates for all the composites produced up to 30 μm of diameter. While the situation was very similar for PVOH89 filled with uMWCNT and oMWCNT in presence of SDS, the dispersion was really smooth with oMWCNT without surfactants.

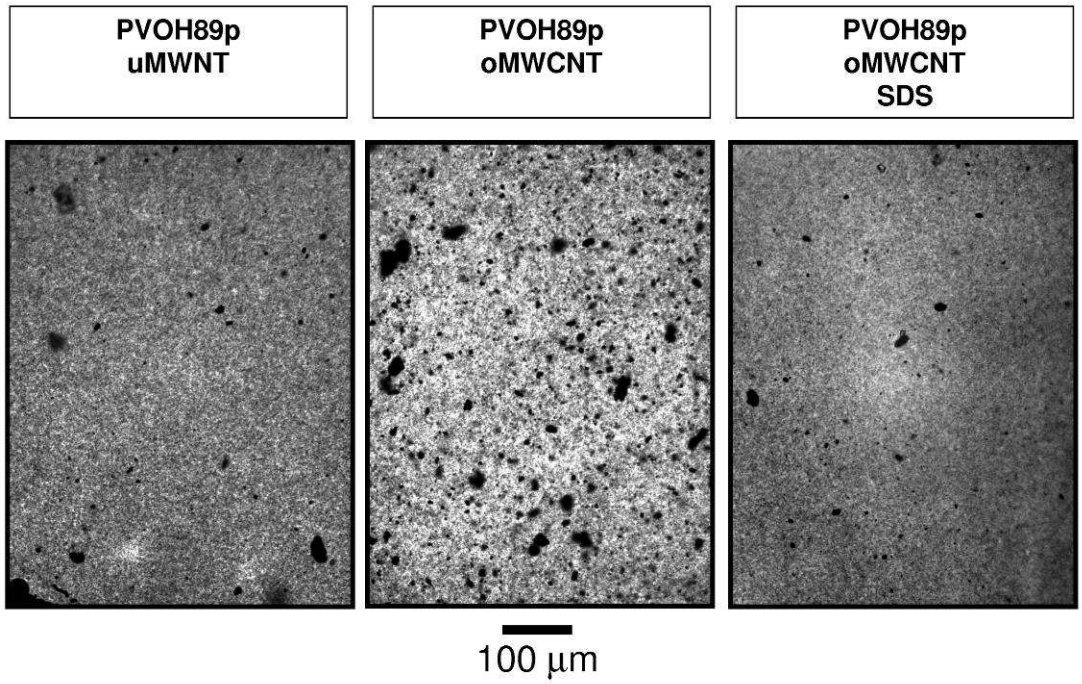

Figure 7.29. OM micrographs of PVOH89p-MWCNT.

8 Discussion

This chapter deals with the discussion of the data presented in the previous chapters. Because there are several themes to discuss, this chapter is divided in paragraphs with different topic.

8.1 The effect of the multiple extrusions on HDPE

The experimental data (see the chapter 5) evidenced as the multiple extrusion on HDPE09 induced a modification of macromolecular structure of HDPE: in particular a thermo-mechanical degradation [146, 159-162] caused by the high temperatures and the high shear stresses during the extrusion process.

The degradation phenomena regarded several aspects:

- the MWD translated to lower molecular weight (M_w) and became narrower (IP) as evidenced by GPC measurements;
- moderate cross-linking phenomena taken place as evidenced by the CSDF analysis, the methyl group content measured from IR spectra and the crystallinity content from DSC. Moreover the absence of the β-relaxation peak in DMTA measurements excluded or limited the possibility of branching phenomena;
- oxidation phenomena induced the presence of carbonyl groups along HDPE chains as evidence by IR spectra.

The most part of these phenomena taken place during the first extrusion, while others had a progressive effect on the polymer. In particular M_w progressively decreased from 144 to 126 kDa and the CSDF evidenced a progressive reduction of the presence of the fraction of the lower and higher weight chains. On the other hand the oxidation taken place essentially during the first extrusion.

The effects of HDPE09 degradation on the macroscopic properties differed: from a general point of view the main difference was present between the molten polymer at 220°C and the bulk material at room temperature. This fact could be related to complex rearrangements of the macromolecular chains induced by the thermo-mechanical degradation: the interaction of different factors (moderate

cross-linking, molecular weight loss, narrowing of MWD, very short branching, carbonyl groups) could have different effect on molten and solid polymer [25, 163]. In details the experimental data evidenced as:

- the rheological curve translated to higher viscosity at low frequency (about 10^{-1} hz) as the number of extrusions increased, while remained unchanged at medium frequency (about 10^{2} hz). While for the HDPE09 powder the begin of the Newtonian plateau at low frequency was evident, the extruded HDPE09 evidenced a clear pseudoplastic behaviour;
- the elastic modulus and the yielding decreased as the number of extrusions increased, while the yielding strain decreased;
- the fracture toughness progressively decreased as the number of extrusions increased and the microcavitation phenomena was reduced after every extrusion;
- the viscoelastic behaviour changed after three extrusion. In particular the creep resistance (creep experiments) and the storage modulus (DMTA experiments) decreased.

The most interesting effects were related to the fracture toughness and the viscoelastic behaviour. Figure 8.1 shows the fracture toughness (i.e. the specific essential work of fracture w_e) as a function of the molecular weight M_w (as the data were obtained after every extrusion). Even if this graph unfortunately does not take into account the effect of cross-linking or branching, the fracture toughness decreased linearly with the molecular weight (1.8 kJ/m^2 for a molecular weight loss of 1 kd): it is opportune to observe that general relation can not applied over a wide range of molecular weight because the reduced number of data.

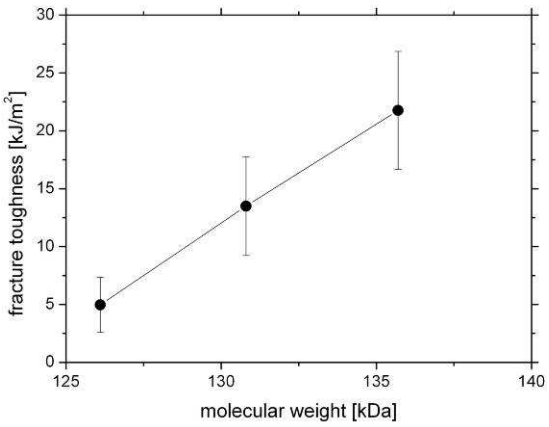

Figure 8.1. Fracture toughness as a function of the molecular weight for HDPE09.

As told before, the creep resistance and the storage modulus decreased as the number of extrusions increased. While the retardation spectra as a function of the retardation time (Figure 5.33) showed

an increasing trend, the relaxation spectra were bell-shaped curves (Figure 5.39) and in particular the curve of HDPE09 extruded three times was narrower than HDPE09 extruded only one time. By taking into account that longer chains (i.e. higher molecular weight) have higher relaxation times [8, 11], it was evident a correlation between the relaxation spectra and the MWD. Even if the irregularity of these curves did not allow to elaborate a pseudo-CSDF, it was evident as the loss of polymer fraction with the lower and higher retardation time was correlated with the loss of the polymer fraction with the lower and the higher molecular weight.

Moreover it is opportune to make some observation about the effect of the macromolecular orientation. The extrusion process induced an higher chain orientation (in the machining direction) in comparison to the compression moulding (see chapter 6): nevertheless the different processing conditions (temperature, stress and time) did not allow a direct comparison. In fact the lower creep resistance of HDPE09 produced by internal mixing and then compression moulding could be related to degradation phenomena that were not analyzed in details in this work.

8.2 The fracture behaviour of HDPE09-CB composites

The EWF parameters combined with microscope observations (OM and TEM) indicate that the fracture behaviour was strictly dependent on the CB type, on the level of dispersion of the filler in the polymer matrix and on the degradation of the polymer matrix. The influence of the last factor (analyzed in the previous paragraph) could be considered by taking into account the relative toughness of the materials, i.e. the ratio of the fracture toughness of HDPE09-CB composites to the one of HDPE09 with the same number of extrusions (Figure 5.22).

If the filler is relatively good dispersed, as in the case of the composites containing 1 vol% of CB226 extruded 2 and 3 times, and 1 vol% of CB1353 extruded 3 times, the fracture toughness markedly increases in comparison to unfilled HDPE09 matrix. On the other hand the fracture toughness slightly decreased or increased if the filler dispersion was poor: the fracture toughness increased sharply only when the filler dispersion was enough good.

Moreover, when a minimum degree of dispersion was achieved (Figure 5.1), the effect of the specific surface area of the CB was evident (Figure 5.22): the highest improvement of the toughness, the higher surface area CB. In fact the effect of CB1353 in comparison to CB226 was evident only at the third extrusion, where the dispersion level was good for both the composites. CB226 reached a good dispersion after the second extrusion and consequently HDPE09-CB226 composites maintained the same improvement of the fracture toughness after the second extrusion and the third one. On the other hand CB1353 reached a good dispersion only after the third extrusion and the fracture toughness increased.

These phenomena could be related with the breaking of the filler agglomerates during the extrusion: both HDPE09-CB underwent the same processing condition, i.e. the shear stresses and energy applied to destroy the agglomerates were the same because the torque applied by the extruder had the same value. The fracture toughness increased sharply from one extrusion to another because the agglomerate dimension decreases with a power law of the applied energy until to reach the primary particles [154-156]: thus the breakage process taken more energy (i.e. more extrusions) in the case of the particles with lower dimension (i.e. CB1353) because the agglomeration forces were the same for CB226 and CB1353 as a first approximation. Furthermore it is opportune to observe that the interaction energy of CB particles increases as their dimension decreases [32]: this fact increases more and more the energy to apply for the deagglomeration.

The increase of the fracture toughness of the HDPE09-CB composites is caused by the increasing microcavitation phenomena [25] induced by the CB during the crack propagation (Figure 5.24 and Figure 5.43). The CB particles acted as nucleation points of additive deformational phenomena, i.e. as an energy dissipation mechanism: in particular the phenomenon became stronger and stronger as the number of extrusions (i.e. the filler dispersion) increased and as the specific surface area of CB increased (both for the composites filled with 1 vol% and 0.5 vol% of CB). Moreover the importance of this phenomenon is evidenced by the increase of the propagation components of the fracture toughness that is the main components of the fracture toughness.

8.3 The creep behaviour of micro- and nanocomposites

In this paragraph the creep behaviour of HDPE based composites with a filler content of 1 vol% would be compared: HDPE25-Cu45, HDPE25-Cu10, HDPE09-CB226, HDPE09-CB1353 and HDPE09-pMWCNT. From a general point of view a creep compliance reduction was observed in the master curve (Figure 4.40 and Figure 5.30): moreover this reduction was constant over the whole range of times (up to 10^{10} s). This fact is good agreement with other results available in literature for composites filled with micrometric particles: Nielsen and Cessna [25, 133, 134] founded that the creep reduction could be closely approximate by the reciprocal of the relative elastic modulus. Unfortunately these data had errors too high in comparison to difference: so a direct comparison was not possible. Nevertheless it is possible to observe as the creep resistance was not influenced by the filler dimension if micrometric particles were considered (i.e. Cu45 and Cu10), while the creep resistance markedly increased with nanometric filler and the difference was presence between nanometric filler with different dimension (i.e. CB226 and CB1353). These considerations are possible because these fillers, i.e. Cu and CB, has the same particle aspect ratio (i.e. about 1, that is they have a spherical shape) and the polymer-filler interaction is only physical,

i.e. no (strong or weak) chemical bond is present. The reduced interaction was confirmed by SEM observations and DMTA: in the case of HDPE09-Cu composites the fracture surface was perfectly smoothing [138], while HDPE25-Cu and HDPE09-CB composites did evidence no particular phenomena in DMTA tests. However it is opportune to remember that HDPE matrices were not the same, i.e. HDPE25, HDPE09 and different processing methods. These considerations are summarized in Figure 8.2, where the relative creep compliance is a function of the filler particle dimension.

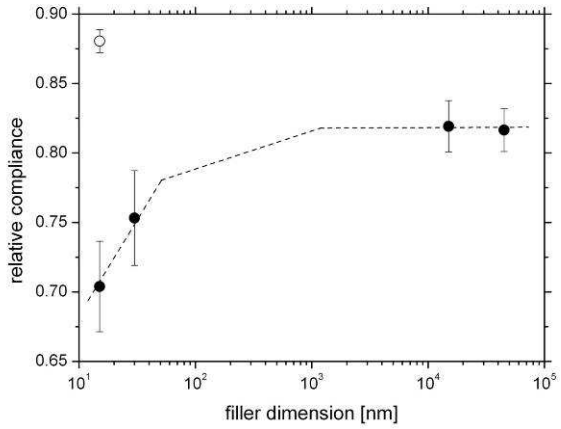

Figure 8.2. Relative compliance as a function of the filler particle dimension for HDPE based composites with a filler content of 1 vol%: HDPE25-Cu, HDPE09-CB (●) and HDPE-pMWCNT (○).

These considerations cannot be directly applied to HDPE09-pMWCNT composites: pMWCNT is a commercial masterbatch that has an unknown composition; the datasheet reports only that is a polyacrylic carrier with a MWCNT content of 50 wt%. In other words the type of interaction is unknown even if DMTA test did not evidenced any particular phenomenon. Moreover the average creep reduction is lower than the corresponding HDPE09-CB composites: even if the specific surface area was lower than both the CBs, the creep reduction was lower than HDPE25-Cu composites too.

The more interesting data in terms of creep behaviour came from the tests in the non-linear region, i.e. at higher stress. In this case the difference between the different materials became really sharp: the main effects of the filler was an increase of the creep life and a reduction of the creep rate in the secondary region. Moreover this effect was stronger and stronger as the filler dimension decreased for both HDPE25-Cu and HDPE09-CB composites as depicted in Figure 8.3 where the relative compliance rate is a function of the filler dimension. However the direct comparison of the effect of the filler dimension for HDPE25-Cu and HDPE09-CB did evidenced a general trend (Figure 8.3):

the different matrix (HDPE25 and HDPE09) probably influenced too much the creep behaviour in non-linear viscoelastic region.

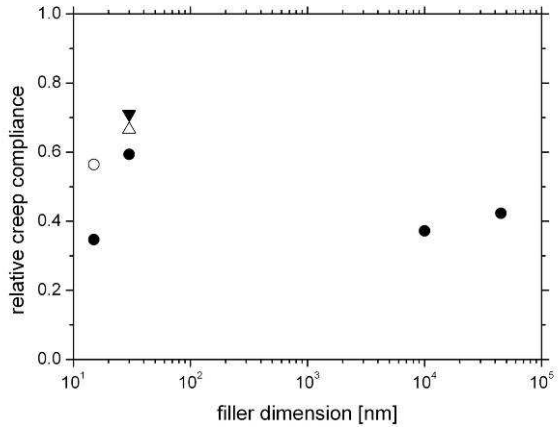

Figure 8.3. Relative creep compliance rate as a function of the filler dimension for HDPE09-Cu and HDPE09-CB composites (●), HDPE09-pMWCNT composites (○), HDPE09-uMWCNT produced in internal mixer at 135°C (▼) and 180°C (△). All the composites had a filler content of 1 vol%.

These effects could be related to the high mobility of the polymeric chains at high stress [116, 124-127, 132]: in this case the filler particles act as physical linking to hinder the movements the polymeric chains and this phenomenon reduces the creep deformation (Figure 8.4). When the filler dimension decreases and the filler content remains constant (as for HDPE composites previously described), the points of physical linking (obviously if the dispersion degree is enough good) increase and probably the reduction of mobility of the polymeric chains under stress become stronger and stronger.

Moreover it is important to observe that all these considerations are valid only with a filler homogeneously dispersed in the polymeric matrix. The short term creep test on all HDPE09-CB composites with a filler content of 1 vol% (see chapter 5) evidenced as the creep resistance of the composites increased as the degree of dispersion increased. Furthermore the effect of specific surface area of CB became evident only when a good dispersion was obtained for all the composites.

In addition a trial analysis was conducted on the creep data obtained for the master curves, i.e. the relative creep compliance (that is the ratio between the compliance of the composites and the one of the polymeric matrix). This analysis is based on the hypothesises that the filler particles and the polymer chains locked by physical linking around the filler particles undergo to creep deformation lower that the bulk polymer that is non influenced by the filler. In this way it possible to evaluate

the region around the filler particle that is under the influence of the filler particles themselves. The thickness t of this interphase region has the following expression:

Equation 8.1

$$t = \left(\frac{\left(1 - D_{composite} / D_{polymer} - \phi\right)}{SSA \cdot \rho \cdot \phi} \right)$$

where $D_{composite} / D_{polymer}$ is the average relative creep compliance, ϕ the filler volume content, SSA and ρ the specific surface area and the density of the filler. The results of this analysis are showed in Figure 8.5. The interphase thickness decreased as the filler dimension decreased for all the composites with low aspect ratio fillers (i.e. HDPE25-Cu and HDPE09-CB). Moreover a linear function in a log-log scale was used to fit and the results was $t = 0.80 \cdot D^{1.1}$: apparently the interphase region had the same dimension of the filler particles.

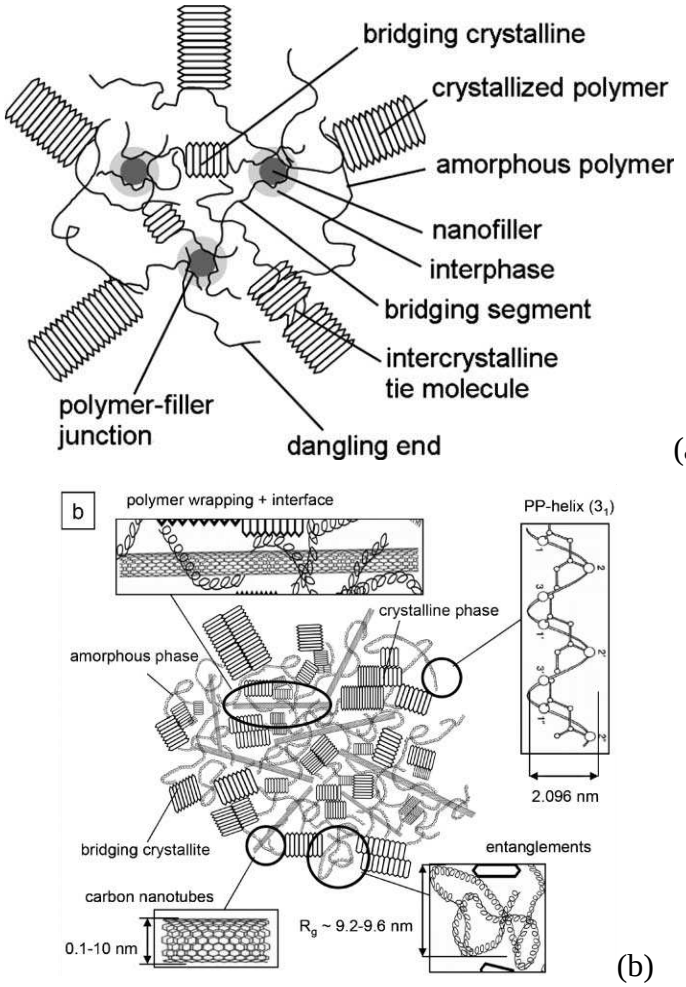

Figure 8.4. Schematically representative structure of nanofiller–semicrystalline polymer composites for (a) spherical filler particles [126] and (b) nanotubes [116].

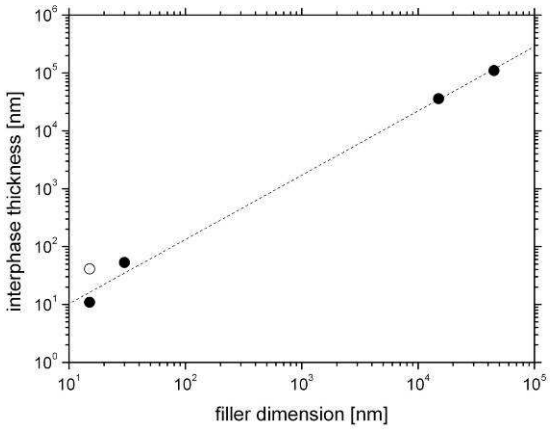

Figure 8.5. Interphase thickness as a function of the filler particle dimension for HDPE based composites with a filler content of 1 vol%: HDPE25-Cu, HDPE09-CB (●) and HDPE09-pMWCNT (○).

8.4 MWCNT based composites

This work investigated the production of MWCNT filled composites by using uMWCNT as provided by the supplier. As the results of chapter 7 evidenced, several methods employed to disperse the MWCNT into polymeric matrices: from the melt mixing to the solution mixing with sonication treatment. However in all the case agglomeration phenomena were evident (Figure 7.12, Figure 7.17, Figure 7.23 and Figure 7.29): even if the intensity of the agglomeration depended on every single case, the typical dimension of these agglomerates was 10 μm or more, i.e. not a nanocomposites was obtained. This difficulty to disperse the MWCNTs is probably related to the mixing conditions: even if the maximum stresses were applied achievable with the internal mixer for long time (20+100 rpm for 5+20 min), they were probably not enough to destroy the MWCNT agglomerates [154-157]. In fact SEM and TEM micrographs evidenced that uMWCNT contained very long nanotubes that were curled one around each other.

On the other side the mechanical properties of HDPE09-uMWCNT was only partially improved: only with very intensive mixing (20+100 rpm for 5+20 min) was able to destroy enough the agglomerates (even if a lot of agglomerates remained) in order to induce an increase of the elastic modulus (about 10%). Anyway the strain at brake sharply decreased for all the composites: at least 10 times in comparison to the matrix, i.e. from 1500-2000% to 100% or less. This fact was directly related to the agglomeration [25, 91]. On the other side PVOH-uMWCNT composites showed an evident increasing of the elastic modulus, i.e. about +20% with a filler content of 0.5 vol% and the filler dispersion was not good in this case too. These results was only partially in agreement with the literature [99, 101, 102, 115, 164] just because the agglomeration.

Table 8.1. Mechanical properties of uMWCNT filled composites: variations of elastic modulus (E) and yielding stress (σ_y) respect to the base polymeric matrix.

Material	Processing	E [%]	σ_y [%]
HDPE09-uMWCNT 0.5 vol%	Extruder	+2	–3
HDPE09-uMWCNT 0.5 vol%	Internal mixer, 135°C, 20+100rpm, 5+20min	+16	+4
HDPE09-uMWCNT 0.5 vol%	Internal mixer, 180°C, 20rpm, 15min	–3	+3
HDPE09-uMWCNT 0.5 vol%	Internal mixer, 180°C, 20+100rpm, 5+20min	+10	+9
PVOH89p-uMWCNT 0.5 vol%	Solution mixing (sonication)	+18	n.a.
PVOH99-uMWCNT 0.5 vol%	Solution mixing (sonication)	+21	n.a.

n.a. = not available

Furthermore the more interesting results were obtained fro the creep experiments on HDPE09-uMWCNT composites produced with internal mixer at 135°C and 180°C with an intensive mixing (20+100 rpm for 5+20 min). The main difference was between the test in the linearly viscoelastic region (i.e. the tests at low stress) and the non-linear viscoelastic region (i.e. the tests at high stress):

- when the stress was low, the composites had the same behaviour of the matrix or worse (Figure 7.21 and Figure 7.22);
- when the stress was high the creep life of the composites increased and the creep rate in the secondary region decreased in comparison to HDPE09 matrix (Figure 7.21 and Figure 7.22).

Moreover the tests conducted for the materials produced at 180°C evidenced an increase of the creep resistance from HDPE09, to the composite with a filler content of 0.05 vol% and then to the composite with a filler content of 0.5 vol% (Figure 7.22).

Probably the same phenomena described in the previous paragraph for HDPE25-Cu and HDPE09-CB composites taken place: the filler particles act as physical linking to hinder the movements the polymeric chains and this phenomenon reduces the creep deformation [116, 124-127, 132]. Moreover, as proposed by Ganss et al. [116] the high stress could induce a rearrangements of the filler in the polymeric matrix (Figure 8.6). This phenomena could not take place at low stress: in this way the filler remained in agglomerates and the creep behaviour was not improved [118, 127].

In conclusion it is interesting to observe a phenomenon present for all the composites filled with uMWCNT. Even if the crystallinity and the melting temperature was not significantly affected by the MWCNTs, the onset temperature of the crystallization shifted up always of about 1°C. This fact was probably correlated with a nucleating effect [124, 165-167]: the agglomeration reduced probably the effects induced by this interaction between the matrix and the filler.

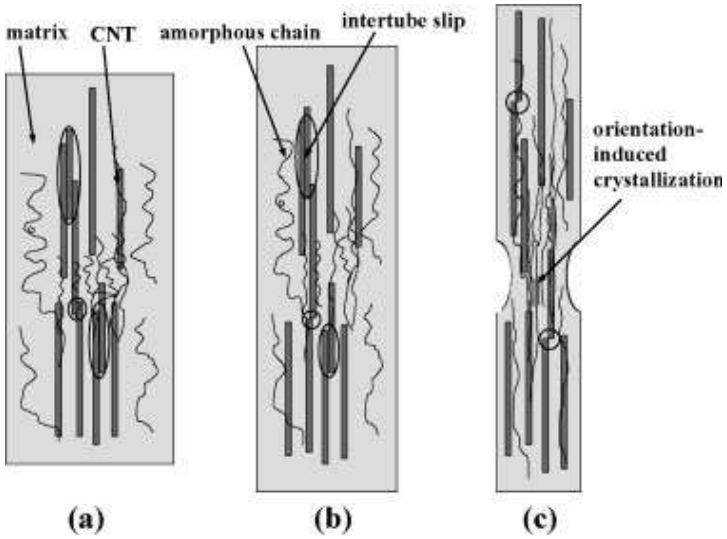

Figure 8.6. Schematic deformation model and orientation-induced crystallization of CNT/PP composite under uniaxial stress: (a) before loading, (b) under small load levels, and (c) under high load levels [124].

8.5 Modification of MWCNTs

The production of composites filled with uMWCNT evidenced as the key factor was the filler dispersion. To allow an easy dispersion, the literature [1, 2, 28, 37] suggest modification treatments of MWCNTs. And for this reason two treatments were employed on uMWCNT:

- an oxidation treatment with boiling HNO_3 in order to introduce new functional groups on the surface and reduce the length of the nanotubes [63-68];
- a modification treatment of the surface of oxidized uMWCNT with silane coupling agents in order to introduce short polymeric chains compatible with polyethylene [73, 74].

EDAX, FTIR and TGA analyses evidenced the presence of carboxylic and hydroxyl groups on the surface [150] and a drastic reduction of the residual catalyst. Even if it was unfortunately not possible to employ a titration analysis [68] in order to determine the exact surface density of these groups, the analyses evidenced as carboxylic acids were the main groups on the filler surface. Moreover TEM micrographs evidenced a sharp shortening of the MWCNT length, i.e. a lower agglomeration with the same preparation method of the sample. This fact could be probably an advantage during the dispersion because less energy would be required to destroy the agglomerates. Moreover the treatment induced an increase of the surface area from 83 to 107 m^2/g as effect of oxidation effect of HNO_3 that removed the impurity [168].

Despite the treatment on MWCNTs, the composites based on PVOH89p and oMWCNT still evidenced a very high agglomeration, that was partially reduced with the help of a surfactant, i.e. SDS. Even if the dispersion would be easier in comparison to uMWCNT, more investigations are required to understand the solution mixing of these systems. Several works [105, 169, 170] found

that the solution quality, i.e. the final dispersion of the composites in this case, was strongly influenced by the type of carbon nanotubes and surfactants and by their concentrations: the work conducted on the system PVOH89p-oMWCNT-SDS-water was undoubtedly not enough to obtain a good filler dispersion condition. The concentration of PVOH89p in the aqueous solution, for example, could be a very important parameters because the presence of PVOH changes the surfactants solution equilibrium and then because the viscosity of the system is increased and more energy for the dispersion is required.

On the other side the silane modification treatment did evidence no results. If silane chains were linked to the MWCNT surface, a new degradation peak had to be present in TGA [152, 153]: unfortunately the TGA curves remained the same founded for oMWCNT before the treatment. This fact, i.e. no reaction, were probably related with the too low hydroxyl content on the MWCNT surface: the silanes have a too low kinetics with the carboxylic acid that were the main groups on oMWCNT. To improve these reactions would be necessary to employ a preliminary reduction treatment to convert the carboxylic acids to hydroxyl groups [73, 74].

9 Conclusions

The EWF parameters combined with microscope observations indicate that the fracture behaviour of HDPE09-CB composites is strictly dependent on the CB type, on the level of dispersion of the filler in the polymer matrix and on the degradation of the polymer matrix. In particular:

- only if the filler is relatively good dispersed, the fracture toughness markedly increases in comparison to unfilled HDPE09 matrix;
- if a minimum degree of dispersion is achieved, as higher the specific surface area of the CB as higher the improvement of the toughness. Moreover the dispersion of CBs with higher specific surface area is more difficult;
- the increasing fracture toughness of the HDPE09-CB composites is caused by the increasing microcavitation phenomena induced by the CB during the crack propagation;
- finally the absolute value of the fracture toughness evaluated with the specific essential work of fracture depends on the HDPE matrix that can undergo a thermo-mechanical degradation during the extrusion process.

The creep behaviour of the HDPE based composites is influenced by the filler dimension (if the same aspect ratio, i.e. the shape, is the same): in particular this work investigated the creep behaviour of composites filled with Cu powders and CBs.

From a general point the filler results to substantially increase the creep resistance of the HDPE matrix. This effect is detectable in the linear viscoelastic region (i.e. at low stresses or temperatures), and it becomes more and more evident in the non-linear viscoelastic or viscoplastic region (i.e. at high stresses or temperatures). Moreover the creep resistance results increased as the filler dimension decreases. While this effect is just a constant reduction of the creep compliance in the linear viscoelastic region, it become stronger and stronger in the non-linear viscoelastic region. In particular the creep life results increasing and the creep rate decreasing as the filler dimension decreases.

The filler particles probably act as physical linking points that hinder the movements the polymeric chains, i.e. they reduce the creep deformation. When the filler dimension decreases and the filler content remains constant, the points of physical linking increases and the reduction of mobility of the polymeric chains under stress become stronger and stronger.

As for the filler particles with low aspect ratio, the addition of a small amount of MWCNTs (pMWCNT or uMWCNT), that have high aspect ratio, can reduces the mobility of the host polymeric chains and this blocking effect substantially increases the creep resistance of the HDPE matrix. The key factor is the degree of dispersion of the filler into the matrix:

- if a minimum degree of dispersion is achieved, the creep resistance increases in the linear viscoelastic region (i.e. at low stresses or temperatures) or at least it do not decrease. Otherwise (i.e. in the case of a poor dispersion) the creep resistance decreases;
- even if the degree of dispersion is not good, the creep resistance increases in the non-linear viscoelastic or viscoplastic region (i.e. at high stresses or temperatures).

The former phenomena are probably related the effect of the poor dispersion, i.e. slipping phenomena occurring the filler particles; while the last phenomena are probably related to rearrangements of the filler in the polymeric matrix induced by high stress.

The production of composites with uMWCNT evidences as the key factor is the dispersion processing: the starting uMWCNT are too agglomerated. For this reason an oxidation treatment with boiling HNO_3 was employed: the main effects were the introduction of carboxylic groups on the MWCNT surface and the reduction of the length. Probably an initial lower entanglement level would reduce the problems related to the filler dispersion.

10 References

1. Ajayan, P.M., P.V. Braun, and L.S. Schadler, *Nanocomposite science and technology*. 2003, Weinheim: Wiley-VCH.
2. Breuer, O., *Big Returns From Small Fibers: A Review of Polymer/Carbon Nanotube Composites.* Polymer Composites, 2004. **25**(6): p. 630-645.
3. Goettler, L.A., K.Y. Lee, and H. Thakkar, *Layered silicate reinforced polymer nanocomposites: Development and applications.* Polymer Reviews, 2007. **47**: p. 291-317.
4. Hashemi, S., *Temperature dependence of work of fracture parameters in polybutylene terephthalate (PBT).* Polymer Engineering and Science, 2000. **40**(6): p. 1435-1446.
5. Thostenson, E.T., Z.F. Ren, and T.W. Chou, *Advances in the science and technology of carbon nanotubes and their composites: a review.* Composites Science and Technology, 2001. **61**: p. 1899-1912.
6. *http://www.isiwebofknowledge.com/*.
7. Peacock, A.J., *Handbook of Polyethylene: Structures, Properties, and Applications*. 2000, New York, N.Y.; Basel: Marcel Dekker.
8. Ferry, J.D., *Viscoelastic properties of polymers*. 3 ed. 1980, New York: Wiley.
9. Findley, W.N., J.S. Lai, and K. Onaran, *Creep and Relaxation of Nonlinear Viscoelastic Materials*. 2 ed. 1989, New York: Dover Pubblications.
10. Lakes, R.S., *Viscoelastic Solids*. 1999, Boca Raton, London, New York, Washington DC: CRC Press.
11. Riande, E., et al., *Polymer Viscoelasticity. Stress and Strain in Practice*. 2000, New York, Basel: Marcel Dekker.
12. McCrum, N.G., B.E. Read, and G. Williams, *Anelastic and dielectric effects in polymeric solids*. 1984, New York: Dover.
13. Plazek, D.J., *A myopic review of the viscoelastic behavior of polymers.* Journal of Non-Crystalline Solids, 1991. **131-133**(2): p. 836-851.
14. *ESIS Test Protocol for Essential Work of Fracture*. 2002.
15. Arkhireyeva, A. and S. Hashemi, *Fracture behaviour of polyethylene naphthalate (PEN).* Polymer, 2002. **43**: p. 289-300.
16. Arkhireyeva, A., S. Hashemi, and M. O'Brien, *Factors affecting work of fracture of uPVC film.* Journal of Materials Science, 1999. **34**: p. 5961-5974.
17. Broberg, K.B., *Critical review of some theories in fracture mechanics.* International Journal of Fracture, 1968. **4**(1): p. 11-19.
18. Cotterell, B. and J.K. Reddel, *The essential work of plane stress ductile fracture.* International Journal of Fracture, 1977. **13**(3): p. 267-277.
19. Hill, R., *On discontinuous plastic states, with special reference to localized necking in thin sheets.* Journal of the Mechanics and Physics of Solids, 1952. **1**(1): p. 19-30.
20. Karger-Kocsis, J., T. Czigány, and E.J. Moskala, *Deformation rate dependence of the essential and non-essential work of fracture parameters in an amorphous copolyester.* Polymer, 1998. **39**: p. 3939-3944.

21. Mai, Y.W. and B. Cotterell, *On the essential work of ductile fracture in polymers.* International Journal of Fracture, 1986. **32**: p. 105-125.
22. Mai, Y.W., et al., *The essential work of plane stress ductile fracture of linear polyethylenes.* Polymer Engineering and Science, 1987. **27**(11): p. 804-809.
23. Saleemi, A.S. and J.A. Nairn, *The plane-strain essential work of fracture as a measure of the fracture toughness of ductile polymers.* Polymer Engineering and Science, 1990. **30**(4): p. 211-218.
24. Mallick, P.K., *Fiber-reinforced composites: materials, manufacturing, and design*. 1988, New York, N.Y. [etc.]: Dekker.
25. Nielsen, L.E. and R.F. Landel, *Mechanical properties of polymers and composites*. 1994, New York, N.Y. [etc.]: Dekker.
26. Hussain, F., et al., *Polymer-matrix nanocomposites, processing, manufacturing, and application: An overview*. Journal of Composite Materials, 2006. **40**: p. 1511-1575.
27. Szleifer, I. and R. Yerushalmi-Rozen, *Polymers and carbon nanotubes—dimensionality, interactions and nanotechnology.* Polymer, 2005. **46**(19): p. 7803-7818.
28. Xie, X.L., Y.W. Mai, and X.P. Zhou, *Dispersion and alignment of carbon nanotubes in polymer matrix: A review.* Materials Science & Engineering R-Reports, 2005. **49**: p. 89-112.
29. Tjong, S.C., *Structural and mechanical properties of polymer nanocomposites.* Materials Science and Engineering R, 2006. **53**: p. 73-197.
30. Qian, D., et al., *Load transfer and deformation mechanisms in carbon nanotube-polystyrene composites.* Applied Physics Letters, 2000. **76**(20): p. 2868-2870.
31. Wichmann, M.H.G., K. Schulte, and H.D. Wagner, *On nanocomposite toughness.* Composites Science and Technology, 2008. **68**(1): p. 329-331.
32. Donnet, J.B., R.C. Bansal, and M.J. Wang, eds. *Carbon black: science and technology*. 1993, Dekker: New York.
33. Wypych, G., *Handbook of fillers*. 2000, New York: ChemTec Publishing.
34. Heidenreich, R.D., W.M. Hess, and L.L. Ban, *A test object and criteria for high resolution electron microscopy.* Journal of Applied Crystallography, 1968. **1**(1): p. 1-19.
35. Jaeger, C., et al., *Spectral properties of carbon black.* Journal of Non-Crystalline Solids, 1999. **258**(1-3): p. 161-179.
36. Iijima, S., *Helical microtubules of graphitic carbon.* Nature, 1991. **354**: p. 56-58.
37. Grobert, N., *Carbon nanotubes - becoming clean.* Materials Today, 2007. **10**(1-2): p. 2835.
38. Haddon, R.C., *Carbon Nanotubes.* Accounts of Chemical Research, 2002. **35**(12): p. 997.
39. Meyyappan, M., ed. *Carbon nanotubes: science and applications*. 2005, CRC press: Boca Raton, Fla. [etc.].
40. Reich, S., Thomsen, and J. Maultzsch, *Carbon nanotubes: basic concepts and physical properties*. 2004, Weinheim: Wiley-VCH.
41. Tomanek, D. and R.J. Enbody, eds. *Science and application of nanotubes*. 2000, Kluwer academic: New York, N.Y. [etc.].
42. Salvetat, J.-P., et al., *Elastic and Shear Moduli of Single-Walled Carbon Nanotube Ropes.* Physical Review Letters, 1999. **82**(5): p. 944-947.
43. Shi, Z., et al., *Purification of single-wall carbon nanotubes.* Solid State Communications, 1999. **112**: p. 35-37.
44. Tohji, K., et al., *Purifying single-walled nanotubes.* Nature, 1996. **383**: p. 679.
45. Xu, Y.-Q., et al., *Controlled Multistep Purification of Single-Walled Carbon Nanotubes.* Nano Letters, 2005. **5**(1): p. 163-168.
46. Ajayan, P.M., et al., *Opening carbon nanotubes with oxygen and implications for filling.* Nature, 1993. **362**: p. 522-525.
47. Ebbesen, T.W., et al., *Purification of nanotubes.* Nature, 1994. **367**: p. 519.
48. Dujardin, E., et al., *Purification of Single-Shell Nanotubes.* Advanced Materials, 1998. **10**(8): p. 611-613.

49. Duesberg, G.S., et al., *Chromatography of Carbon Nanotubes.* Syntethic Metals, 1999. **103**: p. 2484-2485.
50. Duesberg, G.S., et al., *Separation of carbon nanotubes by size exclusion chromatography.* Chemical Communications, 1998. **8**: p. 435-436.
51. Duesberg, G.S., et al., *Chromatographic size separation of single-wall carbon nanotubes.* Applied Physics A, 1998. **67**(1): p. 117-119.
52. Yudasaka, M., et al., *Effect of an organic polymer in purification and cutting of single-wall carbon nanotubes.* Applied Physics A, 2000. **71**(4): p. 449-451.
53. Shelimov, K.B., et al., *Purification of single-wall carbon nanotubes by ultrasonically assisted filtration.* Chemical Physics Letters, 1998. **282**(5-6): p. 429-434.
54. Blase, X., et al., *Boron-Mediated Growth of Long Helicity-Selected Carbon Nanotubes.* Physical Review Letters, 1999. **83**(24): p. 5078-5081.
55. Carroll, D.L., et al., *Effects of Nanodomain Formation on the Electronic Structure of Doped Carbon Nanotubes.* Physical Review Letters, 1998. **81**(11): p. 2332-2335.
56. Khabashesku, V.N., W.E. Billups, and J.L. Margrave, *Fluorination of Single-Wall Carbon Nanotubes and Subsequent Derivatization Reactions.* Accounts of Chemical Research, 2002(35): p. 1087-1085.
57. Bahr, J.L. and J.M. Tour, *Highly Functionalized Carbon Nanotubes Using in Situ Generated Diazonium Compounds.* Chemistry of Materials, 2001. **13**(11): p. 3823-3824.
58. Bahr, J.L., et al., *Functionalization of carbon nanotubes by electrochemical reduction of aryl diazonium salts: A bucky paper electrode.* Journal of the American Chemical Society, 2001. **123**(27): p. 6536-6542.
59. Mitchell, C.A., et al., *Dispersion of Functionalized Carbon Nanotubes in Polystyrene.* Macromolecules, 2002. **35**(23): p. 8825-8830.
60. Bubert, H., et al., *Characterization of the uppermost layer of plasma-treated carbon nanotubes.* Diamond and Related Materials, 2003. **12**(3-7): p. 811-815.
61. Chen, Q., et al., *Plasma Activation of Carbon Nanotubes for Chemical Modification.* Journal of Physical Chemistry B, 2001. **105**(3): p. 618-622.
62. Chen, S., et al., *A new approach to the functionalization of single-walled carbon nanotubes with both alkyl and carboxyl groups.* Chemical Physics Letters, 2005. **402**(4-6): p. 312-317.
63. Dillon, A.C., et al., *A Simple and Complete Purification of Single-Walled Carbon Nanotube Materials.* Advanced Materials, 1999. **11**(16): p. 1354-1358.
64. Jia, Z., et al., *Production of short multi-walled carbon nanotubes.* Carbon, 1999. **37**(6): p. 903-906.
65. Marshall, M.W., S. Popa-Nita, and J.G. Shapter, *Measurement of functionalised carbon nanotube carboxylic acid groups using a simple chemical process.* Carbon, 2006. **44**(7): p. 1137-1141.
66. Rosca, I.D., et al., *Oxidation of multiwalled carbon nanotubes by nitric acid.* Carbon, 2005. **43**(15): p. 3124-3131.
67. Shaffer, M.S.P., X. Fan, and A.H. Windle, *Dispersion and packing of carbon nanotubes.* Carbon, 1998. **36**(11): p. 1603-1612.
68. Hu, H., et al., *Determination of the acidic sites of purified single-walled carbon nanotubes by acid-base titration.* Chemical Physics Letters, 2001. **345**(1-5): p. 25-28.
69. Hill, D.E., et al., *Functionalization of Carbon Nanotubes with Polystyrene.* Macromolecules, 2002. **35**: p. 9466-9471.
70. Liu, J., et al., *Fullerene Pipes.* Science, 1998. **280**(5367): p. 1253-1256.
71. Wang, Y., Z. Iqbal, and S.V. Malhotra, *Functionalization of carbon nanotubes with amines and enzymes.* Chemical Physics Letters, 2005. **402**(5): p. 793-797.
72. Yang, Y., et al., *Electron transfer chemistry of octadecylamine-functionalized single-walled carbon nanotubes.* Electrochimica Acta, 2005. **50**(15): p. 3061-3067.

73. Ma, P.C., J.-K. Kim, and B.Z. Tang, *Effects of silane functionalization on the properties of carbon nanotube/epoxy nanocomposites.* Composites Science and Technology, 2007. **67**: p. 2965–2972.
74. Shanmugharaj, A.M., et al., *Physical and chemical characteristics of multiwalled carbon nanotubes functionalized with aminosilane and its influence on the properties of natural rubber composites.* Composites Science and Technology, 2007. **67**: p. 1813-1822.
75. Curran, S.A., et al., *Thiolation of carbon nanotubes and sidewall functionalization.* Journal of Material Research, 2006. **21**(4): p. 1012-1018.
76. Abdel-Goad, M. and P. Pötschke, *Rheological characterization of melt processed polycarbonate-multiwalled carbon nanotube composites.* Journal of Non-Newtonian Fluid Mechanics, 2005. **128**(1): p. 2-6.
77. Bhattacharyya, A.R., et al., *Effect of encapsulated SWNT on the mechanical properties of melt mixed PA12/SWNT composites.* Chemical Physics Letters, 2004. **392**(1-3): p. 28-33.
78. Cooper, C.A., et al., *Distribution and alignment of carbon nanotubes and nanofibrils in a polymer matrix.* Composites Science and Technology, 2002. **62**(7-8): p. 1105-1112.
79. Foulger, S.H.G., Richard V., *Intelligent Textiles Based on Environmentally Responsive Fibers.* National Textile Center Research Briefs, 2003.
80. McNally, T., et al., *Polyethylene multiwalled carbon nanotube composites.* Polymer, 2005. **46**(19): p. 8222-8232.
81. McNally, T., et al., *Polyamide-12 layered silicate nanocomposites by melt blending.* Polymer, 2003. **44**(9): p. 2761-2772.
82. Pötschke, P., et al., *Rheological and dielectrical characterization of melt mixed polycarbonate-multiwalled carbon nanotube composites.* Polymer, 2004. **45**(26): p. 8863-8870.
83. Pötschke, P., A.R. Bhattacharyya, and A. Janke, *Carbon nanotube-filled polycarbonate composites produced by melt mixing and their use in blends with polyethylene.* Carbon, 2004. **42**(5-6): p. 965-969.
84. Pötschke, P., A.R. Bhattacharyya, and A. Janke, *Melt mixing of polycarbonate with multiwalled carbon nanotubes: microscopic studies on the state of dispersion.* European Polymer Journal, 2004. **40**(1): p. 137-148.
85. Pötschke, P., A.R. Bhattacharyya, and A. Janke, *Morphology and electrical resistivity of melt mixed blends of polyethylene and carbon nanotube filled polycarbonate.* Polymer, 2003. **44**(26): p. 8061-8069.
86. Pötschke, P., S.M. Dudkin, and I. Alig, *Dielectric spectroscopy on melt processed polycarbonate—multiwalled carbon nanotube composites.* Polymer, 2003. **44**(17): p. 5023-5030.
87. Pötschke, P., T.D. Fornes, and D.R. Paul, *Rheological behavior of multiwalled carbon nanotube/polycarbonate composites.* Polymer, 2002. **43**(11): p. 3247-3255.
88. Schartel, B., et al., *Fire behaviour of polyamide 6/multiwall carbon nanotube nanocomposites.* European Polymer Journal, 2005. **41**(5): p. 1061-1070.
89. Tang, W., M.H. Santare, and S.G. Advani, *Melt processing and mechanical property characterization of multi-walled carbon nanotube/high density polyethylene (MWNT/HDPE) composite films.* Carbon, 2003. **41**(14): p. 2779-2785.
90. Valentini, L., et al., *Morphological characterization of single-walled carbon nanotubes-PP composites.* Composites Science and Technology, 2003. **63**: p. 1149–1153.
91. Andrews, R., et al., *Fabrication of Carbon Multiwall Nanotube/Polymer Composites by Shear Mixing.* Macromolecular Materials and Engineering, 2002. **287**(6): p. 395-403.
92. Kearns, J.C. and R.L. Shambaugh, *Polypropylene Fibers Reinforced with Carbon Nanotubes.* Journal of Applied Polymer Science, 2002. **86**: p. 2079–2084.
93. Guo, P., et al., *Fabrication and mechanical properties of well-dispersed multiwalled carbon nanotubes/epoxy composites.* Composites Science and Technology, 2007. **67**: p. 3331-3337.

94. Yeh, M.-K., N.-H. Tai, and J.-H. Liu, *Mechanical behavior of phenolic-based composites reinforced with multi-walled carbon nanotubes.* Carbon, 2006. **44**: p. 1-9.
95. Barraza, H.J., et al., *SWNT-Filled Thermoplastic and Elastomeric Composites Prepared by Miniemulsion Polymerization.* Nano Letters, 2002. **2**(8): p. 797-802.
96. Bonduel, D., et al., *Supported coordination polymerization: a unique way to potent polyolefin carbon nanotube nanocomposites.* Chemical Communications, 2005(6): p. 781–783.
97. Zeng, H., et al., *In situ polymerization approach to multiwalled carbon nanotubes-reinforced nylon 1010 composites: Mechanical properties and crystallization behavior.* Polymer, 2006. **47**: p. 113-122.
98. Kang, M., S.J. Myung, and H.-J. Jin, *Nylon 610 and carbon nanotube composite by in situ interfacial polymerization.* Polymer, 2006. **47**: p. 3961–3966.
99. Cadek, M., et al., *Reinforcement of Polymers with Carbon Nanotubes: The Role of Nanotube Surface Area.* Nano Letters, 2004. **4**(2): p. 353-356.
100. Du, F., J.E. Fischer, and K.I. Winey, *Coagulation method for preparing single-walled carbon nanotube/poly(methyl methacrylate) composites and their modulus, electrical conductivity, and thermal stability.* Journal of Polymer Science Part B: Polymer Physics, 2003. **41**(24): p. 3333-3338.
101. Mi, Y., et al., *Morphological and mechanical properties of bile salt modified multi-walled carbon nanotube/poly(vinyl alcohol) nanocomposites.* Composites: Part A, 2007. **38**: p. 2041–2046.
102. Ryan, K.P., et al., *Multiwalled carbon nanotube nucleated crystallization and reinforcement in poly (vinyl alcohol) composites.* Synthetic Metals, 2006. **156**: p. 332-335.
103. Probst, O., et al., *Nucleation of polyvinyl alcohol crystallization by single-walled carbon nanotubes.* Polymer, 2004. **45**(13): p. 44737-4443.
104. Zhang, X.F., et al., *Poly(vinyl alcohol)/SWNT composite film.* Nano Letters, 2003. **3**(9): p. 1285-1288.
105. Islam, M.F., et al., *High Weight Fraction Surfactant Solubilization of Single-Wall Carbon Nanotubes in Water.* Nano Letters, 2003. **3**(2): p. 269 - 273.
106. Biercuk, M.J., et al., *Carbon nanotube composites for thermal management.* Applied Physics Letters, 2002. **80**(15): p. 2767-2769.
107. Safadi, B., R. Andrews, and E.A. Grulke, *Multiwalled Carbon Nanotube Polymer Composites: Synthesis and Characterization of Thin Films.* Journal of Applied Polymer Science, 2002. **84**: p. 2660–2669.
108. Xiao, K.Q., L.C. Zhang, and I. Zarudi, *Mechanical and rheological properties of carbon nanotube-reinforced polyethylene composites.* Composites Science and Technology, 2007. **67**: p. 177-182.
109. Fakhru'l-Razi, A., et al., *Effect of multi-wall carbon nanotubes on the mechanical properties of natural rubber.* Composite Structures, 2006. **75**: p. 496-500.
110. Chen, L., X.-J. Pang, and Z.-L. Yu, *Study on polycarbonate/multi-walled carbon nanotubes composite produced by melt processing.* Materials Science and Engineering A, 2007. **457**: p. 287–291.
111. Chen, W., X. Tao, and Y. Liu, *Carbon nanotube-reinforced polyurethane composite fibers.* Composites Science and Technology, 2006. **66**: p. 3029-3034.
112. Zhao, P., et al., *Excellent tensile ductility in highly oriented injection-molded bars of polypropylene/carbon nanotubes composites.* Polymer, 2007. **48**: p. 5688-5695.
113. Jin, S.H., Y.-B. Park, and K.H. Yoon, *Rheological and mechanical properties of surface modified multi-walled carbon nanotube-filled PET composite.* Composites Science and Technology, 2007. **67**: p. 3434–344.

114. Yeh, M.-K., N.-H. Tai, and Y.-J. Lin, *Mechanical properties of phenolic-based nanocomposites reinforced by multi-walled carbon nanotubes and carbon fibers.* Composites: Part A, 2008. **39**: p. 677-684.
115. Coleman, J.N., et al., *High-performance nanotube-reinforced plastics: Understanding the mechanism of strength increase.* Advanced Functional Materials, 2004. **14**(8): p. 791-798.
116. Ganss, M., et al., *Temperature Dependence of Creep Behavior of PP–MWNT Nanocomposites.* Macromolecular Rapid Communications, 2007. **28**: p. 1624–1633.
117. Joshi, M. and V. Viswanathan, *High-Performance Filaments from Compatibilized Polypropylene/Clay Nanocomposites.* Journal of Applied Polymer Science, 2006. **102**: p. 2164–2174.
118. Lietz, S., et al., *Improvement of the Mechanical Properties and Creep Resistance of SBS Block Copolymers by Nanoclay Fillers.* Macromolecular Materials and Engineering, 2007. **292**: p. 23-32.
119. Pegoretti, A., A. Dorigato, and A. Penati, *Tensile mechanical response of polyethylene – clay nanocomposites.* eXPRESS Polymer Letters, 2007. **1**(3): p. 123–131.
120. Ranadea, A., et al., *Maleated and non-maleated polyethylene–montmorillonite layered silicate blown films: creep, dispersion and crystallinity.* Polymer, 2005. **46**: p. 7323–7333.
121. Shen, L., et al., *Nanoindentation and morphological studies on nylon 66 nanocomposites. I. Effect of clay loading.* Polymer, 2004. **45**: p. 3341–3349.
122. Shen, L., W.C. Tjiu, and T. Liu, *Nanoindentation and morphological studies on injection-molded nylon-6 nanocomposites.* Polymer, 2005. **46**: p. 11969–11977.
123. Shen, L., et al., *Nanoindentation and Morphological Studies of Epoxy Nanocomposites.* Macromolecular Materials and Engineering, 2006. **291**: p. 1358–1366.
124. Yang, J., et al., *Creep Resistant Polymer Nanocomposites Reinforced with Multiwalled Carbon Nanotubes.* Macromolecular Rapid Communications, 2007. **28**: p. 955-961.
125. Yang, J.-L., et al., *On the characterization of tensile creep resistance of polyamide 66 nanocomposites. Part II: Modeling and prediction of long-term performance.* Polymer, 2006. **47**: p. 6745-6758.
126. Yang, J.-L., et al., *On the characterization of tensile creep resistance of polyamide 66 nanocomposites. Part I. Experimental results and general discussions.* Polymer, 2006. **47**: p. 2791–2801.
127. Zhang, W., et al., *Creep mitigation in composites using carbon nanotube additives.* Nanotechnology, 2007. **18**.
128. Zhang, Z., J.-L. Yang, and K. Friedrich, *Creep resistant polymeric nanocomposites.* Polymer, 2004. **45**: p. 3481–3485.
129. Zhou, T.H., et al., *A novel route for improving creep resistance of polymers using nanoparticles.* Composites Science and Technology, 2007. **67**: p. 2297–2302.
130. Siengchin, S. and J. Karger-Kocsis, *Creep Behavior of Polystyrene/Fluorohectorite Micro- and Nanocomposites.* Macromolecular Rapid Communications, 2006. **27**: p. 2090-2094.
131. Bondioli, F., et al., *High-Density Polyethylene Reinforced With Submicron Titania Particles.* Polymer Engineering and Science, 2008. **48**: p. 448-457.
132. Yang, J., et al., *Resistance to time-dependent deformation of nanoparticle/polymer composites.* Applied Physics Letters, 2007. **91**(1).
133. Cessna, L.C., *Stress-time superposition of creep data for polypropylene and coupled glass-reinforced polypropylene.* Polymer Engineering and Science, 1971. **11**(3): p. 211-219.
134. Nielsen, L.E., *Creep and Dynamic Mechanical Properties of Filled Polyethylenes.* Journal of Rheology, 1969. **13**(1): p. 141-166.
135. Brandrup, J., E.H. Immergut, and E.A. Grulke, eds. *Polymer handbook*. 4 ed. 1999, Wiley-Interscience: Hoboken, N.J. [etc.].
136. Mark, J.E., ed. *Polymer Data Handbook*. 1999, Oxford University Press: Oxford (USA).
137. German, R.M., *Powder metallurgy of iron and steel*. 1998, New York, N.Y. [etc.]: Wiley.

138. DiBenedetto, A.T., *Tailoring of interfaces in glass fiber reinforced polymer composites: a review.* Materials Science and Engineering A, 2001. **302**: p. 74-82.
139. Carreau, J.P., D.C.R. De Kee, and R.P. Chlabra, *Rheology of Polymeric Systems. Principles and Application*. 1997, Munich, Vienna, New York: Hanser Publishers.
140. Traina, M., A. Pegoretti, and A. Penati, *Processing And Electrical Conductivity Of High Density Polyethylene – Carbon Black Composites*, in *XVII Convegno Italiano di Scienza e Tecnologie delle Macromolecole*. 2005: Neaples.
141. Caceres, C.A. and S.V. Canevarolo, *Calculating the chain scission distribution function (CSDF) using the concentration method.* Polymer Degradation and Stability, 2004. **86**: p. 437-444.
142. Canevarolo, S.V., *Chain scission distribution function for polypropylene degradation during multiple extrusions.* Polymer Degradation and Stability, 2000. **709**: p. 71-76.
143. Clarke, R.L. and M. Braden, *Modified Arrhenius equation for the frequrncy dependence of the transition temperatures of polymers.* Biomaterials, 1989. **10**: p. 349-352.
144. Jha, A. and A.K. Bhowmick, *Thermal degradation and ageing behaviour of novel thermoplastic elastomeric nylon-6/acrylate rubber reactive blends.* Polymer Degradation and Stability, 1998. **62**: p. 575-586.
145. Kader, M.A. and A.K. Bhowmick, *Thermal ageing, degradation and swelling of acrylate rubber, fluororubber and their blends containing polyfunctional acrylates.* Polymer Degradation and Stability, 2003. **79**: p. 283-295.
146. Kelen, T., *Polymer Degradation*. 1982, New York: Van Nostrand Reinhold.
147. Brough, I., et al., *Scanning electron micrographs of high density polyethylene fracture surfaces.* Polymer, 2005. **45**(10): p. 3115-3123.
148. Rosca, I.D., et al., *Oxidation of multiwalled carbon nanotubes by nitric acidA.* Carbon, 2005. **43**(15): p. 3124-3131.
149. Lu, K.L., et al., *Mechanical Damage of Carbon Nanotubes by Ultrasound.* Carbon, 1996. **34**(6): p. 814-81.
150. Barbosa, S.E., et al., *Copolymerization of Polypropylene and Functionalized Linear a-Olefin onto Glass Fibers.* Journal of Applied Polymer Science, 2001. **81**: p. 1266-1276.
151. Vast, L., et al., *Preparation and electrical characterization of a silicone elastomer composite charged with multi-wall carbon nanotubes functionalized with 7-octenyltrichlorosilane.* Composites Science and Technology, 2007. **67**: p. 880-889.
152. Fadeev, A.Y., R. Helmy, and S. Marcinko, *Self-Assembled Monolayers of Organosilicon Hydrides Supported on Titanium, Zirconium and Hafnium Dioxides.* Langmuir, 2002. **18**: p. 7521-7529.
153. McElwee, J., R. Helmy, and A.Y. Fadeev, *Thermal stability of organic monolayers chemically grafted to minerals.* Journal of Colloid and Interface Science, 2005. **285**: p. 551-556.
154. Arai, Y., *Chemistry of Powder Production*. 1996, London: Chapman & Hall.
155. Gotoh, K., H. Masuda, and K. Higashitani, eds. *Powder Technology Handbook*. 1997, Dekker: 1997.
156. King, T.A., *Fundamentals of Ceramic Powder Processing and Synthesis*. 1996, San Diego: Academic Press.
157. Kwade, A. and J. Schwedes, *Breaking characteristics of different materials and their effect on stress intensity and stress number in stirred media mills.* Powder Technology, 2002. **122**(2-3): p. 109-121.
158. Peng, Z. and L.X. Kong, *A thermal degradation mechanism of polyvinyl alcohol/silica nanocomposites.* Polymer Degradation and Stability, 2007. **92**: p. 1061e1071.
159. Reich, L. and S.S. Stivala, *Elements of Polymer Degradation*. 1971, New York: McGraw-Hill.

160. Camacho, W. and S. Karlsson, *Assessment of thermal and thermo-oxidative stability of multiextruded recycled PP, HDPE and a blend thereof.* Polymer Degradation and Stability, 2002. **78**: p. 385–391.
161. Cruz, S.A. and M. Zanin, *Evaluation and identification of degradative processes in post-consumer recycled high-density polyethylene.* Polymer Degradation and Stability, 2003. **80**: p. 31-37.
162. Pinheiro, L.A., M.A. Chinelatto, and S.V. Canevarolo, *The role of chain scission and chain branching in high density polyethylene during thermo-mechanical degradation.* Polymer Degradation and Stability, 2004. **86**: p. 445-453.
163. Gupta, R.K., *Polymer and composite rheology*. 2000, New York, N.Y. [etc.]: Dekker.
164. Kanagaraj, S., et al., *Mechanical properties of high density polyethylene/carbon nanotube composites.* Composites Science and Technology, 2007. **67**: p. 3071–3077.
165. Assouline, E., et al., *Nucleation ability of multiwall carbon nanotubes in polypropylene composites.* Journal of Polymer Science Part B: Polymer Physics, 2003. **41**(5): p. 520-527.
166. Bhattacharyya, A.R., et al., *Crystallization and orientation studies in polypropylene/single wall carbon nanotube composite.* Polymer, 2003. **44**: p. 2373–2377.
167. Lozano, K. and E.V. Barrera, *Nanofiber-Reinforced Thermoplastic Composites. I. Thermoanalytical and Mechanical Analyses.* Journal of Applied Polymer Science, 2001. **79**: p. 125-133.
168. Chen, M., et al., *Effect of purification treatment on adsorption characteristics of carbon nanotubes.* Diamond & Related Materials, 2007. **16**: p. 1110-1115.
169. Poulin, P., B. Vigolo, and P. Launois, *Films and fibers of oriented single wall nanotubes.* Carbon, 2002. **40**(10): p. 1741-1749.
170. Vigolo, B., et al., *Macroscopic Fibers and Ribbons of Oriented Carbon Nanotubes.* Science, 2000. **290**: p. 1331-1334.

Publications and congress presentations

Matteo Traina, Alessandro Pegoretti and Amabile Penati. "*Fracture behaviour of high density polyethylene – carbon black composites evaluated by Essential Work of Fracture approach*". Poster contribution at "**8° Convegno Nazionale AIMAT**" (June 27th – July 1st, 2006; Palermo, Italy).

Matteo Traina, Alessandro Pegoretti and Amabile Penati. "*Fracture behaviour of high density polyethylene – carbon black composites evaluated by Essential Work of Fracture approach*". Oral contribution to "**1° Forum Nazionale dei Giovani Rivercati su Materiali Polimerici e Biomateriali**" (September 18th – 20th, 2006; Modena, Italia).

Matteo Traina, Alessandro Pegoretti, Amabile Penati and Silvia Elena Barbosa. "*Creep Behaviour of High-Density Polyethylene - Carbon Black Composites*". Oral contribution at "**3rd China-Europe Symposium on Processing and Properties of Reinforced Polymers**" (June 11th – 15th, 2007; Budapest, Hungary).

Matteo Traina, Alessandro Pegoretti and Amabile Penati. "*Polyethylene – Carbon Black Nanocomposites: Mechanical Response Under Creep and Dynamic Loading Conditions*". Oral contribution at "**VI Convegno Nazionale sulla Scienza e Tecnologia dei Materiali**" (June 12th – 15th, 2007; Perugia, Italy).

Matteo Traina, Alessandro Pegoretti, Amabile Penati. "*Creep Resistance of Polyethylene Micro- and Nanocomposites*". Poster contribution at "**Trento Innovation Conferences in Materials Engineering, 1st Meeting. Advances in Polymers, Composites and Biomaterials**" (December 16th – 19th, 2007; Trento, Italy).

Acknowledgements

First of all, I would like thank my tutors prof. Amabile Penati (Department of Materials Engineering and Industrial Technologies, University of Trento, Italy) and prof. Alessandro Pegoretti (idem) for their constant support throughout my graduate studies.

I would gratefully thank prof. Silvia Elena Barbosa (PLAPIQUI UNS-CONICET, Bahıa Blanca, Argentina) for her warm support during my stay in PLAPIQUI research centre in Bahia Blanca (Argentina).

I would gratefully thank doc. Gloria Ischia (idem) and prof. Stefano Gialanella (idem) for TEM observations, ing. Walter Bonani (idem) for SEM observations, prof. Sandra Dirè (Department of Materials Engineering and Industrial Technologies, University of Trento, Italy) for IR spectra of MWCNTs, prof. Riccardo Ceccato (idem) for adsorption measurements on MWCTNs, doc. Mariangela Fedel (idem) and Cristina Frova (PLAPIQUI UNS-CONICET, Bahıa Blanca, Argentina) for EDAX spectra of MWCNTs, María Julia Yañez (idem) for GPC measurements, Gustavo Massimiliani (idem) and Leica Microsystems SpA (Via Ettore Bugatti 12; 20142 Milano, Italy) for the preparation of ultrathin sections of HDPE09-CB composites by ultramicrotomy.

I would gratefully thank all the people which worked with me in the Polymers and Composites Laboratory of the Department of Materials Engineering and Industrial Technologies (University of Trento, Italy).

Last but not least, I would gratefully thank my family for the loving support trough all of these years. My parents Mario and Ines, and my brother Andrea.